PROTOTYPING FOR THE CENTRAL DETECTOR AND CP-VIOLATION STUDIES WITH THE CMS EXPERIMENT

Davide Francesco Vitè

A thesis submitted for the degree of Doctor of Philosophy of the University of London and Membership of the Diploma of Imperial College

March 1996

Imperial College
London

Abstract

The Large Hadron Collider, the proton-proton accelerator to be built at CERN within the next decade, will start a new generation of High Energy Physics experiments.

The CMS collaboration proposes to build a complex apparatus, described here, to detect signatures of new physics, namely Higgs bosons and SUSY particles, and, at the initial lower luminosities, to investigate B-physics issues. The particle fluxes expected in the CMS Central Detector will demand a proven radiation hardness. Test irradiations of MOS and MNOS structures and prototype silicon microstrip detectors, with ionising and non-ionising particles, are described in this thesis, with annealing behaviours and possible dose rate effects. Facilities and techniques of dosimetry are introduced.

The amount of material in the Central Detector was evaluated at various stages of the design, with realistic descriptions of the complete detector and programs to compute the radiation length of the components of the tracking system.

Several issues of physics to be investigated in CMS were studied: the capability of quantifying CP violation in B-meson decay channels, allowing measurement of the angles of the Unitary Triangle, was considered. The time-integrated and time-dependent CP violation asymmetries were considered, and means of enhancing the potential of the CMS apparatus were investigated.

Acknowledgements

First of all, I would like to express my gratitude to my supervisor, dr. Geoff Hall, who made possible my PhD studies at Imperial College. I deeply appreciated in every occasion his patience, help and support, and he always showed me trust and respect. He guided me throughout the whole of my research, and he has been an example of a prepared, organised, precise and open-minded scientist. I am very much indebted to him.

I had the great opportunity to spend quite some time at CERN, first in the RD20/SSDD group and then in the CMS group, where I could meet many people and friends. I can say I have learnt quite a lot from them. The first I have encountered have been Peter Weilhammer and Anna Peisert, already before I started my PhD at Imperial. I would like to thank them for having partecipated in my education, for having offered me my first job in physics, for their help and support.

Among the scientists I met at Imperial, I thank especially prof. Peter Dornan, head of our HEP group, for his example and for his support, and Richard Wheadon, who taught me so much about silicon microstrip detectors, and showed me many times how physics research should be performed.

Dziękuję to Gregorz Wrochna for the discussions on the CMS muon trigger and acceptances, *kiitos-grazie* to Kati Lassila-Perini for her help in getting me acquainted with `GEANT`; *Danke* to Thomas Meyer, *thanks* to Mike Price, *merci* to Gerard Smadja, *kiitos* to Martti Pimiä and *obrigado* to Rui Ribeiro for discussions and work together, regarding the evaluation of the material budget of the CMS Central Detector.

For many reasons I would like to thank Dario Bisello and the whole of the CMS Padova group, for their friendship and for the office sharing at CERN in particular.

I am grateful to Peter Clay from the Chemical Engineering department at Imperial College, who made available to us the IC gamma cell, and to Steve Watts and Mark Robbins from Brunel University, for the use of the gamma facility at Brunel. I am also indebted to Renato Turchetta and Wojciech Duliński from L.E.P.S.I., and Florent Kuntz and Alain Strasser from A.E.R.I.A.L. at CNRS in Strasbourg, France,

for their help in organising and performing the electron irradiations and dosimetries.

I would like to express my gratitude to Daniel Denegri and Avto Kharchilava for their help, teachings and discussions. Many thanks to Alessandra Caner; I learnt a lot from her when trying to analyse the tracker beam test data. *Molte grazie* to Rino Castaldi, Guido Tonelli, Ronaldo Bellazzini and their groups in Pisa, for many fruitful and friendly discussions. Thanks to Daniele Brambilla, Alessandra Filippi, Szymon Gadomski, Andrea Giraldo, Sergio Lupia, Pascal Pralavorio and Rashid Zuberi, for their friendship as well as for the discussions about physics (but not only).

Many thanks go also to the CMS spokesman, Michel Della Negra, to Ernst Radermacher and to Jim Virdee. I do wish them best of luck for the future of CMS. Thanks also to our efficient and nice secretaries, both at CERN (CMS, PPE) and at Imperial College (HEP).

I was fortunate to be a CERN guide, thanks to Régine Chareyron and Paola Catapano from the *Service des visites.* I could learn a lot about CERN life, experiments and accelerators, and also to talk to people about fundamental research and high energy particle physics.

I also apologise to Music, which I have so badly betrayed in favour of Physics for the last four years. I hope it will have been worthwhile, and I will attempt to get back to Her in the not too far future.

I acknowledge the love and support of my parents and my grandparents and of Antonella, to whom this thesis is dedicated. I do apologise for not having been there far too many times, and I will do my best to improve the situation in the future.

Contents

List of Figures

List of Tables

We are living at a time when the status of man is undergoing profound upheavals. Modern man is progressively losing his understanding of values and his sense of proportions. This failure to understand essential realities is extremely serious. It leads us infallibly to the violation of the fundamental laws of human equilibrium. In the domain of music, the consequences of this misunderstanding are these: on one hand there is a tendency to turn the mind away from what I shall call the higher mathematics of music in order to degrade music to servile employment, and to vulgarize it by adapting it to the requirements of an elementary utilitarianism [...]. On the other hand, since the mind itself is ailing, the music of our time, and particularly the music that calls itself and believes itself pure, *carries within it the symptoms of a pathologic blemish and spreads the germs of a new original sin. The old original sin was chiefly a sin of knowlegde; the new original sin, if I may speak in these terms, is first and foremost a sin of non-acknowledgement—a refusal to acknowledge the truth and the laws the proceed therefrom, laws that we have called fundamental. What then is this truth in the domain of music? And what are its repercussions on creative activity?*

Let us not forget that it is written: "Spiritus ubi vult spirat" (St. John, 3: 8). What we must retain in this proposition is above all the word WILL. The Spirit is thus endowed with the capacity of willing. The principle of speculative volition is a fact [...].

Igor Stravinski, *Poetics of Music,* lectures at Harvard College (1939-1940), transl. by A. Knodel and I. Dahl, Harvard Univ. Press (1942, 1947, 1970), lect. 3, 47-48.

Tu ne quaesieris, scire nefas, quem mihi, quem tibi
finem di dederint, Leuconoe, nec Babylonios
temptaris numeros. Ut melius, quidquid erit, pati.
Seu pluris hiemes seu tribuit Iuppiter ultimam,
quae nunc oppositis debilitat pumicibus mare
Tyrrhenum: sapias, vina liques, et spatio brevi
spem longam reseces. Dum loquimur, fugerit invida
aetas: carpe diem quam minimum credula postero.

Horace, *Carmina,* liber I no. XI (23 b.C.).

Introduction

During the different periods in the history of mankind, research in physics changed, sometimes dramatically, sometimes smoothly, and its focus, and even the meaning of *Physics* itself, varied with time. But what unchanged remained was its definition as a science—or discipline—of *understanding nature and its laws* and of *predicting the future,* i.e. calculating more or less precisely how nature would behave if defined initial conditions were imposed on a system whose evolution was kept under observation.

Very different domains have been investigated in this struggle for deeper and deeper understanding: astronomy, mechanics, gravitation, dynamics, optics, thermology and thermodynamics, fluidodynamics, material sciences, electricity and magnetism, atomic physics and radioactivity amongst many others, and eventually *quantum mechanics* and *relativity,* which opened wide the doors towards the high energy particle physics of today.

Methods, tools and background knowledge are now very different from those of Democritus, Pythagoras or Aristotle, but surprisingly the focus of research today is somehow more than ever oriented towards the nature of matter and its most elementary laws. We still want to believe that nature behaves in a *simple* and *smooth* way, and we want to organise coherently but as simply as possible all sets of data available to us, unifying wherever possible even rather different properties for the pure sake of unity and simplicity.

But is nature indeed simpleΓ Prof. Dennis Sciama, astrophysicist, mentions three possible explanations of the origin of the universe and of life and intelligence as we know them today: *chance, God* or *harmony* [i.1]. Cosmology and particle

physics inevitably lead to philosophical consequences in terms of basic and simple questions with extremely difficult answers. Many of us would find it hard to believe that everything which exists originated completely randomly or, on the contrary, was made and prepared in every detail for us. The harmony of nature as we know it, without being perfect, seems to be a plausible explanation. Those who prefer to believe in chance or in God might still define harmony a 'good God', or 'good luck'...

Universal physical constants, as e.g. the electron charge, with its implications for the elements and their stability, and also for light (photosynthesis) and vacuum properties, may have the values they actually have for the sake of an overall, cosmic harmony, from the most elementary laws to the widest universality. Another example is the total mass of the universe, sufficient or not for gravity to stop the proven cosmic expansion.

It is worth mentioning the theory put forward by the astrophysicist and cosmologist Edward Harrison, according to which our universe was created by the *intelligence* of a former universe, where physics and its laws were *essentially* (but not completely) identical. The theory of the *natural selection of universes* would propose that intelligent life created (consciouslyΓ unconsciouslyΓ) universes similar to its own, some of which were favourable to the birth of a new life with a higher degree of intelligence, and so on.

This selection process *à la Darwin* would explain why the values of the physical constants are 'the right ones' for life (as we know it...): the universes where the constants would have been less propitious came to an extinction, but the most favourable universes propagated the 'species' and made it evolve [i.2].

Particle physics today seems to be the core of both high energy physics and cosmology, and the general picture we now have can at the same time explain available data very well, and leave questions and challenges for the deep quest beyond. This picture is usually called the *Standard Model* of elementary particles and interactions.

The different forces of nature, redefined by field theory in terms of fundamental interactions, have been reduced in number to three, thanks to recent experiments performed in the last decade: *electroweak, strong* and *gravitational.* There are even hopes for further unifications.

Each fundamental interaction has a defined quantum field and one or more vector bosons responsible for the exchange of the interaction.

These fundamental interactions and the corresponding vector bosons are summarised in table i, along with some related properties [i.3, i.4]. As an example, the

relative strengths of interactions involving two protons in a nucleus are compared in table ii [i.4].

The thick dictionary of pseudo-elementary particles, compiled throughout this century and containing as many as a few hundred items, i.e. far too many to be considered elementary, has been ordered very elegantly, making use of only three families of pairs of quarks and leptons (table iii), with a total of twelve really elementary particles (and their C-symmetric companions, i.e. the corresponding antiparticles).

Precision LEP data exclude further lepton families, and the 'next-to-last' building block of this model was officially added this year (1995), when the CDF and DØ experiments at Fermilab observed evidence of production of the sixth, (lastΓ) and heaviest quark, the *top* quark. Fig. i shows a plot for the reconstructed top mass distribution, obtained by CDF [i.5].

CERN and a worldwide scientific community have proposed to build the LHC accelerator and its experiments because proton-proton collisions at the TeV centre-of-mass energy scale will allow, by the year 2005, an extensive search for the last missing brick of the Standard Model, which is at the same time the starting point for searches beyond: the Higgs boson, i.e. the heavy particle responsible for the primordial spontaneous symmetry breaking.

The Standard Model is practically based upon this symmetry breaking, which gave masses to light and heavy particles, and to the vector bosons $W^{\pm}$ and Z^0, while the photons (and the neutrinosΓ) remained massless.

As first examples of Higgs search, fig. ii and fig. iii show Higgs mass plots, for different precision electroweak data [i.6], and for a global fit to top and Higgs masses [i.7].

The Standard Model

The Standard Model is nowadays believed to describe physics correctly at least up to ~200 GeV, i.e. the energy region experimentally accessible up to now. This is based on the fact that all experimental tests of the predictions of this model have turned out to be positive. Of course the model is not yet completely tested, having many of its predictions not yet checked at all, for example those concerning the Higgs sector. Nevertheless, up to now the model is in perfect agreement with all experimental findings.

From a theoretical point of view, the Standard Model is not just based on an *effective* Lagrangian, as for example the *Fermi* theory of weak interactions is, but it is a *renormalisable field theory* [i.8].

The Standard Model is based on the gauge group

$$\mathrm{SU(3)}_C \times \mathrm{SU(2)}_\mathrm{W} \times \mathrm{U(1)}_Y$$

for the strong, electromagnetic and weak interaction between elementary particles: $\mathrm{SU(3)}_C$ is the symmetry group at the basis of the theory of strong interactions between coloured quarks and gluons [i.9], while $\mathrm{SU(2)}_\mathrm{W} \times \mathrm{U(1)}_Y$ is the symmetry group of the so-called *Glashow-Salam-Weinberg* theory [i.10], which describes accurately electroweak phenomena [i.11].

The gauge group for electroweak interactions contains an isovector triplet of weak SU(2) gauge fields, $\mathbf{A}_\mu$, and a neutral $\mathrm{U(1)}_Y$ gauge field, B_μ: from the orthogonal superimposition of A_3 and B, one gets the photon and the Z boson, while from the combination of A_1 and A_2 the bosons W^+ and W^- are obtained: $W^\pm_\mu = 1/\sqrt{2}\,\left(A^1_\mu \pm i\,A^2_\mu\right)$. The elementary particles are classified in *three generations of quarks and leptons,* arranged in SU(2) doublets and singlets according to their chirality:

$$I. \quad \begin{pmatrix} u \\ d \end{pmatrix}_L \quad \bar{u}_R \quad \bar{d}_R \qquad \begin{pmatrix} \nu_e \\ e^- \end{pmatrix}_L \quad e^+_R$$

$$II. \quad \begin{pmatrix} c \\ s \end{pmatrix}_L \quad \bar{c}_R \quad \bar{s}_R \qquad \begin{pmatrix} \nu_\mu \\ \mu^- \end{pmatrix}_L \quad \mu^+_R$$

$$III. \quad \begin{pmatrix} t \\ b \end{pmatrix}_L \quad \bar{t}_R \quad \bar{b}_R \qquad \begin{pmatrix} \nu_\tau \\ \tau^- \end{pmatrix}_L \quad \tau^+_R$$

The requirement of a definite chirality is a consequence of the parity non-conservation of electroweak interactions: it has been found experimentally that the weak charged currents contain only left handed spinors. For the same reason, in order to avoid the presence of right handed charged currents, the right handed components belong to weak isospin singlets. The neutrino is assumed to be massless: ν_R is absent.

The charge of the 'up' component of each quark weak isodoublet is $+2/3$, while it is $-1/3$ for the 'down' component; the electric charge is related to the weak hypercharge Y[1], the generator of the U(1) group, by the relation

$$Q = T_3 + Y \,,$$

[1]Some authors define the weak hypercharge as $Y/2$, and the relation with the electric charge and the weak isospin becomes $Q = T_3 + Y/2$.

where T_3 is the diagonal component of the weak isospin operator. The hypercharge is $+1/6$ for each quark belonging to isodoublets ($T_3 = \pm 1/2$), while it is respectively $-2/3$ for the right-handed 'up'-like antiquarks, and $+1/3$ for the right-handed 'down'-like antiquarks, both belonging to weak isospin singlets. On the contrary, since in every leptonic SU(2) doublet each charged lepton ($Q = -1$) is paired with a chargeless neutrino, the hypercharge for every doublet is $-1/2$, and it is $+1$ for the right-handed lepton.

A conventional mechanical mass term in the Lagrangian density of matter fields cannot be introduced, as it would violate the SU(2) gauge symmetry: therefore, in this theory, the particle masses can arise only by means of a *spontaneous symmetry breaking* of SU(2). For this purpose one introduces a doublet of complex *'Higgs'* scalar fields, usually of the form

$$\phi = \begin{pmatrix} \phi^+ \\ \phi^0 \end{pmatrix}$$

The mass term is now written in an invariant way.

The field

$$(\phi^0 + \bar{\phi^0})/\sqrt{2}$$

gives mass not only to all fermions–neutrinos excluded–but even to the gauge bosons. The charged gauge bosons receive a mass

$$M_W = \frac{1}{2} g_2 \, v \, ,$$

one of the neutral ones receives a mass

$$M_Z = \frac{1}{2} v \sqrt{g_1^2 + g_2^2} \, ,$$

while the other, the photon, remains massless. Here v represents the vacuum expectation value of the Higgs neutral field, and g_1 and g_2 are the gauge couplings related to the gauge fields U(1) and SU(2): these three parameters can be experimentally determined by the electromagnetic coupling constant e, the Fermi coupling constant G_F and a measurement of the strength of weak neutral currents.

Using the Weinberg angle θ_W, by which the gauge fields are orthogonalised, the following relations hold:

$$\frac{G_F}{\sqrt{2}} = \frac{g_2^2}{8 M_W^2} = \frac{1}{2} v^2 \, , \text{ and}$$

$$e = g_2 \sin\theta_W = g_1 \cos\theta_W \, ,$$

by which v is determined to be of the order of 250 GeV, and

$$M_W \simeq \frac{38 \text{ GeV}}{\sin\theta_W}$$

as well as

$$M_Z \simeq \frac{38 \text{ GeV}}{1/2 \sin 2\theta_W} ;$$

from the strength of the weak neutral currents one obtains

$$\sin^2\theta_W \simeq 0.22 .$$

The consistency of the W and Z masses with this prediction is a sensitive test of the model. However, the mass of the remaining scalar field, the Higgs particle, remains a completely undefined parameter. To this point, the Standard Model does not make any definite predictions: a neutral scalar particle should exist with a mass somewhere between $\sim$10 and $\sim$1200 GeV; the upper limit is claimed by the request of unitarity conservation on the WW scattering amplitude and the validity of perturbative methods.

No predictions arise from the model concerning the quark and lepton masses either. All mass terms are provided by Yukawa couplings, and they have to be conveniently adjusted in order to obtain the measured values of the fermion masses, which thus are inserted in the model 'by hand'; moreover, the wide difference of masses between the different generations is not completely understood yet.

In addition to this, the quark mass matrix is not diagonal in the weak basis: the mass eigenvalues are obtained by a mixing between different generations. The mixing occurs by means of the Kobayashi-Maskawa matrix [i.12], whose detailed description will be given later.

Anyway, the electroweak sector is now considered to be fairly well understood; conversely, the strong part of the model is less consolidated, due to a major difficulty given by the rapid *running* of the coupling constant with the energy scale. In this case the symmetry group is $SU(3)_C$, and by gauging it we obtain QCD, the currently favoured model for strong interactions.

The gauge bosons of QCD are eight massless gluons of spin 1; each of them, as well as each quark is given a 'colour' quantum number: more precisely, each field belongs to a triplet state of colour. Some evidence exists in favour of the presence of this new internal degree of freedom: for instance, it helps when solving some technical problems like quark statistics, the π^0 decay rate and the existence

of triangle anomalies (mentioned in section 6.1); experimentally, it explains the behaviour of the ratio R

$$R = \frac{\sigma(e^+e^- \rightarrow \text{hadrons})}{\sigma(e^+e^- \rightarrow \mu^+\mu^-)} ,$$

and the existence of the Ω^- baryon, made of three quarks s.

The strong interaction is *colour blind,* in the sense that it is invariant under the $SU(3)_C$ group transformations which mix up colours. At present, there is no evidence that physical hadrons are not colour singlets: this is the reason why coloured quarks and gluons are generally believed to be *confined* at low energies, but at very high energies, i.e. at very short distances, they should behave as free particles.

Beyond the Standard Model

In spite of its success, recently confirmed by the discovery of the top quark, the Standard Model is probably not the final theory of the world since, apart from gauge couplings, it needs some *twenty* free parameters to adjust masses, mixing angles and Yukawa couplings; the Higgs sector is still completely mysterious.

It is worth adding that among the properties of the Higgs particle, it turns out that its mass is subject to *quadratic divergences* in perturbation theory. The problem of quadratic divergences may be solved in the framework of supersymmetry [i.13]: according to supersymmetric field theories, every fermion has to be paired with a bosonic *superpartner,* and vice-versa, so that the divergent contributions from each particle cancel out at the end.

The SUSY extension of the Standard Model with the minimum number of particles is known as Minimal Supersymmetric Standard Model (MSSM): in addition to all the properties of Standard Model, it has to contain a soft mechanism for the breakdown of supersymmetry that splits the masses of the known particles from those of their SUSY partners. The particle content is more than doubled: for example, in order to respect all gauge invariances and to give masses to all the fermions, one has to introduce at least *two* Higgs doublets; after symmetry breaking, one is left with three spin zero particles, two scalars and one pseudoscalar, the lighter of which may be identified with the Standard Model Higgs.

So, apart from a real improvement in the convergence properties of the model, SUSY theories essentially do not add anything new to our knowledge with respect to the questions arisen by the Standard Model, like the origin of the fermion masses or the reason of the three generations.

Another trend of development is proposed in the framework of *grand unified theories,* whose aim is to unify the gauge interactions $\mathrm{SU}(3) \times \mathrm{SU}(2) \times \mathrm{U}(1)$ in a larger group. The simplest model unifies the gauge group in SU(5) [i.14]: this means essentially that the three coupling constants g_3, g_2 and g_1 would be unified to a unique constant.

The fact that at an energy of the order of a hundred GeV the three coupling constants are very different from each other is not a strong indication for unification. At the moment this minimal model has indeed some difficulties, because of the absence of the proton decay at the predicted rate [i.15].

interaction	**electromagnetic**	**weak**	**strong**	**gravitational**
property	electric charge	weak isospin	colour	mass (energy)
particles feeling the interaction	all charged particles	quarks and leptons	quarks and gluons	all
mediators	photon	$W^{\pm}$, Z^0	gluons	graviton (?)
mass	0.	81/91 GeV/c^2	0.	0.
charge	0.	± 1, 0	0.	0.
$spin^{parity}$	1^-	$1^{\mp}$	1^-	2^+
range	∞	$\sim 10^{-18}$ m	$\sim 10^{-15}$ m	∞

Table i. Fundamental interactions and vector bosons.

interaction	strength (relative to electromagnetic)
electromagnetic	1
strong (residual)	~ 20
weak	10^{-7}
gravitational	10^{-36}

Table ii. Relative strengths of interactions for two protons in a nucleus.

$$\begin{pmatrix} u \\ d \end{pmatrix} \quad \begin{pmatrix} c \\ s \end{pmatrix} \quad \begin{pmatrix} t \\ b \end{pmatrix}$$

$$\begin{pmatrix} e^- \\ \nu_e \end{pmatrix} \quad \begin{pmatrix} \mu^- \\ \nu_\mu \end{pmatrix} \quad \begin{pmatrix} \tau^- \\ \nu_\tau \end{pmatrix}$$

Table iii. Quark and lepton families.

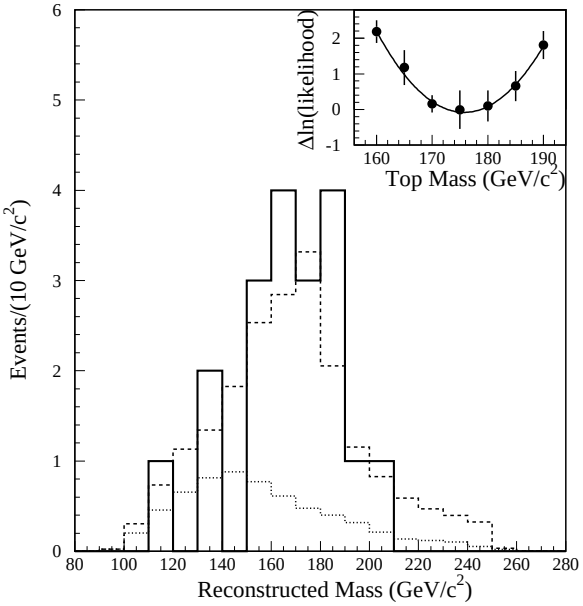

Fig. i. Reconstructed mass distribution for the b-tagged W + $\geq$ 4-jet events at CDF [i.5].

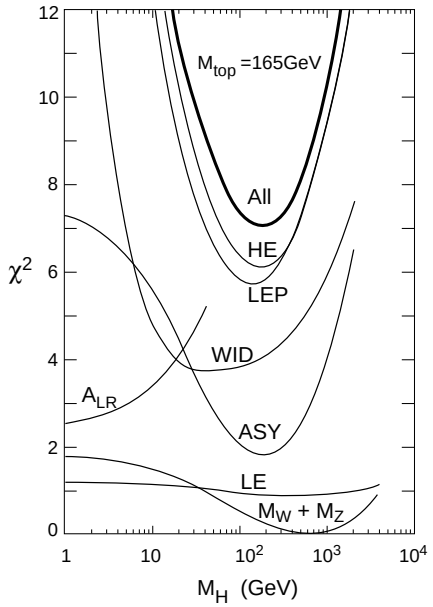

Fig. ii. χ^2 as a function of the Higgs mass, for different precision electroweak data [i.6].

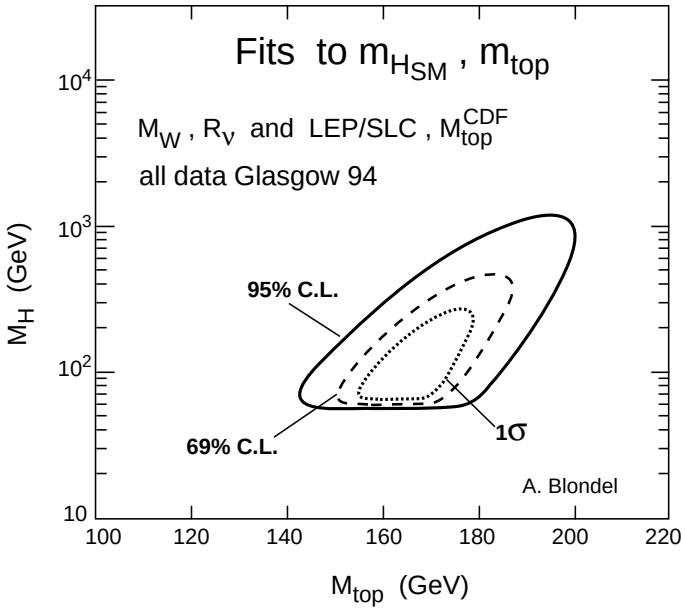

Fig. iii. Contours of constant χ^2 for the global fit to top and Higgs masses [i.7].

Chapter 1

The CMS experiment

The next generation of High Energy Physics experiments will start with the construction and operation of the next collider to be built at CERN, Geneva, Switzerland: the *Large Hadron Collider,* or **LHC**. Construction of this 14 TeV center-of-mass symmetric proton-proton collider has been approved by the CERN Council in December 1994, and the beginning of operation is presently foreseen in the year 2004. LHC will use the presently existing and operating accelerators, namely the PS Booster, the PS and the SPS proton synchrotrons, as injectors.

The prospects for possible physics studies, particularly in the Standard Model (SM) and Minimal Supersymmetric Standard Model (MSSM) *Higgs* searches, are very wide and aimed at probing thoroughly the Standard Model, enhancing every possibility of detecting signatures of new physics, but without forgetting that LHC will be intrinsically a beauty- and top-factory. Heavy ion collisions are also part of the already planned LHC experimental programme.

LHC will be the biggest hadron collider ever built and operated since the *Tevatron* collider, a 2 TeV center-of-mass proton-antiproton collider, operating since 1987 at Fermilab, Batavia, Illinois (USA), with the CDF and DØ experiments presently in the data taking phase.

The LHC nominal full luminosity of 10^{34} cm^{-2}s^{-1} (referred to as *high luminosity*) will be reached gradually from the start-up time, thus allowing initial data taking at a luminosity of about 10^{33} cm^{-2}s^{-1} (referred to as *low luminosity*). This period of probably a couple of years will be used for low luminosity physics such as B-physics and CP-violation studies among others.

Typical integrated luminosities per 'year' of operation are defined to be 10^4 pb^{-1} for low luminosity LHC operation, and 10^5 pb^{-1} for high luminosity operation. A 'year' of LHC operation in considered to be equal to 10^7 s, corresponding to about 116 equivalent 24-hour days of uninterrupted operation.

The basic concept of the **CMS** *(Compact Muon Solenoid)* detector for operation at the LHC was presented at the LHC Workshop in Aachen in October 1990 [1.1], and consisted of a *compact* detector with an optimised muon detection system, thus implying a strong magnetic field, generated by a solenoid.

Since the Evian meeting in March 1992 [1.2], where the **CMS** proto-collaboration, constituted of 49 institutions, presented an Expression of Interest, the following objectives were already forming the basis of the conceptual design of the complete detector:

- a long and large radius superconducting solenoid, providing a high magnetic field (4 T) and containing in its bore the central tracking and the calorimeters;
- a very good, redundant and compact muon detection system;
- the best possible electromagnetic calorimeter, consistent with the choice of the magnet;
- high quality central tracking, reconstructing all high p_t charged tracks with good efficiency and momentum resolution;
- a financially affordable detector, to be first built in a *staged* version, if unavoidable.

The muon detection system consists of four muon stations, both in the barrel and in the endcaps of the detector, also containing detectors dedicated to the trigger. Between each station one or more layers of iron constitute the return yoke of the CMS magnet.

The decision on the medium for the electromagnetic calorimeter was taken in Autumn 1994, after R&D activities and tests: CMS is now proposing to construct a high-resolution, high-granularity lead tungstate ($PbWO_4$) totally active crystal electromagnetic calorimeter, the strictest requirements on which are dictated by the detection of the intermediate mass (80 GeV to 140 GeV) Higgs boson decaying into two photons.

The central detector, composed of silicon pixel detectors, silicon microstrip detectors and microstrip gas chambers, provides tracking with secondary vertex reconstruction and good momentum and impact parameter resolution.

The CMS Letter of Intent (LoI) was presented in October 1992 [1.3], and more recently the open presentation of the CMS Technical Proposal (TP) took place on January 19th, 1995 [1.4].

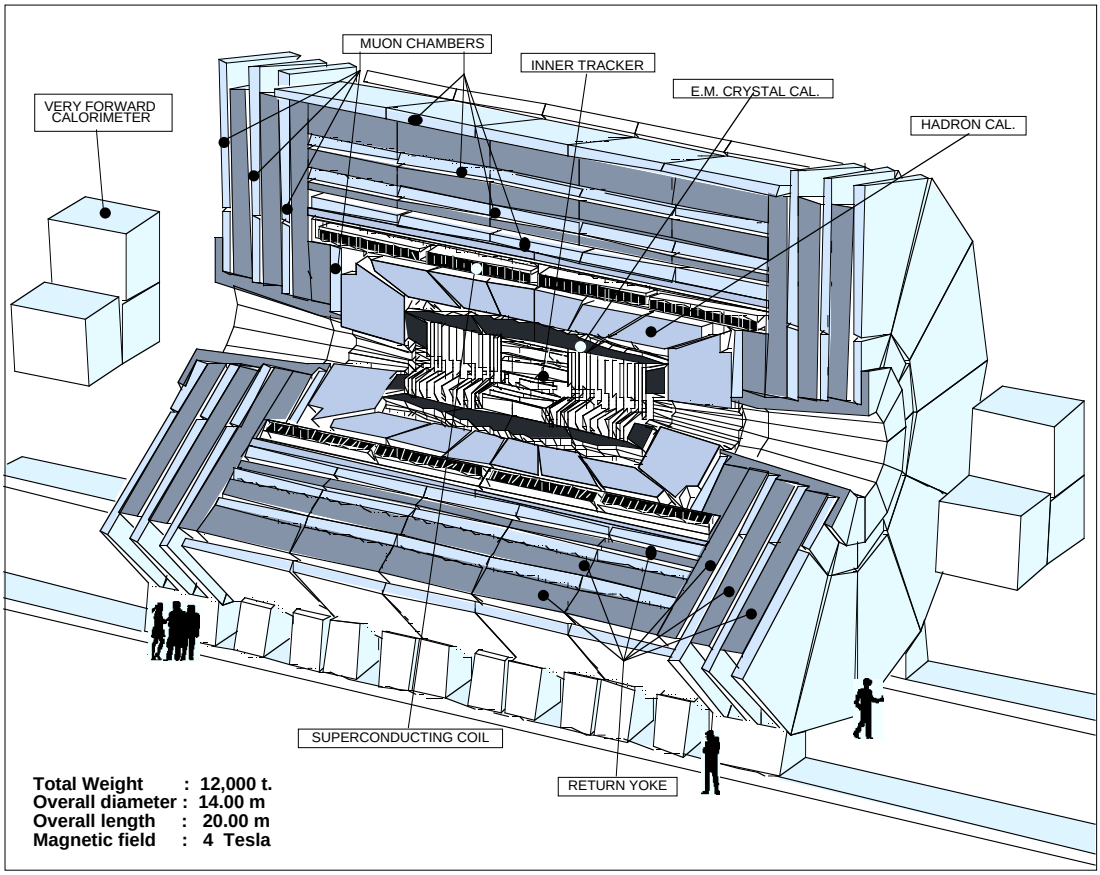

Fig. 1.1. Three-dimensional view of the CMS detector.

The estimated total cost of the complete CMS detector is now about 450 million Swiss Francs (about 230 million GB Pounds).

The complete CMS design, as it is described in the Technical Proposal, is shown in fig. 1.1, representing a three-dimensional view of the detector; fig. 1.2 shows the longitudinal view of CMS, whilst in fig. 1.3 a transverse view of the detector is shown.

The CMS collaboration is a worldwide collaboration of universities and research institutes, both from CERN member- and non member-states; a summary is shown in table 1.1. The Imperial College group is involved in detector and front-end electronics developments for the CMS central detector, in software developments and in simulations of the physics performance of the CMS apparatus in general and of the central detector in particular.

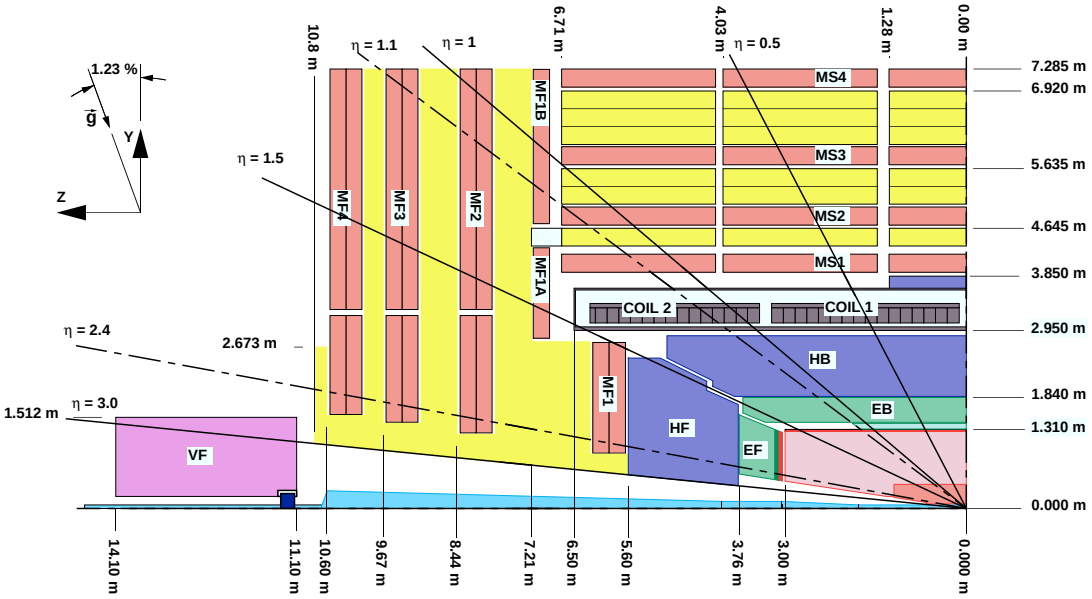

Fig. 1.2. Longitudinal view of the CMS detector.

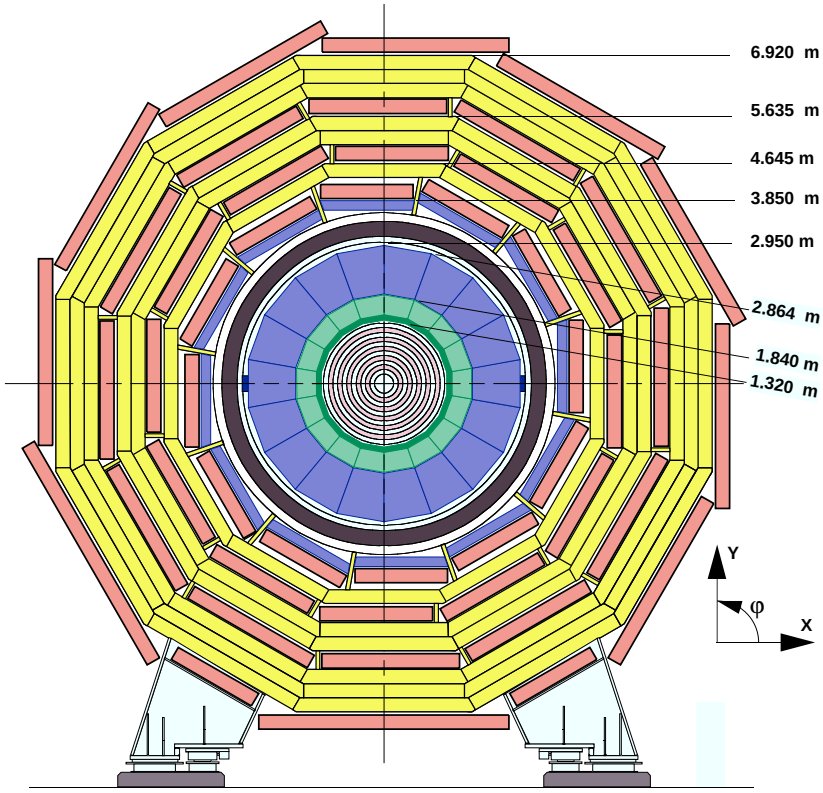

Fig. 1.3. Transverse view of the CMS detector.

	Institutions	**Collaborators**
CERN Member States	60	607
Non-member States (excl. USA)	35	344
USA	37	292
Total	132	1243

Table 1.1. Summary of physicists and engineers in the CMS collaboration (December 1994).

Parameters	**protons**	**Pb ions**
Circumference	26.659 km	
Dipole field	8.386 T	
Number of 14.2 m dipoles (MB)	1232	
Number of 3.1 m quadrupoles (MQ)	386	
Operational energy	14 TeV	1148 TeV
Energy per proton/nucleon	7 TeV	2.76 TeV
Luminosity	10^{34} cm^{-2}s^{-1}	10^{27} cm^{-2}s^{-1}
Bunch spacing	7.48 m	37.4 m
Bunch separation	24.95 ns	124.75 ns
Bunch interval	40 MHz	8 MHz
Particles/ions per bunch	10^{11}	10^{8}
Particles/ions per beam	4.7×10^{14}	5.2×10^{10}

Table 1.2. Main LHC parameters for proton and lead ion collisions [1.5].

1.1 Physics expected at the LHC

The CMS proton-proton collider experiment is a general purpose detector designed and optimised for the discovery and the thorough investigation of the Standard Model (SM) Higgs boson, over a wide mass range.

Signatures of other possible electroweak symmetry breaking mechanisms, such as the Minimal Supersymmetric Standard Model (MSSM) Higgs bosons, will be detectable, and a broad programme of top, beauty and tau physics will be possible. Heavy ion LHC operation has also been considered and simulated.

It is not possible to describe here all the new physics possibilities which will be open at the LHC: detailed summaries can be found in [1.3, 1.4]. B-physics and CP-violation will be addressed again later in detail (Chapter 6).

The main LHC parameters are summarised in table 1.2 [1.5]. It is obvious that, in this new colliding particle environment, some experimental issues will arise, at

levels never reached before:

1. very high rate operation: bunch crossing frequency for proton-proton collisions of 40 MHz;
2. high fluxes of charged and neutral particles: high radiation environment;
3. ~20 proton-proton interactions occur per bunch crossing, at the full design luminosity;
4. high detector granularity, thus unprecedented numbers of read-out channels, to keep the occupancies acceptable;
5. complex multiple-level trigger algorithms.

The physics programme will now be outlined briefly.

1.1.1 LHC physics at high luminosity

The LHC will be built to generate proton-proton collisions at a luminosity of 10^{34} cm^{-2}s^{-1} and at a centre-of-mass energy of 14 TeV. Some typical cross sections for proton-proton collisions, as a function of the centre-of-mass energy, are shown in fig. 1.4, where the corresponding production rates at the LHC design conditions (~10^9 collisions/s, i.e. about 20 interactions per bunch crossing) are also indicated.

The most important physics topic during high luminosity operation of the LHC is undoubtedly the search for the mechanisms responsible for electroweak symmetry breaking. The Standard Model (SM) Higgs boson is the first possibility for such a mechanism, and it will be detectable in CMS over a wide mass range. Table 1.3 shows some favourable final states for different Higgs mass ranges.

As an example, fig. 1.5 shows the 2γ mass plot, for an integrated luminosity of 10^5 pb^{-1} (one year at high luminosity), with H $\rightarrow \gamma\gamma$ signals superimposed at $m_H =$ 90, 110, 130 and 150 GeV. This possible intermediate mass SM Higgs boson channel has been used as a benchmark for the optimisation of the CMS electromagnetic calorimeter. Fig. 1.6 shows the signal significance contours for the same channel, always for 10^5 pb^{-1}. Even after three years of low luminosity operation, with an integrated luminosity of about 3×10^4 pb^{-1}, a Higgs discovery in this final state would be possible, but with a lesser signal significance over a narrower Higgs mass range.

The minimal extension of the Standard Model (SM) to a supersymmetric theory is the Minimal Supersymmetric Standard Model (MSSM), whose Higgs sector contains one charged ($H^{\pm}$), two CP-even (h, H) and one CP-odd (A) light elementary

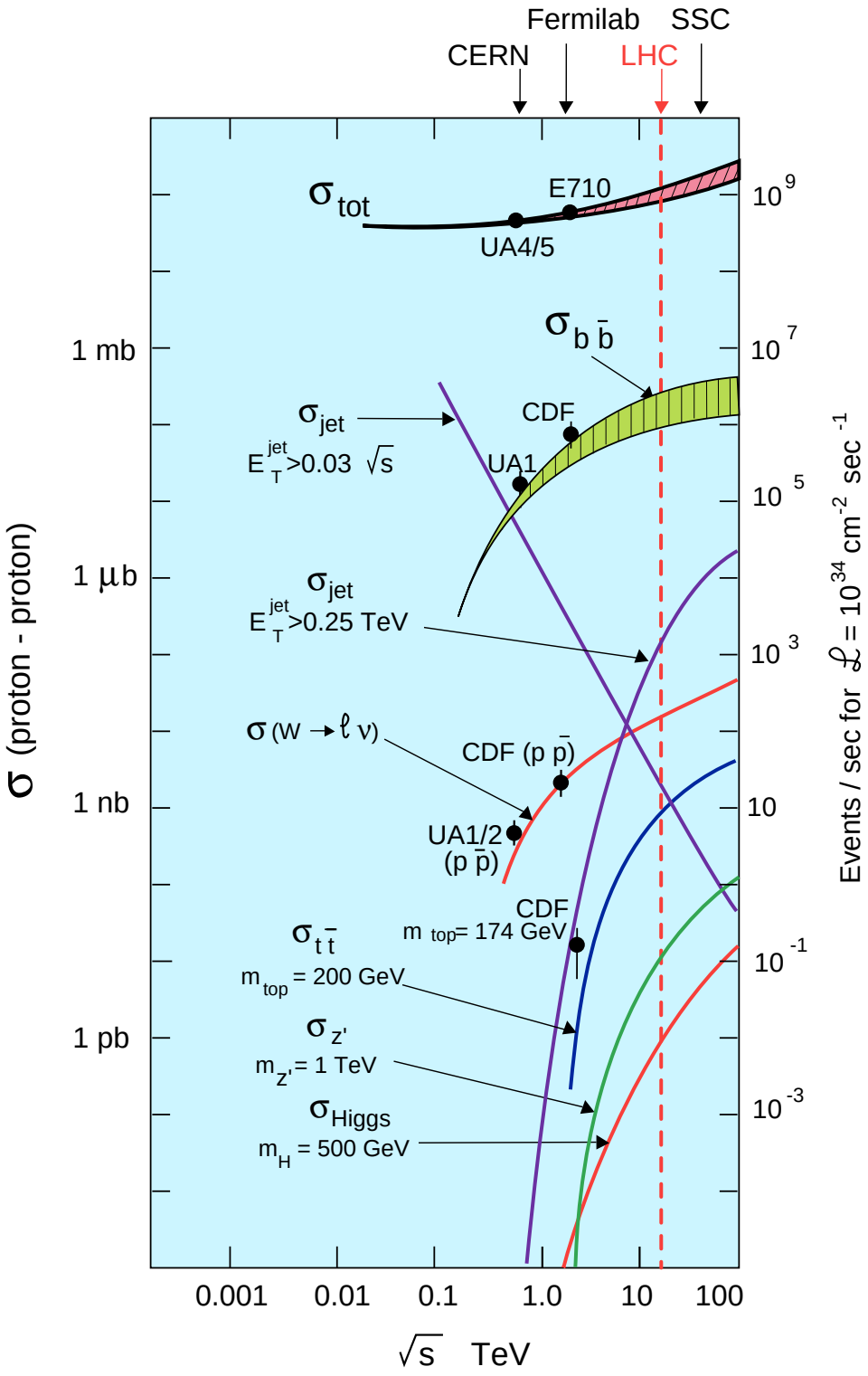

Fig. 1.4. Typical cross sections for proton-proton collisions.

final states	**mass ranges**
H $\rightarrow \gamma\gamma$ H $\rightarrow \gamma\gamma$ with hard jets ass. product. HW, H$t\bar{t}$ (H $\rightarrow \gamma\gamma$)	80 GeV $\leq m_H \leq$ 140 GeV
H $\rightarrow$ ZZ* $\rightarrow 4l^{\pm}$ H $\rightarrow$ ZZ $\rightarrow 4l^{\pm}$ H $\rightarrow$ ZZ $\rightarrow 2l^{\pm}\,2\nu$	130 GeV $\leq m_H \leq$ 200 GeV 200 GeV $\leq m_H \leq$ 650 GeV 500 GeV $\leq m_H \leq$ 1 TeV
H $\rightarrow$ WW $\rightarrow l\nu$ jj H $\rightarrow$ ZZ $\rightarrow ll$jj	$m_H \simeq$ 1 TeV $m_H \simeq$ 1 TeV

Table 1.3. Favourable final states for different Higgs mass ranges.

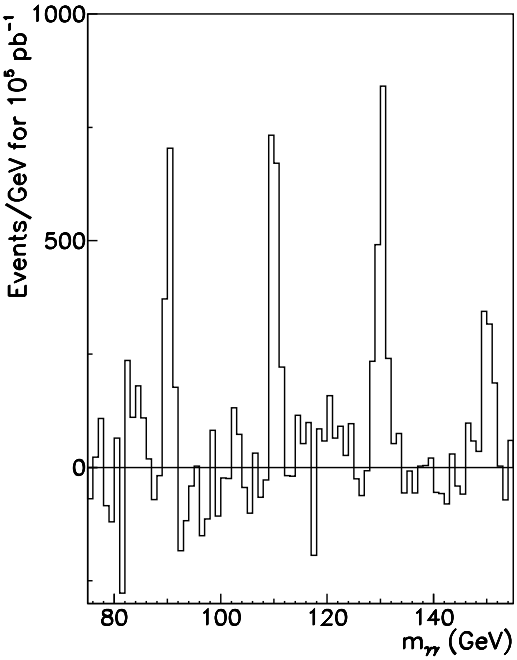

Fig. 1.5. H $\rightarrow \gamma\gamma$ mass plot.

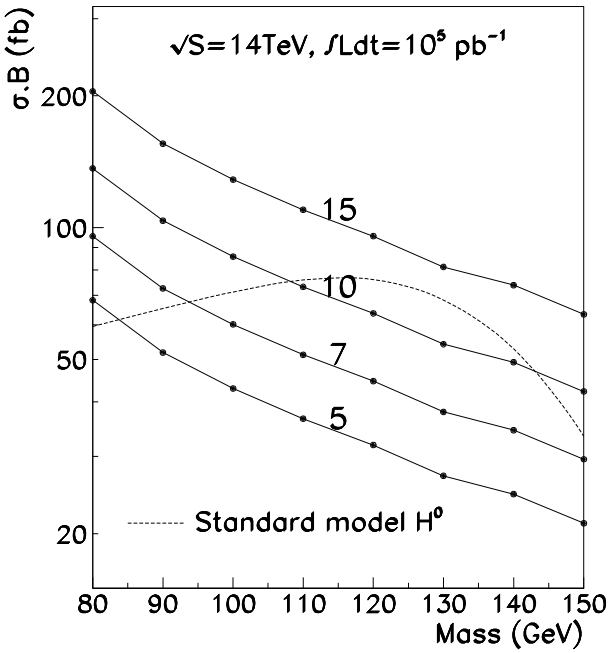

Fig. 1.6. Signal significance contours for H $\rightarrow \gamma\gamma$.

Higgs boson states. Their masses and couplings can be expressed in terms of two parameters, m_A and tanβ .

Some of the possible channels which will be explored to detect the existence of MSSM Higgs bosons are listed in table 1.4. Figure 1.7 shows the 5σ significance contours, in the MSSM (m_A , tanβ) space, explorable through various SUSY Higgs channels.

Finally, supersymmetric gluons – *gluinos* – and quarks – *squarks* – will be searched for in a mass region above the range to be reached by the enhanced luminosity Tevatron accelerator at Fermilab, i.e. for $m_{\tilde{g},\tilde{q}} > 300$ GeV. Other high-luminosity physics possibilities are described elsewhere [1.3, 1.4].

1.1.2 LHC physics at low luminosity

The first few years of operation at low luminosity will allow extensive studies of beauty and top physics, while preparing for high luminosity running.

The large $b\bar{b}$ production rate will in particular enable rare decay searches and CP-violation studies, with possible improvements on the precisions by then reached elsewhere on some measurements. The main B-physics possibilities in CMS will be CP-violation studies ($B_d^0 \rightarrow J/\psi\, K_s^0$, $B_d^0 \rightarrow \pi^+\pi^-$, etc.), control channels for CP-

MSSM Higgs boson searches
h, H $\rightarrow \gamma\gamma$
H $\rightarrow$ ZZ*, ZZ; h $\rightarrow$ ZZ*
h, H, A $\rightarrow \tau\tau \rightarrow l^{\pm} + \mathrm{h}^{\pm} + \mathrm{X}$
t $\rightarrow \mathrm{H}^{\pm}$ b $\rightarrow \tau\nu$b
h, H, A $\rightarrow \mu^{+}\mu^{-}$
h, H, A in ass. product. $b\bar{b}\,\mathrm{H}_{\mathrm{SUSY}}$
A $\rightarrow$ Zh $\rightarrow ll\,b\bar{b}$

Table 1.4. MSSM Higgs bosons searches.

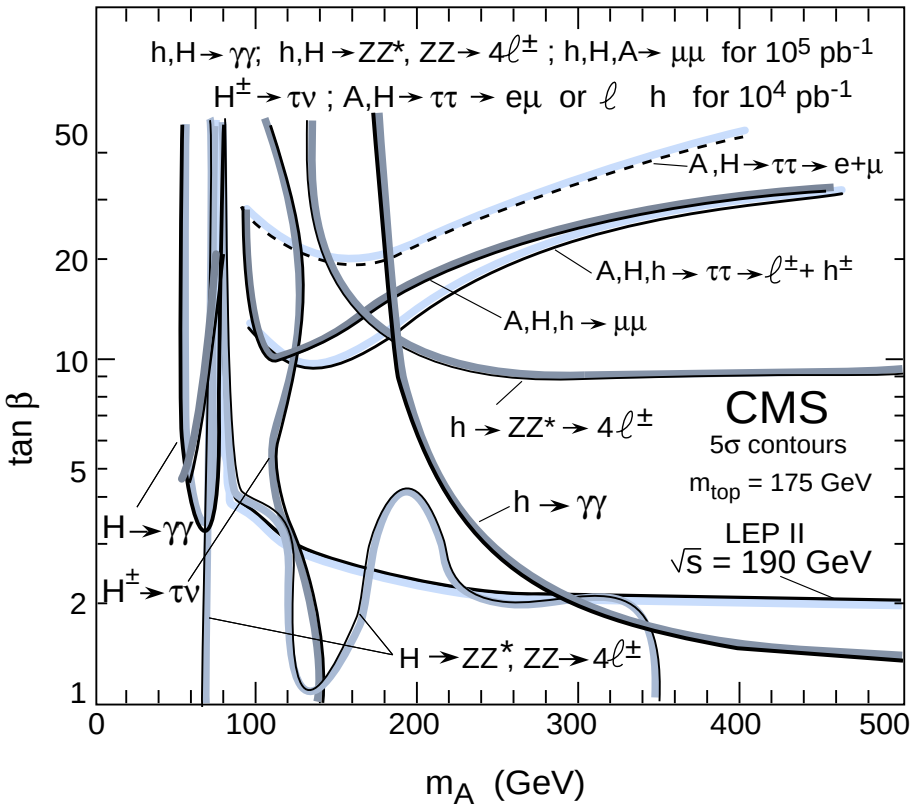

Fig. 1.7. 5σ significance contours in the MSSM (m_A , tanβ) space.

violation, production asymmetries and dilution factors, rare decays, $B_s^0/\bar{B}_s^0$ oscillations and B-baryon studies. B-physics and CP-violation will be discussed more completely in Chapter 6.

Other important topics, such as top physics, have been discussed in [1.3]. In addition, prompt photon production, anomalous gauge couplings via WZ and Wγ production, jet production, total cross sections and multiparticle production will be studied.

Finally, Higgs boson searches in the mass range of 200 to 500 GeV, and squark and gluino searches will also be investigated at the initial lower luminosities.

1.1.3 Heavy ion physics

The LHC machine will be also used as a heavy ion collider, with a centre-of-mass energy of about 5.5 TeV per nucleon pair, at a luminosity of about 10^{27} cm^{-2}s^{-1} , relative to PbPb collisions. Nuclides such as ^{16}O, ^{40}Ca, ^{97}Nb and ^{208}Pb are expected to be used for this purpose. Unprecedented collision energy densities of 4 to 8 GeV/fm^3 should be above the threshold for quark-gluon plasma (QGP) formation, a new form of deconfined hadronic matter.

One of the cleanest signatures of the formation of this new state of matter would be the observation of anomalies in the production rates of heavy quark bound states ($c\bar{c}$ and $b\bar{b}$), J/ψ, ψ' and the Υ family (Υ, Υ', Υ''), with respect to those in proton-proton collisions. These resonant states would decay into muon pairs, then detected by the CMS muon spectrometer.

As an example, figure 1.8 shows the mass distributions of opposite sign muon pairs for PbPb and CaCa collisions, after 15 days of running: the Υ, Υ', Υ'' peaks would be clearly visible, and anomalies could be detected.

The possibility of observing jet quenching in CMS was also studied; jets would be produced early in the heavy ion collisions, and they would first propagate through the QGP, interacting with its constituents, before escaping, therefore carrying information about the deconfined hadronic matter. In this study, the CMS calorimeters obviously play a crucial role.

Concluding, simulations show that only a few days of heavy ion operation at the LHC would already allow CMS to investigate the nature of the QGP, thanks to its muon spectrometer and calorimeter performance.

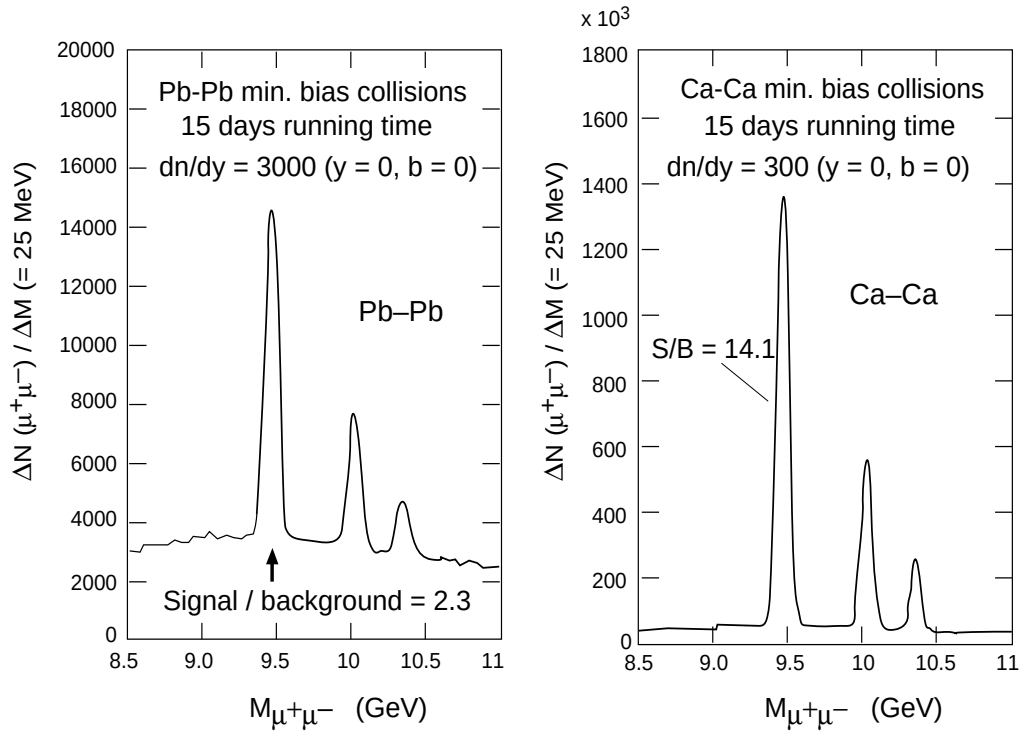

Fig. 1.8. Mass distributions of opposite sign muon pairs for PbPb and CaCa collisions.

1.2 Description of the CMS detector

The 4π CMS detector can generally be subdivided in one 'barrel' region and two identical 'forward' or 'endcap' regions, also normally referred to simply as *barrel* and *forward* or *endcaps.*

A characteristic feature of CMS is a large superconducting solenoid, 13 m long and with an inner radius of 2.95 m, which will provide a uniform magnetic field of 4 T. The 1.8 m thick saturated iron yoke, instrumented with layers of muon stations, will return the magnetic flux, with a field of about 2 T, thus simplifying the design by using a single magnet. The large bending power of the magnet will allow both precise inner and muon tracking, and flexible muon trigger thresholds.

A large fraction of the soft charged tracks generated by minimum bias events will be bent into spirals by the high field, and will not reach the outer regions of the central tracker, thus simplifying (relatively) pattern recognition and track reconstruction.

The high magnetic field and the iron return yoke keep the whole detector compact and smaller. The overall length (excluding the very forward calorimeters) and diameter are respectively 22 m and 14.6 m; its total weight will be about 14500 tons.

The standard set of coordinates used to identify space points within the CMS detector makes use of the z-coordinate, with axis parallel to the beam line and origin at the nominal interaction point, and of the projection of the point onto the (r, ϕ) plane—or (x, y) plane—i.e. the *transverse plane.*

The *pseudorapidity* η is also used frequently,

$$\eta = \frac{1}{2} \ln \left(\frac{p + p_z}{p - p_z} \right) = -\ln \tan \frac{\vartheta}{2} \ , \tag{1.1}$$

ϑ being the zenith angle measured from the positive z-semiaxis, p and p_z being respectively the total momentum of a particle—with pseudorapidity η—and its projection onto the z-axis ($\vec{p} = \vec{p}_T + \vec{p}_z$, $|\vec{p}_z| = |\vec{p}| \cos \vartheta$).

It must be noted that the pseudorapidity η is often imprecisely identified, probably for the sake of conciseness, with the *(true) rapidity* y,

$$y = \frac{1}{2} \ln \left(\frac{E + p_z}{E - p_z} \right) = \ln \left(\frac{E + p_z}{m_T} \right) = \tanh^{-1} \left(\frac{p_z}{E} \right) \ , \tag{1.2}$$

where E is total energy of the particle ($E^2 = p^2 + m^2$) and m_T is the transverse mass ($m_T^2 = m^2 + p_x^2 + p_y^2 = E^2 - p_z^2$). This misidentification is obviously more inexact the more massive the particle in question is, the two units becoming identical for massless particles.

These units, in particular the rapidity y, are used in particle physics because rapidity distributions such as dN/dy or $d\sigma/dy$ are invariant for Lorentz boosts in the z-direction, i.e. $y \rightarrow y - \tanh^{-1} \beta$ under such transforms, where β is, in this case, the relative velocity v_z/c for the Lorentz frame considered. Therefore, transformations to different reference frames under boosts along the beam axis simply result in a shift in the origin of y [1.6, 1.7].

The position uncertainty of the primary vertex of proton-proton interactions is given by the LHC parameters to be $\sigma_x \simeq \sigma_y \simeq 20$ μm in the transverse plane, but only $\sigma_z \simeq 5.3$ cm along the beam axis. This feature must be considered when designing the geometry of the detectors, in order to allow full coverage over a wide possible z-position of the primary vertex, which will be then reconstructed with an rϕ-precision of $\sim$10–15 μm and with a z-precision of $\sim$20–50 μm, thanks to the central detector tracking capabilities, in particular of the pixel detector.

The sub-components of the CMS detector will now be briefly described: the central detector (tracker), the electromagnetic and hadron calorimeters, and the muon system [1.8, 1.9]. An understanding of their expected performance is crucial for the evaluation of the physics potential through simulations.

1.2.1 The central detector

The core of the CMS experiment is constituted by the *central detector* (or *[inner] tracker*), which will be composed of silicon pixel, silicon microstrip and microstrip gas detectors, forming a barrel and two endcap regions and arranged in single- and double-sided detector layers providing on average 12–14 points per charged track travelling throughout its volume.

The aim of the tracking system is to reconstruct charged tracks with good efficiency and good momentum resolution. All tracks with $p_t > 2$ GeV/c should be reconstructed up to $|\eta| \sim 2.5$–2.6, and the required momentum resolution is $\Delta p_t/p_t \sim 0.1\, p_t$ (p_t in TeV/c); the particle charge would be identifiable up to $p_t \sim 2$ TeV/c.

A selective background rejection for interesting physics signals requires as good a momentum resolution as possible. At high luminosity, 15–20 minimum bias events will be superimposed on the interesting signal event, giving ~500 soft tracks in the tracker region. Therefore, high granularity to keep occupancies low, high precision, good pattern recognition and high track finding efficiency are basic requirements for a tracking detector at the LHC.

Transverse momentum and impact parameter resolution, as well as secondary vertex reconstruction in the transverse plane and in the full 3D space, are benchmarks for the evaluation of the tracker capabilities in the different p_t , η and luminosity regimes. The simulated physics performance of the central detector will be discussed in more detail later, when addressing the issue of B-physics studies at low luminosity (Chapter 6).

The conceptual view of the CMS central detector is shown in fig. 1.9: the lines denote the corresponding active layers or discs, the thicker lines representing the double-sided readout, which is implemented on ~50 % of the strip detectors.

The detector modules in the barrel part of the 'microstrip tracker' are distributed with a *spiral* geometry, arising from the tilt and arrangement of the detectors in a space frame structure with circular layers. A continuous structure maintains the same number of channels and an equivalent geometrical coverage with equal average number of hits per charged track—thus the equivalent discrete layers indicated in fig. 1.9. This structure provides ease of cable and services routing and access to the modules.

The whole of the tracker, with the possible exception of the pixel detectors, is divided and supported by a *wheel* structure: nine independent and similar wheels 25 cm wide—this dimension defining also the detector module and strip lengths—

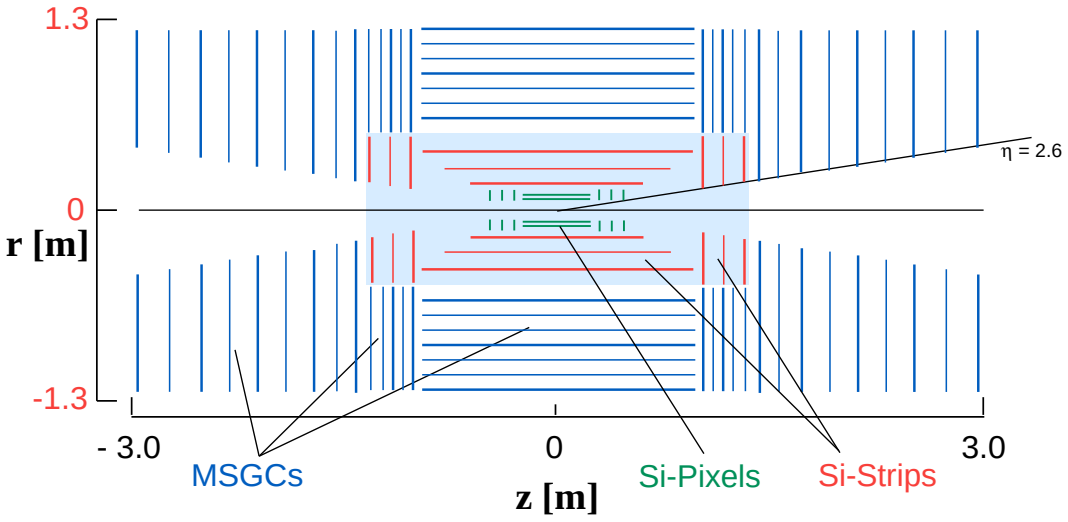

Fig. 1.9. Conceptual view of the CMS central detector (tracker).

form the barrel region; 14 wheels will constitute each endcap part. The whole central detector is contained in a cylinder 6 m long and with a diameter of 2.6 m.

Table 1.5 shows in some detail the components of the tracker, with number of layers/discs and of channels, and resolutions for each sub-detector unit. Some 800 units will form the barrel and each endcap pixel detector; more than 1500 modules will compose the silicon microstrip sub-detector, while the whole of the MSGC tracker will be formed by some 16000 units or modules.

The different module components and configurations will be described later, when discussing the detailed evaluation of the amount of material composing the central detector (Chapter 5).

Two main issues regarding a tracker for an experiment at the LHC arise with unprecedented importance and challenge at the same time: the design, development and implementation of a viable front end electronics scheme, and the realisation of all components—detectors, electronics, cabling, support structure—in technologies resistant to the expected radiation levels and allowing many years of operation at high LHC luminosity, with appropriate safety margins. The environmental and physical conditions which will have to be faced will be extreme.

Basic requirements for an LHC tracking electronics system are an acceptable signal to noise performance, with implications for both the electronics and the detector parameters (such as strip lengths for the silicon microstrips), a speed sufficient to enable a 25 ns signal bunch event timing, a power consumption limited to a few mW per readout channel, a pipeline delay of $\sim$3 μs, to allow for level-1 trigger

Detector	layers or discs	channels	element size/pitch (μm)	(r, ϕ) res. (μm)	z or r res.
Pixel barrel	2	5.5×10^7	125×125	15	11–17 μm
Pixel endcaps	3	2.2×10^7	50×300	15	90 μm
Si strips–single	1 (barrel) 2 (endcaps)	1.0×10^6	50	15	–
Si strips–stereo	2 (barrel) 4 (endcaps)	1.8×10^6	50/200	15	1 mm
MSGCs–single	4 (barrel) 14 (endcaps)	4.8×10^6	200	40	–
MSGCs–stereo	3 (barrel) 14 (endcaps)	6.5×10^6	200/400	40	2 mm

Table 1.5. Size, number of layers, number of channels and resolutions of the CMS central detector components.

signal arrival, and a realistically acceptable cost.

The problem of the radiation tolerance demanded for LHC tracking detectors will be addressed in detail in Chapters 2, 3 and 4.

1.2.2 The CMS calorimeters

Thanks to the large solenoid bore, the calorimeters can be installed inside the coil, thus avoiding degradation of their performance due to particle interactions with the coil material before showering in the calorimeters. The central detector is then the major component of the material seen by particles produced in the interactions and travelling towards the calorimeters. For this reason, the material budget of the CMS central detector has been evaluated in detail; results and discussions will be presented in Chapter 5.

Fig. 1.10 shows the layout of the barrel and forward CMS calorimeters: the primary function of the *electromagnetic calorimeter* (ECAL), made of high resolution lead tungstate ($PbWO_4$) crystals, is the precise measurement of electrons and photons; employed jointly with the *hadron calorimeter* (HCAL), it allows the measurement of the energy and the direction of particle jets. In the forward regions, the ECAL extends up to $|\eta| = 2.6$, and the HCAL up to $|\eta| = 3.0$.

$PbWO_4$ crystals have been chosen for the ECAL because of the short radiation length ($X_0 \simeq 9$ mm) and of the small Molière radius ($\sim$2.0 cm) of $PbWO_4$, thus leading to a compact calorimeter. The crystals in the barrel region start at a radius

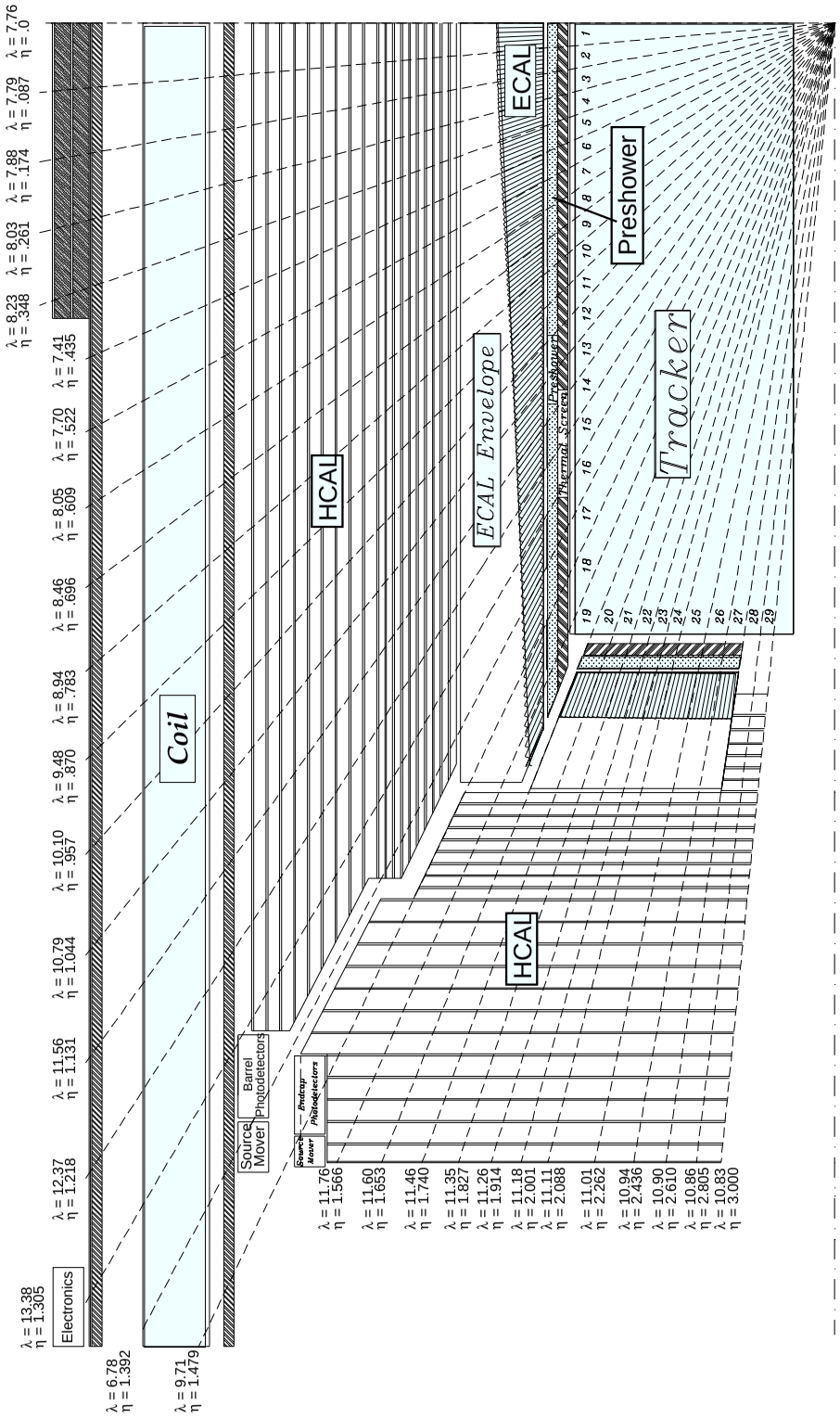

Fig. 1.10. The layout of the CMS preshower, electromagnetic calorimeter and hadron calorimeter for barrel and endcap regions (HCAL tower structure indicated).

of $\sim$1.4 m, and in the forward at z $\sim$3.2 m, and they are 24 cm long ($\simeq$ 26 radiation lengths). The crystal layout is visible in fig. 1.10.

The requirement of good energy resolution is dictated by the search for the intermediate mass Higgs boson, which would decay into two photons, and whose natural width in this 80–140 GeV mass range would be rather small ($\ll$ 1 GeV).

Because of space constraints inside the coil, the HCAL absorber must have a short radiation length and a low atomic number Z, not to degrade muon momentum resolution just behind the coil, and it should be non-magnetic. Copper has been chosen as the absorbing material, whilst the active elements will be plastic scintillators with wavelength shifting fibre readout, arranged, in the barrel and in the forward parts, in layers alternate with the absorber to constitute the sampling tower structure. The tile tower size will be 0.09 $\times$ 0.09 in the (η, ϕ) space, in the region $|\eta| < 2.0$. Granularity and time resolution must allow suppression of bunch crossing pile-up.

The very forward region, from $|\eta| = 2.7$ up to $|\eta| = 5.0$, is covered by complementary fast and radiation hard *very forward calorimeters* (VFCAL), located at $\pm$11 m from the interaction point. They improve, thanks to the extended hermetic coverage, the CMS capability of measuring the missing transverse energy ($E_t^{\rm miss}$) with a good resolution, and of identifying very forward jets.

1.2.3 The muon system

Detection of and triggering on muons at the LHC requires large rapidity coverage and good efficiency of the CMS muon subsystem to provide full identification, triggering and momentum measurement capabilities, both for low and high luminosity physics. Muons will be first measured in the central detector (inner tracker) inside the uniform 4 T field, and then they will be identified and measured in the four muon stations which compose the barrel (MS1–MS4) and the forward (MF1–MF4) CMS muon spectrometer.

Fig. 1.11 shows the cross section of the CMS muon system: each station in the barrel region is composed of *drift tube* detectors (DTs), and of *resistive plate chambers* (RPCs). RPCs are fast dedicated trigger detectors with an excellent time resolution ($\sim$2 ns) to provide unambiguous bunch crossing identification.

The forward muon spectrometer stations are composed of *cathode strip chambers* (CSCs), and of trigger dedicated RPCs, as before, up to $|\eta| = 2.1$ only, with space left at higher rapidities for possible future higher rate dedicated trigger detectors, thus expanding the present CMS muon acceptance.

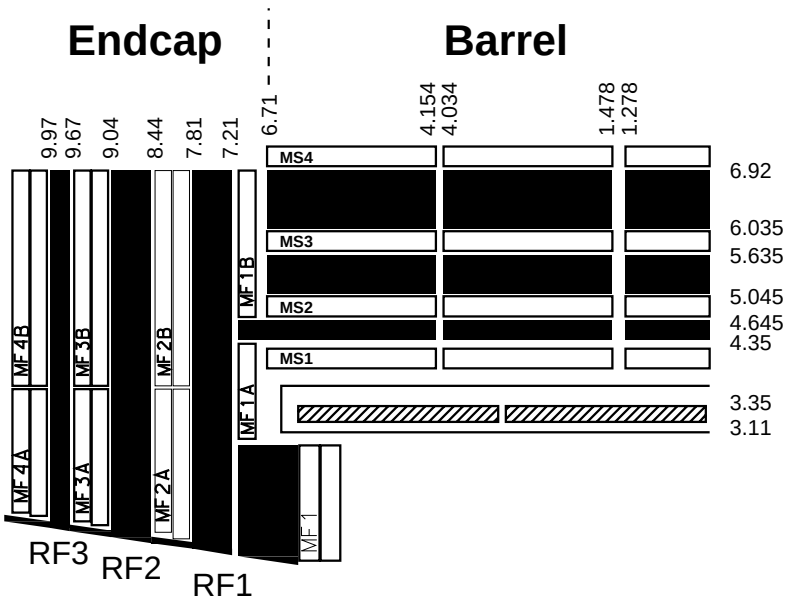

Fig. 1.11. Cross section of the CMS muon system, showing placement of the barrel and endcap muon stations.

The CMS muon system provides altogether an excellent muon trigger performance over the full rapidity and momentum ranges, as well as identifying and measuring muons from high- and low luminosity physics interactions. The transverse momentum resolution $\Delta p_t/p_t$ for the muon system alone (stand-alone mode), for $0 < |\eta| < 2$, has been estimated to be ~6–10 % for a 10 GeV/c p_t track, ~7–20 % for a 100 GeV/c track and ~15–35 % for a 1 TeV/c track. This measurement should be guaranteed at any luminosity. After matching with the central detector information, now the transverse momentum resolutions, for $0 < |\eta| < 2.4$, would become ~0.5–1.0 %, ~1.5–5 % and ~5–20 % for 10 GeV/c, 100 GeV/c and 1 TeV/c p_t tracks respectively. Correct charge assignment up to a track momentum of 7 TeV/c for the full η coverage, and a beam crossing identification efficiency greater then 99 % complete the performance of the muon spectrometer.

1.3 Trigger and data acquisition

A significant problem which the LHC experiments are confronting is the implementation of complex on-line triggering systems able to reduce the event rate from ~1 GHz (data flow at high luminosity) down to less than 100 Hz, currently thought to be a safe upper limit imposed by permanent data storage on magnetic media.

In ten years time technology may well have evolved and be able to provide higher on-line storage capability but a safety margin is required by uncertainties in LHC rates and detector performance.

The level-1 trigger will base its decision on calorimeter and muon first-level processors, reducing the data rate below ~100 kHz using partial event information. The detector front-end electronics are synchronous with the level-1 trigger processor and pipelined, with a pipeline depth corresponding to ~3 μs. The 'virtual' level-2 trigger also uses partial event information, making use of a high bandwidth read-out network and of a high processing power event filter, implemented on an on-line *processor farm,* further reducing by at least one order of magnitude the amount of information to be processed by the level-3 algorithms. Following a positive decision at level-2, the full information from the bunch crossing will be analysed in the *processor farm* for the level-3 decision, with a final event rate of 10-100 Hz.

The CMS level-1 muon trigger will identify muons, measure their transverse momentum and identify the bunch crossing from which they originated. The four types of first level muon trigger are:

1. inclusive single muon trigger ($p_t^{\rm cut} \sim$ 20–100 GeV) at high luminosity;
2. inclusive double muon trigger ($p_t^{\rm cut} \sim$ 7–10 GeV) at high luminosity;
3. low p_t single muon trigger ($p_t^{\rm cut} \sim$ 9–10 GeV) at low luminosity;
4. low p_t double muon trigger ($p_t^{\rm cut} \sim$ 3–5 GeV) at low luminosity.

Energy losses in the calorimeters and the magnetic field set a lower bound on possible muon p_t thresholds of about 2.5 GeV/c for triggering and 2 GeV/c for identification.

As an example, in the case of the inclusive single muon trigger, figure 1.12 shows the p_t cuts necessary to keep the corresponding rate at a reference value of 3 kHz, at the luminosities of 10^{32}, 10^{33} and 10^{34} cm^{-2}s^{-1} : respectively, ~4.5, ~10 and ~25 GeV [1.10]. The value of 3 kHz is considered to be a safe maximum rate allowable to the single muon trigger, to keep the total level-1 trigger rate at about 30 kHz, with about half of the bandwidth filled with muon triggers and half with electromagnetic triggers.

The level-1 calorimeter trigger should select single- and multi-electron and photon events, as well as jet and large missing transverse energy ($E_t^{\rm miss}$) events, with good efficiency over a large pseudorapidity range. The total electron/photon trigger rate, dominated by the QCD background, should not exceed ~15 kHz. Details on trigger algorithms and typical thresholds can be found elsewhere [1.4].

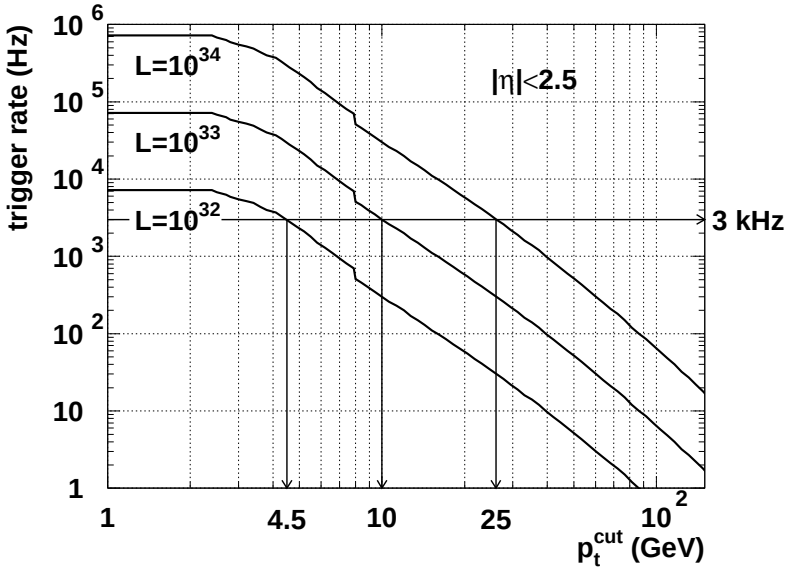

Fig. 1.12. Inclusive single muon level-1 trigger rates and corresponding trigger cuts for a 3 kHz rate at different luminosities.

Figure 1.13 shows the level-1 single electron/photon trigger rates at high luminosity as a function of the E_t threshold, for the *sliding window* algorithm, with and without isolation requirements (QCD jet production background and minimum bias included). For instance, an $E_t^{\rm cut}$ of 30 GeV for a single electron/photon would correspond to a rate of about 5 kHz, after the isolation requirements.

Studies of single electron and dielectron trigger rates are also important at low luminosity, namely for B-physics studies. As an example, a 5 kHz total rate would correspond to an imposed E_t threshold of about 15 GeV for an isolated single electron at low luminosity [1.11, 1.12].

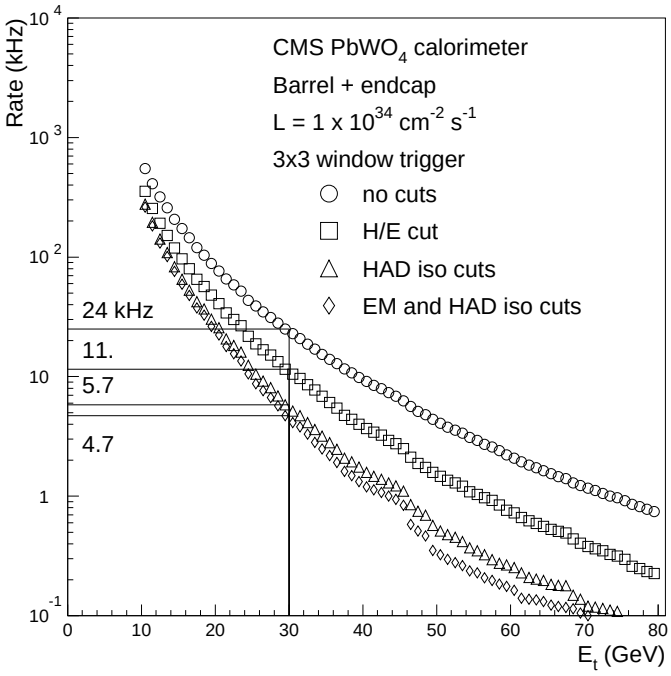

Fig. 1.13. Level-1 single electron/photon trigger rates at high luminosity (QCD background and minimum bias included) as a function of E_t threshold, with and without isolation requirements (*sliding window* algorithm).

Chapter 2

Introduction to radiation damage studies

Because of the unprecedented levels of radiation which particle detectors will have to withstand in the LHC environment, especially in the innermost regions, radiation damage studies are crucial to prove the feasibility of devices with a lifetime comparable to the experiment. Operation at LHC is expected to last for some ten years.

In this chapter the radiation damage studies will be introduced, describing briefly the radiation levels expected at the LHC and the irradiation facilities used—a few for the first time—for this purpose. The techniques of dosimetry used will be described, in particular for the two gamma facilities. Finally, the RAL ISIS neutron irradiation facility will be mentioned, as it has also been used for all the neutron test irradiations of silicon prototypes.

2.1 Radiation levels expected at the LHC

The first 10 years of LHC operation will provide a total integrated luminosity of 5×10^5 pb^{-1}. All components of an LHC experiment must be built and proven to be resistant to this hostile environment, providing satisfactory performance after such a period of time, with safety margins.

The region of the central tracking detectors will be exposed to the flux of primary particles originated from the interaction region, and to the neutron albedo emerging from the calorimeters. The strong magnetic field will bend the charged particles, so that a considerable fraction of the more damaging low energy particles will not reach the outer regions.

Fig. 2.1 shows the neutron and charged (hadronic) particle fluxes, in terms of

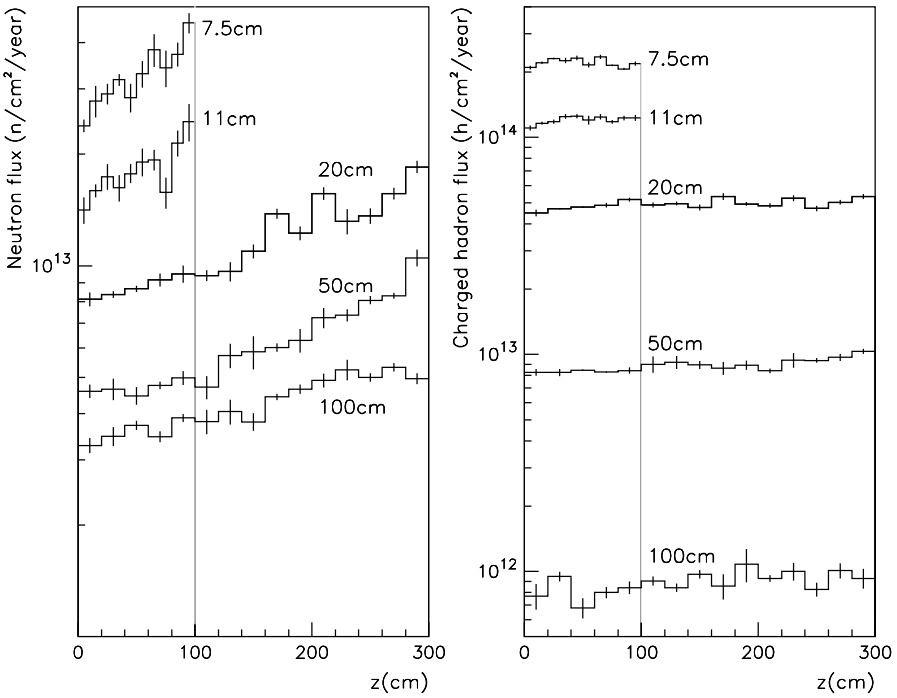

Fig. 2.1. Neutron and charged hadron fluxes at various radii in the central detector cavity [2.1].

particles per cm^2 *per year,* at different radii from the beam-pipe. Typically, the neutron flux is rather uniform, and of the order of 10^{13} cm^{-2} year^{-1}. Close to the beam-pipe, the charged particle flux, which decreases with the radius (at first approximation as $1/r^2$), is dominated by low energy pions, while at larger radii the neutron albedo dominates the fluxes [2.1].

The particle fluence is responsible for the component of the radiation damage defined as *bulk damage.* The energy deposited by charged particles mainly causes ionisation: the related damage is particularly important for the thin layers at the surface of the devices, where changes in the charge density have consequences for the electronic characteristics and the performance of detectors, and it is therefore described as *surface damage.*

The *radiation dose* in the materials is measured in terms of energy deposited. The unit of dose is the *gray (Gy),* defined as 1 joule kg^{-1} (i.e. 6.24×10^{12} MeV kg^{-1}). Also commonly used is the *rad;* 1 Gy corresponds to 100 rad. The estimated radiation dose at various radial positions within the CMS central detector is shown in fig. 2.2 [2.1].

It must be pointed out that particle fluxes and doses can only be estimated with uncertainties, due, among other reasons, to the lack of the precise proton-

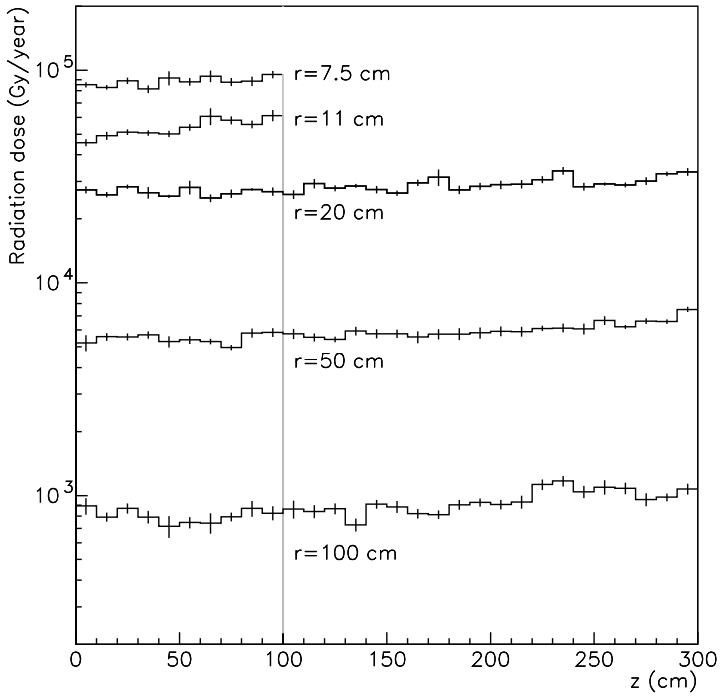

Fig. 2.2. Radiation dose at various radii in the central detector (1 kGy = 100 krad) [2.1].

proton inelastic cross-section at the LHC energy, and of particle distributions and multiplicities. Also, realisitic detector geometry, material descriptions and localised non-uniformities add to the uncertainties in the estimate of the neutron albedo. Uncertainties of a factor of $\sim$2 for the neutron flux and $\sim$1.5 for the primary charged particle flux should be considered to ensure a large safety margin [2.1].

Results from systematic studies performed after the Technical Proposal showed that the values of dose rates and fluxes then presented were pessimistic, and that they should be rescaled with a factor of $\sim$0.8, keeping the same error bars of $\sim$30% [2.2], mainly because of the differences introduced by the new versions of the event generators and by the choices of initialisation parameters.

2.2 Irradiation facilities used

A few irradiation facilities have been used to perform exposures of MOS and MNOS capacitors (described in Chapter 3) and of silicon microstrip detector prototypes (described in Chapter 4). The test exposures of the three facilities, characterised and used for the first time, will be now briefly described. Table 2.1 summarises the type of radiation and the typical dose rates.

facility	**type of radiation**	**typical dose rate** (rad/s)
Strasbourg	electrons	$\sim$ 1–6 $\times$ 10^4
Brunel	gammas	$\sim$ 1
Imperial College	gammas	$\sim$ 2–3 $\times$ 10^2

Table 2.1. Typical dose rates of the electron and gamma facilities used.

2.2.1 The Strasbourg AERIAL electron accelerator

A number of irradiations have been performed since May 1992 at the *electron beam facility* at A.E.R.I.A.L. in Strasbourg (France). This accelerator could provide a beam of 2.0–2.2 MeV electrons; the beam current could be set within the 10–100 μA range, and it was measured by dumping the beam into a Faraday cup.

The samples to be irradiated were positioned in an aluminium box, on a sheet of paper, inserted on a conveyor, driven from the control room outside the shielded area and made to pass under the beam. The dose to be given to a sample was set within a certain range by changing the beam current and the speed with which the sample was moved under the beam spot.

The beam at the exposure point can be approximated to a gaussian spot of 8.4 cm FWHM, and it was 'swept' by a periodic magnetic field (with a frequency of 20 Hz) up to a maximum width of 20 cm in the direction perpendicular to motion of the samples.

The dose rates delivered were high, of the order of a few tens of krad/s; the total dose received by the irradiated samples was measured independently by means of dosimetry films irradiated with each sample [2.3]. This technique of dosimetry and its precision will be described in section (2.3.2).

2.2.2 The Brunel University gamma cell

The *gamma cell* at Brunel University (UK) was used to perform a few sets of irradiations of MOS and MNOS capacitors. It is characterised by a very low dose rate, at most of the order of $\sim$1 rad/s. The small point-like Co^{60} source is mechanically moved from the shielded storage area to the inside of the cell within a thick flexible pipe, which can be adjusted to fit in fixtures holding source and samples [2.4].

The source profile was evaluated by measuring the doses received during a test

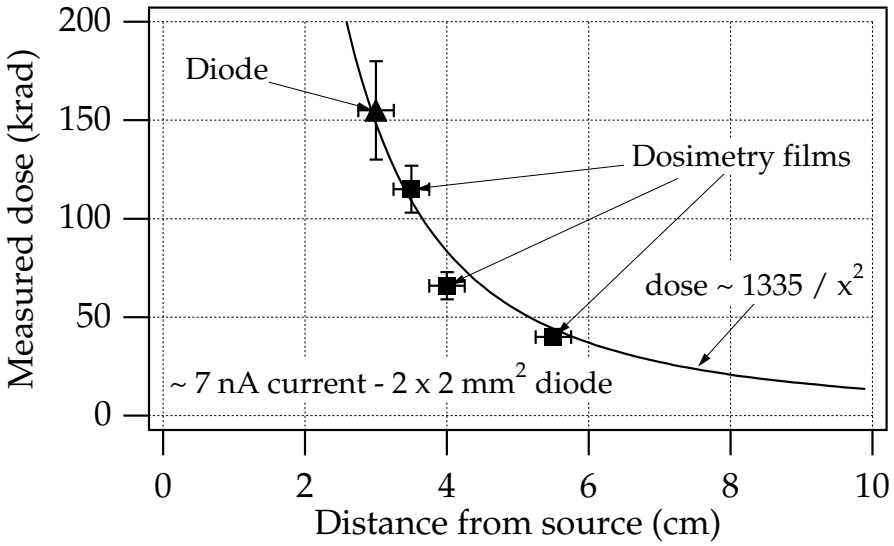

Fig. 2.3. Source profile of the gamma facility at Brunel University: measured doses as a function of the distance after 48.5 hours of exposure.

exposure of 48.5 hours, as a function of the distance from the source, i.e. from the end window of the pipe, and it is shown in fig. 2.3. Two different dosimetry techniques were used, namely the dosimeter film and the diode photocurrent, as described in section (2.3). Results from both methods agree and fit well a $1/d^2$ behaviour, as expected.

2.2.3 The Imperial College gamma cell

The *Imperial College gamma cell* was used for the first time for test irradiations of silicon devices for HEP. Built in the department of Chemical Engineering, it has been used for tests of materials, for radiation studies of chemical compounds, and also for sterilisation of biological samples with long exposures.

This irradiation facility consists of six independent Co^{60} sources, which can be lowered from the shielded storage area down to the exposure cell through metal pipes, reaching at the end six aluminium rods. When all are exposed, the sources occupy the vertices of an hexagon, in the middle of which a circular chuck, with a diameter of $\sim$10 cm, is located; samples to be irradiated can be left on this chuck [2.5].

It is possible to select, from the control room, any combination of the six sources to obtain different dose rates, but a symmetric geometry must be chosen to maintain uniformity of dose rate throughout the whole of the volume exposed. Fig. 2.4 shows

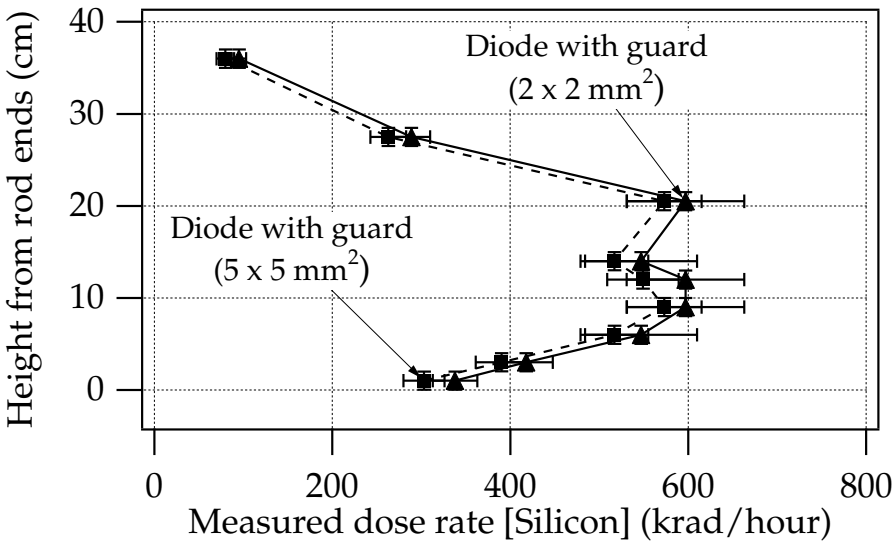

Fig. 2.4. Height profile of the gamma facility at Imperial College.

the height profile of the gamma source when the samples were positioned at its centre. It was then possible to understand where the dose rate was higher and more uniform. This dosimetry has been carried out making use of two different silicon diodes.

Exposures can also be made leaving the samples at some distance from the central chuck and at about the same height, therefore approximating the six sources to a unique point-like source. For such a configuration, fig. 2.5 shows the source profile in terms of dose rate as a function of the distance in cm from the centre of the chuck; also in this case, the relative dose rates measured with a silicon diode fit well a $1/d^2$ behaviour. Both profiles have been estimated with all sources exposed.

2.3 Techniques of dosimetry

Two independent techniques of dosimetry have been used to measure the dose received by each sample irradiated: the measurement of the dark current through a silicon diode, and irradiation of the dosimetry film FWT 60.00. This also represented an important consistency check on the estimated dose rates delivered by the facilities: more precision than that achievable by estimation was needed for the irradiation studies. Table 2.2 compares results of dose measurements taken during three different test irradiations.

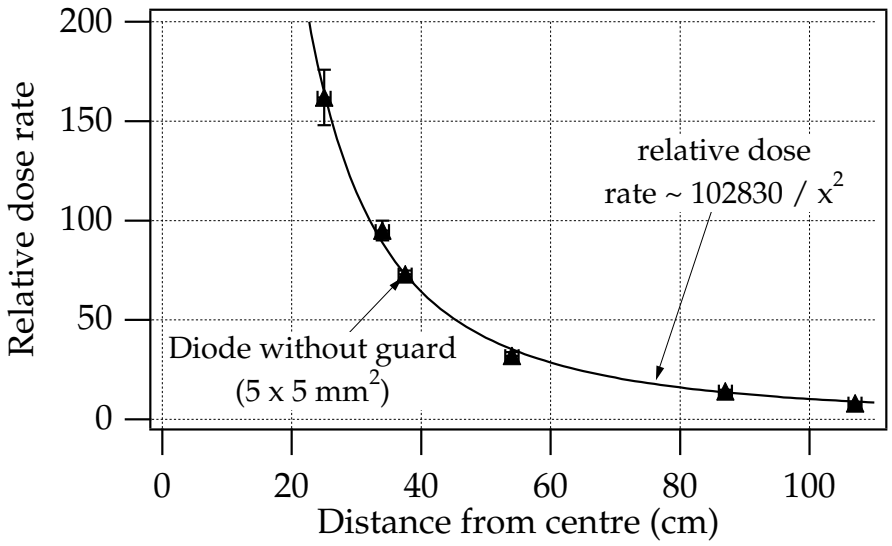

Fig. 2.5. Source profile of the gamma facility at Imperial College: measured dose rates as a function of distance.

irradiation	photo-current	exposure time	diode V_{bias}	total received dose (krad) diode	FWT 60.00
Imperial College (1)	$\sim 2\ \mu$A	10 min	0 V	150 ± 15	150 ± 15
Imperial College (2)	$\sim 2\ \mu$A	99 min	0 V	1390 ± 20	1210 ± 120
			50 V	1230 ± 20	
Brunel	~ 7 nA	48.5 h	0 V	155 ± 25	(see fig. 2.3)

Table 2.2. Diode and film dosimetries compared (2×2 mm^2 diodes with guard ring—FWT 60.00 films).

2.3.1 Silicon diodes

The total dose received during an exposure can be measured considering the change in the dark current (or leakage current) of a reverse biased silicon diode, which represents the *photocurrent* induced by the ionising radiation. An estimate of the dose received can be thus made with the relation

$$\text{dose (eV/kg)} \simeq \Delta I_L \cdot \frac{3.6\ \text{eV/[e-h]}}{e \cdot M_a} \cdot T_{\text{exp}}\ , \tag{2.1}$$

where ΔI_L is the difference between the diode dark current measured before and after the beginning of the exposure, 3.6 eV is the energy required to create an electron-hole pair [2.6], e is the electron charge, M_a is the active mass of the diode and T_{exp} is the total duration of the exposure. The dose thus expressed in eV/kg is then rescaled to rad.

For the accuracy of the dosimetry it is important to use a diode with a guard-ring, to define the active area from which the current is collected [2.7].

2.3.2 Dosimeter films

The *dosimeter film FWT 60.00,* provided by A.E.R.I.A.L. in Strasbourg (F), has been used to measure the doses received by the samples. It consists of a solid radiochromic solution deposited on a thin (50 μm) transparent nylon film, with a surface of 1 cm^2. During exposures to electron, gamma or X-radiation, the photo-ionisation causes changes in the intensity of the blue colour of the film, proportional to the absorbed dose. The film is then developed with a photometric measurement giving with good reproducibility ($\pm$3 %) the value of the received dose, within the 0.5–200 kGy range (50 krad–20 Mrad). The response is rather independent of the type of radiation, from the dose rate (up to 10^8 Mrad/s,) and from environmental conditions such as temperature or humidity [2.3, 2.8].

The measured dose after film development was expressed by A.E.R.I.A.L. in terms of *water equivalent dose,* i.e. of the dose which would have been received by water. It has always been rescaled to the dose in silicon, with the simple approximated relation $D_{\rm Si} \simeq 0.82\, D_{\rm w}$. The error on the values given by this dosimetry has been pessimistically assumed to be $\pm$10 %, to take into account all factors degrading its precision.

2.4 The RAL ISIS neutron facility

Many neutron irradiations have been performed making use of the *ISIS neutron facility* at the Rutherford Appleton Laboratory (UK). The neutrons used for the radiation damage studies are produced when the 70 MeV protons accelerated by a linac are not captured by the RF field of the synchrotron ISIS, into which the main beam is being injected. This fraction of protons is stopped by a graphite collector, which then produces spallation neutrons. An assembly above the collector holds the samples to be irradiated with the neutrons emerging perpendicularly to the main proton beam. The energy spectrum of such neutrons is similar to that expected in the LHC environment, with a typical energy around $\sim$1 MeV. The total fluence, measured in neutrons/cm^2, varies with the duration of the exposure and the distance of the sample from the collector [2.9].

Chapter 3

Ionising radiation damage studies of MOS capacitors

The technique of exposing relatively simple MOS and MNOS capacitors to ionising radiation allows studies of charge deposition in the silicon dioxide in a simplified way with respect to the realistic case of complex microstrip devices. Surface effects strongly influence interstrip behaviour and characteristics such as interstrip resistance and capacitance; therefore studies of surface effects in irradiated MOS devices are also relevant to microstrip detector developments.

The MOS and MNOS capacitors used will be described, and the different exposures, with electrons and gammas, are commented on. The oxide charge formation under different gate conditions and different radiation dose rates has been studied; annealing behaviour has been monitored.

3.1 The MOS and MNOS capacitors

The *MOS capacitor* and its properties have been widely described in the literature (e.g. in [3.1], [3.2] and [3.3]). Briefly, it consists of a metal-oxide-semiconductor structure, made of an aluminium contact (*gate*) to a $\sim$1 μm silicon dioxide (SiO_2) layer deposited on top of the silicon bulk. On the backplane an ohmic contact is also usually realised. The device thus formed is an MOS capacitor, sometimes also called MOS *diode.*

MOS capacitors are the most common *MIS* (metal-insulator-semiconductor) structures, particularly useful to study surface effects in semiconductor technology, as their behaviour depends on the accumulated and induced charges in the dioxide.

If the silicon substrate is n-type, electrons will be the majority carriers and holes the minority carriers. This type of MOS capacitor will be considered for the rest of

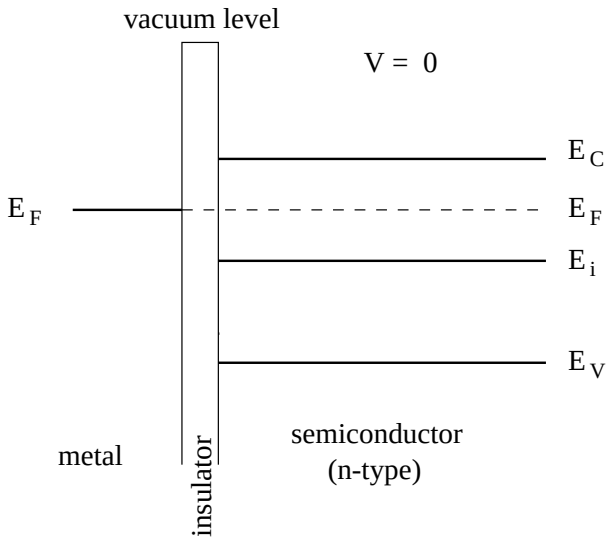

Fig. 3.1. Energy-band diagram of an ideal MOS capacitor on n-type silicon substrate at $V_g = 0$ V.

this section, as devices of this type were used for the studies described here. Fig. 3.1 shows energy-band diagram of an ideal MOS capacitor when $V_g = 0$ V. E_F is the Fermi level, E_C is the lower bound of the conduction band and E_V is the upper bound of the valence band. E_i represents the intrinsic energy level in silicon.

The situation would be analogous for an MOS capacitor on a substrate of p-type silicon, with the appropriate modifications. The behaviour with respect to gate polarisation would be symmetrical.

The *flat-band voltage* V_0 is defined as the gate voltage at which no electric field is present across the oxide. For an *ideal* MOS capacitor, this condition would be fulfilled with $V_0 = 0$. V; in the case of a *real* MOS structure, the flat-band voltage is not zero, because of the presence of charge in the oxide which creates an electric field, with *bending* of the energy bands in silicon as a consequence. A voltage has thus to be applied to the gate to compensate the effects of the oxide charge and to flatten the bands. The flat-band voltage therefore measures the oxide charge.

The silicon-oxide interface is characterised by the presence of fixed oxide charge centres, mainly positive, not mobile under an applied electric field across the oxide. This positive ionic charge in the oxide, very close to the silicon, is responsible for the non-zero flat-band voltage of MOS capacitors even before exposure to ionising radiation[1].

[1]It must be said that the MOS flat-band voltage would not be null even if no charges were trapped in the oxide and no surface states existed, because of an additional potential originated by the *work function difference,* representing the difference of the work made by an electron to leave the gate metal and to leave the silicon substrate: $W_{ms} = W_m - W_s$. This is due to the fact that

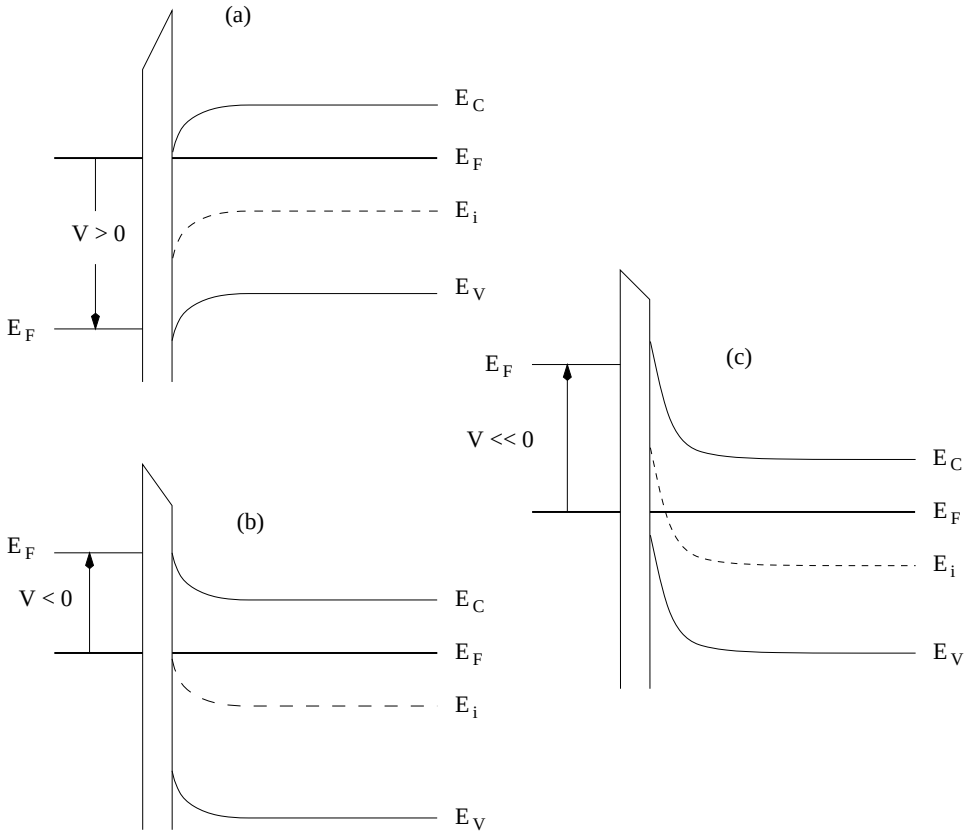

Fig. 3.2. Energy-band diagrams of an ideal MOS capacitor on n-type silicon substrate when $V_g \neq 0$ V: (a) accumulation [$V_g > 0$ V], (b) depletion [$V_g < 0$ V], (c) inversion [$V_g \ll 0$ V].

There are also active interface states, constituted by traps with energy levels within the silicon bandgap, whose occupancy varies with the gate bias [3.4].

Depending on the voltage V_g applied to the gate with respect to the flat-band voltage V_0, the MOS capacitor—with the substrate of n-type silicon—can be biased to three different conditions. Fig. 3.2 shows the energy-band diagrams of an ideal MOS capacitor, in the band bending approximation:

1. when $V_g \geq V_0$, the electron concentration in the region near to the oxide interface increases, and this condition is defined as *accumulation* (a). The depth of the negative space charge in silicon is so small that the capacitance at accumulation, $C_{\rm acc}$, coincides with that due to the oxide layer only, $C_{\rm ox}$:

$$C_{\rm acc} \;=\; C_{\rm ox} \;=\; \epsilon_0 \, \epsilon_{\rm ox} \, \frac{A}{d_{\rm ox}} \;, \tag{3.1}$$

where ϵ_0 is the electric permittivity of free space ($\sim$8.85 pF/m), $\epsilon_{\rm ox}$ is the

the gate and the bulk are not made of the same material [3.4].

relative dielectric constant of the silicon dioxide ($\sim$3.9), A is the capacitor gate area and $d_{\rm ox}$ is the oxide thickness;

2. when $V_g \leq V_0$, the concentration of the majority carriers (electrons) begins to diminish near the silicon-oxide interface, as free electrons are repelled from that region as an effect of the negative charge on the gate. This situation is defined *depletion* (b), and the capacitance seen from the gate diminishes as an additional contribution from the depleted region below the gate is added in series to $C_{\rm ox}$. The region without free charge carriers effectively increases the separation between the MOS capacitor 'plates', i.e. the metal gate and the undepleted semiconductor;
3. increasing further the negative potential on the gate ($V_g \ll V_0$), the depletion region extends and becomes wider in the semiconductor, until the point where it becomes energetically favourable for holes (i.e. the minority carriers) to concentrate at the interface instead, and the depth of the depletion layer reaches a maximum. The energy bands bend above the Fermi level in this situation. This condition is called *inversion* (c), since the charge carriers near the silicon-oxide interface are holes instead of electrons. Many free carriers are therefore near the interface: the MOS structure capacitance, evaluated with a quasi-static measurement, rises back to $C_{\rm ox}$, while measurements performed at high frequency give the constant low value of full depletion, $C_{\rm inv}$ [3.3, 3.5] [2].

Exposure to ionising radiation will result in an enhancement of the positive oxide charge density, with the consequent modifications of the MOS electrical properties. The mobility of electrons in the oxide is much greater than that of holes: so if an electron-hole pair generated is separated by any field present in the oxide and escapes recombination, the electron will rapidly reach the positive electrode, while the hole will slowly drift towards the negative electrode, with a high chance of becoming trapped within the oxide (but usually at the interface), thus resulting in an overall positive charge build-up [3.2].

The oxide charge density n_q (charge/cm^2) can be evaluated at any step of exposure or annealing by measuring the flat-band voltage V_0, to which the charge density is related by the relation

$$n_q \simeq \frac{C_{\rm acc} \cdot V_0}{e \cdot A} \,, \tag{3.2}$$

[2] If a quick highly negative voltage pulse is applied to the gate, the condition called *deep depletion* is reached, where the depletion region extends beyond its normal quasi-static limits, as if the pulse had been so fast as not to allow slower holes to collect at the interface forming the inversion layer [3.3].

where e is the electron charge. The oxide charge density increase due to ionising radiation will be discussed in section 3.3.

The flat-band voltage is therefore an important MOS parameter, and it is evaluated experimentally by means of several techniques. The most precise are based on the comparison between the experimental and the theoretical *CV-curves* (i.e. the slopes of the capacitance measured between the gate and the substrate as a function of the gate voltage) of the same MOS device, also comparing quasi-static and high frequency measurements [3.4].

Approximate methods, if limited precision is satisfactory for the purpose, consist in considering the flat-band voltage V_0 either equal to the voltage at which the lowest value of capacitance is reached with a quasi-static measurement, or equal to the voltage at which a capacitance intermediate between its inversion and accumulation values is reached in a high frequency (e.g. 100 kHz) measurement. The latter is the method used here, and the error in this approximation has practically no consequence for this study.

It is also possible to estimate the oxide thickness $d_{\rm ox}$ with the formula

$$d_{\rm ox} \simeq \frac{\epsilon_0 \cdot \epsilon_{\rm ox} \cdot A}{C_{\rm acc}} \,, \tag{3.3}$$

derived from (3.1). The value thus obtained can be compared to the specifications given by the manufacturers.

If a thin layer ($\sim$0.1 μm) of *silicon nitride* (Si_3N_4) is added between the metal and the oxide layers, the structure thus formed can be described as a *MNOS* capacitor. The deposition of this additional layer is a technique now frequently used in silicon detector production, to improve the yield of microstrip detectors by reducing the number of *pinholes,* i.e. small channels through the dioxide which would short-circuit a diffusion strip to its metal read-out line. The presence of the nitride changes the behaviour of the capacitor, as new interfaces (dioxide–nitride and nitride–metal) are created. The capacitors from the RD20 prototype batches are of the MNOS type, as the nitride was deposited on some of the wafers during the production processes (see also Chapter 4).

Characteristics before exposure of the MOS and MNOS capacitors used for the irradiation tests are summarised in table 3.1, where dimensions, capacitances at accumulation and at inversion, flat-band voltages and estimated charge densities are reported, with some geometrical parameters.

As an example of the measurements performed at each step of the irradiation programme, fig. 3.3 shows some CV-curves of MNOS capacitors, irradiated with

device	**area** (mm^2)	**acc. cap.** (pF)	**inv. cap.** (pF)	**flat-band voltage** (V)	**charge density** (q/cm^2)	SiO_2 **layer** (μm)	Si_3N_4 **layer** (μm)
SI UV1 MOS	1.0×1.0	42.	5.	$-3.$	$\sim 7 \times 10^{10}$	~ 0.8	—
RD20 TS MNOS	1.0×1.0	35.	4.	$-11.$	$\sim 3 \times 10^{11}$	~ 0.9	~ 0.1
RD20 3X MNOS	1.5×1.5	80.	11.	$-11.$	$\sim 3 \times 10^{11}$	~ 0.9	~ 0.1

Table 3.1. Characteristics of unirradiated MOS and MNOS capacitors.

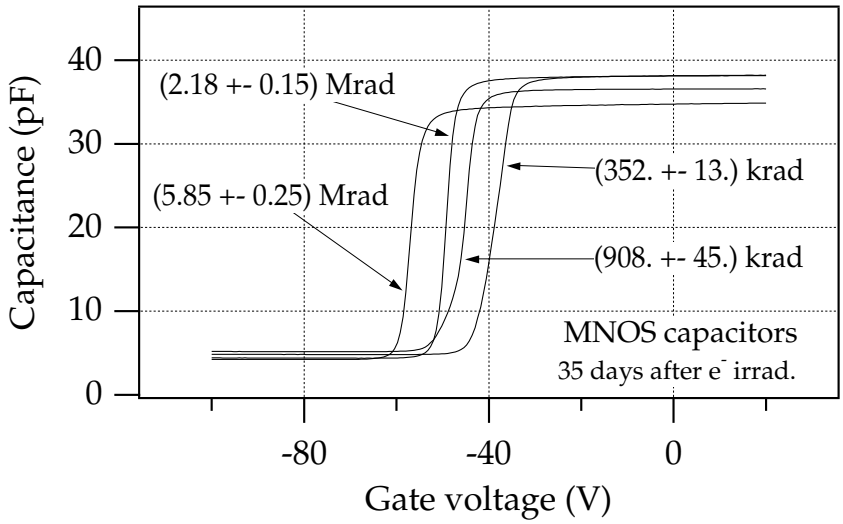

Fig. 3.3. CV-curves of electron-irradiated MNOS capacitors (high-frequency measurement).

different doses of electrons, after room temperature annealing of 35 days: the *flat-band voltage* shifts have been caused by the charge deposited in the oxide by the ionising radiation. With reference to the MOS properties described before, e.g. for the case of the capacitor irradiated with (352 ± 13) krad, it is possible to identify along the CV-curve the accumulation ($V_g \geq -30$ V), depletion ($V_g \sim -40$ V) and inversion ($V_g \leq -50$ V) regions.

All measurements were taken with high frequency CV-meters, and the MOS capacitor impedance was extracted at 100 kHz using a C_S–R_S model, in which the device was approximated to a capacitance in series with a resistance. This model best fits the MOS structure, where the capacitance represents the MOS capacitor itself and the resistance represents the silicon bulk.

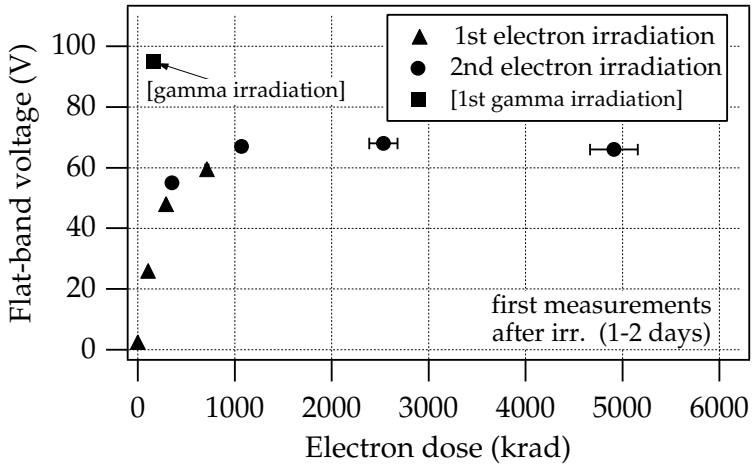

Fig. 3.4. Electron-irradiated MOS capacitors: flat-band voltage as a function of received dose.

3.2 Irradiations performed

The various sets of irradiations performed at the electron irradiation facility at A.E.R.I.A.L. in Strasbourg, and at the gamma cells at Brunel University and at Imperial College, will now be described. The measurements taken at the various steps of the exposure programmes will be summarised by means of plots, and all results will be compared and commented in sections 3.3, 3.4 and 3.5.

Three sets of irradiations were performed using the electron facility in Strasbourg, up to a total dose of ∼6 Mrad; figs. 3.4 and 3.5 show the plots of the flat-band voltage as a function of the received dose, for the irradiated MOS and MNOS capacitors. The plotted flat-band voltages are the first measured after the exposure (actually 1–2 days after). The evolution of the measured oxide charge density following the last irradiation are reported in figs. 3.6 and 3.7; the last measurements were taken after room temperature annealing for more than 200 days. The capacitors had been left unconnected (i.e. floating) during the exposures, because of the configuration of the irradiation facility.

The first irradiation made using the gamma cell at Brunel University delivered ∼160 krad of gammas to MOS and MNOS capacitors, with the gate either biased at −100 V (i.e. with the capacitor in inversion) or left floating during the exposure. Figs. 3.8 and 3.9 show the oxide charge density annealing following this exposure and up to ∼150 days after, with the different gate conditions.

The second irradiation consisted of ∼150 krad of electrons given to sets of capacitors, with the gate biased at +100 V, 0 V and −100 V, to complete the study of the

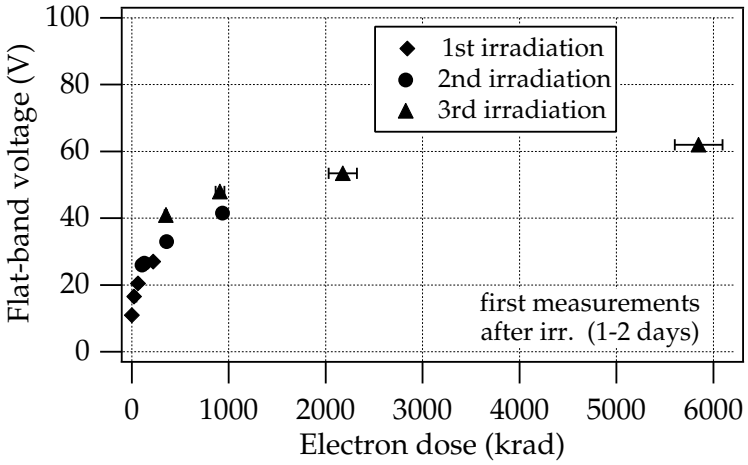

Fig. 3.5. Electron-irradiated MNOS capacitors: flat-band voltage as a function of received dose.

different gate conditions. The flat-band voltage V_0 after irradiation was no longer measurable in the case of the capacitors kept in accumulation during the exposure, being beyond the range of the measuring instruments ($V_0 < -100$ V). The flat-band voltage shift, as measured immediately after the exposure, and the annealing of the oxide charge density up to ~60 days after the irradiation are both shown in figs. 3.10 and 3.11.

The series of exposures made at the gamma cell at Imperial College delivered doses of ~300, ~600 and ~900 krad, with two different dose rates (~60 krad/hour and ~600 krad/hour), to sets of MOS and MNOS capacitors, with the gate biased at −30 V and at 0 V with respect to the bulk: the flat-band voltage shifts after the exposure are shown in figs. 3.12 and 3.13.

Finally, figs. 3.14 and 3.15 show the beginning of the annealing of the flat-band voltage shift after that exposure, for both dose rates: measurements were taken only until 20 days after the irradiation, enough to show consistency with the previous data.

3.3 Oxide charge density increase

Exposure to ionising radiation of MOS devices results mainly in two effects:

1. positive space-charge build-up within the silicon dioxide, larger if the gate is biased to a non-zero potential with respect to the silicon substrate;

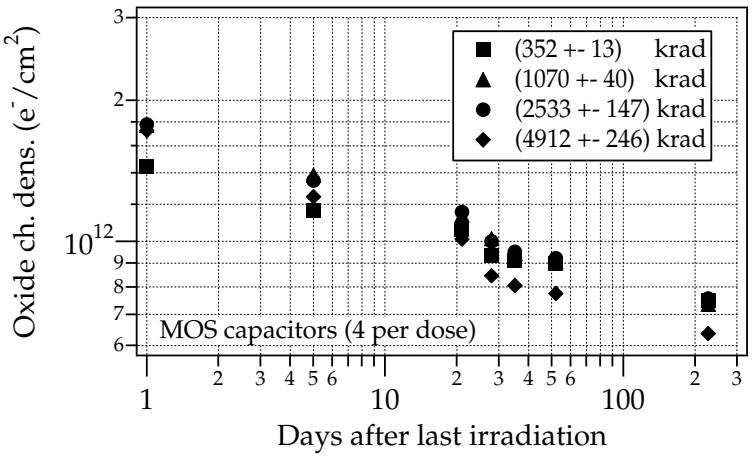

Fig. 3.6. Electron-irradiated MOS capacitors: oxide charge density annealing.

2. increase in the surface state density at the interface between silicon and oxide.

The effect of positive charge creation on the flat-band voltage shift is larger if the gate voltage is kept *positive* during the irradiation, compared to the situation when the gate is negatively biased; this happens because a positive space-charge layer closer to the silicon-oxide interface will have a greater effect on energy band bending than in the case of the positive charge being accumulated near to the oxide-metal gate interface [3.6].

A model explaining qualitatively the positive oxide charge buildup and its behaviour with gate bias was proposed by Zaininger [3.7] and by Grove and Snow [3.8]: some of the electron-hole pairs generated in the oxide by the ionising radiation recombine, but most are driven towards the electrodes following the electric field applied across the oxide. Very few electrons are trapped in the oxide as their drift velocity is high, while holes are much slower and have a greater probability of becoming trapped.

The permanent hole traps are mainly located near the metal–oxide interface. If a positive voltage is applied to the MOS gate, the holes will drift towards this interface with a high chance of becoming trapped, thus sensibly increasing the positive oxide charge. If, on the other hand, a negative voltage is applied to the gate, only the small fraction of holes belonging to the charge pairs produced near the metal–oxide interface will be trapped there, before drifting towards the metal gate, with a lower chance of becoming trapped [3.4].

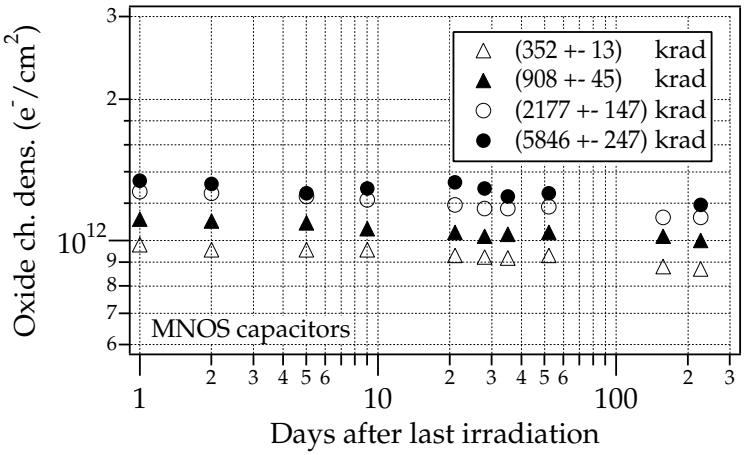

Fig. 3.7. Electron-irradiated MNOS capacitors: oxide charge density annealing.

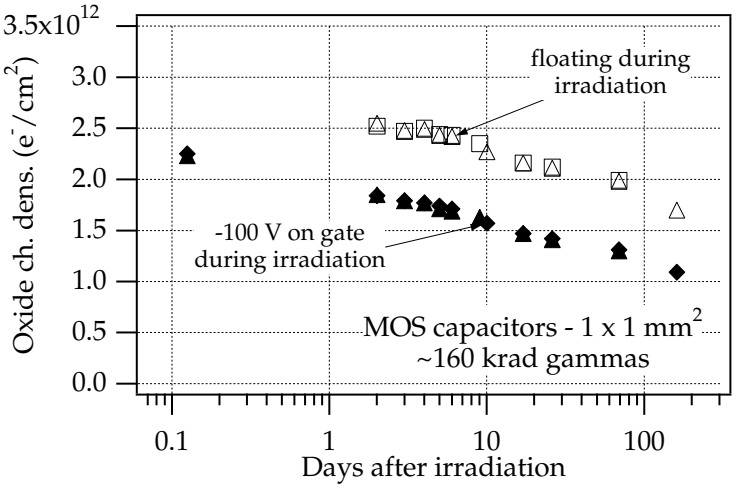

Fig. 3.8. Gamma-irradiated MOS capacitors at Brunel Univ.: oxide charge density annealing.

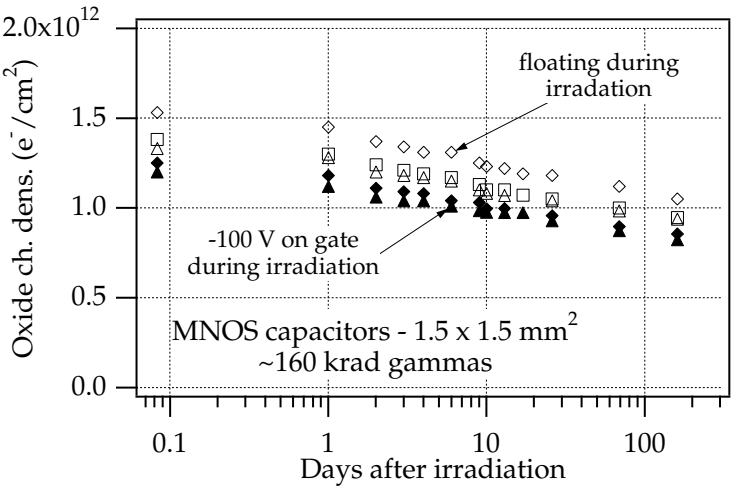

Fig. 3.9. Gamma-irradiated MNOS capacitors at Brunel Univ.: oxide charge density annealing.

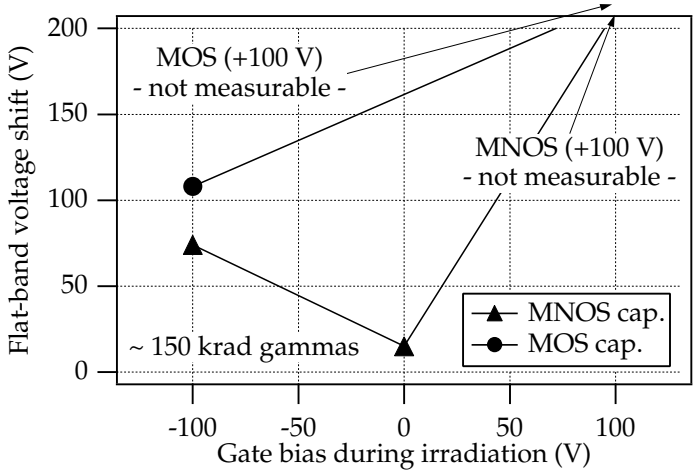

Fig. 3.10. Gamma-irradiated MOS and MNOS capacitors at Brunel Univ. under different gate conditions: flat-band voltage shift.

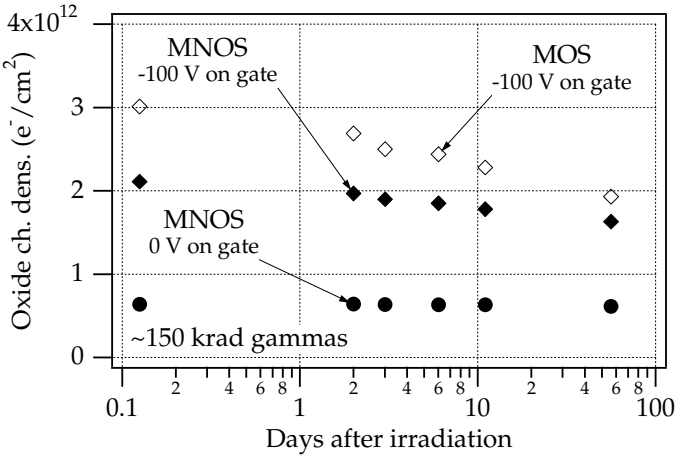

Fig. 3.11. Gamma-irradiated MOS and MNOS capacitors at Brunel Univ. under different gate conditions: oxide charge density annealing.

The oxide charge build-up in the irradiated MOS and MNOS capacitors was measured through the flat-band voltage; the range of electron doses showed a saturation effect, which occurred after $\sim$1 Mrad for the MOS device, whilst in the case of the MNOS capacitor the further increase was less than 20–30 % after $\sim$2 Mrad.

The irradiations with gammas of MOS and MNOS capacitors showed the important influence of the different gate bias on the quantity of oxide charge accumulated: the flat-band voltage (negative) increase was more pronounced when the gate was left unconnected than when it was biased at -100 V; when biased at $+100$ V, it increased beyond the available measurement range, showing a bigger effect, as explained above.

The saturation effect experimentally seen can be explained using the model described above. After a certain radiation dose, most of the hole traps at the metal–oxide interface will have become occupied, therefore the probability for a hole to become trapped will decrease and most of the charge pairs produced by further radiation will drift and reach the electrodes without becoming trapped.

With the irradiations at Imperial College, a smaller difference was seen between biasing the gate at 0 V and at -30 V; because of the flat-band voltage shift induced during the irradiation, these two gate conditions became equivalent soon after the beginning of the exposure, i.e. $V_0 < V_g$ in both cases.

The behaviour of the MNOS capacitors after irradiation was similar to that of the MOS capacitors, with the exception that the effect of the exposure seemed to have been moderated by the presence of the nitride, resulting in a less pronounced increase in the (negative) MNOS flat-band voltage V_0. The saturated charge density

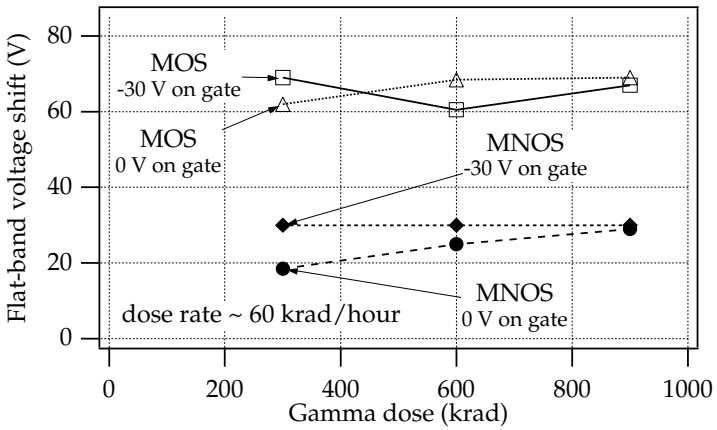

Fig. 3.12. Gamma-irradiated MOS and MNOS capacitors at Imperial College: lower dose rate.

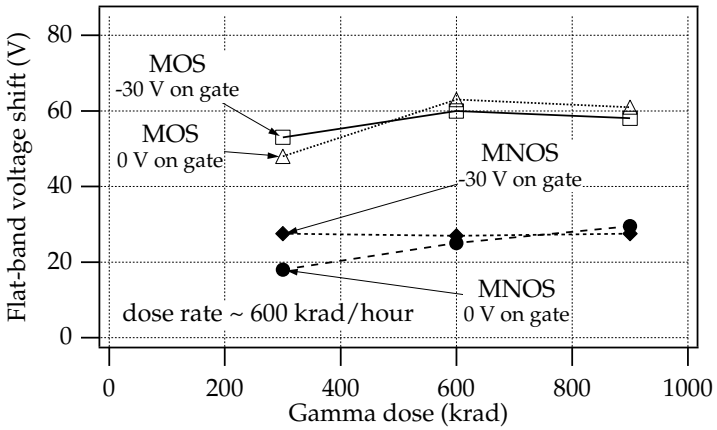

Fig. 3.13. Gamma-irradiated MOS and MNOS capacitors at Imperial College: higher dose rate.

is therefore lower for the MNOS capacitors.

3.4 Dose rate effects

The dose rates of ionising radiation delivered during the irradiation programme were spread over five orders of magnitude (table 2.1); therefore, the effect of different dose rates was observed, again more noticeably in the case of MOS capacitors than for the MNOS capacitors.

Direct comparison of results after dose rates different by an order of magnitude was made during the second set of gamma irradiations at Imperial College, where the dose rate was selected by varying the distance of the samples from the source.

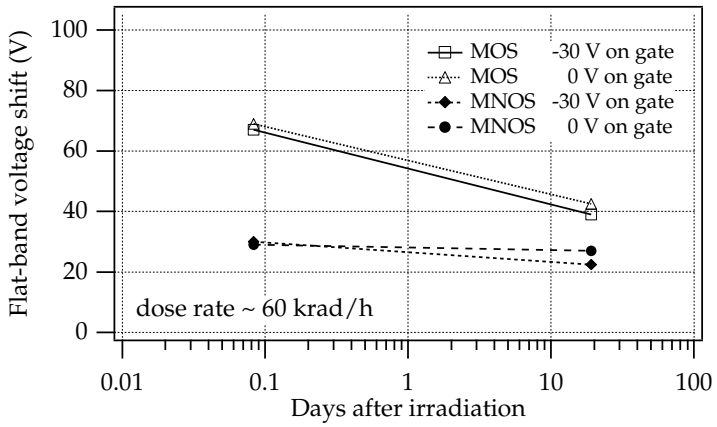

Fig. 3.14. Flat-band voltage shift annealing after gamma irradiations at Imperial College: lower dose rate.

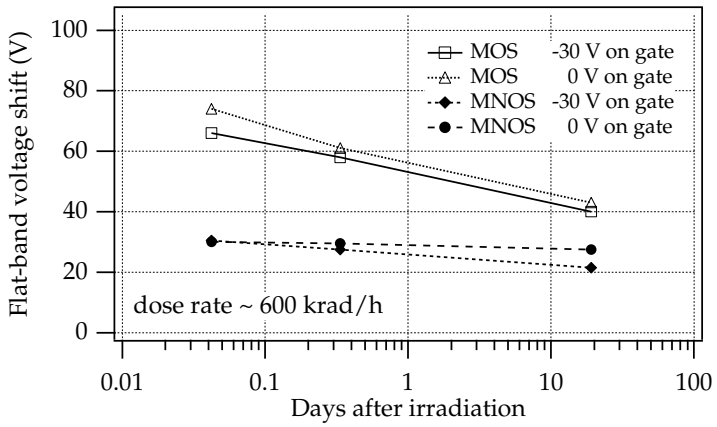

Fig. 3.15. Flat-band voltage shift annealing after gamma irradiations at Imperial College: higher dose rate.

Particularly at lower doses (i.e. at ~300 krad), a bigger effect in the flat-band voltage shift occurred at the lower dose rate. This observation is particularly important as the dose rates normally used for the radiation studies of silicon prototypes are much higher, for practical reasons, than in the LHC environment, where the radiation will be collected at low dose rates continuously over many years of operation.

Finally, to the plot of the flat-band voltage as a function of the received electron dose of fig. 3.4 the additional point from a low dose rate gamma irradiation of a similar MOS device has been added. The comparison, even considering the different conditions of exposure, shows that more oxide damage (in terms of charge deposition) occurred at the much lower gamma dose rate. In both cases the gate had been

left floating during the exposure.

The dose rate effect seen could be explained by the particular conditions of exposure, with a difference in the dose rates of more than four orders of magnitude. A very fast delivery of ionising radiation could not have left time enough for the holes to be trapped at the metal–oxide interface, while a very low dose rate would almost correspond to a quasi-static situation, where short term annealing could also leave place for more charge to be trapped in the oxide.

3.5 Annealing

Annealing in the charge oxide has been monitored over a long period of time after the electron irradiations and the gamma exposure at Brunel University. After $\sim$200 days following the last exposure to electrons, the oxide charge density had dropped steadily by $\sim$60 % for all received doses in the case of the MOS capacitors; the maximum drop for the MNOS capacitors was of $\sim$10 % only, during the same period. In the latter case, though, less charge had been accumulated during the exposure to the same total doses. This annealing inhibiting effect was already observed on integrated circuits and CCDs with the nitride layer [3.9].

Similarly, $\sim$150 days after the gamma irradiation at Brunel Univ. the oxide charge density had dropped by $\sim$50 % in the case of the MOS devices and by $\sim$30 % for the MNOS, both when the capacitors had been left floating or at inversion during the exposure.

Finally, practically no annealing was seen for the MNOS capacitors whose gates had been kept grounded (i.e. at 0 V) during the exposure to the gammas.

3.6 Conclusions

After a certain dose of ionising radiation, saturation in the oxide charge density was reached both for MOS and MNOS capacitors. Long-term annealing was much more evident for MOS than for MNOS devices, also because in the latter case less charge had been accumulated during the exposure to the same total doses.

The gate bias condition during the exposure had a major influence on the quantity of charge accumulated in the oxide because of the irradiation. Finally, dose-rate effects have been observed, again more pronounced in the case of MOS devices [3.10].

These results are relevant to LHC silicon microstrip detectors, when considering effects related to oxide charge accumulation at surfaces, e.g. when evaluating the

field-plate technique used to ensure strip isolation on the ohmic side (i.e. the n-side) of a microstrip detector [3.11]. If this technique is implemented, the ionising radiation, to which the detectors would be exposed, will cause changes in the interstrip isolation properties of these particular MOS-strip structures. Long-term operation of such devices must be ensured (see also Chapter 4).

Chapter 4

Radiation hardness studies of silicon microstrip detectors

In this chapter the radiation hardness studies of silicon microstrip detectors will be described. They consist in measurements of strip capacitances on different p-side microstrip prototypes, and in exposures to ionising radiation, namely electrons and protons, and to neutrons. Some n-side microstrip prototypes have also been evaluated before irradiation, and their measured capacitances will be presented.

Silicon detectors will not be discussed in detail here. This type of particle detector has been produced and developed for a few decades, originally for nuclear physics and spectroscopy applications. Microstrip detectors have already been widely used in recent years as subsystems of high energy physics experiments both in fixed target and in collider geometries, and described in the literature ([4.1], also for an extensive bibliography on this subject). Semiconductor physics (i.e. band structure, doping, charge carriers, signal formation and collection) and technology have also been extensively described ([4.2], and its bibliography).

The principle of charged particle detection is simple: the detector is essentially constituted of a reverse biased diode junction, at whose electrodes the pairs of electrons and holes generated by charged particles traversing the depleted semiconductor are collected. The typical detector thickness is $\sim$300 μm. One or both electrodes (anode and cathode) are subdivided in arrays of *microstrips*, i.e. thin diodes (or pseudo-diodes). Both strip width and strip pitch are normally of the order of a few tens of microns.

The diode structure, the signal collection and the bulk damage and related annealing effects are discussed briefly. The main emphasis here is on surface effects, particularly the behaviour of microstrip capacitances after irradiation. Extensive descriptions of radiation damage effects can be found in the above cited bibliographies, and particularly in [4.3, 4.4, 4.5].

These studies have been performed in the framework of the RD20 collaboration [4.6], aimed at developing high resolution silicon strip detectors and associated front-end electronics for experiments at high luminosity at the LHC. In particular, the microstrip prototypes were designed, produced and evaluated by RD20.

As an example, figs. 4.1 and 4.2 show two wafer layouts of silicon prototypes produced in 1992 at S.I. (Senter for Industriforskning [now SINTEF], Oslo, Norway), the RD20 p-side and n-side test structures [4.7, 4.8]. These wafers had been designed and prototyped to enable complete and extensive investigations of all detector related properties and parameters, including mask layout, manufacturing with industries, detector prototype evaluation and extensive performance tests. Radiation damage studies were performed with ionising and non-ionising particles; annealing was considered under different temperature and biasing conditions.

Time showed that it was necessary to perform these studies in a very systematic way, designing specific prototypes and measuring them carefully under every aspect. A large number of parameters, with different weights, is involved in detector fabrication and performance, and their influence, more or less precisely known, had to be consistently and thoroughly investigated.

The various test structures and detector prototypes are visible; the largest prototypes are DC- and AC-coupled microstrip devices, 4 and 2 cm long, with 50 and 100 μm pitch, designed e.g. to evaluate the detector performance as a function of the strip width. Both p-stop and field-plate techniques have been used to isolate the strip on the n-side structures, as described in section 4.3.

The issues of leakage current, depletion voltage, strip isolation, strip capacitance, oxide properties and bulk and surface radiation damage have been of particular concern; some of them will be addressed in this chapter. Both p-side and n-side structures were used for this purpose.

A number of smaller devices surrounds the central ones on both wafers. They consist mostly in diodes, photodiodes and MNOS capacitors, which have been used e.g. for the studies described in Chapter 3. Some general purpose test structures were also included, to test in a simplified way important parameters such as polysilicon resistance, diode currents and capacitances, and MOS properties on tiny devices realised with the same techniques as the bigger microstrip prototypes.

Other issues such as metal sheet resistance, oxide breakdown voltage and wedge strip geometries could also be addressed, thanks to these prototypes batches. Effect of these studies was the spread of knowledge and experience among the collaboration, thanks to the prototypes available to the laboratories for the different evaluations.

The work presented in the following led to results included in RD20 status re-

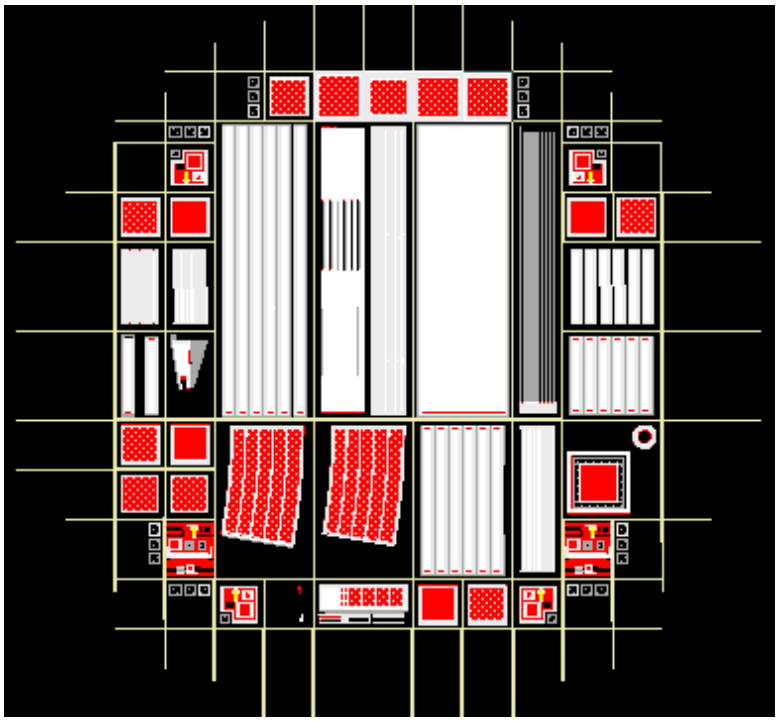

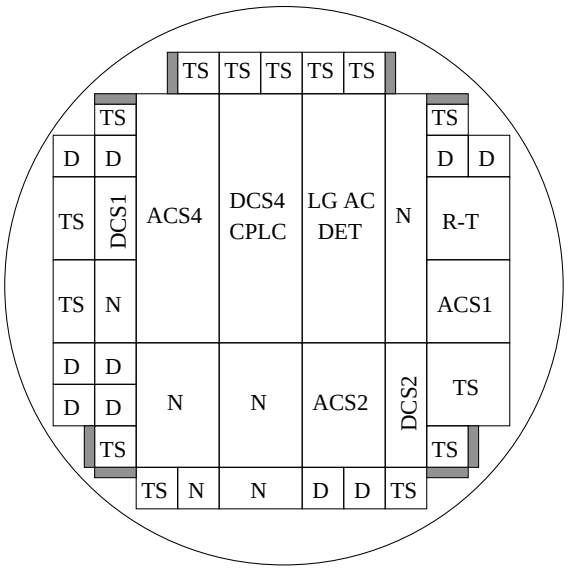

TS	test structure
D	diode
ACS1 ACS2 ACS4	AC strips 1,2,4 cm long
DCS1 DCS2 DCS4 CPLC	DC strips 1,2,4 cm long coupling test structure
R-T	reach-through
N	other devices
LG AC DET	detector prototype
	MNOS caps.

Fig. 4.1. Wafer layout of the p-side silicon prototypes for RD20.

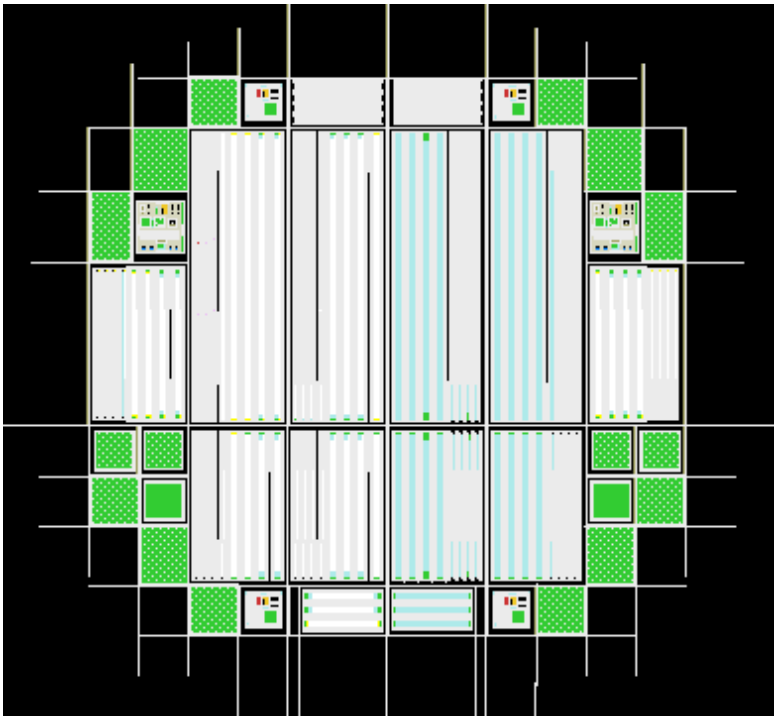

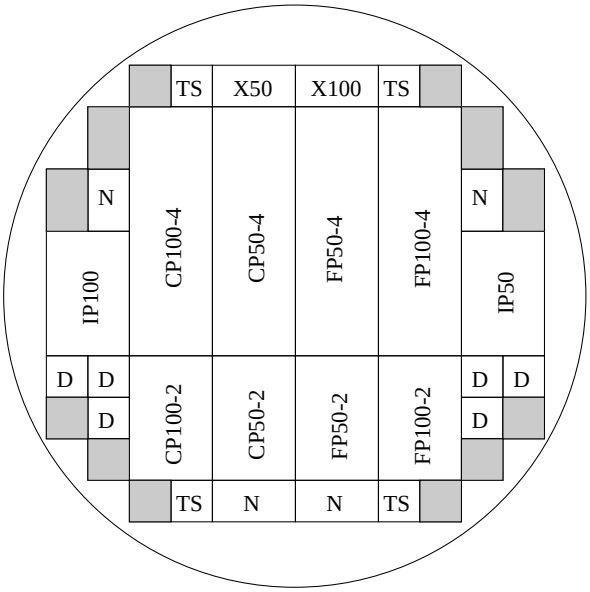

TS	test structure
D	diode
FP50-4 FP50-2 FP100-4 FP100-2	field plates strips
CP50-4 CP50-2 CP100-4 CP100-2	common p-stop strips
IP50 IP100	individual p-stop strips
X50 X100	double metal crossings
N	other devices

Fig. 4.2. Wafer layout of the n-side silicon prototypes for RD20.

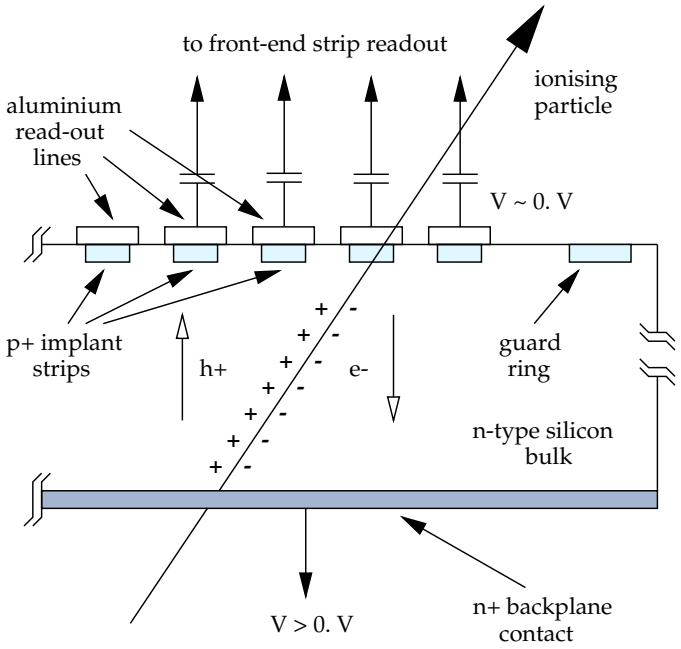

Fig. 4.3. Schematic cross-section of a silicon microstrip detector, single sided, DC-coupled (silicon dioxide layer not shown).

ports [4.9, 4.10] and in published papers about radiation tolerance studies of silicon microstrip detectors for the LHC [4.11, 4.12, 4.13].

4.1 Silicon microstrip detectors

The principle of operation of a silicon microstrip detector is represented in fig. 4.3, where a schematic cross-section of a *single sided* (i.e. with strips on the p^+-n *junction* side only) *DC-coupled* microstrip detector is shown. The layer of silicon dioxide (SiO_2) has not been drawn for simplicity.

If a layer of SiO_2 is interposed between the aluminium read-out lines and the p^+ implant strips, the capacitor coupling the strip to the front-end electronics is realised on the detector itself. Such a detector is usually described as *AC-coupled.*

When microstrips are realised on both sides of the detector, i.e. on the *ohmic* side as well, at the n-n^+ pseudo-junction, two-dimensional information is provided by the same detector, now described as *double-sided.* Fig. 4.4 shows layouts of the p- and n-sides of a double-sided silicon microstrip detector with small angle stereo strips. In this case, the front-end electronics are located at the same end of the detector, on the two opposite surfaces.

An alternative configuration would consist in orthogonal strips on the two sur-

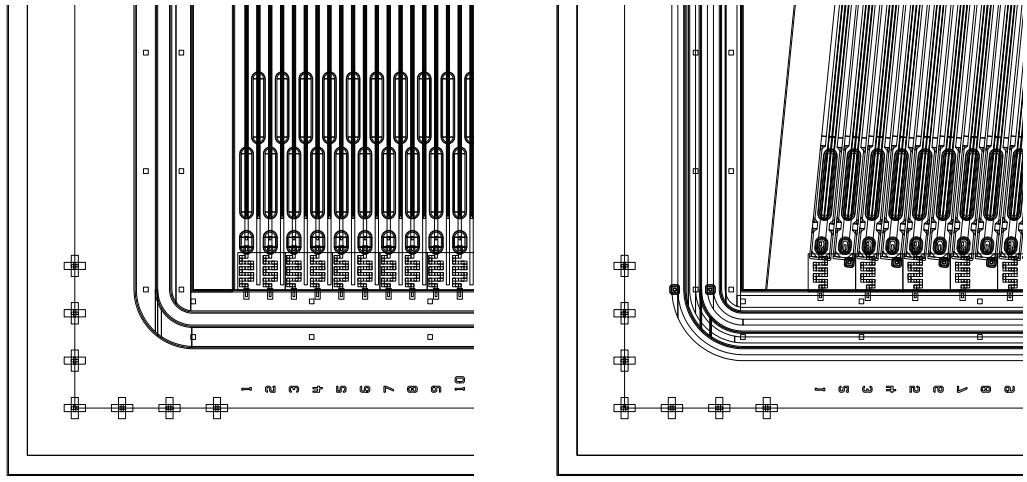

Fig. 4.4. Schematics of the p-side (left) and of the n-side (right) of a double-sided silicon microstrip detector with small angle stereo strips.

faces, with the front-end electronics located at different edges of the detector as a consequence, unless a means of reconducting the orthogonal strips to be read at the same detector end is realised (e.g. with the technique of double-metal layers separated by polyimide).

Three important detector characteristics which are always evaluated on prototypes and which are used in the optimisation of microstrip design and manufacturing technology are *leakage current* (or *dark current*), *interstrip isolation* and *interstrip capacitance.*

The leakage current is the current flowing through the detector under bias, in absence of a signal generated by a charged particle crossing the active volume of the detector.

Three different components contribute to the total leakage current: *generation, diffusion* and *surface* currents. The generation current originates in the thermal creation of electron–hole pairs within the depleted region of the detector, while the diffusion current is due to pairs created in the undepleted neutral region. In thermal equilibrium charge pairs are continually generated in the crystal, and would recombine in absence of an electric field across the semiconductor. When operating normally, a microstrip detector is fully depleted and therefore the measured leakage current is due only to the generation term.

The surface term is the least quantifiable and it can be often substantially reduced by means of *guard ring* structures, realised all around the active surface of the detectors to draw as much surface current as possible away from the active region.

Some surface contributions, e.g. from processing conditions, are unavoidable.

Because of consequences for electronic noise, leakage currents must be kept as low as possible, with achievable values of the order of a few nA/cm^2. Exposure to heavy particle fluxes (i.e. protons, neutrons, pions) results in an increase of the leakage current per unit volume $\Delta I/V$, which is commonly parameterised as

$$\frac{\Delta I}{V} \;=\; \alpha\,\phi\;, \tag{4.1}$$

where ϕ is the fluence of irradiation, measured in particles per cm^2, and α is a constant of the order of $\sim 10^{-16}$–10^{-17} A $\cdot$ cm^{-1}, depending on the particle type and energy.

The interstrip isolation is evaluated by measuring the electric resistance between neighbouring strips, which should ideally be as high as possible, to approximate every single strip to an independent diode. Isolation on the ohmic side (i.e. the n-side) of a double-sided detector must be achieved by means of special techniques, as there is no junction between the n$^+$-strips and the n-type bulk, and therefore the interstrip resistance would not be satisfactory if microstrips were realised exactly as on the junction side. These techniques will be mentioned when describing the measurements performed on n-side microstrip prototypes (section 4.3).

The strip isolation must remain acceptable also after the detector has been exposed both to ionising radiation and to heavy particle fluxes: the former is mainly responsible for surface effects, which modify the oxide charge density, while the latter modifies the effective doping concentration $N_{\rm eff}$ of the substrate, which eventually *inverts* (e.g. at a neutron fluence of $\sim 10^{13}$ cm^{-2}) and becomes similar to p-type silicon. The junction side (n bulk–p$^+$ strips) becomes pseudo-ohmic (inverted bulk–p$^+$ strips), and the ohmic side (n bulk–n$^+$ strips) becomes a pseudo-diode (inverted bulk–n$^+$ strips).

The parameterisation of donor removal and acceptor creation following exposure to a particle fluence ϕ is normally expressed by [4.14]:

$$N_{\rm eff} \;\simeq\; N_D\, e^{-c\phi} \;-\; N_A \;-\; \beta\,\phi\;, \tag{4.2}$$

where N_D and N_A are respectively the donor and the acceptor concentrations before the irradiation, β and c are the parameters to be extracted from the fitted data. The model is based on the assumption that the donor removal rate is proportional to the donor density, while the acceptor creation takes place at a constant rate with fluence.

This parameterisation describes quite well the available data. Values of β range

e.g. from 0.02 to 0.08 cm^{-1} for fast (i.e. $\sim$1 MeV) neutrons; the parameter c is of the order of 10^{-13} cm^2 [4.5].

The initial donor concentration N_D is of the order of 10^{11}–10^{12} cm^{-3}, to keep the full depletion voltage acceptable ($V_d \sim q\,N_D\,d^2\,/\,2\,\epsilon \sim 7.7 \times 10^{-10}$ V $\cdot$ m $\cdot$ $N_D\,d^2$; thus, for $d \sim 300$ μm and $N_D \sim 10^{11}$ [10^{12}] cm^{-3}, $V_d \sim 7$ [70] V). The corresponding resistivities are of the order of a few k$\Omega \cdot$ cm; thus the material currently used for silicon microstrip detectors is *high resistivity* silicon [4.1].

The total strip capacitance (C_{TOT}) to the detector system, as seen by the signal at the input of the front-end electronics excluding the coupling capacitor, is usually considered as the sum of the capacitance of the strip considered towards the opposite surface, C_B, and of the contributions given by the i-th order neighbour strips, C_i:

$$C_{TOT} = C_B + C_1 + C_2 + C_3 + \ldots \,. \tag{4.3}$$

The three main components of C_{TOT} are the capacitance to the nearest neighbours C_1, the capacitance to the second order neighbours C_2, and the capacitance to the backplane C_B. The sum of C_1 and C_2 is usually called 'interstrip capacitance', as the contributions of higher order neighbours become negligible.

C_{TOT} depends on the detector geometry, i.e. on the strip pitch and width, as well as on the detector thickness (for the C_B contribution). C_{TOT} is normally measured per unit of strip length, and is of the order of $\sim$1 pF/cm for the detectors used.

The technique of measurement of strip capacitances is rather complicated: the contributions (4.3) are measured separately, by excluding the unwanted ones from the test circuit. Fig. 4.5 shows the electrical connections, usually realised by means of contacts to the detector bonding pads using a probe station, for two different strip measurement configurations, i.e. for the strip to backplane and for the interstrip capacitance measurements. The instrument used for all measurements presented in the following was a Keithley high frequency CV-analyser, with a test pulse of 100 kHz; the detector was normally biased at 100 V via an external electrometer–bias supply.

Even though strip capacitance measurements are conceptually simple, it requires care and experience to perform such measurements, because of the many parameters involved in this operation (detector conditions, quality of contacts, minimisation of stray contributions especially), and also not to damage the detector prototype under test when making probe contacts.

Again, the detector must be designed to withstand extended exposure to damaging radiation without an increase of its strip capacitances beyond an acceptable

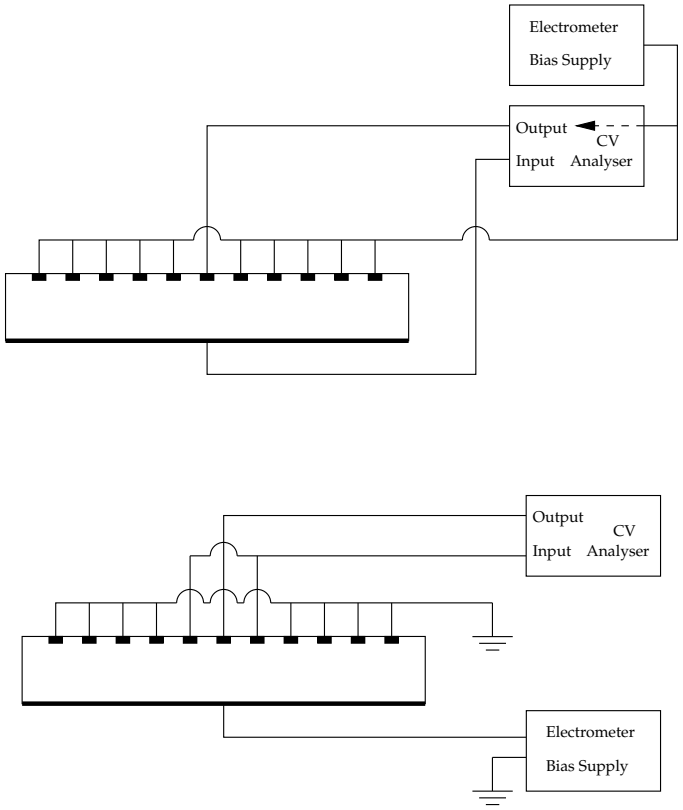

Fig. 4.5. Measurement of microstrip capacitances: measurement scheme for strip to backplane capacitance (upper) and for interstrip capacitance (lower).

limit. An aim of the irradiation programmes performed here was to investigate and optimise this aspect of detector radiation hardness.

The measured strip capacitances were also compared to their theoretical values obtained from a simulation program previously originally developed, which evaluates the different microstrip capacitance contributions by means of a purely geometrical calculation, making use of a variational method. A full description of this technique and results have been described in [4.15, 4.16].

As an example, fig. 4.6 shows the calculated total strip capacitance as a function of the width/pitch ratio, in the case of a 300 μm thick detector, for two different pitch values. Only the first and second order neighbours have been considered. The graph shows that the strip capacitance is a fairly simple function of this ratio, which turns out to be the most important geometrical parameter to be considered when optimising detector capacitances. For a strip pitch of 50 μm and a strip width of 10 μm, the calculated total strip capacitance would be of the order of $\sim$1 pF/cm. The strip capacitances are dominated by geometry, at least prior to exposure to irradiation.

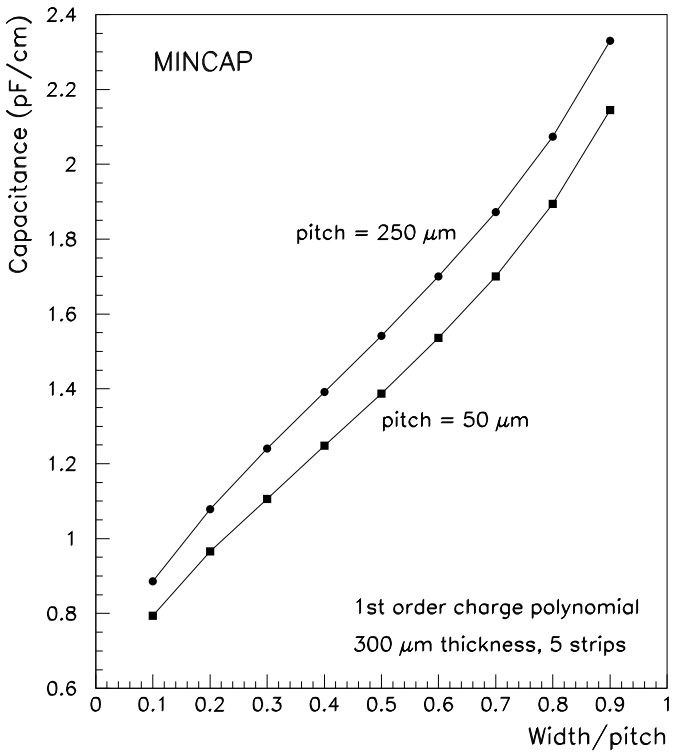

Fig. 4.6. Variational microstrip capacitance calculation [4.15, 4.16]: total strip capacitance as a function of strip width/pitch.

4.2 Exposures of microstrip test structures for strip capacitance studies

I organised and performed a few sets of exposures of microstrip prototypes to ionising radiation, to evaluate the subsequent evolution of strip capacitances and their behaviour with time, during annealing at room temperature.

Detectors were irradiated with electrons, for the first time within the RD20 collaboration. A set of irradiations with protons has also been performed, in collaboration with the University of Padova. The tests have been carried out measuring before and after irradiation all detector parameters relevant to these studies, such as depletion voltage, interstrip capacitance and interstrip resistance.

The RD20 devices irradiated with electrons (section 4.2.1) and protons (section 4.2.2) have been described in [4.7]: they consist in DC-coupled microstrip test structures, with six groups of nine strips at a constant pitch of 50 μm. The strip length varied from 1 to 4 cm, but all capacitances have been expressed per unit of strip length to ease comparison.

Table 4.1 shows the values of the nominal strip and metal widths for the six

nominal strip width	nominal metal width	nominal strip width	nominal metal width
5 μm	10 μm	20 μm	15 μm
10 μm	15 μm	30 μm	20 μm
15 μm	20 μm	40 μm	20 μm

Table 4.1. Nominal strip and metal widths for RD20 p-side microstrip prototypes, DC- and AC-coupled (50 μm pitch).

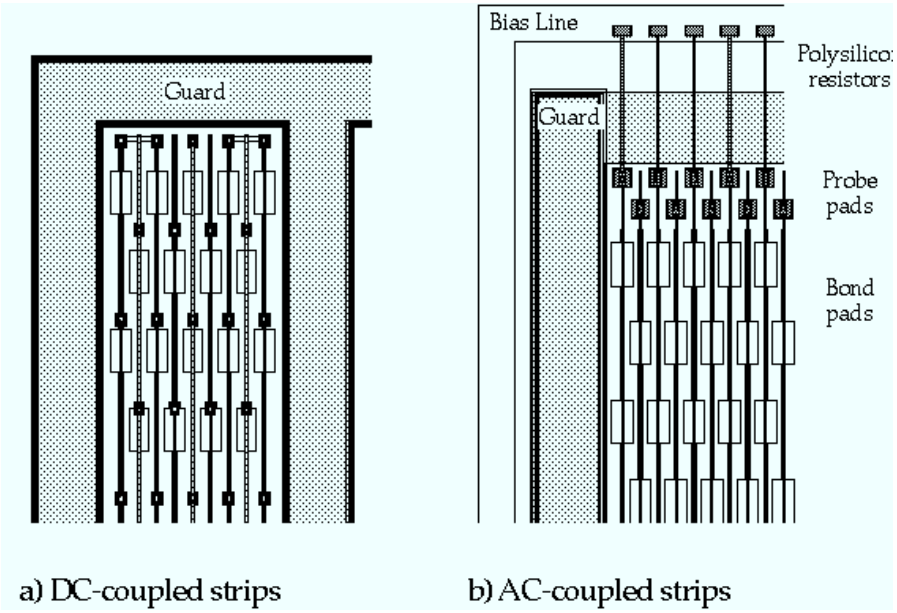

Fig. 4.7. Schematic of DC-coupled (a) and AC-coupled (b) RD20 microstrip test structures.

strip groups. In reality, the strips turned out to be 2–4 μm wider than designed because of unexpected widening of the diffusion layer during processing. Therefore, in quite a few structures the widest strips were shorted together despite a nominal separation of 10 μm.

Fig. 4.7 shows a schematic of the DC-coupled microstrip test structures, along with the similar AC-coupled prototypes realised on the same wafer produced at S.I., Oslo, Norway. A common guard surrounds the strip groups and separates them from each other. The three outer strips on either side with respect to the centre are connected together, to facilitate probing for strip measurements. Thus, only the three central strips had been left independent.

Two important features of this wafer production have been the realisation of an additional silicon nitride layer on top of the silicon oxide as dielectric for strip

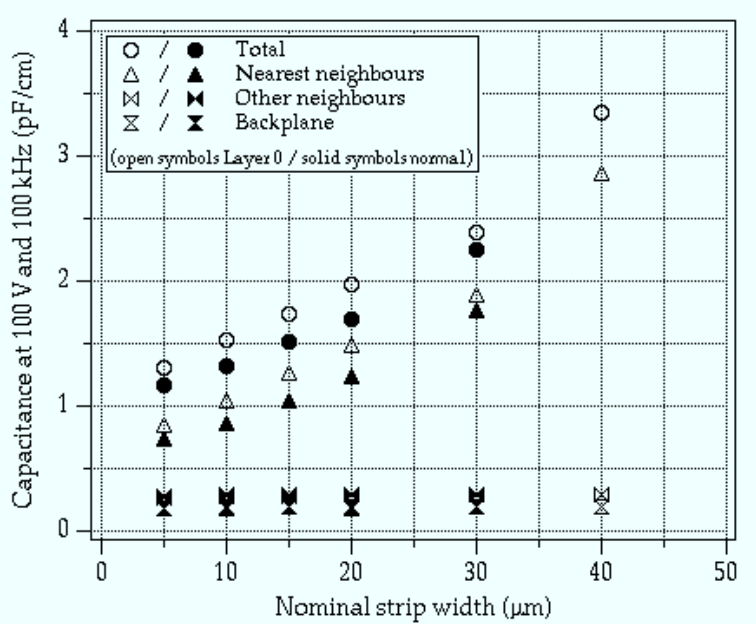

Fig. 4.8. Microstrip capacitances of unirradiated DC-coupled test structures at 100 V, 100 kHz, showing a breakdown of the different contributions to the total.

coupling capacitors and MOS capacitors (as already mentioned in section 3.1), and a phosphorus field implantation between the strips on half of the wafers, referred to as 'layer 0'. The purpose of the layer 0 was to ensure strip isolation if the oxide charge was too low [4.12], and test structures with and without this layer have been compared under different aspects.

4.2.1 Electron irradiation of p-side RD20 microstrips

The electron irradiations were performed at A.E.R.I.A.L., as described in section 2.2.1, up to a total dose of (5.6 ± 0.2) Mrad. Four microstrip test structures were irradiated to different doses, to enable a complete study of strip capacitance modifications after exposure over a wide dose range, and of subsequent annealing.

Measurements of the test structures were taken before the irradiation, as described before, allowing the different contributions to the strip capacitances to be separated. They are summarised in fig. 4.8, which shows the capacitances for the six strip groups. The nearest neighbour capacitance increases with the strip width, as predicted, while the other neighbour and the backplane contributions are practically a constant term of a few tenths of a pF/cm.

The total strip capacitances range from $\sim$1.2 pF/cm for the 5 μm strips, up to $\sim$2.3 pF/cm for the 30 μm strips, for the structures without layer 0. When

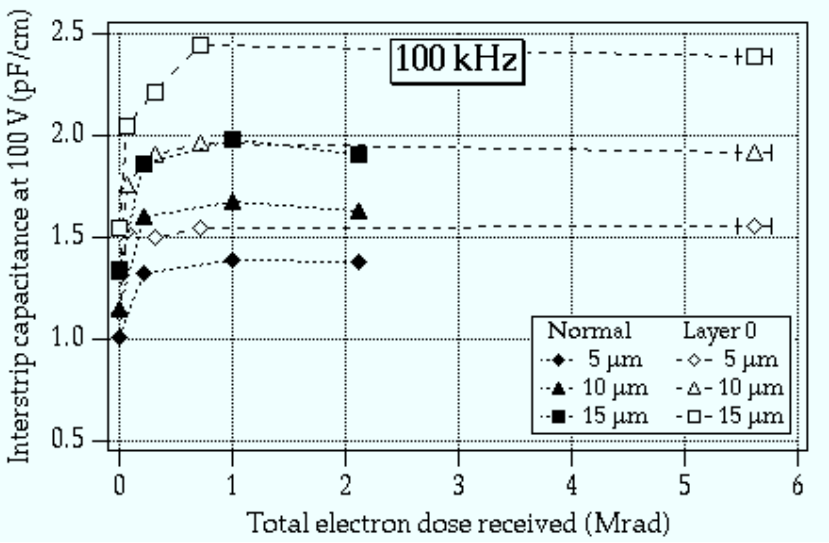

Fig. 4.9. Interstrip capacitance at 100 V, 100 kHz, as a function of electron dose for DC-coupled strips (with and without layer 0).

the layer 0 is present, the capacitances are on average already 10 % higher before irradiation, the increase showing essentially in the nearest neighbour contribution. This is an important observation as design and technology have to be optimised to minimise the strip capacitance.

The plot of the interstrip capacitance as a function of electron dose, presented in fig. 4.9, shows a saturation effect similar to that observed in the case of MOS and MNOS capacitors. After a total electron dose of ~1 Mrad, the capacitances essentially remained at a constant plateau, up to doses of ~5.6 Mrad. The plateau value is about 40–50 % higher than the pre-irradiation value for the structures without layer 0, and about 50–70 % higher for the structures with layer 0. Thus, the presence of the layer 0 enhanced the strip capacitance increase following exposure to ionising radiation.

It is interesting to plot the interstrip capacitance as a function of strip width for the devices irradiated (fig. 4.10), showing the increase with increasing (nominal) strip width for structures without layer 0. The plot also shows that after ~1–2 Mrad of electrons the interstrip capacitance raised from ~1 pF/cm to ~1.4 pF/cm for the 5 μm wide strips, and from ~1.5 pF/cm to ~2.1 pF/cm for the 20 μm strips.

The CV-behaviour of the strip capacitances after irradiation was also examined and compared to that before: fig. 4.11 shows the interstrip capacitance as a function of the applied bias voltage, for the case of strips without layer 0 exposed to a dose of (2.1 ± 0.2) Mrad. The values quoted in results and comparisons always correspond

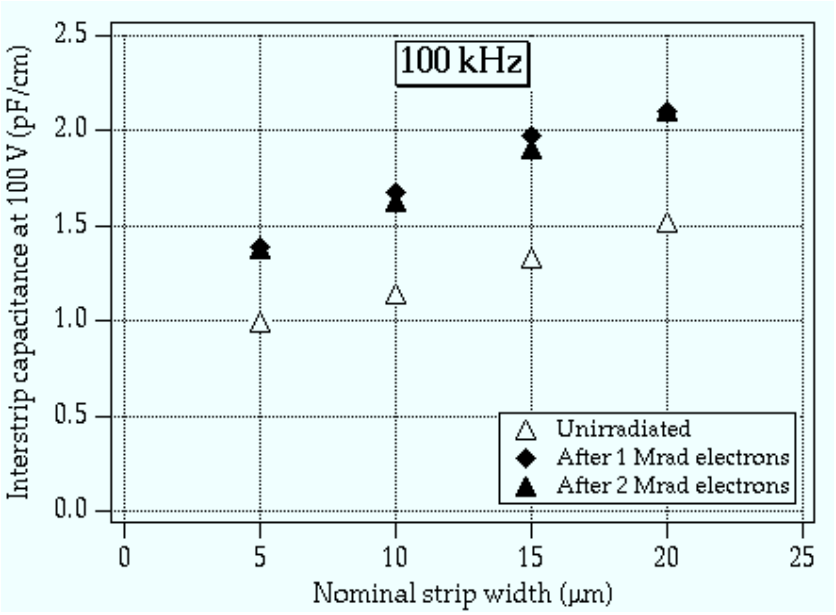

Fig. 4.10. Interstrip capacitance at 100 V, 100 kHz, as a function of strip width for electron irradiated DC-coupled strips (without layer 0).

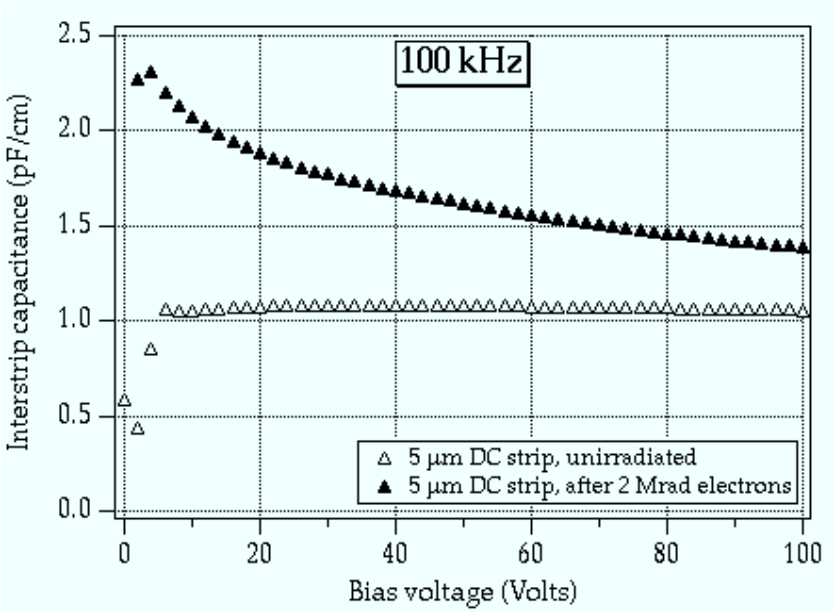

Fig. 4.11. Interstrip capacitance at 100 kHz as a function of bias voltage for electron irradiated DC-coupled strips (without layer 0).

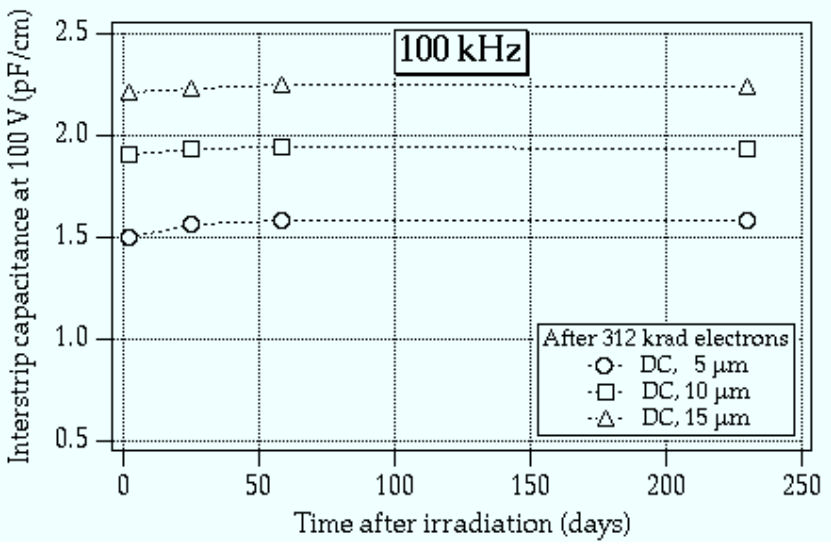

Fig. 4.12. Time dependence of interstrip capacitance at 100 V, 100 kHz, for electron irradiated DC-coupled microstrips (with layer 0).

to the bias voltage of 100 V.

The curves before and after irradiation are different: before irradiation the strip capacitance remained almost constant after a bias voltage of ~10 V had been applied, showing no further decrease with increasing bias, while the capacitance after irradiation depends strongly on the applied bias, and decreases without yet reaching a flat minimum in the region of 100 V.

Therefore operation at high voltage appears to be necessary to minimise the strip capacitance after ionising radiation, and even bias voltages higher than 100 V (the 'standard' from past experience) could be envisaged, once the oxide has been proven to withstand high fields without break down effects. This may well become necessary anyway to keep the detector over-depleted after inversion will have occurred and the depletion voltage has substantially increased.

The strip capacitances were measured a few more times to observe possible annealing effects, up to 230 days after the end of the exposure. Fig. 4.12 shows the time dependence of the interstrip capacitance for a received electron dose of (312 ± 20) krad, on structures with layer 0. Not only was no decrease seen, but there appears to be a slight tendency towards capacitance increasing. The absence of capacitance decrease can be explained by the presence of the silicon nitride layer on top of the silicon dioxide, which was already shown to limit, if not to inhibit, oxide charge annealing (section 3.5).

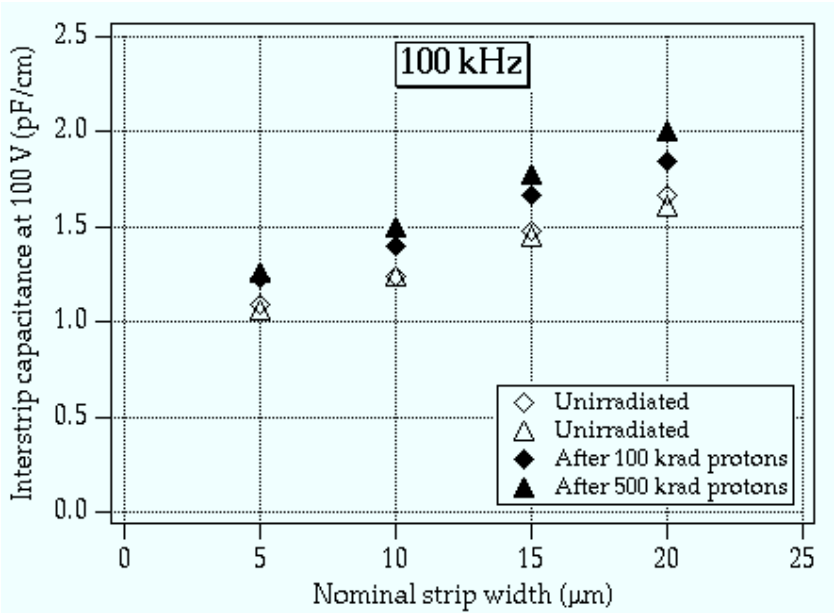

Fig. 4.13. Interstrip capacitance at 100 V, 100 kHz, as a function of strip width for proton irradiated DC-coupled strips (without layer 0). Open symbols refer to the corresponding pre-irradiation values.

4.2.2 Proton irradiation of p-side RD20 microstrips

A set of proton irradiations of p-side RD20 microstrip test structures (without layer 0) has also been performed.

The irradiations were carried out at the *Laboratori Nazionali di Legnaro (Legnaro National Laboratory,* Padova, Italy, making use of a 7 MV *Van der Graaf* proton accelerator. The beam of (6 $\pm$ 0.2) MeV protons was measured to have an area of 1 cm^2 and are known to have a penetration depth in silicon of about 300 μm, i.e. similar to the silicon sample thickness. Irradiations and dosimetry have been described in [4.17]. Total doses of $\sim$100 and $\sim$500 krad have been delivered to two different samples.

The dosimetry was performed by measuring the proton fluence on the samples with two surface barrier silicon detectors, which counted the protons scattered back from two thin gold films located on the beam line; the dose rate was of the order of a few krad per minute. The precision thus obtained is of $\sim$15 % [4.17].

The interstrip capacitances ($C_1 + C_2$) before and after exposure are plotted against the nominal strip width in fig. 4.13 for the first four strip groups only. The observed increase was limited to $\sim$20 % of the pre-irradiation value, with a capacitance of $\sim$1.2 pF/cm for the narrowest strips (5 μm nominal width) up to $\sim$2.0 pF/cm for the widest strips considered (20 μm) after 500 krad of protons.

nominal strip width (μm)	actual strip width (μm)	strip pitch (μm)	actual width / pitch ratio	nominal strip width (μm)	actual strip width (μm)	strip pitch (μm)	actual width / pitch ratio
20	24	40	0.60	40	44	100	0.44
20	24	80	0.30	40	44	140	0.31
20	24	120	0.20	40	44	180	0.24
20	24	160	0.15	100	104	160	0.65

Table 4.2. Strip geometries of the neutron irradiated SI UV1 p-side microstrip prototypes.

It must be noted that protons are a cause of both surface effects, because of their charge, and of bulk effects, because of their mass. Surface effects, as described in section 3.3, result in oxide charge increase at the silicon-oxide interface, and therefore in a strip capacitance increase, though more limited than in the case of electron irradiations.

4.2.3 Neutron irradiation of p-side SI microstrips

As a part of the strip capacitances studies, I measured some microstrip prototypes which had been irradiated with neutrons at the ISIS facility at RAL (section 2.4). These test-structures belonged to a previous prototype production (called SI UV1), already mentioned in section 3.1. Neither the layer 0 nor the silicon nitride layer were present on these structures.

The microstrip prototypes used are formed by three groups of strips with different widths; their geometries are summarised in table 4.2. They were designed to study strip parameters within a wide range of widths and gaps. As mentioned before, strip widths can more realistically be estimated to be $\sim$4 μm wider than the design value, due to widening of the diffusion layer during processing. Strips with 20 and 40 μm nominal widths are 3.8 cm long, while the widest strips (100 μm) are only 1.45 cm long. All capacitance values are again quoted in pF/cm.

Samples with delivered neutron fluences of $\sim 4 \times 10^{12}$, $\sim 10^{13}$ and $\sim 3 \times 10^{13}$ cm^{-2} were measured; the irradiation was performed leaving the samples unbiased. Results are summarised in fig. 4.14 in the form of a plot of the total strip capacitance (C_{TOT}) as a function of the realistic strip width/pitch ratio. This form is particularly convenient to ease comparison. Values after irradiation range from $\sim$1.2 pF/cm to $\sim$2 pF/cm, and show a limited increase of $\sim$10–15 % with respect to the pre-irradiation values. This increase comes mainly from the nearest neighbour

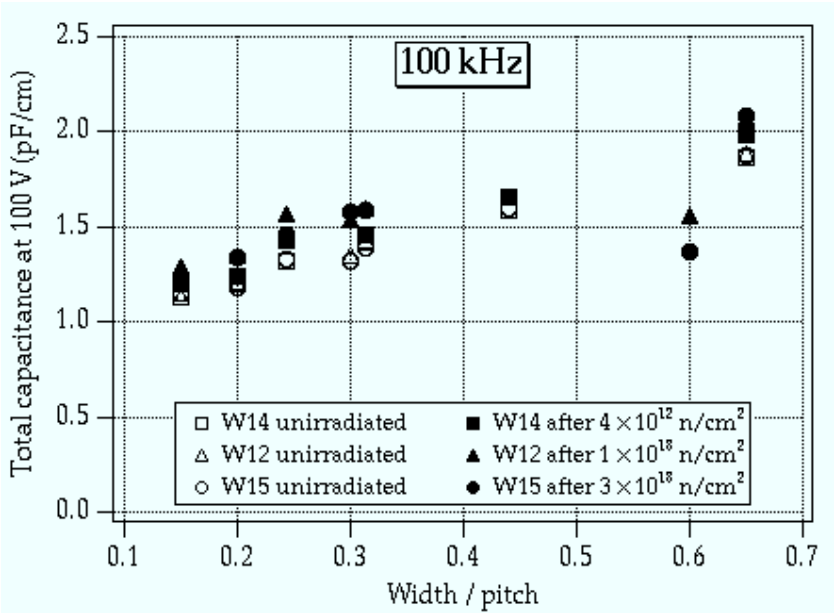

Fig. 4.14. Total strip capacitance for the neutron irradiated DC-coupled microstrips at 100 V, 100 kHz.

contribution.

As one would not expect neutron exposure to modify strip capacitances significantly, it is probable that this effect had been caused not only by the neutrons themselves[1], but also from ionising particles originating from the activation of the material in the neighbourhood of the sample (e.g. supports and containers) during the irradiation[2] [4.11].

Some RD20 DC-coupled microstrip prototypes, similar to those used for the electron irradiations, were also exposed at RAL to a very high neutron fluence of $\sim 1 \times 10^{14}$ n/cm^2. As this value is well beyond inversion, a very high bias voltage (>250 V) would have been necessary to deplete completely the device. But the range of the measuring instruments was already enough to show the tendency of the interstrip capacitances to go essentially back to their pre-irradiation values, once full depletion would have been reached, confirming the expectation of no major modifications to the interstrip capacitances following neutron irradiation.

[1] A systematic error in the neutron fluence estimates was discovered at a later stage, and it may have been such that type inversion had actually not been reached. If indeed type inversion had occurred, the low-field effect on the p-side could have contributed to the strip capacitance increases, enhancing the effect of low oxide charge levels [4.18].

[2] The estimated contamination of the ISIS neutron flux with ionising particles is e.g. of the order of 0.1 % for protons (in fluence) and of 10 % for gammas (in dose) [4.19]. The latter value in particular can be consistent with the observed strip capacitance increase, which could be attributed to a few hundred krad ionising radiation, for corresponding fluences.

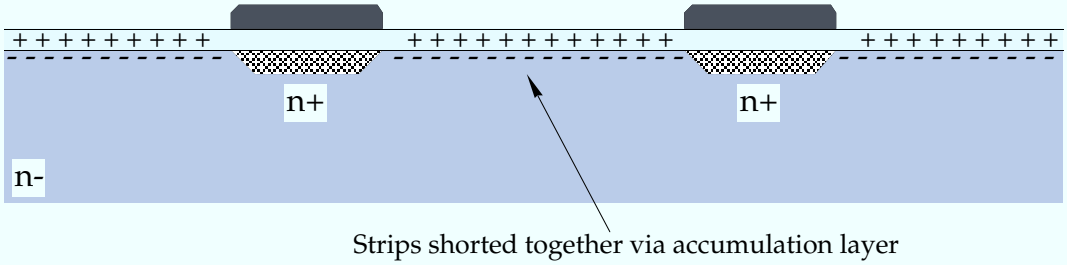

a) No isolation

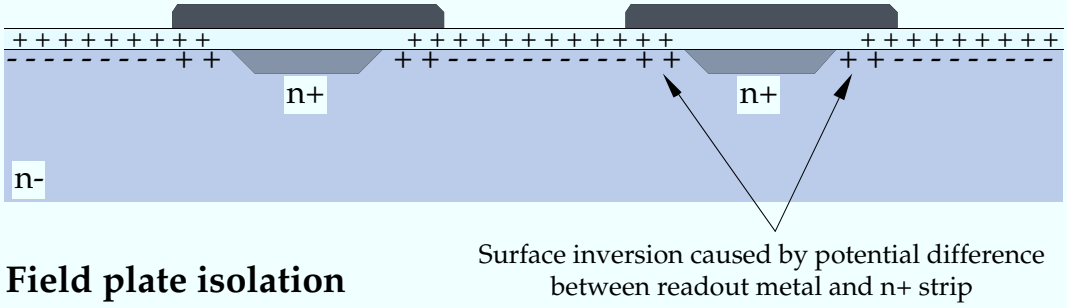

b) Field plate isolation

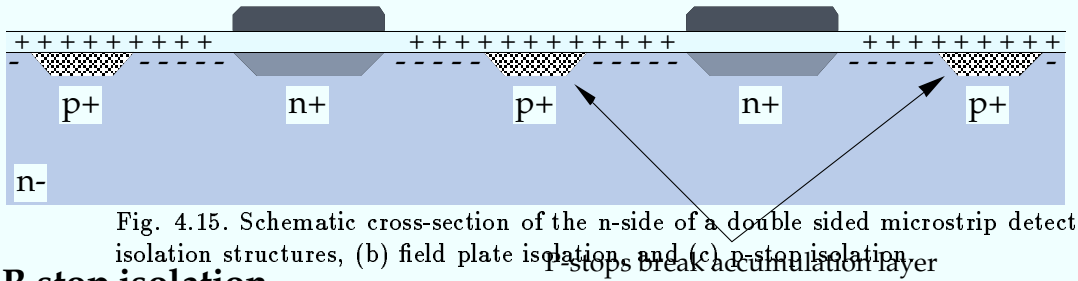

Fig. 4.15. Schematic cross-section of the n-side of a double sided microstrip detector, with (a) no isolation structures, (b) field plate isolation, and (c) p-stop isolation.

c) P-stop isolation

4.3 Measurements of unirradiated p-stop n-side RD20 microstrips

The devices on the n-side RD20 prototype wafers (fig. 4.2) are fully described in [4.8]. The many detectors and test-structures contained were aimed at enabling full characterisation of microstrips realised on the n-side, i.e. on the ohmic side of a double-sided detector.

The main issue was the evaluation of the two most common techniques of strip isolation on the n-side, the *field-plate* and the *p-stop* techniques, and a comparison between them. Fig. 4.15 shows schematically a cross-section of the n-side of a microstrip detector. The configurations without strip isolation, with field-plate isolation and with p-stop isolation are all represented, with some spatial charge distributions.

The field-plate technique consists in designing the metal read-out strips wider than the n^+-strips below, from which they are separated by the oxide (and the

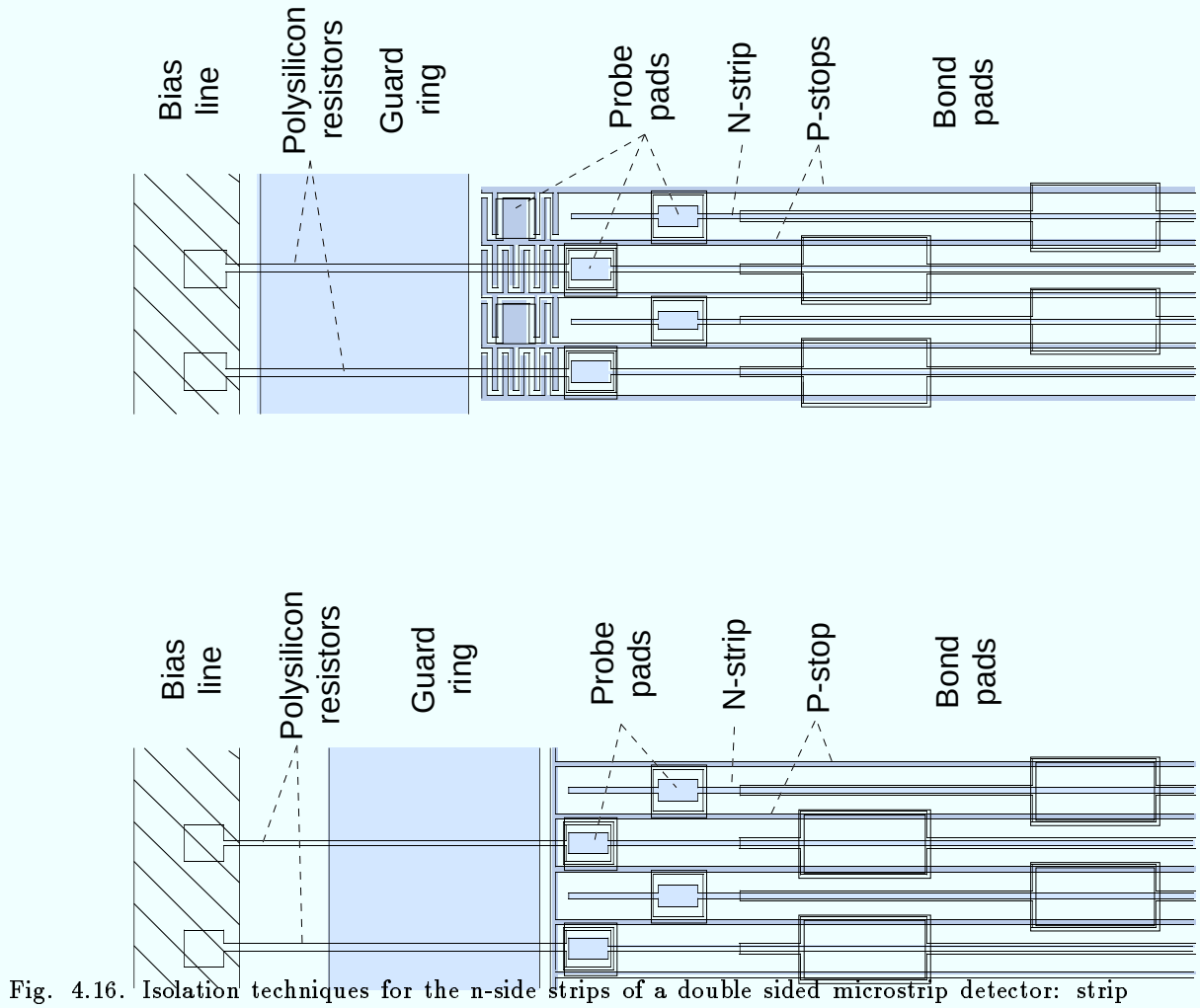

Fig. 4.16. Isolation techniques for the n-side strips of a double sided microstrip detector: strip layouts.

nitride, if applicable). By applying a potential difference between the metal read-out lines (i.e. the field-plates), and the n^+-strips, charge inversion at the surface occurs and neighbouring n^+-strips become isolated. Because of the applied field across the oxide, this technique requires the oxide to withstand prolonged operation under bias without phenomena of charge leaking, i.e. without creating, temporarily or permanently, *pinholes.* Pinholes are microscopic charge channels through which current can flow between the n^+-strips and the read-out lines. Imperfections in the oxide layer may already be present, and high electric fields may cause the creation of conductive channels.

Isolation between neighbouring n^+-strips can alternatively be realised by means of a set of p^+-strips, called 'p-stops', which effectively break the accumulation layer. These p-stops are situated in each gap between the strips and prevent currents from flowing from one strip to another. The p-stops can be all connected together (*common* p-stop configuration), or else be independent from every other (*individual* p-stop configuration). The p-stop strips can be left floating: when the detector is biased and depleted, they will reach their operating voltage, which was also measured during this prototype characterisation.

Fig. 4.16 shows the two isolation techniques, with the common and individual

CP50 – IP50 groups	nominal strip width	nominal p-stop width	CP100 – IP100 groups	nominal strip width	nominal p-stop width
I	5 μm	5 μm	I	5 μm	65 μm
II	5 μm	12 μm	II	25 μm	45 μm
III	5 μm	20 μm	III	40 μm	30 μm
IV	10 μm	10 μm	IV	65 μm	5 μm

Table 4.3. Nominal strip and p-stop widths for RD20 n-side microstrip prototypes CP50/IP50 (50 μm pitch) and CP100/IP100 (100 μm pitch).

options for the p-stops, implemented on the microstrip test-structure used, but for the corresponding AC-coupled devices.

I performed a complete evaluation of the strip capacitances of the p-stop n-side microstrips, before irradiation. The results were subsequently compared to the values after photons and neutron irradiations, and results have been presented in [4.10] and [4.13].

The geometrical characteristics (i.e. the n-strip and p-stop widths) of the devices used for this study are summarised in table 4.3. These microstrip test-structures have been usually referred to as *CP* or *IP,* depending if the p-stop was 'common' or 'independent', followed by a number (*50* or *100*) indicating the strip pitch in μm. On each there were four groups of DC-coupled and four of AC-coupled strips, with different strip widths. Only the DC-coupled strips have been considered for the strip capacitance measurements described in the following. Seven strips formed each group of the DC-coupled devices with 50 μm pitch, and only five strips each group with 100 μm pitch.

Three different doping concentrations were used for the p-stop strips, namely 1×10^{11}, 9×10^{11} and 5×10^{13} cm^{-2}. Only the highest was proven to perform fully satisfactorily in terms of strip isolation under all conditions, and to those particular ones the results in the following will refer, even though all of them have been evaluated.

As an example, figs. 4.17 and 4.18 shows the capacitance components of the common p-stop devices with pitches of 50 and 100 μm respectively, plotted for each of the four strip groups.

The total capacitance increases, as expected, with increasing strip width, and the backplane contribution is essentially insensitive to the strip geometry. A total strip capacitance of $\sim$2.1–2.4 pF/cm was measured at 100 kHz for the 50 μm pitch

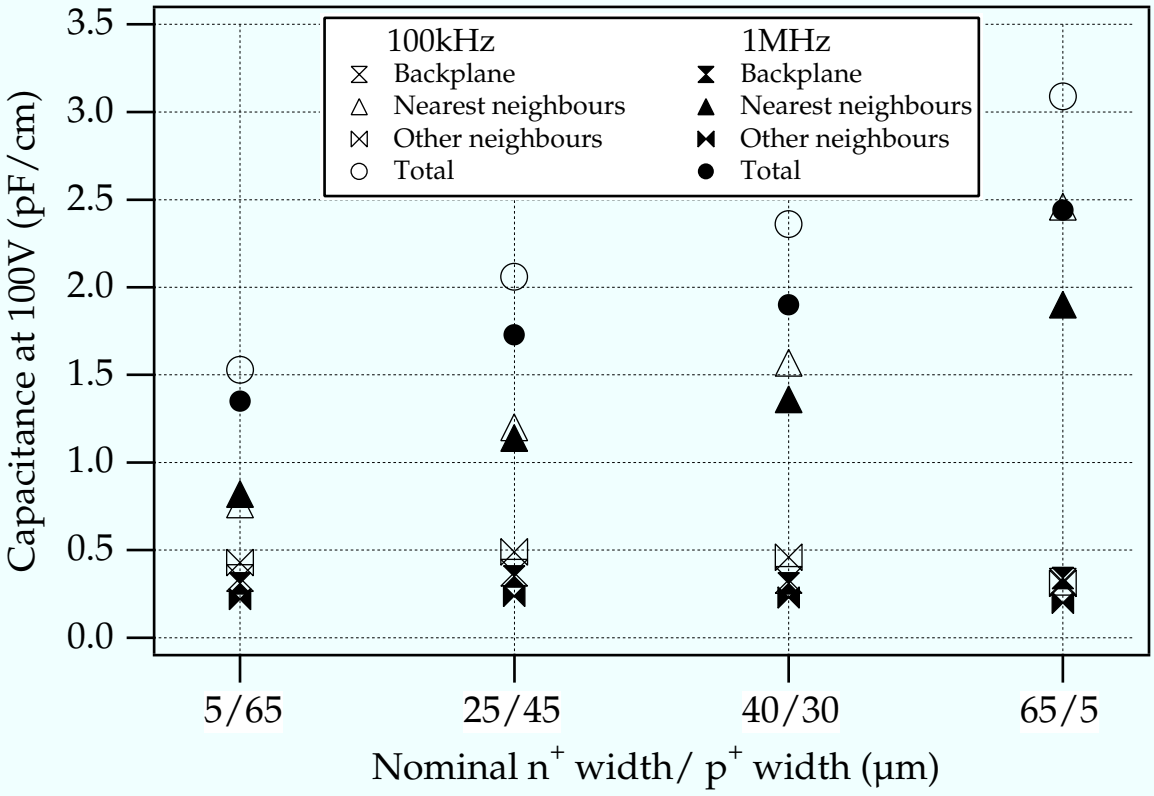

Fig. 4.18. Capacitances of unirradiated common p-stop n-side strips at 100 V, 100 kHz (100 μm pitch).

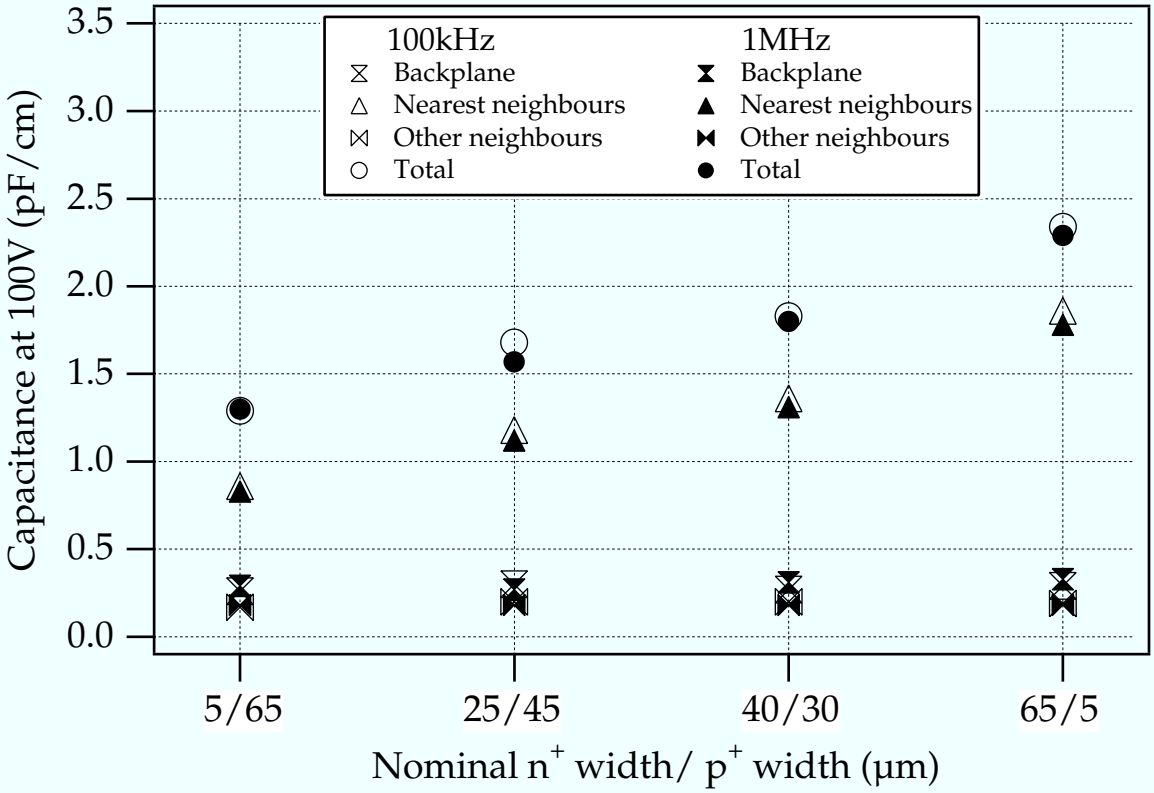

Fig. 4.19. Capacitances of unirradiated individual p-stop n-side strips at 100 V, 100 kHz (100 μm pitch).

common p-stop devices, but measurements at 1 MHz gave a lower total capacitance, of ~1.5–1.8 pF/cm, as the nearest neighbour and also the other neighbour contributions turned out to be dependent on the frequency. All values refer to an applied bias voltage of 100 V.

The frequency dependence issue has been addressed in [4.13]; this effect can be explained taking into consideration the behaviour of the interstrip capacitance as a function of the p-stop voltage. In the case of measurements taken at 1 MHz, the capacitances are already close to their lower limit for the p-stop voltage corresponding to the operating point, while values taken at 100 kHz have not yet reached their lower plateau values, always at the operating p-stop voltage.

An important difference was found between common and individual p-stops: the total strip capacitance of the individual p-stop devices was on average lower and practically did not change with frequency compared to the case of the common p-stop devices. Fig. 4.19 summarises the strip capacitance of the individual p-stop strips with 100 μm pitch before irradiation, measured at 100 V and 100 kHz. Values ranging from ~1.3 to ~2.3 pF/cm, depending on the strip widths, were measured on the individual p-stop 100 μm pitch devices. These values are to be compared with those found in the corresponding common p-stop configurations (~1.5–3.1 pF/cm at 100 kHz, ~1.4–2.5 pF/cm at 1 MHz).

The common p-stop network was shown to couple the higher order neighbours

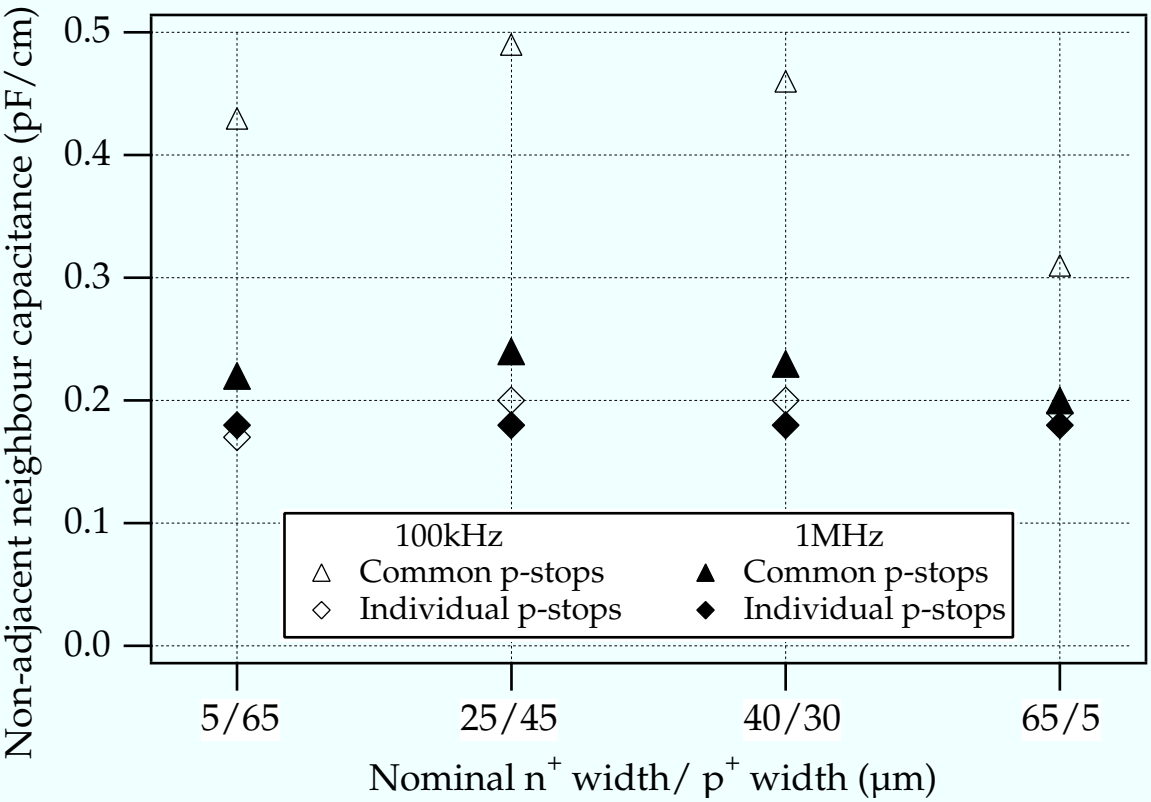

Fig. 4.20. Non-adjacent neighbour capacitance for common and individual p-stop n-side strips at 100 V, 100 kHz (100 μm pitch, unirradiated).

in a stronger way between themselves, probably with some signal sharing between the strips. A contribution higher than the one given by the same components in the individual p-stop configuration was found for the non-adjacent neighbours. This contribution to the strip capacitance is plotted in fig. 4.20, where the non-adjacent neighbour capacitances for common and individual p-stop n-side strips with 100 μm pitch are compared. They were measured before irradiation, at 100 V, and at 100 kHz and 1 MHz frequencies.

My responsibility was for the measurement of the strip capacitances prior to irradiation only. For completeness, two plots showing the changes in the microstrip capacitance following exposure to photons and neutrons will be presented. The radiation damage studies were performed on the same structures measured before the irradiation tests, and are fully described in [4.13].

Fig. 4.21 shows the nearest neighbour capacitance for common p-stop n-side strips with 50 μm pitch, as a function of the received photon dose. The capacitances were measured at 100 V, 1 MHz. The irradiation was carried out making use of the Imperial College gamma facility. Saturation was found after $\sim$1 Mrad.

Fig. 4.22 shows the nearest neighbour capacitance for common p-stop n-side 100 μm pitch strips, measured at 100 V, 1 MHz, before and after neutron and photon irradiations. While essentially no increase is seen following neutron damage, a limited nearest neighbour capacitance increase was found, e.g. of $\sim$15 % for the widest strips, after 6 Mrad of Co^{60} photons.

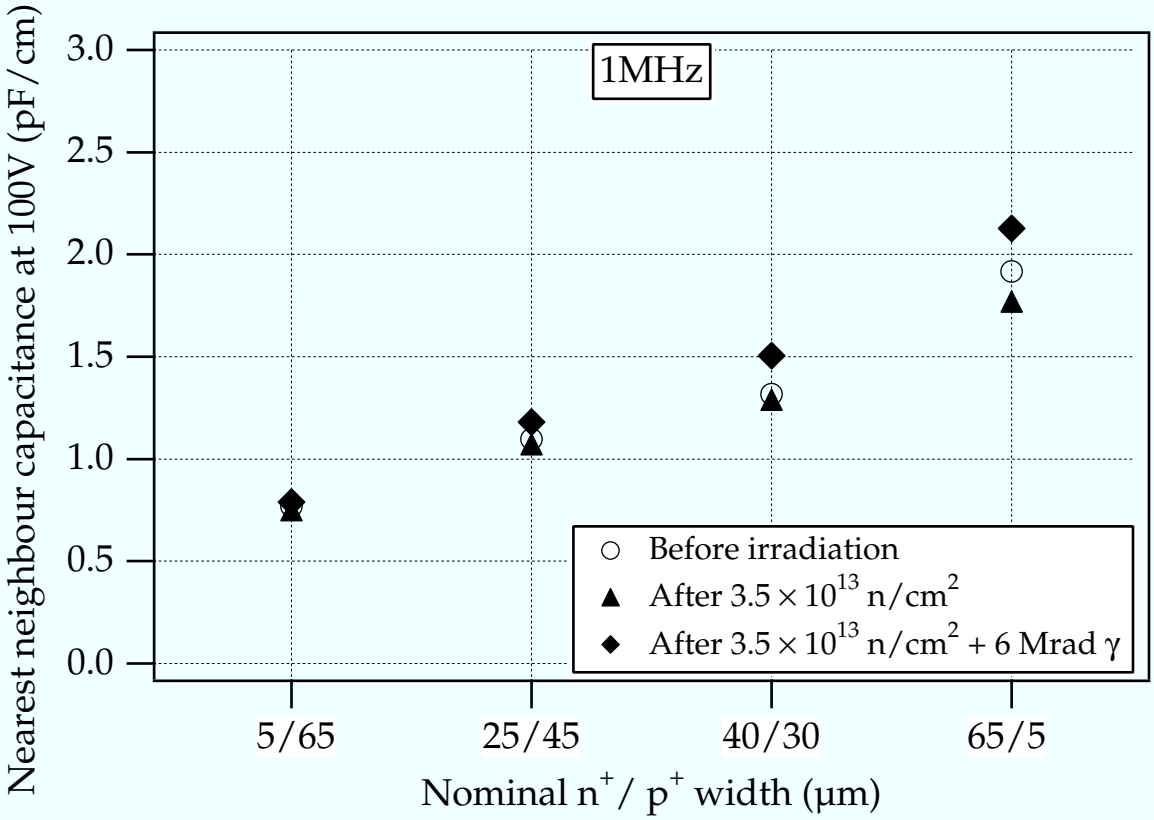

Fig. 4.22. Nearest neighbour capacitance for common p-stop n-side strips at 100 V, 1 MHz (100 μm pitch) after neutron and photon irradiations [4.13].

4.4 Summary and conclusions

Extensive studies of the strip capacitances of silicon detector prototypes for application at the LHC have been performed.

Irradiations with ionising and non-ionising particles of several p-side microstrip test structures have been carried out. The evolution of strip capacitances following exposure was monitored. After surface radiation damage caused by ionising radiation, the strip capacitances increase but remain tolerable. Neutron damage did not substantially change strip capacitances, even at very high fluences.

The values of strip capacitance did not decrease with time after exposure to electrons, as the silicon nitride layer inhibits oxide charge annealing.

The RD20 n-side prototypes have been evaluated before irradiation, and the p-stop isolation technique investigated. Full sets of interstrip capacitance measurements have been performed on these structures.

Chapter 5

The material budget of the CMS Central Detector

Optimisation of the central detector involves, among other, minimisation of the amount of material, both from the point of view of the individual modules and of the overall mechanical and geometrical design. The total budget must be maintained as low as possible, in order not to degrade the performance of the calorimeters because of energy loss by particles traversing the materials of which the central detector is made.

Various iterations of the central detector design were performed, aiming at meeting both technology requirements and material budget constraints, while taking into account the physics implications as well.

5.1 Radiation length and energy losses

The *radiation length* X_0 of a material is a unit particularly useful when considering the energy losses of high energy electrons (and positrons) and photons. It is defined as the (mean) distance over which a high-energy electron loses by *bremsstrahlung* a fraction $1/e$ ($\sim$63.2 %) of its initial energy E_o [5.1]:

$$\Delta E_{X_0} = \left(1 - \frac{1}{e}\right) E_o \simeq 0.632\, E_o \,, \tag{5.1}$$

where ΔE_{X_0} is the energy lost after a path corresponding to one radiation length. This relation follows from the expression of the total radiation loss of an electron traversing a thickness dx of medium:

$$\left(\frac{dE}{dx}\right)_{\text{rad}} = -\frac{1}{X_0} E \,, \tag{5.2}$$

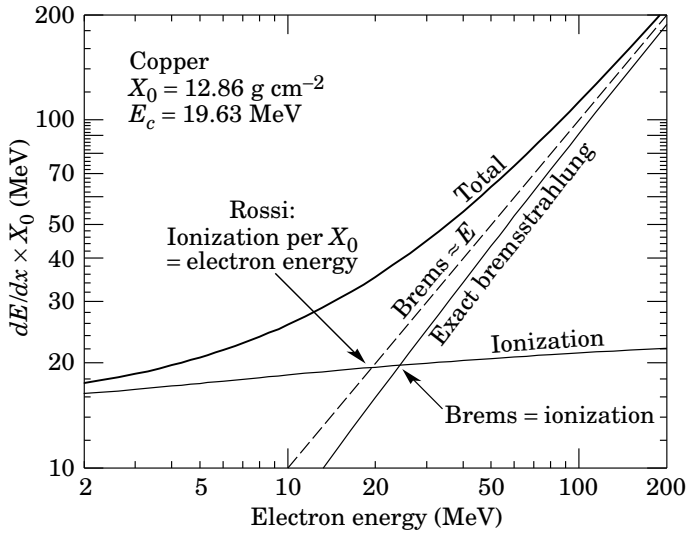

Fig. 5.1. Ionisation and bremsstrahlung energy loss and critical energy definition for electrons in copper, as a function of the electron energy (from [5.2]).

whose solution for a finite thickness x is

$$E_x = E_0 \ \exp\left(-\frac{x}{X_0}\right) \ , \tag{5.3}$$

E_x being the average energy of the electron after a path x in the medium considered [5.2, 5.3].

Charged particles other than electrons lose energy mainly by ionisation when traversing matter, the radiative effects becoming moderately important with increasing particle energies, while the electron and photon energy losses are essentially due to bremsstrahlung and pair production, at the energy scales applicable to CMS.

The energy at which the electron loss rate by bremsstrahlung becomes equal to the loss rate by ionisation, in a given material, and beyond which the contribution given by bremsstrahlung becomes predominant, is the *critical energy* E_c; it is usually approximated with the formula $E_c \simeq (800 \text{ MeV})/(Z + 1.2)$ [5.2], which gives e.g. $E_c \sim 52$ MeV for silicon, ~26 MeV for copper and ~9.6 MeV for lead. It is clear that in the typical energy domain of electrons and photons to be fully detected within CMS, the loss is dominated by bremsstrahlung.

The radiation length is thus an appropriate unit with which to measure the material thickness of a tracking system, if one considers the electron and photon energy losses before their arrival to the electromagnetic calorimeters, where their energy should be measured as precisely as possible.

As an example, fig. 5.1 and fig. 5.2 show the ionisation and bremsstrahlung energy loss for electrons. Fig. 5.1 shows the total energy loss and its two components

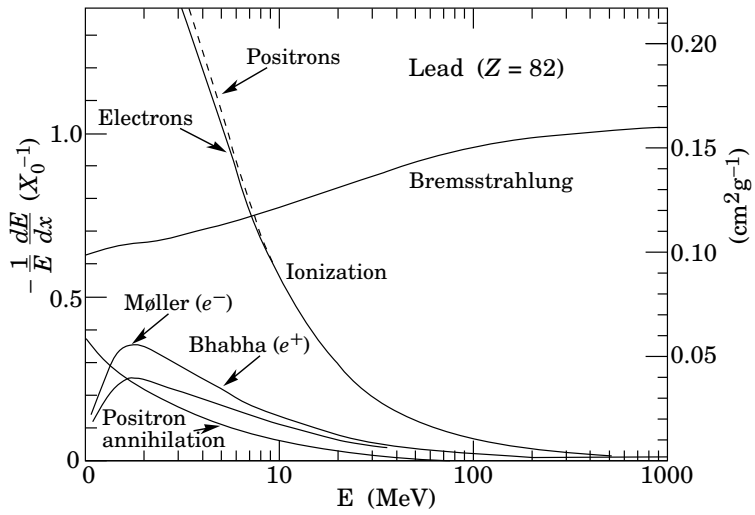

Fig. 5.2. Ionisation and bremsstrahlung fractional energy loss for electrons in lead, as a function of the electron energy (from [5.2]).

in copper, with the critical energy point at ∼26 MeV. Fig. 5.2 shows the fractional energy loss in lead, per unit of radiation length, as a function of the electron energy; it can be seen that bremsstrahlung dominates for electron energies bigger than ∼10 MeV. Both figures are extracted from [5.2].

The situation is quite different for charged particles other than electrons: the critical energy for muons and pions is of the order of several hundred GeV (e.g. in iron). Therefore the energy loss which in most cases prevails for charged particles is ionisation.

The value of X_0 depends on the atomic number of the element, and was calculated by Y. S. Tsai to be [5.2, 5.4]:

$$\frac{1}{X_0} = 4\,\alpha\,r_e^2\,\frac{N_A}{A}\left\{Z^2\left[L_{\rm rad} - f(Z)\right] + Z\,L'_{\rm rad}\right\}\,, \tag{5.4}$$

where α is the fine structure constant ($\simeq 1/137$), r_e is the classical electron radius ($e^2/4\pi\,\epsilon_0\,c^2$), N_A is Avogadro's number, A and Z are respectively the atomic mass and the atomic number of the element, $L_{\rm rad}$ and $L'_{\rm rad}$ are tabulated numbers and finally $f(Z)$ is an appropriate function of Z (details in [5.2]).

O. I. Dahl fitted the data to provide a functional dependence on Z [5.2]:

$$X_0 \simeq \frac{716.4\ {\rm g\,cm^{-2}}\,A}{Z\,(Z+1)\,\ln\left(287/\sqrt{Z}\right)}\,, \tag{5.5}$$

with results in good agreement (normally better than 2.5 %) with (5.4).

Material	**Radiation length** *(cm)*	**Material**	**Radiation length** *(cm)*
silicon	9.36	beryllia	14.3
kapton	28.4	aluminium	8.9
tin	1.21	copper	1.43
alumina	7.2	carbon fibre	25.0
quartz glass	10.2	mylar	28.6
rohacel	790.0	water	36.1

Table 5.1. Radiation length (in cm) of some materials considered for the central detector.

The radiation length of a compound or a mixture can be computed by applying *Bragg's rule* for the stopping power dE/dx [5.1]

$$\frac{1}{\rho}\frac{dE}{dx} = \sum_j \frac{w_j}{\rho_j}\left(\frac{dE}{dx}\right)_j , \tag{5.6}$$

which gives for the radiation length X_0

$$\frac{1}{X_0} = \sum_j \frac{w_j}{X_j} , \tag{5.7}$$

where ρ_j and X_j are respectively the density and the radiation length of the jth element, expressed in mass thickness units. The w_j's are the fractions by weight of each element in the mixture, defined as

$$w_j = \frac{a_j A_j}{\sum_i a_i A_i} , \tag{5.8}$$

where A_j is the atomic weight of the jth element and a_j is the number of atoms of the jth element in the compound [5.1].

The dimensions of the radiation length X_0 , obtained from (5.4), are $[\mathrm{m} \cdot \mathrm{l}^{-2}]$, i.e. of a mass divided by a length squared; thus it is measured in g/cm^2. The radiation length is often quoted and used after having been divided by the density ρ of the material, leading to the dimensions of a length.

The radiation length of some materials considered for this study are reported in table 5.1. The material budget in radiation length units is normally plotted as a function of the absolute value of the pseudorapidity η rather than of the angle ϑ (see equation (1.1) in section 1.2).

An important feature of the material budget of a tracking system is the purely geometrical property normally referred to as the $1/\sin\vartheta$ *effect:* when a particle travels at a polar angle ϑ other than 90 degrees, its path through a medium will increase

by a factor of $1/\sin\vartheta$ with respect to the path seen at $\vartheta = 90$ degrees. Therefore, an increase in the material budget is usually seen with increasing pseudorapidities.

5.2 CMS central detector design considered

The CMS central detector has been briefly described in section 1.2.1, which is the design included in the Technical Proposal [5.5].

In the following, a former version of the central detector design will be used, described in *CMS Status Report and Milestones* (15 October 1993) [5.6], and all results refer to this particular design [5.7]. The main differences between the two versions are the presence in the more recent of a silicon pixel microvertex detector, and the explicit analysis of the beam pipe and outer service contributions. The beam-pipe gives a small contribution of $\sim$0.5 % of a radiation length at $\eta = 0$, rising to $\sim$3 % at $|\eta| = 2.5$. The pixel detector gives an additional contribution of $\sim$3 % of a radiation length for $0 \leq |\eta| \leq 0.5$, rising to $\sim$8 % for rapidities in the 1.5–2.0 range [5.8, 5.9], but this is the least well defined sub-detector system. These two additional contributions are shown in fig. 5.15 [5.8, 5.9], which will be commented on in section 5.7.

The results presented in the following sections were obtained with the design version of 1993, as that was the first review of the material budget of the CMS central detector since the LoI [5.10]. Major changes had occurred in the meantime: the spatial distribution of the detectors was reconsidered, in view of overall performance and design optimisation, and more realistic and detailed definitions of the detector modules, complete with cabling and services, were made.

It is in principle possible to update the design used to any new version, changing or rewriting the geometry and module descriptions, while keeping the same main program to perform the radiation length calculations.

5.3 The program used

The FORTRAN program GEDS was written to perform the calculation explicitly; this program was an extension of a previous version, GEDWEE, which only took into account the silicon microstrip modules in the barrel [5.11].

The program makes use of the GEANT *detector simulation* package [5.12] to describe the geometry of the central detector and to evaluate the material, in radiation

lengths, seen by a particle generated in a region close to the interaction point and travelling outwards on a straight line, throughout the detector.

In order to graphically visualise the results obtained in the form of text files generated by submitting the program as a batch job, a set of macros has been written, using the PAW package [5.13], which produce graphs in the form of PostScript files.

The program simultaneously evaluates the contributions to the total budget, as given by the different materials, writing also various totals and subtotals to the output file. It typically required $\sim$1 s/event of *VAX*-type CPU-time, with some 30000–40000 events for a reliable average over the z-position of the vertex and over th azimuthal coordinate φ. Steps in pseudorapidity η of 0.0375 have been used, ranging from 0. to 3. A complete analysis therefore required significant amounts of computing time.

5.4 Definition of detector modules

The definition of detector modules represented a real challenge at that point of the detector design as, for the first time, realistic modules were required, both for the silicon microstrips and for the microstrip gas chambers [5.14]. Some difficulties were encountered, particularly where detailed information was unavailable or uncertain; in those cases, reasonable assumptions and approximations had to be made.

The level of detail which it was possible to define, depended on the component considered. The detector modules were defined in a very precise way, down to the hybrid components, particularly for the barrel section, while the biggest uncertainties were related to support, cabling and cooling systems. Assumptions e.g. on the position and length of cables, on the geometrical design of the support discs and of the distribution of the elements composing the forward parts, among other, were made.

As an example, the layout of the barrel silicon module used is shown in fig. 5.3, complete with hybrids, front-end electronics, control chips, coupling capacitors, optical modulators, carbon fibre lateral rails and cooling system. Detailed definitions of the elements have been similarly made for the other modules (silicon microstrips in the forward part; microstrip gas chambers in the barrel and in the forward parts).

Descriptions of the modules can be found in [5.6, 5.7]. The components of the barrel *silicon microstrip* and *microstrip gas chamber* single sided, double-ended readout modules are summarised in tables 5.2 and 5.3 respectively. The geometrical

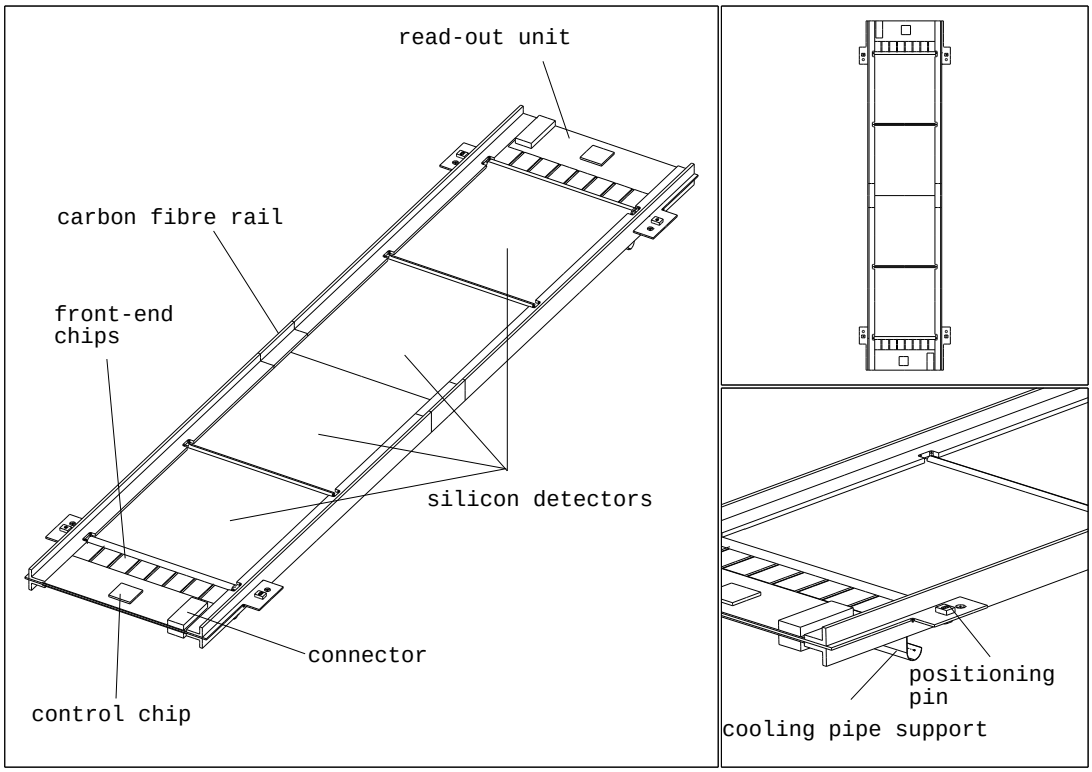

Fig. 5.3. Layout of the barrel silicon module.

element	**no.**	**material**	**radiation length** *(cm)*	**width** *(mm)*	**length** *(mm)*	**thickness** *(mm)*
substrates	4	silicon	9.36	54.	62.5	0.300
heat bridges	2	beryllia	14.3	54. 54.	28. 1.	1. 4.
multilayer **hybrids**	2	kapton aluminium	28.4 8.9	54.	18.	0.200 0.075
front-end chips	16	silicon	9.36	6.	10.	0.350
control chips	2	silicon	9.36	8.	8.	0.350
front-end **capacitors**	16	tin alumina	1.21 7.2	4.	4.	0.170 0.680
optical modulators	2	(silicon)	(9.36)	1.5	5.	3.
module frame	1	carbon fibre	25.0	0.250	250.	8.

Table 5.2. Components of the barrel *silicon microstrip* module (51.2×250 mm^2 active area, single sided, double-ended readout).

element	no.	material	radiation length *(cm)*	width *(mm)*	length *(mm)*	thickness *(mm)*
substrates	2	glass (quartz)	10.2	108.	125.	0.300
heat bridges	2	beryllia	14.3	100. 100.	28. 0.3	0.300 4.
multilayer hybrids	2	kapton aluminium	28.4 8.9	100.	18.	0.200 0.075
front-end chips	8	silicon	9.36	6.	10.	0.350
control chips	2	silicon	9.36	8.	8.	0.350
front-end capacitors	8	tin alumina	1.21 7.2	4.	4.	0.170 0.680
optical modulators	2	(silicon)	(9.36)	1.5	5.	3.
module frame	1	carbon fibre	25.0	0.250	250.	8.
mylar foil	1	mylar aluminium	28.6 8.9	108.	250.	0.050 0.010

Table 5.3. Components of the barrel *microstrip gas chamber* module (102.4 $\times$ 250 mm^2 active area, single sided, double-ended readout).

dimensions and the radiation length of the relevant material have been indicated for each element.

The active area of the barrel silicon module is 51.2 $\times$ 250 mm^2, achieved by mounting and daisy-chaining in pairs four detectors, each with 62.5 mm long strips. The active area of the barrel microstrip gas chamber module is 102.4 $\times$ 250 mm^2. Similar modules were defined for the forward parts of the central detector.

Some assumptions to reduce the amount of material were made, in some cases with technological implications still needing a final proof of feasibility:

- aluminium as conductor for the kapton multilayer hybrids, instead of standard copper;
- aluminium high voltage cables for the microstrip gas chambers, again replacing standard copper;
- thin aluminised mylar foils as gas tight drift electrodes for the microstrip gas chambers, excluding additional glass plates;
- small size optical modulators, with material dominated by the package, assumed to be predominantly silicon;
- realisation of double-sided detectors using the same substrates, thus excluding a back-to-back technique;
- high radiation length (25 cm) carbon fibre as support structure as well as material for module frames;

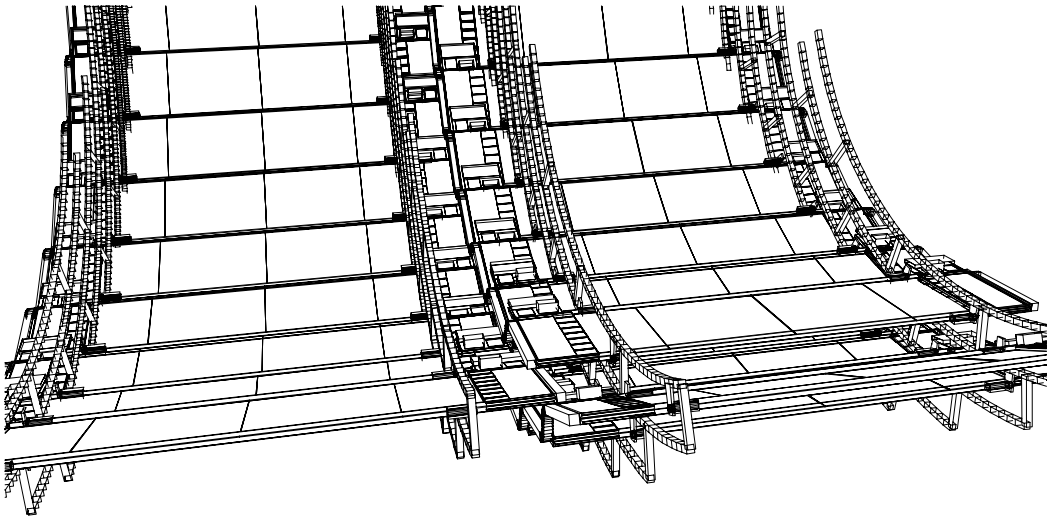

Fig. 5.4. View of two adjacent barrel wheels with silicon modules.

- no intermediate connectors or interconnecting cards within the tracker region.

Prototyping and advanced full scale system design should ensure that the above listed assumptions are achieved, otherwise alternative solutions will have to be found to keep the total material budget within acceptable limits. Only the first two items listed above would represent a serious problem, if found not to be realistic.

A view of two adjacent barrel wheels, partially filled with silicon modules, is shown in fig. 5.4. The space frame constituting the mechanical support of the barrel of the central detector is also visible, with small overlaps of sensitive areas between neighbouring wheels.

5.5 Cables and services

For the purpose of appropriate cable and service allocation to the different part of the central detector, as well as to provide a conceptual design for routings towards the outside of the tracker volume, the detector modules within each barrel wheel can be conceptually arranged into *spirals* and *superlayers:*

i. silicon microstrip modules, located at 9 different radii and forming the *first* superlayer: 16 spirals (i.e. 16 modules at each radius), 144 modules;

ii. inner microstrip gas chamber modules, located at 7 different radii and forming the *second* superlayer: 24 spirals, 168 modules;

iii. outer microstrip gas chamber modules, located at 9 different radii and forming the *third* superlayer: 32 spirals, 288 modules.

Fig. 5.5 shows a section of a barrel wheel, with the silicon microstrip and microstrip gas chamber superlayers. The resulting apparent spiral structure is visible [5.5]. The module disposition in this figure is only conceptual and does not correspond exactly to the design used in the following.

Similarly, the MSGC-only forward wheels are formed by anuli of detector modules and of *rohacel* spacers, realised on the two opposite faces of back-to-back discs to form a complete forward wheel. Small overlaps in r were designed, while the 'open MSGC' design, with modules glued side by side – without dead areas – to form a complete anulus within a unique gas volume, does not require a sensitive area overlap in ϕ.

The total number of detector anuli is 10, i.e. 5 per disc; the number of modules per anulus increases from 26, for the innermost anulus, to 76 for the outermost, always for the particular design used. Fig. 5.6 shows the section of a microstrip gas chamber forward wheel, with details of the module arrangement in overlapping discs and anuli [5.5].

Forward wheels, four on each side, where silicon microstrip and gas microstrip modules were designed to be on the same discs, were considered as an appropriate extension of the MSGC-only forward wheel concept, with reasonable assumptions regarding the silicon microstrips. That design has evolved since.

I will now describe in detail the design assumptions made for cables and services going out of the tracker volume; the numbers are quoted *per barrel-forward wheel:*

(a) optical fibres: *one* silica ribbon, with a section of 3 mm $\times$ 250 μm, per detector read-out module;

(b) kapton cables for module low voltage power and other signals: *one* multi-layer strip cable, 20 mm wide, 100 μm thick, per detector read-out module, with 50 % of kapton and 50% of aluminium on average;

(c) MSGC high voltage cables: aluminium cables, with a diameter of 1 mm, thus distributed:

- barrel wheels: *two* cables per spiral per superlayer, i.e. 112 cables per wheel,

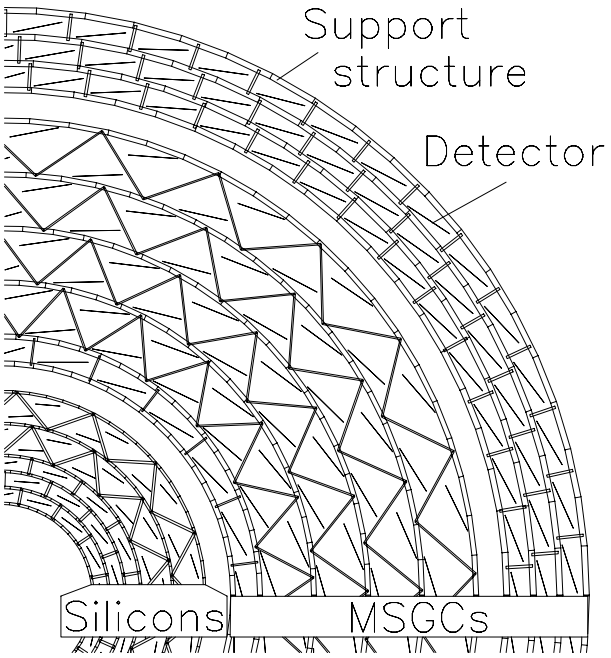

Fig. 5.5. Section of a barrel wheel (conceptual view): silicon microstrip and microstrip gas chamber superlayers and apparent spiral structure (from [5.5]). This design does not correspond exactly to the design used for the material budget evaluation.

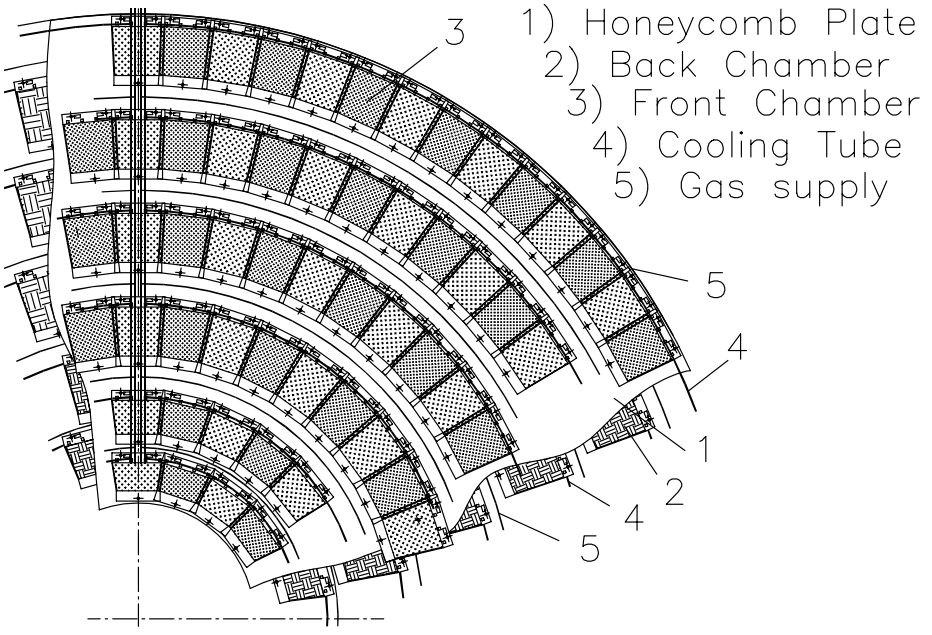

Fig. 5.6. Section of a microstrip gas chamber forward wheel with details of the module arrangement in overlapping discs (from [5.5]).

- forward wheels: *two* cables per anulus, i.e. 20 cables per forward wheel;

(d) MSGC gas pipes: aluminium pipes, with a square section of 3 mm $\times$ 3 mm and 500 μm thick walls, giving a total aluminium section of 5 mm^2 (the gas has been neglected), thus distributed:

- barrel wheels: *two* pipes per MSGC spiral, i.e. 64 pipes per barrel wheel,
- forward wheels: *two* pipes per anulus, i.e. 20 pipes per forward wheel;

(e) water cooling pipes: aluminium pipes, with a square section of 4 $\times$ 4 mm^2 and 500 μm thick walls, with water inside, giving an equivalent aluminium section of $\sim$11 mm^2, thus distributed:

- barrel wheels: *two pipes* per spiral, i.e. 64 pipes per barrel wheel,
- forward wheels: *two* pipes per anulus, i.e. 20 pipes per forward wheel.

The previous are reasonable assumptions made at the time of this evaluation. Some uncertainties, due e.g. to the implicatons of the single- and double-sided readout schemes for both types of strip detectors, were handled considering the most pessimistic scenario. Some additional factors depend on the exact service routings, particularly for the two microstrip gas chamber superlayers, where the 25 cm long modules are read from both sides (inner superlayer, 12.5 cm long strips) or from one side only (outer superlayer, 25 cm long strips).

5.6 Evaluation of the amount of material

The amount of material of the central detector was evaluated with the program and the design described above; an important feature of the calculation has been the average over the position of the vertex along the beam axis z and on the azimuthal angle φ.

The position of the primary interaction point at the LHC will be spread around the designed collision point (i.e. around $z = 0$) with a gaussian distribution, characterised by a σ of $\sim$5.3 cm [5.5]. Values typically from $z = -10$ cm to $z = +10$ cm have been used for the calculation, with 1 cm steps and proper weights. Steps of 18 or 20 degrees in φ, for each value of pseudorapidity and of z, covered the full 360 range.

The estimated total budget for the complete central detector, barrel and forward, as a function of the pseudorapidity η, is shown in figure 5.7. With the design used (i.e. excluding pixels, beam pipe and outer services), the total material budget was $\sim$15 % of a radiation length in the central part of the tracker ($0.0 \leq |\eta| \leq 1.0$), and $\sim$30 % in the region $\sim 1.4 \leq |\eta| \leq 1.8$, with a quite steep decrease in the pseudorapidity region beyond. In the same figure are shown the totals for the barrel and forward parts, splitting them also into the components given by the silicon microstrips, the microstrip gas chambers and the mechanical supports.

The contributions given by the elements comprising modules and services are given in figures 5.8 and 5.9 for the barrel parts of the silicon microstrips and of the microstrip gas chambers respectively. The forward parts are shown similarly in figures 5.10 and 5.11. Parts of the material due to services such as cabling and cooling have been attributed to the different subsections of the detector.

This study represented an important source of information for the optimisation of the design and the choice of materials; several iterations with different designs and materials were repeated, to understand the implications of various choices. The influence of the various elements composing the detector sub-modules was particularly considered: detector substrates, hybrids and complete front-end electronics. Cabling, cooling, services and support structure played also a major role during these iterations.

Plots of the material budget as a function of the pseudorapidity η and of the distance r from the beam axis z ($r = \sqrt{x^2 + y^2}$) have been produced. Figures 5.12 5.13 and 5.14 show the 3-d plots for the complete detector, the barrel components and the forward part, respectively.

The behaviour of the material budget as a function of azimuth φ has also been studied, and no non-uniformities have been found [5.7].

5.7 Material budget calculation for the Technical Proposal

The material budget has also been evaluated by means of a second method, which makes use of AutoCAD drawings of the detector and a FORTRAN ray-tracing program [5.8, 5.9]. This method gives a faster estimate of the material budget distribution, as the definition of the subcomponents is less detailed, but it does not consider an average on the z-position of the vertex. Both methods give results in good agreement [5.6].

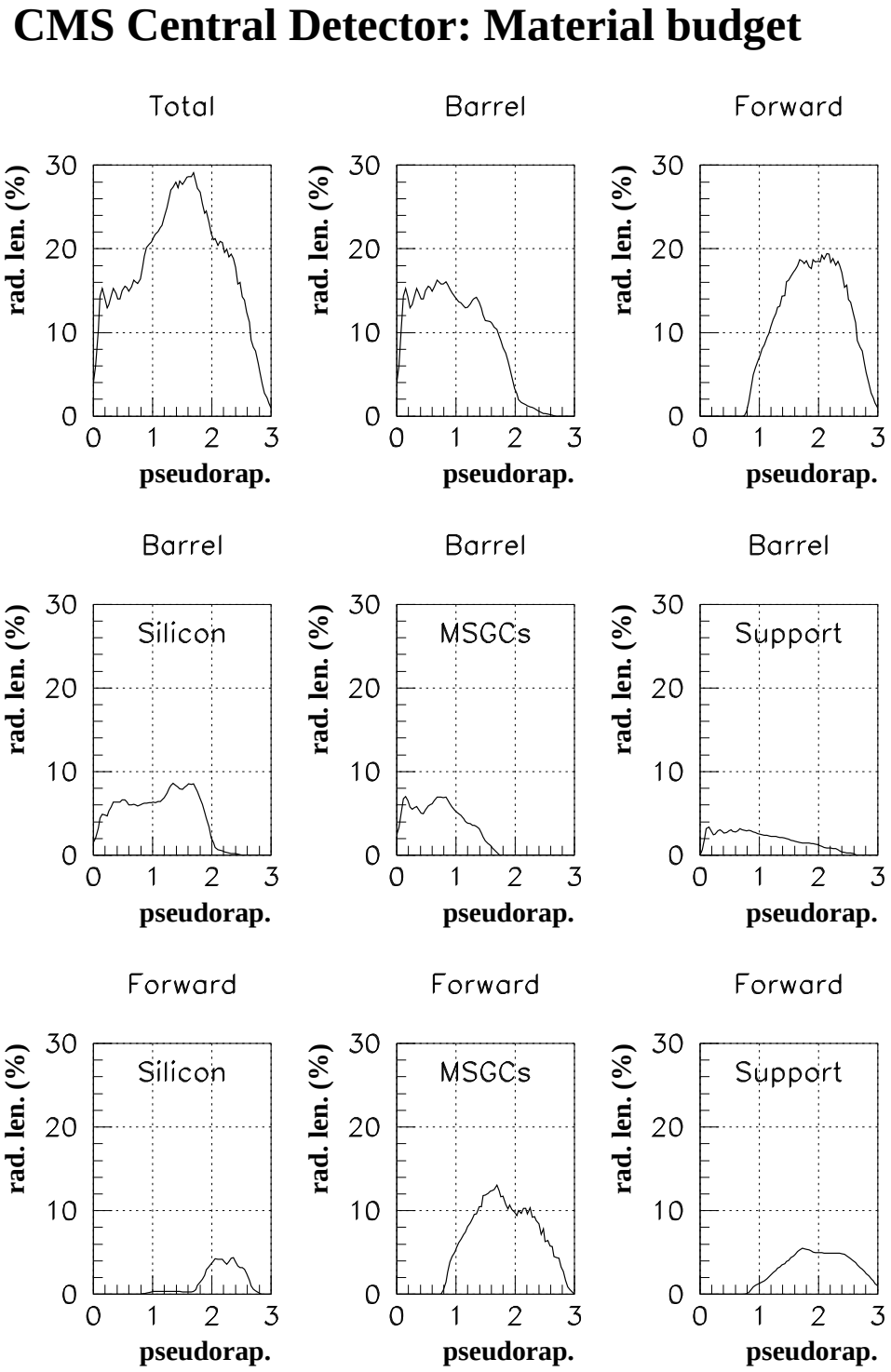

Fig. 5.7. Material budget of the central detector: totals (1993 design; beam pipe, silicon pixels, outer services not included).

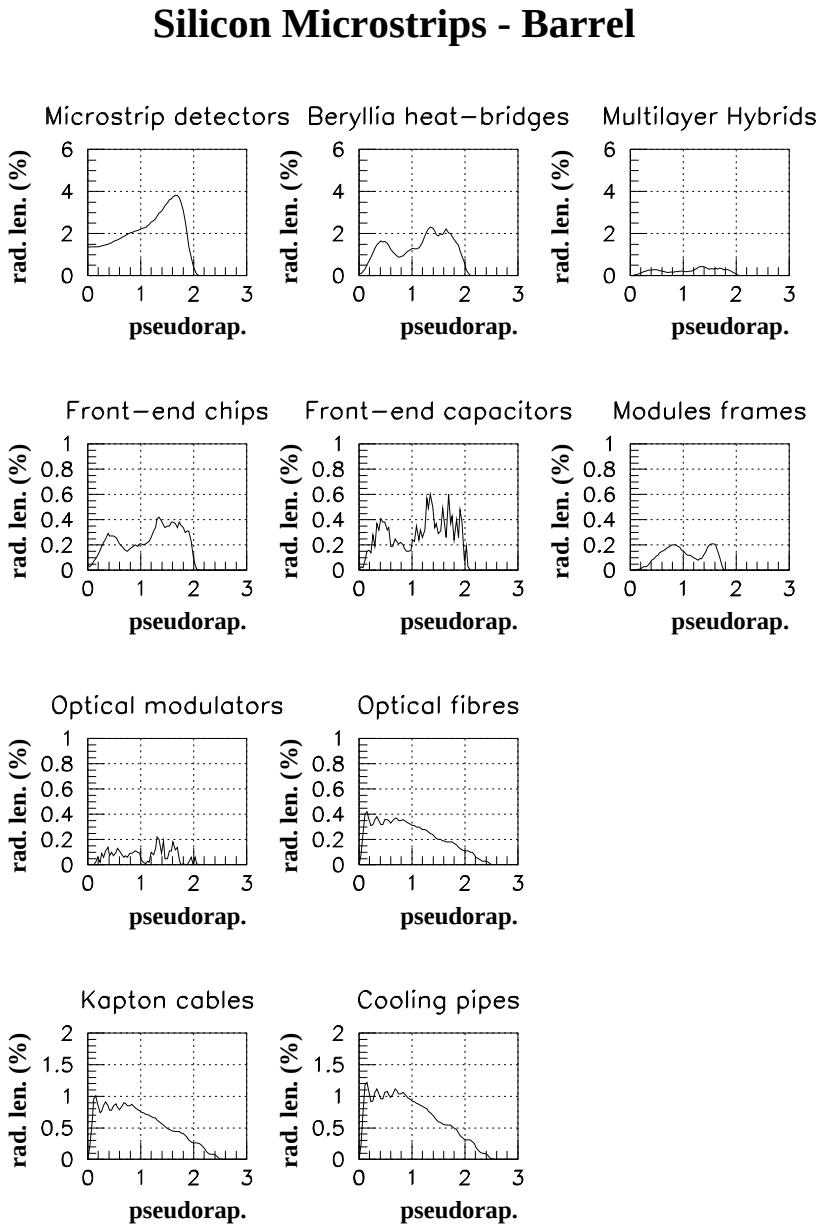

Fig. 5.8. Material budget of the central detector: barrel silicon microstrips (1993 design).

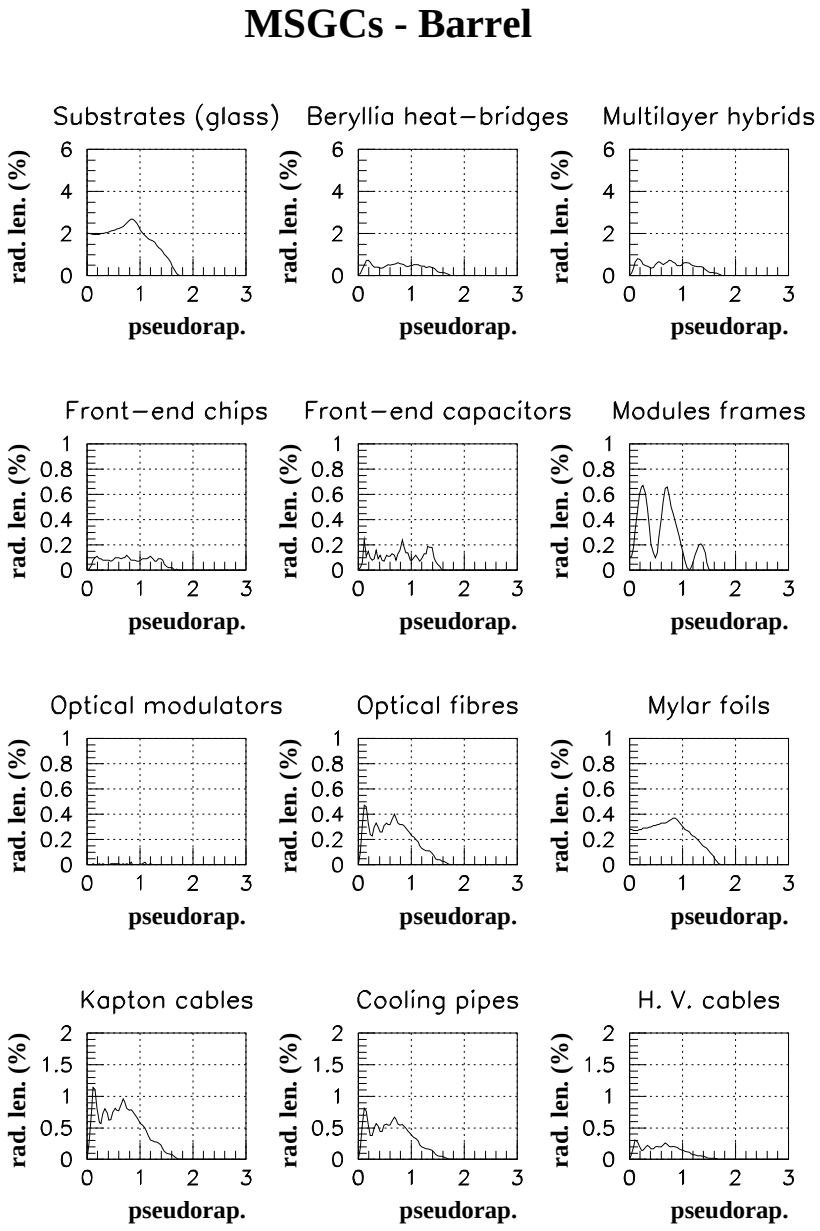

Fig. 5.9. Material budget of the central detector: barrel MSGCs (1993 design).

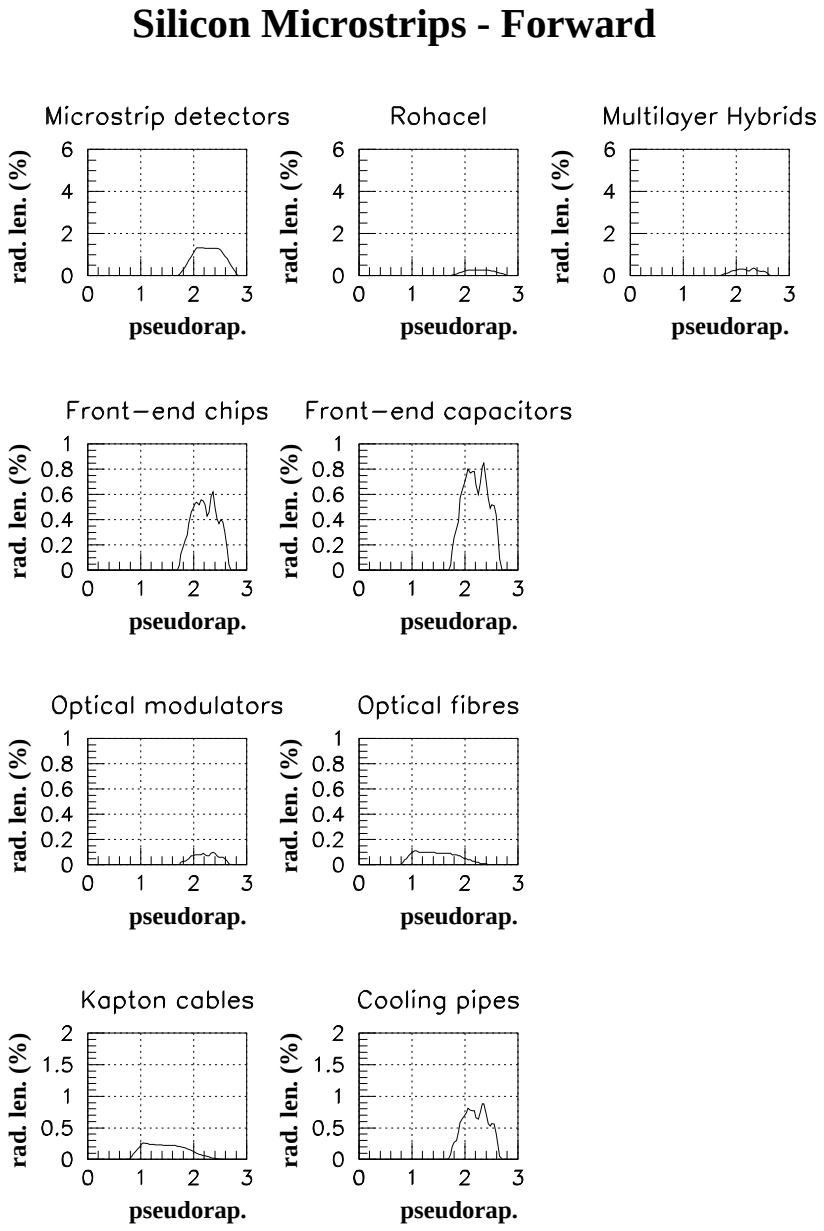

Fig. 5.10. Material budget of the central detector: forward silicon microstrips (1993 design).

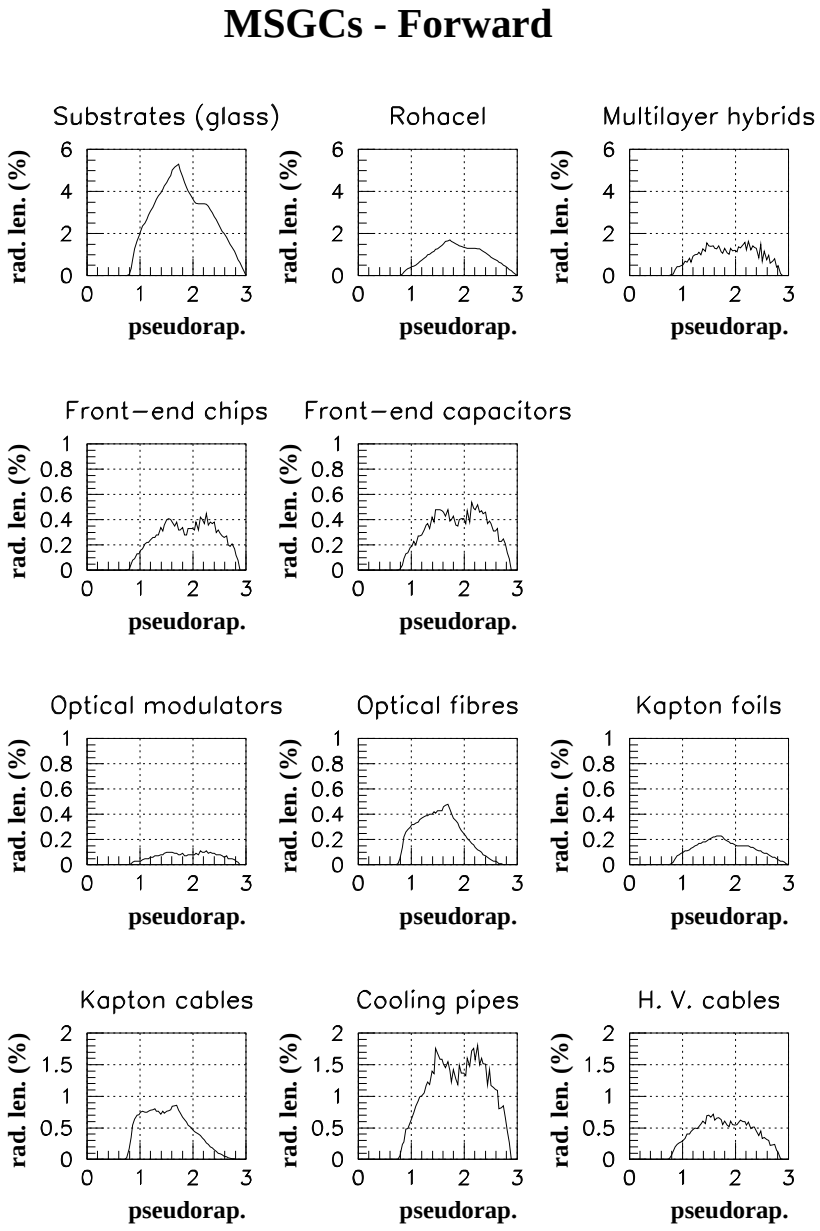

Fig. 5.11. Material budget of the central detector: forward MSGCs (1993 design).

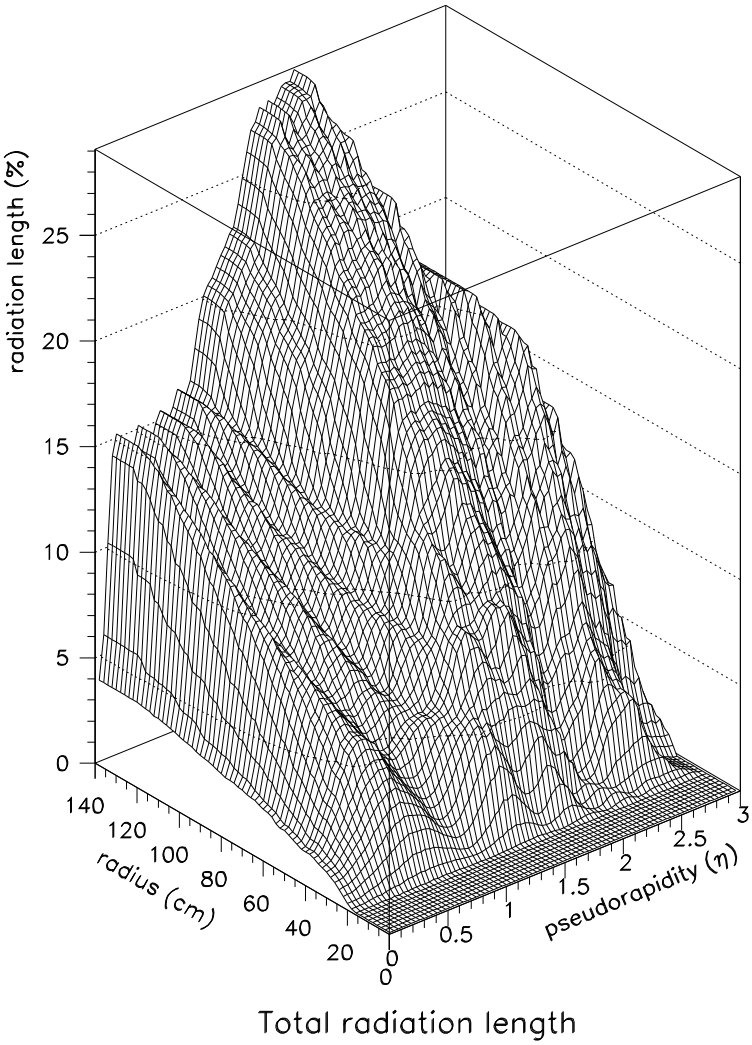

Fig. 5.12. Material budget of the central detector as a function of η and r: total (1993 design; beam pipe, silicon pixels, outer services not included).

This last method has been used to give the estimate for the 1995 Technical Proposal; the corresponding results are included here for completeness. My responsibility was for the first calculation only, and to check the agreement between the methods.

Figure 5.15 shows the material budget of the CMS central detector [5.8, 5.9]: the upper plot shows the total up to the ECAL preshower, with the separate contributions from the beam-pipe, the central detector itself, and the outer support structure and services.

The total material budget of the central detector only is $\sim$20 % of a radiation length in the central part of the tracker ($0.1 \leq |\eta| \leq 1.0$), and $\sim$40 % in the region $1.2 \leq |\eta| \leq 1.7$, slowly decreasing beyond, down to $\sim$10 % for $|\eta| \sim 3.0$.

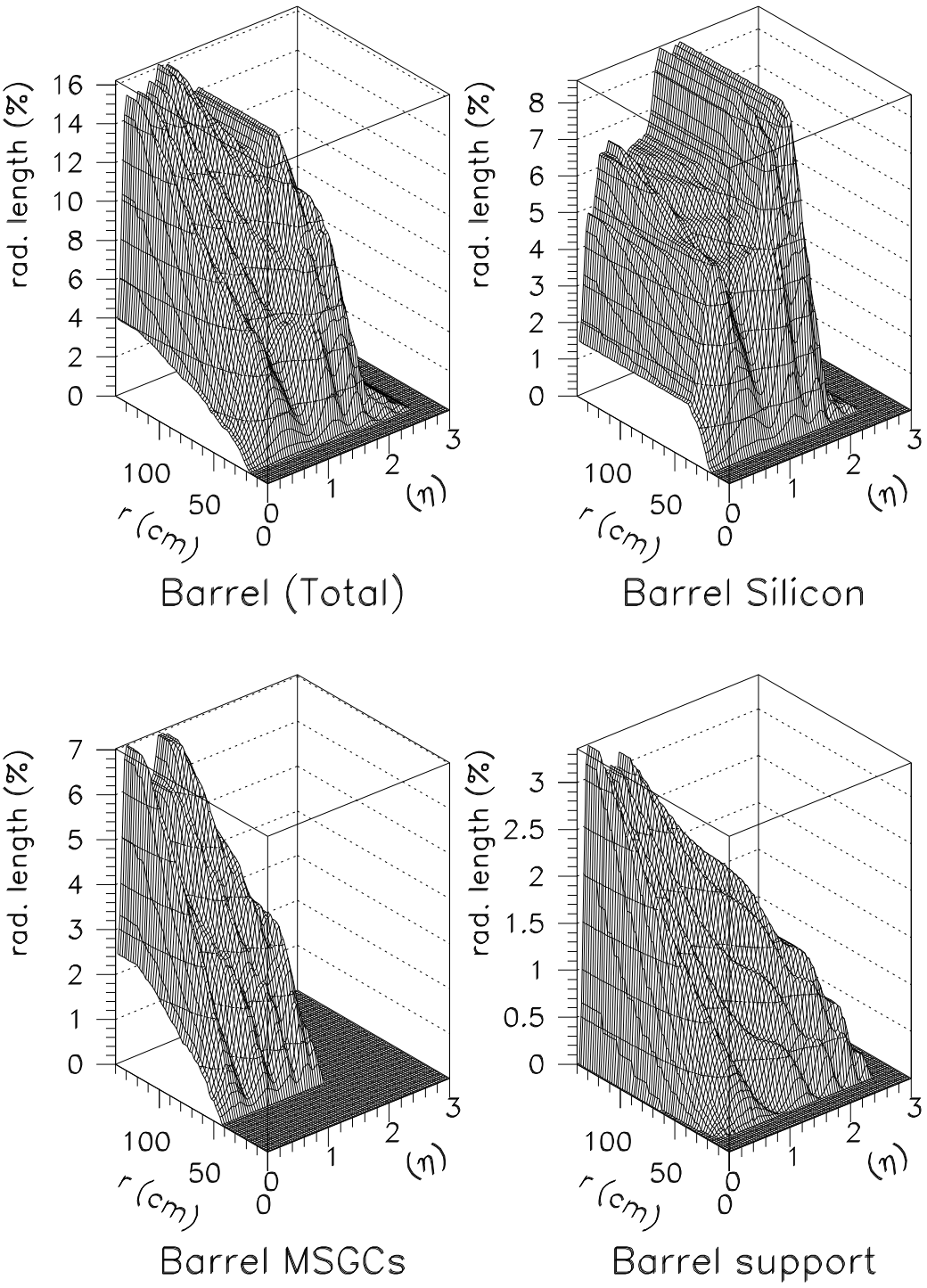

Fig. 5.13. Material budget of the central detector as a function of η and r: barrel (1993 design).

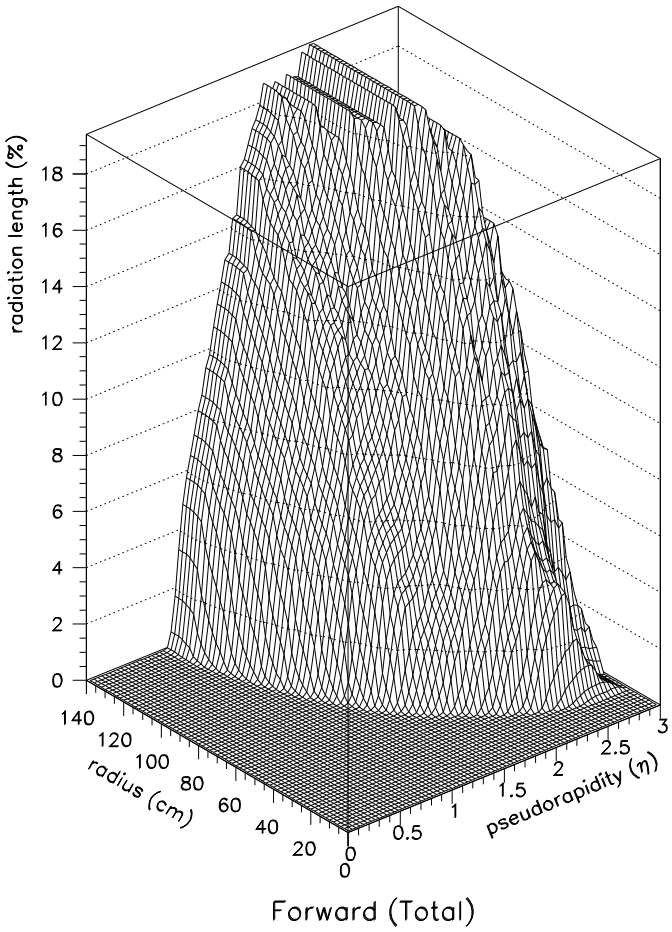

Fig. 5.14. Material budget of the central detector as a function of η and r: forward (1993 design).

The shape of the total amount of material as a function of pseudorapidity, excluding the ECAL preshower and including the beam-pipe, can be approximated with two plateaus at ~25–30 % for $0.1 \leq |\eta| \leq 1.0$ and $1.7 \leq |\eta| \leq 2.5$, reaching a maximum of ~50 % for $1.0 \leq |\eta| \leq 1.4$ and a top of ~60 % for $1.4 \leq |\eta| \leq 1.7$, and decreasing below 20 % for $|\eta| \geq 2.5$.

The lower plot in fig. 5.15 shows the sub-components of the central detector, i.e. the barrel and the forward silicon microstrips and microstrip gas chambers, and the inner pixel detector (with reference to fig. 1.9), also obtained with the second method described above [5.8, 5.9].

The material budget of the CMS central detector is bound to be subject to modifications in the future, because of both more realistic definition of the detector modules and, particularly, evolution of the support structure design. The wheel structure and the spiral/disc concept will be revisited and optimised, also to accommodate the inner pixel microvertex in a more integrated way.

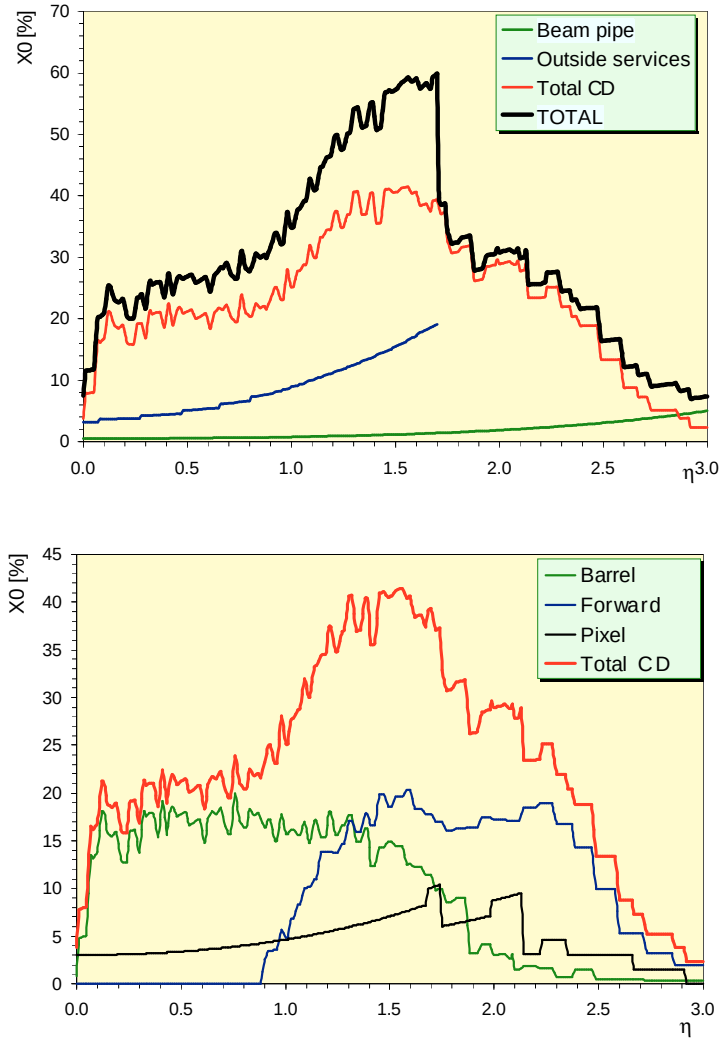

Fig. 5.15. Material budget of the CMS central detector: 1995 Technical Proposal design [5.8, 5.9].

There is the possibility of more drastic modifications to the present design, with obvious consequences on the amount of material. The thermal shielding between the silicon tracker and the rest will involve, for instance, an additional contribution, as the connections between the front-ends and the outside of the detector will do. High voltage supplies to the microstrip gas chambers, for instance, could possibly require dedicated hybrids, and the requirement of system modularity could involve the insertion, within the tracker volume, of 'interconnecting cards' or 'repeaters' between groups of detector modules, which at the present design level were not foreseen.

An important issue is where it would be best to locate additional material which in future could become necessary to add within the tracking system. Cabling, cooling and other services will find only in the next years a definite configuration and

material identification. The regions most sensitive to any material additions appear now to be within the rapidity range [$\sim$1, $\sim$1.8], where the total material budget is higher already, but it must be noted that the central rapidity region [0, $\sim$1] is where most of the interesting events for some Higgs search channels will be concentrated. Moreover, the innermost regions are the most delicate with respect to bremsstrahlung recovery, as mentioned in the next section (5.8), implying that material should be added as close to the electromagnetic calorimeter as possible, ideally at a radius higher than the last sensitive layers.

5.8 Conclusions on material budget studies

The aim of this work was to provide a tool for evaluating the material budget, in units of radiation length, of the complete CMS central detector. The main challenge was to simulate *realistic modules,* taking into account as many elements as possible. The novel *spiral* design was described using the GEANT package, even though the definition of the barrel part was too detailed to be used efficiently for other tracking simulations, due to the amount of CPU-time needed to process a single event. Some assumptions had to be made for the design of the *forward* part, specially for those wheels incorporating silicon microstrips and microstrip gas chambers.

Cabling, optical fibres, kapton cables, microstrip gas chamber high voltage cables, cooling pipes and the overall mechanical structure were considered as realistically as possible, with some uncertainties in the overall technical design and in some mechanical details, which will require further optimisation and proof of feasibility.

As an example of the relevance of these studies to the CMS performance, the benchmark channel H $\rightarrow \gamma\gamma$ can be used. Supposing m_H = 100 GeV, the distribution of the amount of material (as in the Technical Proposal [5.8]) as a function of rapidity, convoluted with the geometrical distribution of the two decay photons, gives $\sim$27 % of a radiation length as the thickness of material traversed by each photon on average. This corresponds to a probability of $\sim$20 % for each photon to convert within the tracker region, i.e. in $\sim$40 % of the H $\rightarrow \gamma\gamma$ events at least one photon converts into an electron–positron pair [5.15].

The conversion must be recovered off-line. Recovery is easier if conversion occurs in the outermost regions of the tracker, i.e. as close to the electromagnetic calorimeter as possible. Therefore, the inner regions of the central detector are in this respect the most sensitive to photon conversion, and it should be avoided to add material there (fig. 5.12).

These results have been presented in *CMS Status Report and Milestones* [5.6]. This work is not to be considered finished: changes in the overall design and in the detector modules can still cause important variations to the different contributions to the total material budget of the CMS central detector.

Chapter 6

B-physics and CP-violation studies in CMS

B-physics and CP-violation studies in CMS represent a very interesting subject, which will be addressed during the first years of CMS data taking. The main issue will be the observation of CP-violating effects, leading to the measurement of the parameters of the Cabibbo-Kobayashi-Maskawa (CKM) matrix, or of the *unitarity triangle,* as described in the next section.

The $b\bar{b}$ production cross-section $\sigma_{b\bar{b}}$ for proton-proton interactions at the LHC is only estimated with large uncertainties arising, among other, from perturbative QCD calculations and from the limited knowledge of the gluon structure function. Independent estimates give $\sigma_{b\bar{b}} \approx 0.1$–$0.9$ mb as overall expected range [6.1]. In the following, it will be assumed

$$\sigma_{b\bar{b}}\,(14\ \text{TeV}) \;=\; 0.5\ \text{mb}\,. \tag{6.1}$$

Fig. 6.1 shows the $b\bar{b}$ relative production cross-sections for gluon splitting and gluon fusion processes [6.2], obtained with PYTHIA 5.6 [6.3, 6.4] supposing (6.1). Statistics for gluon splitting are usually much lower than that for gluon fusion because of the longer computing time requested by PYTHIA to generate gluon splitting events. This latter process increases the $b\bar{b}$ cross section by a factor of $\sim$3 with respect to gluon fusion only [6.2]. Fig. 6.2 and fig. 6.3 show examples of the Feynman diagrams for the two processes.

One year of low luminosity LHC operation will give about 5×10^{12} $b\bar{b}$ events, $\sim$50 % of which will have both b-hadrons in the geometrical acceptance of the CMS detector, i.e. $|\eta| < \sim 2.5$.

Violation of CP-conservation was discovered in 1964 by Christenson et al. [6.5] in neutral kaon decays, and up to now remains the only case experimentally proven of such non-invariance.

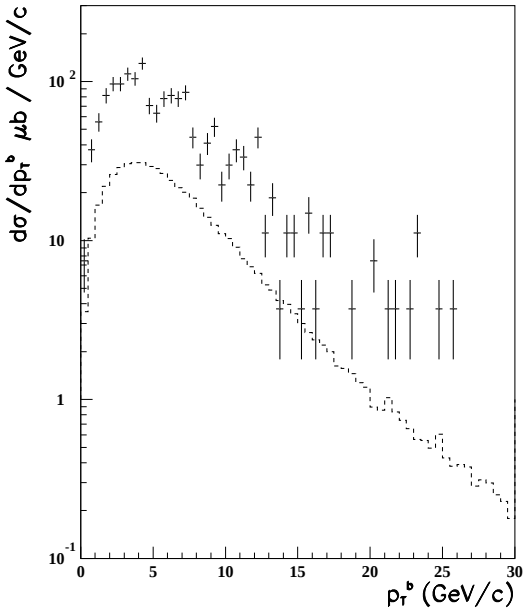

Fig. 6.1. $b\bar{b}$ production cross-sections for gluon splitting (markers) and gluon fusion processes (dashed line) from PYTHIA 5.6 [6.2], supposing $\sigma_{b\bar{b}}$ (14 TeV) = 0.5 mb.

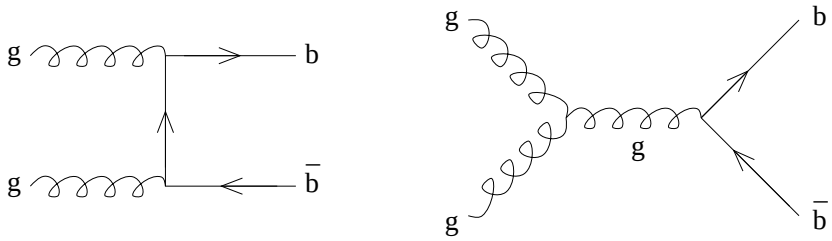

Fig. 6.2. Two possible $b\bar{b}$ production diagrams with gluon fusion processes.

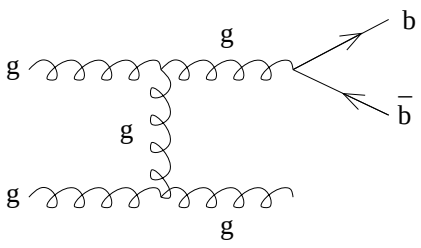

Fig. 6.3. A possible $b\bar{b}$ production diagram with a gluon splitting process.

CP is the composite operation of *parity inversion* P and *charge conjugation* C; they are both examples of *discrete* transformations. P is the operation corresponding to the transformation

$$P\,\psi(\vec{r},t) \;\rightarrow\; \psi(-\vec{r},t)\;, \tag{6.2}$$

i.e. a spatial reflection. C reverses the signs of the particle *charge* and *magnetic moment,* substituting particles with their corresponding antiparticles.

Until the observation of the CP-violating decays $K_L \rightarrow \pi^+\pi^-$, $K_L \rightarrow \pi^0\pi^0$, $K_L \rightarrow \pi^\pm\, e^\mp\, \nu$ and $K_L \rightarrow \pi^\pm\, \mu^\mp\, \nu$, all elementary processes were supposed to be invariant under CP-conjugation [6.6].

The general *theorem of CPT invariance,* derived from basic principles of quantum field theory, demands that all interactions be invariant under the successive application of the three operations C, P and T, performed in any order [6.7]. The consequence of this and of CP-violation effects is that some kinds of interactions will not be invariant under the *time-reversal* operation T:

$$T\,\psi(\vec{r},t) \;\rightarrow\; \psi^*(\vec{r},-t)\;. \tag{6.3}$$

Therefore tests of T-symmetry breaking and also of the general CPT theorem become very important for today's particle physics and cosmology.

In this chapter, the theory behind CP-violation in the B-sector will be introduced, and the experimental evaluation of CP-asymmetries will be described. The CMS detector performance relevant to these studies will be mentioned.

The estimates of sensitivities to the time-dependent and time-integrated asymmetries will be presented. After a mention of other studies, B-physics in the next decade will be briefly discussed.

6.1 Introduction to CP-violation studies

In the Standard Model of electroweak interactions the contribution to the Hamiltonian due to the charged-current weak interaction is expressed by

$$\mathcal{H}_{\rm wk}^{\rm ch} \;\simeq\; \frac{g}{2\sqrt{2}}\; W^\alpha \sum_{q_\lambda={\rm u,c,t}}^{q_l={\rm d,s,b}} V_{\lambda l}\; \overline{q}_\lambda\; \gamma_\alpha(1-\gamma_5)\; q_l\;, \tag{6.4}$$

where W^α is the $W^\pm$-boson field, g is the weak coupling constant (related to the Fermi coupling constant G by the relation $G/\sqrt{2} = g^2/8m_W^2$; $G \simeq 10^{-5}$ GeV^{-2}), $\overline{q}_\lambda$ and q_l represent the quark fields, and $\gamma_\alpha(1-\gamma_5)$ is the space-time structure matrix

operator, typical of weak interaction processes. The $V_{\lambda l}$ are complex coefficients which form the *Cabibbo-Kobayashi-Maskawa quark mixing matrix* $\mathrm{V_{CKM}}$. Out of the three generations of quark doublets, the +2/3-charge quarks (u, c, t) are unmixed by convention, while the mixing of the −1/3-charge quarks (d, s, b) is expressed by the 3×3 unitary CKM matrix:

$$\begin{pmatrix} \mathrm{d}' \\ \mathrm{s}' \\ \mathrm{b}' \end{pmatrix} = \mathrm{V_{CKM}} \begin{pmatrix} \mathrm{d} \\ \mathrm{s} \\ \mathrm{b} \end{pmatrix} = \begin{pmatrix} \mathrm{V_{ud}} & \mathrm{V_{us}} & \mathrm{V_{ub}} \\ \mathrm{V_{cd}} & \mathrm{V_{cs}} & \mathrm{V_{cb}} \\ \mathrm{V_{td}} & \mathrm{V_{ts}} & \mathrm{V_{tb}} \end{pmatrix} \begin{pmatrix} \mathrm{d} \\ \mathrm{s} \\ \mathrm{b} \end{pmatrix} . \tag{6.5}$$

The CKM formulation is an extension to the three quark families of Cabibbo's mixing theory [6.8], which included mixing between the first two families making use of a single real parameter, Cabibbo's angle θ_C:

$$\begin{pmatrix} \mathrm{d}' \\ \mathrm{s}' \end{pmatrix} = V_C \begin{pmatrix} \mathrm{d} \\ \mathrm{s} \end{pmatrix} = \begin{pmatrix} \cos\theta_C & \sin\theta_C \\ -\sin\theta_C & \cos\theta_C \end{pmatrix} \begin{pmatrix} \mathrm{d} \\ \mathrm{s} \end{pmatrix} ; \tag{6.6}$$

V_C, Cabibbo's mixing matrix, is easily recognisable to be unitary:

$$V_C \, V_C^T \;=\; V_C^T \, V_C \;=\; \mathbf{1}_2 \, ; \tag{6.7}$$

$V_C^\dagger = V_C^T$, as V_C is in particular real.

Cabibbo's original mixing hypothesis was formulated in 1963, when three flavours only (u, d, s) were known. The fourth quark (c) hypothesis was formulated by Glashow, Iliopoulos and Maiani in 1970 [6.9], to account for the absence of neutral weak currents changing the strangeness number.

In 1974 the J/ψ resonance was discovered independently by Augustin et al., at the ∼3.1 GeV SPEAR e^+e^- collider at SLAC [6.10], and by Aubert et al., with a fixed target experiment (28 GeV protons on beryllium) at Brookhaven [6.11]. The J/ψ resonances were explained as $c\bar{c}$ bound states.

In 1977 the Υ resonance was found at FNAL [6.12], and explained as a $b\bar{b}$ bound state. But CP-violation found in the K-sector already suggested to Kobayashi and Maskawa in 1973 that the presence of a third quark family (b, t) could be at the origin of those effects [6.13].

The existence of a third quark family could also be justified on the ground of a possible symmetry between the lepton and the quark families: after the discovery of the τ lepton by M. Perl in 1975 [6.14], also at the SPEAR e^+e^- collider but at a centre-of-mass energy of ∼5 GeV, the number of leptonic families increased to three.

The claim for the symmetry was strengthened by the necessity to solve severe theoretical problems, like the *triangle anomalies* (1972). The triangle anomalies consist in axial-vector current contributions which would have 'destroyed' the gauge invariance of the weak interaction 'quasi-renormalisable' theory, unless the theory was enlarged, introducing additional fermion fields corresponding to particles still unobserved at the time (i.e. the third quark family) [6.15]. The Feynman diagrams concerned contain fermion (quark and/or lepton) *loops* coupled to axial and/or vector currents, always with an odd number of axial currents [6.16]. An example can be the $Z \rightarrow \gamma\gamma$ decay via a triangular fermion loop diagram.

To cancel out these kinds of anomalies, the *net charge* of *all* fermions is required to be *zero.* Considering now the three lepton and quark families (table iii in the Introduction), one obtains

$$-3\ |e| + 3\left[3\left(+\frac{2}{3}\ |e|\right) + 3\left(-\frac{1}{3}\ |e|\right)\right] = 0\ ,$$

which accounts for the three negatively charged leptons (e^-, μ^-, τ^-), the three $+2/3$-charged (u, c, t) quarks and the three $-1/3$-charged quarks (d, s, b). An additional colour factor (3) is included in the quark charge contribution [6.17]. The chargeless neutrinos do not give any contribution, obviously.

The expression of the weak charged current from (6.4), making use of the Cabibbo-Kobayashi-Maskawa matrix, is of the form

$$\mathcal{J}^{\mu}_{\text{weak}} \sim \left(\ \overline{\text{u}},\ \ \overline{\text{c}},\ \ \overline{\text{t}}\ \right) \gamma_{\alpha}(1-\gamma_5)\ \text{V}_{\text{CKM}} \begin{pmatrix} \text{d} \\ \text{s} \\ \text{b} \end{pmatrix} . \tag{6.8}$$

The fact that the V_{CKM} elements are in general complex numbers and not real, as the elements of V_C were, is at the origin of CP-violation within the Standard Model. The amplitude describing processes including weak vertices and their corresponding V_{CKM} elements will have an overall complex phase. This phase, if interfering with other amplitudes, can cause CP-violating effects.

6.2 CP-violation in the B sector

The condition of unitarity of the V_{CKM} matrix, expressed by

$$\text{V}_{\text{CKM}}\,\text{V}^{\dagger}_{\text{CKM}} = \text{V}^{\dagger}_{\text{CKM}}\,\text{V}_{\text{CKM}} = \mathbf{1}_3\ , \tag{6.9}$$

or equivalently

$$\mathbf{1}_3 = \begin{pmatrix} V_{ud}^* & V_{cd}^* & V_{td}^* \\ V_{us}^* & V_{cs}^* & V_{ts}^* \\ V_{ub}^* & V_{cb}^* & V_{tb}^* \end{pmatrix} \begin{pmatrix} V_{ud} & V_{us} & V_{ub} \\ V_{cd} & V_{cs} & V_{cb} \\ V_{td} & V_{ts} & V_{tb} \end{pmatrix} = \mathbf{1}_3 \ , \tag{6.10}$$

leads to several relations, out of which

$$V_{ub}^* V_{ud} + V_{cb}^* V_{cd} + V_{tb}^* V_{td} = 0 \tag{6.11}$$

is particularly relevant to our studies.

A commonly used parameterisation of V_{CKM} has been proposed by Wolfenstein [6.18]:

$$V_{CKM} \simeq \begin{pmatrix} 1-\lambda^2/2 & \lambda & A\lambda^3[\rho - i\eta(1-\lambda^2/2)] \\ -\lambda & 1-\lambda^2/2 - i\eta A^2\lambda^4 & A\lambda^2(1+i\eta\lambda^2) \\ A\lambda^3(1-\rho-\eta) & -A\lambda^2 & 1 \end{pmatrix} + O(\lambda^5) \ . \tag{6.12}$$

This parameterisation makes use of the three real parameters A, η and ρ, and of λ, related to Cabibbo's angle by the relation

$$\lambda = \sin\theta_c \simeq (0.2205 \pm 0.0018) \quad [6.19] \ . \tag{6.13}$$

The relation (6.11) can be now rewritten as

$$V_{td} + V_{ub}^* \approx \lambda V_{cb} + O(\lambda^4) \ , \tag{6.14}$$

making use of (6.12) up to third order in λ. It is usual to consider this relation as the equation of a triangle in the (ρ, η) complex plane, with $V_{cd}\, V_{cb}^*$ on the real axis, and rescaling all sides by $|V_{cd}\, V_{cb}^*| \approx \lambda\, |V_{cb}| + O(\lambda^4)$:

$$\frac{V_{ub}^*}{\lambda\, V_{cb}} + \frac{V_{td}}{\lambda\, V_{cb}} = 1 \ . \tag{6.15}$$

The base of this triangle is now real and of unit length. The so-called *unitarity triangle* thus formed is shown in fig. 6.4 (from [6.20]): the three vertices are in the points

$$A = (\rho, \eta) \qquad B = (1, 0) \qquad C = (0, 0) \qquad , \tag{6.16}$$

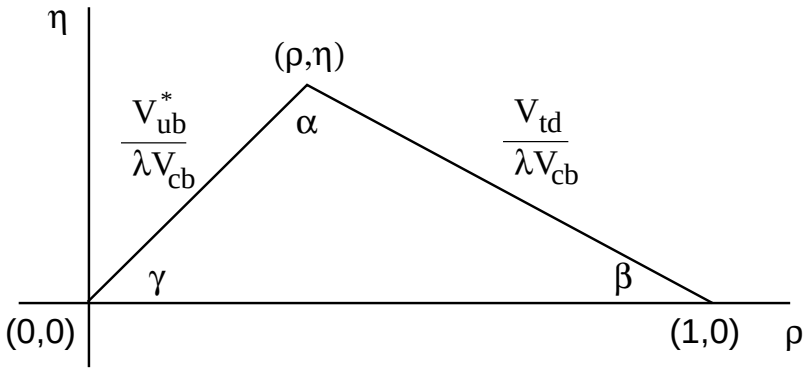

Fig. 6.4. The unitarity triangle (from [6.20]).

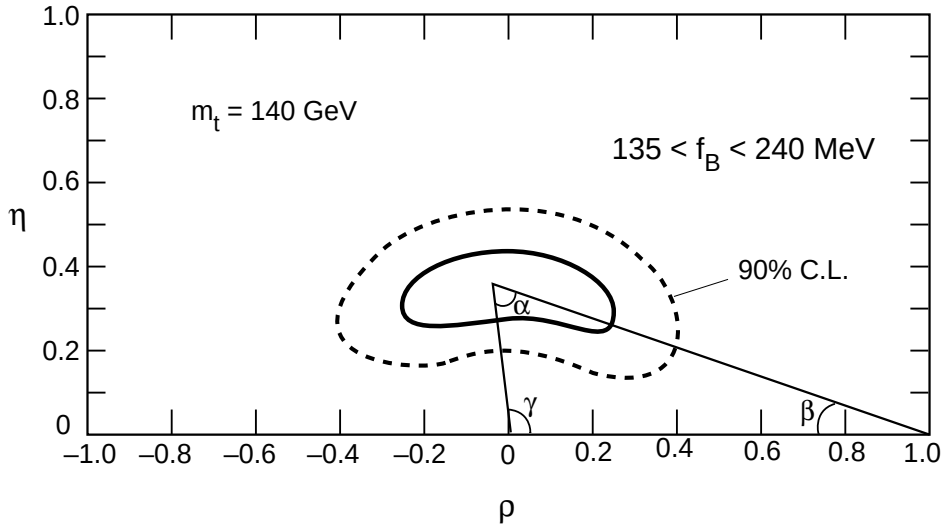

Fig. 6.5. The unitarity triangle with the 1993 experimental constraints [6.21].

and the corresponding angles have values

$$\alpha = \pi - \beta - \gamma \qquad \beta = -\arg(V_{td}) \qquad \gamma = -\arg(V_{ub}) \quad , \tag{6.17}$$

always in the Wolfenstein parameterisation.

Fig. 6.5 shows the unitarity triangle in the ρ-η space, with the experimental constraints as of 1993 [6.21], having supposed a top quark mass m_t of 140 GeV, and the B-meson decay factor[1] f_B constrained within the range [135, 240] MeV. The full line triangle represents the best fit.

[1] f_B is the leptonic B decay constant, defined by $\langle 0 | \bar{d} \gamma_\mu \gamma_5 b | \bar{B}^0 (p) \rangle = i p_\mu f_B$ [6.22]. The 1994 f_B value quoted by A. Ali is (180 $\pm$ 50) MeV, compatible with lattice-QCD and QCD sum rules estimates [6.23].

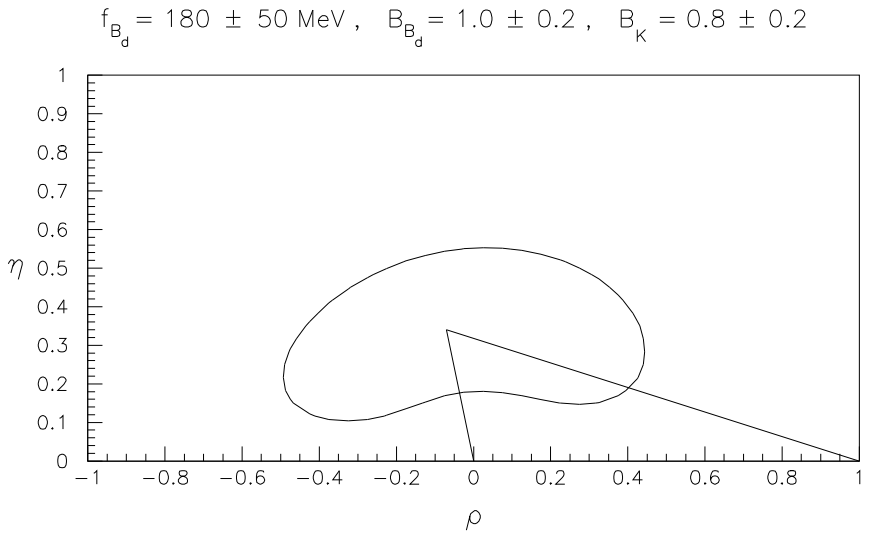

Fig. 6.6. Allowed region in the ρ-η space from the fit to both experimental (1995) and theoretical parameters, and unitarity triangle representing the best fit (from [6.24]).

The 1995 update is shown in fig. 6.6 (from [6.24]), with a simultaneous fit to both experimental and theoretical parameters. The solid line contains the 95 % C.L. region, and again the triangle drawn shows the best fit. The values of $m_t\,(pole) = (170 \pm 11)$ GeV, $\lambda = 0.2205$, $\tau(B_d) = (1.57 \pm 0.05)$ ps, and of $f_B = (180 \pm 50)$ MeV, $\hat{B}_{B_d} = (1.0 \pm 0.2)$ and $\hat{B}_K = (0.8 \pm 0.2)$ were used[2].

The most probable values result to be $\sin 2\alpha \sim 0.88$, $\sin 2\beta \sim 0.57$ and $\sin^2\gamma \sim 0.95$, e.g. for $\hat{B}_K = 0.8$, $\hat{B}_{B_d} = 1.0$ and $f_B = 180$ MeV, but the full ranges at the 95 % C.L. are still wide [6.24]:

$$\begin{aligned} -1.0 \;&\leq\; \sin 2\alpha \;\leq\; 1.0 \\ 0.21 \;&\leq\; \sin 2\beta \;\leq\; 0.93 \\ 0.12 \;&\leq\; \sin^2\gamma \;\leq\; 1.0 \end{aligned} \tag{6.18}$$

($\sin^2\gamma$ could possibly be extracted from the decays $B_s \to \rho K^0_s$, $B_s \to D^{\pm}_s K^{\mp}$ and $B^{\pm} \to D^0_{\rm CP}(\bar{D}^0_{\rm CP})\; K^{\pm}$, with $D^0_{\rm CP} \to \pi^+\pi^-,\; K^+K^-$,...). If $\sin 2\alpha < 0.4$, one finds $\sin 2\beta \geq 0.3$. $\sin 2\alpha$ can be zero or close to it.

These ranges are correlated. As an example, table 6.1 (from [6.24]) shows the allowed ranges corresponding to five different values of $f_{B_d}\sqrt{\hat{B}_{B_d}}$, i.e. of the product of the coupling constants, having fixed $\hat{B}_K = 0.8$.

[2] $\hat{B}_K$ is the 'renormalisation-scale independent parameter' for the kaon system, representing the bad knowledge of the hadronic matrix element $\langle K^0 | \left(\bar{d}\,\gamma^{\mu}\,(1-\gamma_5)\,s\right)^2 | \bar{K}^0 \rangle$. $\hat{B}_{B_d}$ is the analogous for the B system [6.20].

$f_{B_d}\sqrt{\hat{B}_{B_d}}$ (MeV)	$\sin 2\alpha$	$\sin 2\beta$	$\sin^2\gamma$
130.	0.46 — 0.88	0.21 — 0.37	0.12 — 0.39
155.	0.75 — 1.00	0.31 — 0.56	0.34 — 0.92
180.	−0.59 — 1.00	0.42 — 0.73	0.68 — 1.00
205.	−0.96 — 0.92	0.49 — 0.86	0.37 — 1.00
230.	−0.98 — 0.60	0.57 — 0.93	0.28 — 0.97

Table 6.1. Allowed ranges for $\sin 2\alpha$, $\sin 2\beta$ and $\sin^2\gamma$, corresponding to different values of the coupling constant $f_{B_d}\sqrt{\hat{B}_{B_d}}$; $\hat{B}_K = 0.8$ (from [6.24]).

Within the Standard Model, CP-violation in the B sector would show itself if all the three angles were different from zero, and indeed compatible with a triangle. The sides of the triangle could be measured from non-CP-violating effects as an independent consistency check. CP-violation would therefore imply $\eta \neq 0$.

If CP is violated in a way not compatible with this description, it would be a clear sign of phenomena *beyond the Standard Model.*

The simplest way to provide evidence for CP-violation in the B sector is to measure experimentally the asymmetries of B-meson decay rates into a definite final state $|f\rangle$, i.e. $N(B \to f)$, $N(B \to \overline{f})$, $N(\overline{B} \to f)$ and $N(\overline{B} \to \overline{f})$. As already mentioned, to produce non zero asymmetries an interference between two weak amplitudes is needed in the decay $B \to f$.

In the following, only the *(indirect) mixing-induced* CP-violation will be considered. This type of CP-violation originates from the interference between the processes $B^0 \to f$ and $B^0 \to \bar{B}^0 \to f$ (and their CP-conjugates), due to $B^0/\bar{B}^0$ mixing. The two quark line diagrams responsible for the $B^0/\bar{B}^0$ mixing via two $W^\pm$ bosons and (u, c, t) quarks are shown in fig. 6.7 (from [6.19]).

There can also exist *direct* CP-violation if two amplitudes contribute to the same B-meson decay, e.g. via a tree and a penguin diagram at the same time. Direct CP-violation could be searched for cleanly in charged B-meson decays, such as $B^\pm \to \pi^0 K^\pm$, where no mixing occurs. For this $B^\pm$ decay channel fig. 6.8 shows examples of quark line diagrams representing the tree and penguin contributions to the decay.

A third type of CP-violation would be induced by a difference $\Delta\Gamma$ in the widths of the two mass eigenstates. It is usually defined as *(purely) indirect* CP-violation, and it is expected to be very small in the B-system.

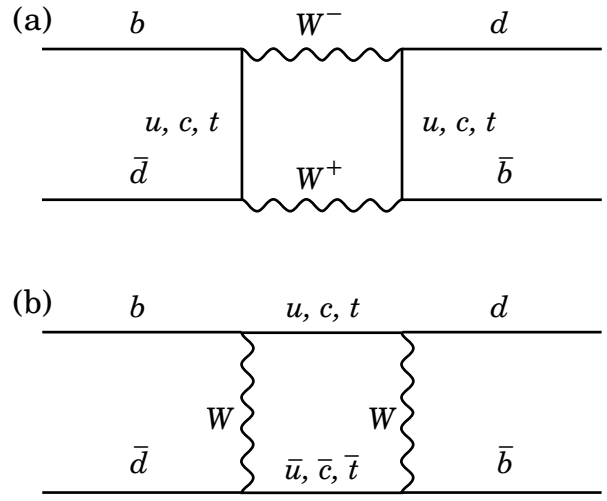

Fig. 6.7. Quark line diagrams for $B^0/\bar{B}^0$ mixing (from [6.19]).

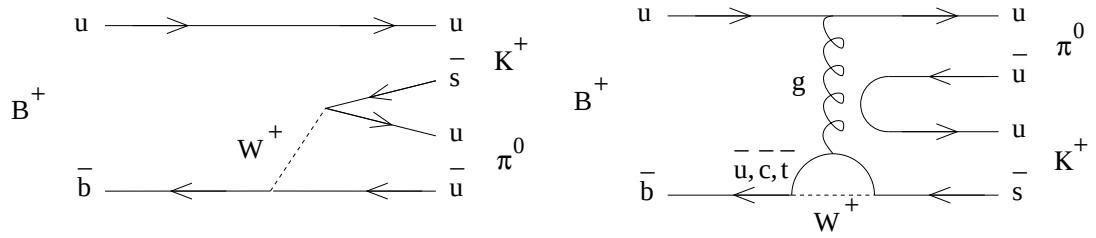

Fig. 6.8. Examples of quark line diagrams representing the $B^+ \to \pi^0\, K^+$ decay: tree (left) and penguin diagram (right).

Considering selected B^0 decay modes, where only one weak amplitude contributes and therefore CP-violation is purely induced by mixing, it is possible experimentally to obtain direct information about the CKM phase. The four decay rates should be measured, taking into account the time evolution of the B_d^0 due to mixing:

$$|B_d^0\,(t)\rangle \;=\; e^{-i\,(m\,-\,i\frac{\Gamma}{2})\;t}\;\left[\cos\left(\frac{\Delta m}{2}\,t\right)\;|B_d^0\,\rangle \;+\; i\omega\,\sin\left(\frac{\Delta m}{2}\,t\right)\;|\overline{B_d^0}\rangle\right] \qquad (6.19)$$

(and similarly for $|\overline{B_d^0}(t)\rangle$), where m is the $B_d^0/\bar{B}_d^0$ average mass, Δm the mass difference, Γ the common width, and ω a mixing phase factor.

If the final state f is a CP eigenstate

$$|\,\overline{f}\,\rangle \;=\; \eta_{\rm CP}\,|\,f\,\rangle\;, \qquad (6.20)$$

the CP-asymmetry takes the form

$$\mathcal{A}_f \;=\; \frac{N(B^0 \;\to f) - N(\bar{B}^0 \;\to \bar{f})}{N(B^0 \;\to f) + N(\bar{B}^0 \;\to \bar{f})}\,, \tag{6.21}$$

and it is dependent on the proper time[3] of the B-meson. The decay rates are expressed by

$$N_t\,(B^0_d \;\to f) \;\propto\; e^{-\frac{t}{\tau}} \left[1 + \eta_{CP}\, \sin 2\phi_i\, \sin\left(x_d\, \frac{t}{\tau}\right)\right] \tag{6.22}$$

and

$$N_t\,(\bar{B}^0_d \;\to \bar{f}) \;\propto\; e^{-\frac{t}{\tau}} \left[1 - \eta_{CP}\, \sin 2\phi_i\, \sin\left(x_d\, \frac{t}{\tau}\right)\right]\,, \tag{6.23}$$

where ϕ_i is the angle of the unitarity triangle involved, x_d is the $B^0_d/\bar{B}^0_d$ mixing parameter

$$x_d \;=\; \frac{\Delta m}{\Gamma}\,, \tag{6.24}$$

and t/τ is the proper time in units of the average B^0_d lifetime τ ($\tau \;=\; \Gamma^{-1}$).

Two B^0_d decays to CP eigenstates were considered particularly, up to now, for CP-violation studies in CMS:

i. $B^0_d/\bar{B}^0_d \;\to J/\psi\, K^0_s$ ($b \to c$ quark transition), and

ii. $B^0_d/\bar{B}^0_d \;\to \pi^+\pi^-$ ($b \to u$ quark transition),

as they lead to the direct measurement of the angles β and α, respectively, of the unitarity triangle. They will be described in detail and commented upon in the next sections.

Fig. 6.9 shows, as an example, the decay rates for $B^0_d \;\to \pi^+\pi^-$ and $\bar{B}^0_d \;\to \pi^+\pi^-$, as a function of t/τ [6.25]. The two decay rates are equal at $t/\tau \;=\; \pi/x_d \;\simeq\; 4.6$, having considered $x_d \;\simeq\; (0.69 \pm 0.18)$. This value was quoted in [6.26], and was derived from the measurement of the time-integrated mixing parameter[4] performed by the Argus collaboration in electron-positron scattering at the $\Upsilon(4S)$ energy ($\sim$10.6 GeV). The 1994 updated world average is $x_d \;\simeq\; (0.76 \pm 0.06)$ [6.23], and it is based both on time-integrated and time-dependent measurements [6.27]. The

[3]The *proper* time (t) of a particle is defined in the reference frame of the particle itself at rest, while the *flight* time (t') is defined in the frame of the laboratory, i.e. in the reference frame of the detector through which the particle is identified, and it corresponds to the particle lifetime as seen in the laboratory frame. The Lorentz transforms imply $t' \;=\; \gamma\, t$, where $\gamma \;=\; \left(1 - \beta^2\right)^{-1/2}$ and $\beta \;=\; v/c$.

[4]The time-integrated mixing parameter χ_d (χ_s) is the total probability that a produced B^0_d (B^0_s) decays as a $\bar{B}^0_d$ ($\bar{B}^0_s$), or vice-versa: $\chi_{d,s} \;=\; \int_0^\infty P_{d,s}(t)\, dt$, where $P_{d,s}(t) \;=\; \frac{1}{2}\, e^{-t/\tau}\, \left[1 - \cos\left(x_{d,s}\, \frac{t}{\tau}\right)\right]$. x_d and x_s are obtained with the relations $x_{d,s} \;=\; \sqrt{\chi_{d,s}/(0.5 - \chi_{d,s})}$.

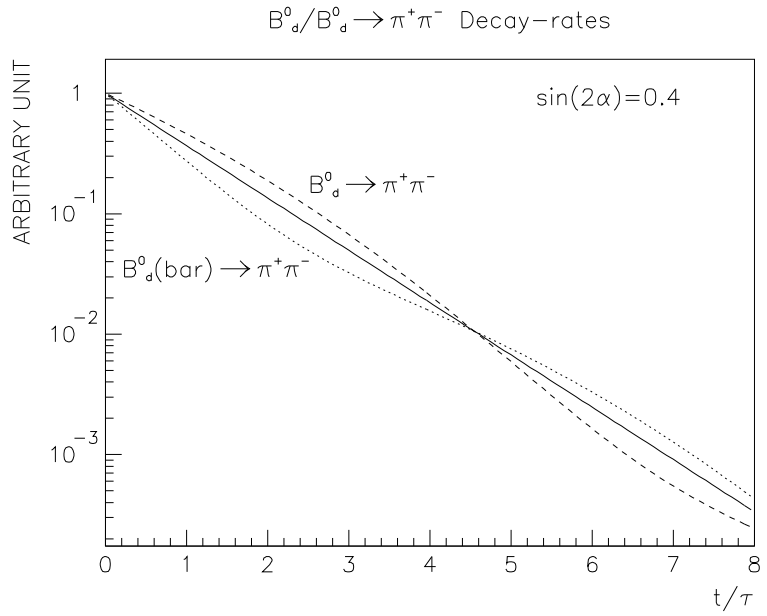

Fig. 6.9. $B^0/\bar{B}^0 \to \pi^+\pi^-$ decay rates as a function of proper time [6.25].

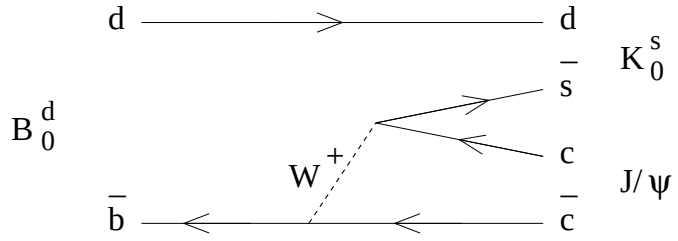

Fig. 6.10. Tree quark line diagram representing the $B^0_d/\bar{B}^0_d \to J/\psi\, K^0_s$ decay.

latter measure Δm directly, and x_d is obtained using the measured B^0_d lifetime[5] and (6.24).

The tree quark line diagram for the $B^0_d/\bar{B}^0_d \to J/\psi\, K^0_s$ decay channel is shown in fig. 6.10, while fig. 6.11 and fig. 6.12 show, respectively, the tree and penguin quark line diagram contributions to the $B^0_d \to \pi^+\pi^-$ decay.

The theoretical *time-dependent asymmetries* for these two channels take respectively the forms

$$\mathcal{A}_\beta\,(t/\tau) \;=\; \frac{N\,(B^0_d \to J/\psi K^0_s\,) \;-\; N\left(\bar{B}^0_d \to J/\psi K^0_s\right)}{N\,(B^0_d \to J/\psi K^0_s\,) \;+\; N\left(\bar{B}^0_d \to J/\psi K^0_s\right)} \;=\; -\sin 2\beta\;\sin\left(x_d\,\frac{t}{\tau}\right) \tag{6.25}$$

[5]The 1994 average for the B^0 lifetime quoted by [6.19] is (1.50 ± 0.11) ps; the 1994 value from CDF is $(1.57 \pm 0.18 \pm 0.08)$ ps [6.28].

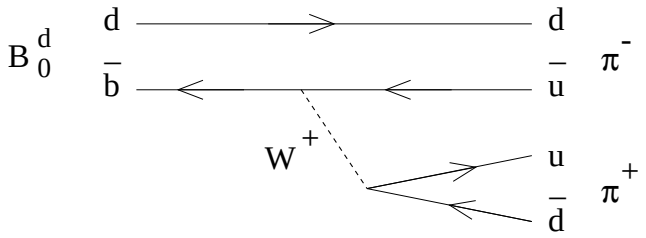

Fig. 6.11. Tree quark line diagram representing the $B_d^0 \to \pi^+\pi^-$ decay.

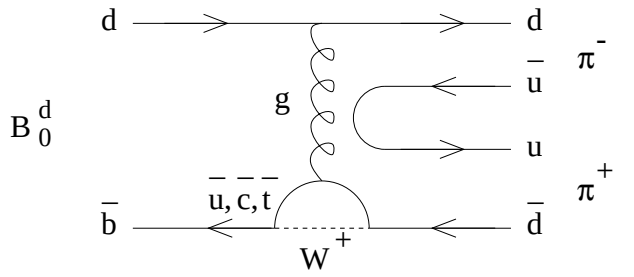

Fig. 6.12. Example of penguin quark line diagram contributing to the $B_d^0 \to \pi^+\pi^-$ decay.

and

$$\mathcal{A}_\alpha\,(t/\tau) \;=\; \frac{N\,(B_d^0 \to \pi^+\pi^-\,) \;-\; N\left(\bar{B}_d^0 \to \pi^+\pi^-\right)}{N\,(B_d^0 \to \pi^+\pi^-\,) \;+\; N\left(\bar{B}_d^0 \to \pi^+\pi^-\right)} \;=\; +\sin 2\alpha\;\sin\left(x_d\,\frac{t}{\tau}\right)\;. \tag{6.26}$$

The different signs of (6.25) and (6.26) are due to the fact that $\eta_{CP} = +1$ for $\pi^+\pi^-$ ($CP\;|\pi^+\pi^-\,\rangle = +\,|\pi^+\pi^-\,\rangle$), and $\eta_{CP} = -1$ for $J/\psi\,K_s^0$ ($CP\;|J/\psi\,K_s^0\,\rangle = -\,|J/\psi\,K_s^0\,\rangle$).

The expression (6.26) is derived neglecting any penguin diagram contribution to the decay amplitude, which in this case might reach ~20 %, even though theoretical uncertainties are still large [6.21, 6.29, 6.30]. In this channel, the tree and penguin diagrams have different weak phases which will then interfere, producing direct CP-violation along with the indirect CP-violation, thus polluting the cleanliness of the measurement. Some recovery is possible by means of a compared *isospin analysis* [6.31] of the processes $B_d^0 \to \pi^+\pi^-$, $B_d^0 \to \pi^0\pi^0$ and $B^+ \to \pi^+\pi^0$ [6.32]. In the case of the $B_d^0 \to J/\psi\,K_s^0$ channel, the tree and penguin diagrams have the same weak phases and therefore do not interfere [6.32].

It is also possible to consider the corresponding *time-integrated asymmetries,* performing an integration over the proper decay time, starting in general from a time t_0 :

$$\mathcal{A}_{\phi_i}^{\rm INT} \;=\; \int_{t_0}^{+\infty} \mathcal{A}_\phi(t/\tau)\,{\rm d}t \;=\; \eta_{CP}\;\; D_{\rm int}(t_0)\;\;\sin 2\phi_i\;, \tag{6.27}$$

where ϕ_i stands for both α and β, and $D_{\rm int}\,(t_0)$ is a *dilution factor,* smaller than 1, due to the time integration

$$D_{\rm int}\,(t_0) \;=\; \frac{\sin\left(x_d\,\frac{t_0}{\tau}\right)\;+\;x_d\;\cos\left(x_d\,\frac{t_0}{\tau}\right)}{1\;+\;x_d^2}\;, \tag{6.28}$$

and obtained from the integral ratio

$$\frac{\displaystyle\int_{t_0}^{+\infty}\sin\left(x_d\,\frac{t}{\tau}\right)\,e^{-\frac{t}{\tau}}\,{\rm d}t}{\displaystyle\int_{t_0}^{+\infty}e^{-\frac{t}{\tau}}\,{\rm d}t} \;=\; \frac{\tau\,e^{-\frac{t_0}{\tau}}\;\frac{1}{1\;+\;x_d^2}\;\left[\sin\left(x_d\,\frac{t_0}{\tau}\right)\;+\;x_d\;\cos\left(x_d\,\frac{t_0}{\tau}\right)\right]}{\tau\,e^{-\frac{t_0}{\tau}}}\;. \tag{6.29}$$

If the integration over time starts at $t_0 = 0$, i.e. if no cuts are applied to the B_d^0 decay time, the integration dilution factor takes the value:

$$D_{\rm int}\,(t_0 = 0) \;=\; \frac{x_d}{1\;+\;x_d^2} \;\simeq\; 0.47 \qquad (x_d \;\simeq\; 0.69)\;. \tag{6.30}$$

6.3 Measurement of the asymmetries

When trying to measure the asymmetries, inevitably some additional *dilution factors* have to be considered, as some phenomena interfere with the CP-violating effects and 'dilute' them. The measurable time-dependent asymmetry takes then the form:

$$\mathcal{A}_{\phi_i}^{\rm meas}\,(t/\tau) \;=\; \mathcal{A}_0 \;+\; D_{\rm tot}\;\;\mathcal{A}_{\phi_i}\,(t/\tau)\;, \tag{6.31}$$

where $\mathcal{A}_{\phi_i}\,(t/\tau)$ is the same as in (6.25) or (6.26), depending on the channel, and $\mathcal{A}_0$ accounts for the $B^0/\bar{B}^0$ production asymmetry, as LHC is a proton-proton machine [6.33], and for possible asymmetries of the apparatus. In the following, $\mathcal{A}_0 \;\simeq\; 0$ will be assumed; the $B^0/\bar{B}^0$ production asymmetry should be at the percent level, and could be measured, making use of *control channels* like e.g. $B_d^0 \;\rightarrow J/\psi\,K^{*0}$ [6.34]. Also possible axial asymmetries of the experimental apparatus could be estimated, with control channels such as $B_s^0 \;\rightarrow J/\psi\,\phi$, where no CP-violation is expected within the Standard Model [6.2].

$D_{\rm tot}$ is the overall dilution factor, given by the product

$$D_{\rm tot} \;=\; D_m \cdot D_t \cdot D_{S/B} \;, \tag{6.32}$$

where D_m, D_t, and $D_{S/B}$ are the dilution factors due to the *mixing* of the associated B-hadron, to its *tagging* and to the *background* events respectively.

The decay of the associated B-hadron produced allows the identification of the decaying $B^0/\bar{B}^0$, by using the semileptonic decays of the former. At the quark level,

$$\begin{aligned} b \;&\rightarrow\; W^-\, c \;\rightarrow\; l^-\, \bar{\nu}_l\, c \qquad \text{and} \\ \bar{b} \;&\rightarrow\; W^+\, \bar{c} \;\rightarrow\; l^+\, \nu_l\, \bar{c} \;. \end{aligned} \tag{6.33}$$

The charge of the lepton allows the tagging at production of the B meson. Therefore, the presence of a negative (positive) lepton tag will indicate the presence of a decaying B^0 ($\bar{B}^0$) 'on the other side'.

At the beginning, only muon tagging was considered for CP-violation studies with CMS, because of the much 'cleaner' environment. Now the possibility of tagging with electrons is also being investigated.

The associated B-hadron produced, if it is a B_d^0 or a B_s^0, can mix with its antistate before decaying, leading to a wrong identification. The dilution factor due to this mixing has the form

$$D_m \;=\; \sum_{i=1}^{4} \frac{p_i}{1 \,+\, x_i^2} \;=\; p^{\pm} \,+\, \frac{p_d^0}{1 \,+\, x_d^2} \,+\, \frac{p_s^0}{1 \,+\, x_s^2} \,+\, p_\Lambda \;\simeq\; 0.75 \;, \tag{6.34}$$

where the p_i's are the production rates of the B-hadrons, assumed to be

$$\begin{aligned} p^{\pm} \;&=\; p(B^{\pm}) \;=\; 0.40 \;, \qquad p_d^0 \;=\; p(B_d^0) \;=\; 0.40 \;, \\ p_s^0 \;&=\; p(B_s^0) \;=\; 0.12 \;, \qquad p_\Lambda \;=\; p(\Lambda_b) \;=\; 0.08 \;, \end{aligned} \tag{6.35}$$

and the x_i's (x_d , x_s) quantify the oscillations of the neutral B-mesons. $x_s \;\simeq\; 10$ has been assumed. Λ_b is the B-baryon formed by the quarks *udb*.

Independently of this effect, a wrong tag can be assigned to the $B^0/\bar{B}^0$ meson because of other reasons, leading to the presence of a lepton which is incorrectly related to the associated B-hadron, and the additional tagging dilution factor can be expressed by

$$D_t \;=\; \frac{\mathrm{N(right\ tags)} \,-\, \mathrm{N(wrong\ tags)}}{\mathrm{N(right\ tags)} \,+\, \mathrm{N(wrong\ tags)}} \;=\; 1 \,-\, 2\,W \;, \tag{6.36}$$

where W is the fraction of wrong tags

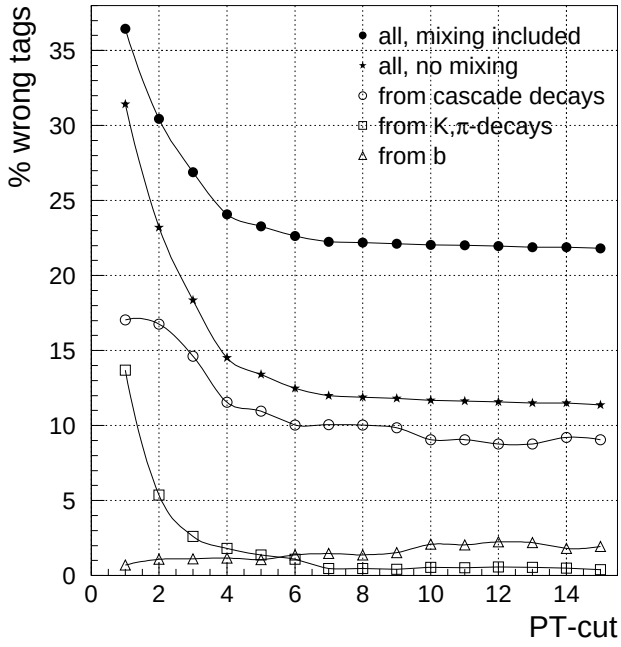

Fig. 6.13. Fraction of wrong muon tags W as a function of the cut on p_t ($\mu_{\rm tag}$) [6.35].

$$W = \frac{\mathrm{N(wrong\ tags)}}{\mathrm{N(total)}} . \tag{6.37}$$

In the case of muon tagging, the greatest contribution to W is given by *cascade decays* such as $b \to c \to \mu$, where the muon is of the opposite charge compared to the $b \to \mu$ semileptonic b-quark decay. Other sources of mistags are K and π decays, and additional $b\bar{b}$ and $c\bar{c}$ pairs in the same event.

Fig. 6.13 from ref. [6.35] shows the fraction W of wrong muon tags, as a function of the cut on p_t ($\mu_{\rm tag}$), for the different mistag sources. Because of the hard fragmentation and of the large mass of the b-quark, the muons originating from semileptonic decays have a large transverse momentum. B-events were simulated with PYTHIA [6.3, 6.4], and the muons in the event were analysed: the tagging muon is considered to be the one with the highest transverse momentum, excluding, in the case of the $B_d^0 \to J/\psi\, K_s^0$ channel, the reconstructed muons coming from the J/ψ decay. The fraction of wrong tags decreases if harder cuts on p_t ($\mu_{\rm tag}$) are applied [6.35]. Fig. 6.13 also shows the fraction of wrong tags after having added the mixing effect, which is included in D_m.

Finally, the dilution due to the contamination of the signal event sample with background events is expressed by the factor

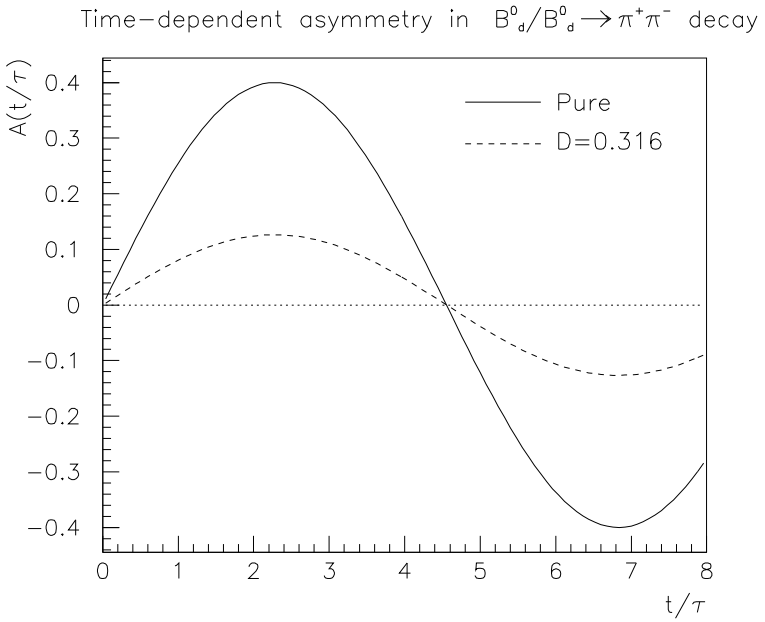

Fig. 6.14. Theoretical time-dependent asymmetry for $B^0/\bar{B}^0 \to \pi^+\pi^-$, undiluted and diluted with $D_{\rm tot} = 0.316$, for $\sin 2\alpha = 0.4$ [6.25].

$$D_{S/B} \;=\; \frac{N_S}{N_S + N_B}\;, \tag{6.38}$$

where N_S and N_B are the number of signal and background events, respectively.

As an example, fig. 6.14 shows the theoretical time-dependent asymmetry for the decay channel $B^0/\bar{B}^0 \to \pi^+\pi^-$, undiluted – $\mathcal{A}_\beta\,(t/\tau)$, full line – and diluted – $\mathcal{A}_\beta^{\rm meas}\,(t/\tau) \;=\; D_{\rm tot}\;\mathcal{A}_\beta\,(t/\tau)$, dashed line – with an overall dilution factor $D_{\rm tot} \simeq 0.3$, having supposed $\sin 2\alpha = 0.4$ [6.25].

The measured time-integrated asymmetry has then the form

$$\mathcal{A}_{\phi_i}^{\rm INT}\,({\rm meas}) \;=\; \eta_{CP}\;\; D_{\rm int}(t_0)\; D_{\rm tot}\;\;\sin 2\phi_i\;, \tag{6.39}$$

and the statistical sensitivity to the CP-violation parameters $\sin 2\phi_i$ achievable with a time-integrated measurement can be expressed by

$$\delta^{\rm INT}\,(\sin 2\phi_i) \;\sim\; \frac{1}{(D_m\,D_t\,D_{S/B})\,D_{\rm int}}\;\frac{1}{\sqrt{N_{\rm TOT}}} \;=\; \frac{1}{(D_m\,D_t)\,D_{\rm int}\,\sqrt{D_{S/B}}}\;\frac{1}{\sqrt{N_S}}\;, \tag{6.40}$$

having assumed $\mathcal{A}_{\rm meas} \ll 1$. $N_{\rm TOT}$ represents the total number of recorded events ($N_{\rm TOT} \;=\; N_{\rm S} \;+\; N_{\rm B}$).

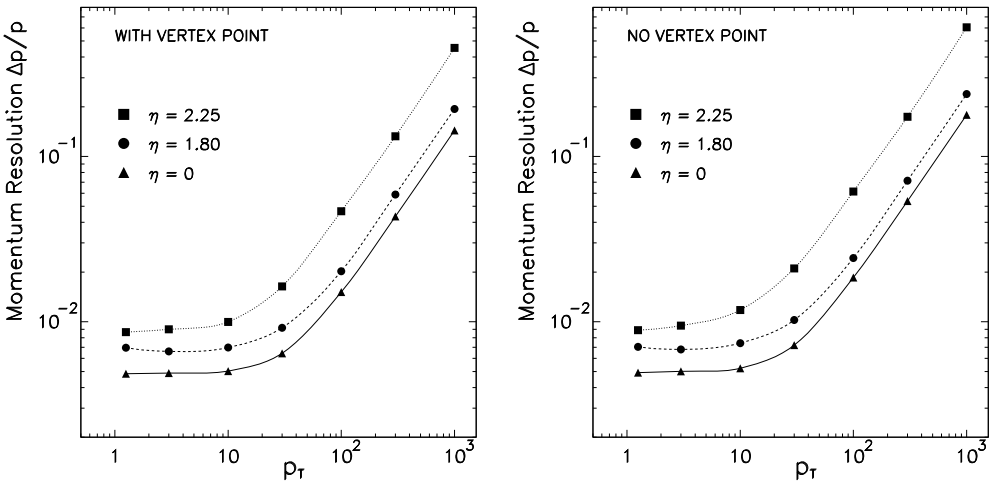

Fig. 6.15. CMS momentum resolution as a function of p_t for three rapidities, with (left) and without vertex constraint (right) [6.36].

6.4 B-physics studies in CMS: detector performance

The CMS detector has been described in Chapter 1. Relevant to these studies is the detector performance, in particular the momentum resolution, the impact parameter resolution, the secondary vertex reconstruction and the K^0 reconstruction efficiency.

The proposed pixel detector close to the interaction vertex will improve b-tagging, tracker momentum resolution and secondary vertex reconstruction. It would consist of two layers in the barrel region, at radii of 7.7 cm and 11.7 cm, and of three discs in the forward region, with 7.5 cm $< r <$ 15 cm, and $|z|$ =39, 54 and 69 cm, ensuring a rapidity coverage up to $|\eta| \simeq 2.6$.

Fig. 6.15 shows the momentum resolution as a function of the track transverse momentum p_t , for three rapidities (η = 0., 1.8 and 2.25, i.e. for central, intermediate and forward tracks), with and without vertex constraint [6.36].

No vertex constraint is used for tracks of particles from B decays, as they are not associated to the primary vertex because of the B^0 flight path.

For low p_t (p_t < 10. GeV/c) tracks, the momentum resolution $\Delta p/p$ is ~0.5 %, ~0.7 % and ~0.9 % at the three rapidities mentioned above, respectively.

The impact parameter resolution for a single track is an important quantity for b-physics in general, i.e. also for b-tagging in hard collisions (top quark production, associated $Hb\bar{b}$ production, search for $H \rightarrow b\bar{b}$ decays). It should be smaller than

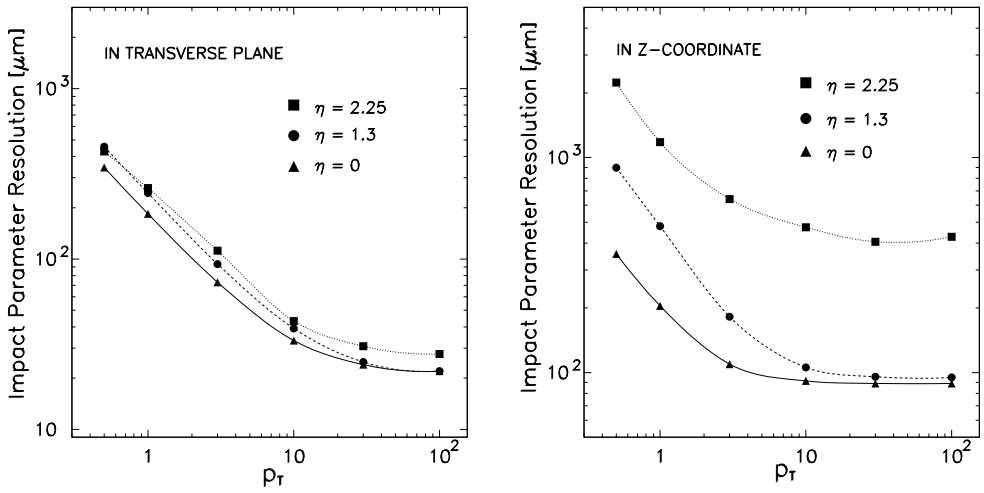

Fig. 6.16. CMS impact parameter resolution as a function of p_t for three rapidities, in the transverse plane (left) and in the z-coordinate (right) [6.36].

$c\,\tau(B^0) \simeq 450$ μm to ensure high efficiency and purity.

Fig. 6.16 shows the impact parameter resolution as a function of p_t for three rapidities [6.36]. The asymptotic high momentum impact parameter resolution is $\sim$23 μm in the transverse plane and $\sim$90 μm along the z-coordinate in the central region ($|\eta| \leq 1.5$), but for a 10 GeV/c (3 GeV/c) transverse momentum track it degrades to $\sim$40 μm ($\sim$90 μm) in the transverse plane and to $\sim$110 μm ($\sim$150 μm) along the z-coordinate (central region). On top of this, the error on the primary vertex should be folded in.

The uncertainty on the position of the primary vertex has been estimated to be $\sigma_x = \sigma_y \sim 20$ μm (transverse plane) and $\sigma_z \sim 5.3$ cm (along the z-direction) [6.2, 6.37].

An efficient and precise secondary vertex reconstruction is very important for B-physics. The secondary vertex resolution in the transverse plane has been estimated to be of the order of 100 μm [6.38]. The possibility of reconstructing secondary vertices in three dimensions is also being considered, and it could improve the present performance.

After having been evaluated with detailed GEANT [6.39] descriptions of the central detector, these resolutions have been parameterised as functions of particle pseudorapidity and transverse momentum, into fast routines for momentum and impact parameter smearing [6.36].

The $K_s^0 \rightarrow \pi^+\pi^-$ reconstruction efficiency was estimated simulating B events with K_s^0 decays and about 200 tracks per bunch crossing, i.e. with a few minimum

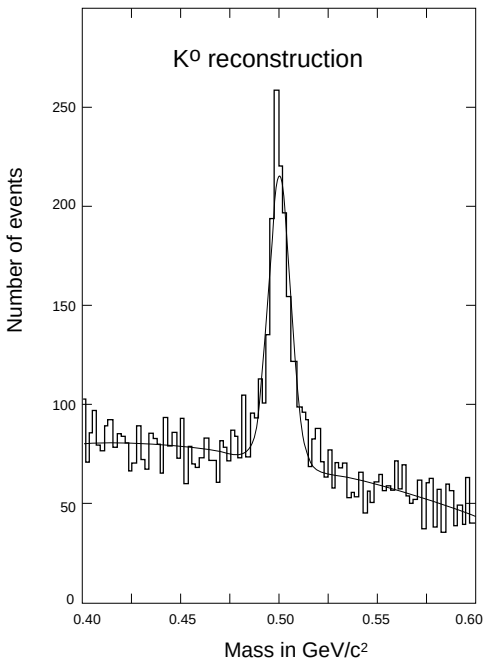

Fig. 6.17. The reconstructed invariant mass for $K_s^0 \to \pi^+\pi^-$, with combinatorial background. $\sigma\,(K_s^0\,) \simeq 8.6$ MeV/c^2, ~200 tracks per bunch crossing at low luminosity, $p_t^{\pi} > 700$ MeV/c^2 [6.40].

bias events superimposed. A track finding algorithm optimised for low transverse momentum tracks was developed [6.40], where CMS would attempt to find all tracks with $p_t > 350$ MeV/c, in the low luminosity regime.

The single track finding efficiency was estimated to be about 95 % for tracks with $p_t > 600$ MeV/c. Fig. 6.17 shows the reconstructed invariant mass for all pairs of tracks from a secondary vertex separated in the transverse plane from the primary vertex by at least 2 cm, including the combinatorial background from the same events. The K_s^0 peak is clearly visible, with a mass resolution of ~8.6 MeV/c^2, and an average signal to background ratio of about 2:1.

The reconstruction efficiency was also considered: within the CMS rapidity coverage and after the cuts imposed on the transverse momentum of the pion candidates ($p_t^{\pi} > 0.7$ GeV/c) for the $B_d^0 \to J/\psi\, K_s^0$ event simulation, the average $K_s^0 \to \pi^+\pi^-$ efficiency resulted to be about 35 %, having required at least six points per track [6.35, 6.37, 6.40].

The CMS muon trigger has been introduced in section 1.3. For the channels relevant to CP-violation, the low p_t single and double muon triggers will be used, as it will be explained in the following.

Presently, the possibility of electron tagging is under investigation; this would

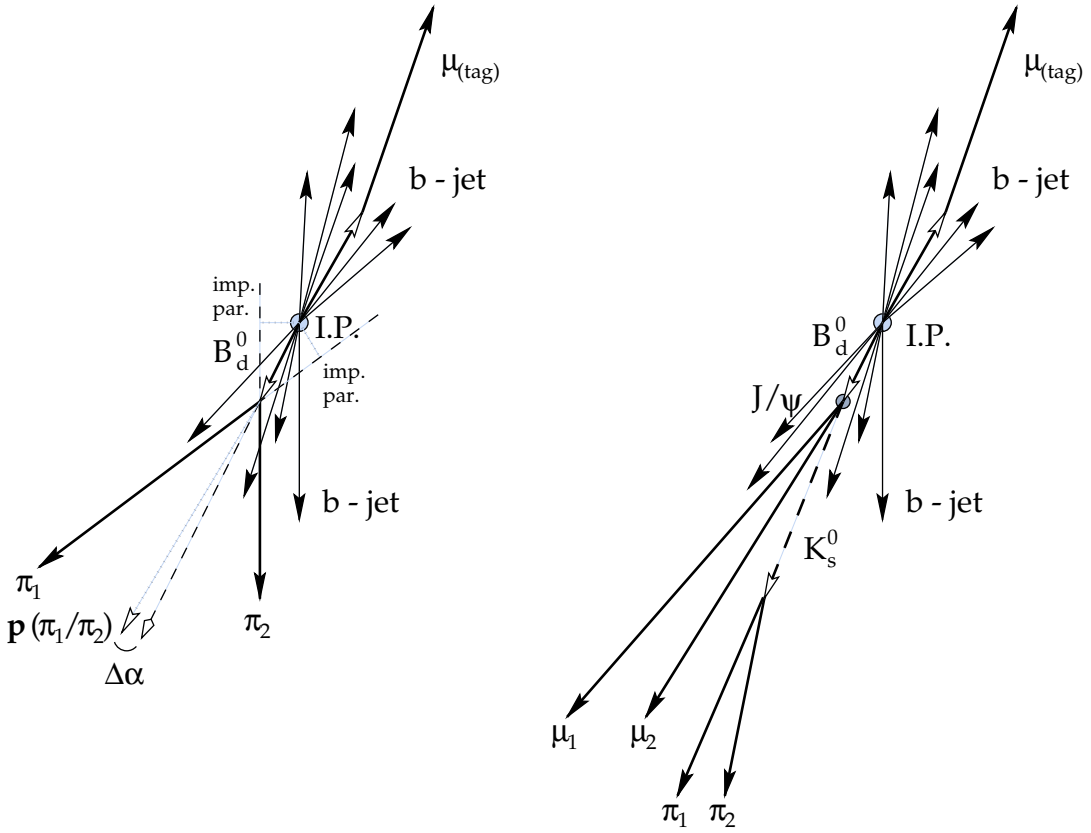

Fig. 6.18. Schematics of particle topology for the CP-violating decays $B_d^0 \to \pi^+\pi^-$ (left) and $B_d^0 \to J/\psi\, K_s^0$ (right).

involve also low p_t single electron or combined muon-electron triggers.

6.5 Time-integrated asymmetries

The evaluation of the achievable sensitivities to the CP-violating asymmetries with a time-integrated measurement will be presented first. In the following, the methods used will be described in detail. The results presented will refer explicitly to the CMS design version and to the simulation assumptions as presented in the Technical Proposal [6.37]. Nevertheless, the methods developed have a general character and are applicable to different initial assumptions and configurations.

In particular, in the first months of 1996 it is expected that the whole of the CP-violation studies will be updated, in view of a few modifications of the CMS design and to the structure functions within PYTHIA [6.3, 6.4] for proton-proton interactions, which were not yet implemented in the following.

Fig. 6.18 shows a simplified scheme of the particle topologies for the CP-violating

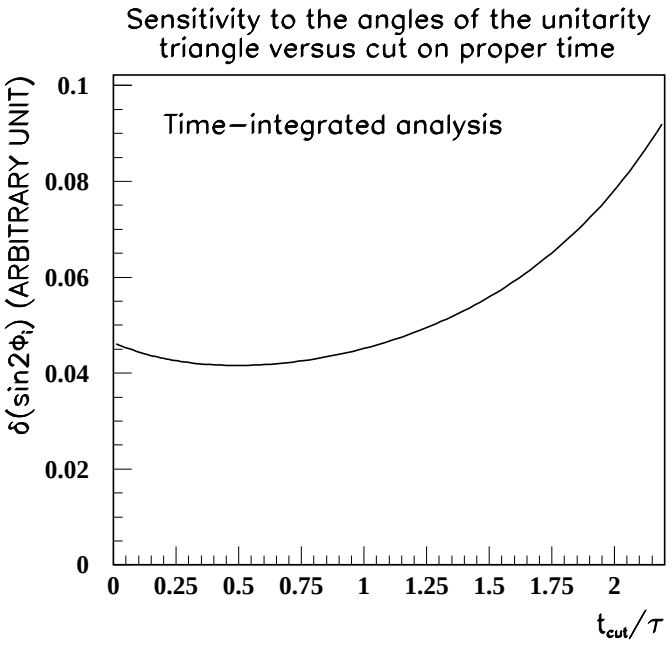

Fig. 6.19. Sensitivity to the angles of the unitary triangle as a function of the cut on the proper time (time-integrated analysis) [6.42].

decays $B_d^0 \to \pi^+\pi^-$ and $B_d^0 \to J/\psi\, K_s^0$, in the case of muon tagging.

The sensitivity, achievable with a time-integrated analysis, to the angles of the unitarity triangle, in arbitrary units, is shown in fig. 6.19 as a function of the cut on the B^0 proper time [6.41, 6.42]. It presents a local minimum at $t_{\rm cut}/\tau \simeq 0.5$.

6.5.1 The B_d^0 $(\bar{B}_d^0) \to \pi^+\pi^-$ channel

The events simulated contain a tagging muon and two *hard tracks,* giving an invariant mass[6] window around the B_d^0 mass. The challenging task is to extract as much $B_d^0 \to \pi^+\pi^-$ signal as possible from the large combinatorial background.

Simulations for the channel B_d^0 $(\bar{B}_d^0) \to \pi^+\pi^- + \mu_{\rm tag}$ have been performed using the PYTHIA Monte Carlo event generator [6.3, 6.4], having assumed the $b\bar{b}$ cross section (6.1) at an LHC centre-of-mass energy ($\sqrt{s}$) of 14 TeV.

Gluon splitting, gluon fusion and flavour excitation have been considered as mechanisms leading to the production of $b\bar{b}$ pairs [6.42].

The B-hadron branching production rates (6.35) were used, with the following

[6]The invariant mass m, reconstructed e.g. from two decay particles, is defined as $m^2 = (E_1 + E_2)^2 - \sum_{i=1}^{3} (p_{1,i} + p_{2,i})^2$, where E_1, E_2 and $\vec{p}_1$, $\vec{p}_2$ are the energies and the 3-momenta of the decay particles respectively.

decay branching ratios:

(a) BR $(B_d^0 \to \pi^+\pi^-) = 2 \cdot 10^{-5}$;

(b) BR $(B_d^0 \to K\pi) =$ BR $(B_s^0 \to K\pi) =$ BR $(B_s^0 \to KK) = 2 \cdot 10^{-5}$;

(c) BR $(\Lambda_b \to p\,\pi) = 5 \cdot 10^{-5}$;

(d) BR $(\mathrm{b} \to \mu\, X) = 0.1$.

The values of 5.2794 GeV/c^2, 5.3686 GeV/c^2 [6.43] and 5.64 GeV/c^2 [6.44] were used for the masses of B_d^0 , B_s^0 and Λ_b , respectively.

The PYTHIA default value of 1.31 ps for the mean lifetime has been assumed for *all* B-hadrons. This is an underestimation when compared to more recent measurements and averages, which give e.g. [6.45]

$$\tau_B \text{ (inclusive)} = 1.48 \pm 0.03 \quad \text{ps} , \tag{6.41}$$

and, for the exclusive lifetimes,

$$\begin{aligned} \tau\,(B^+) &= 1.62 \pm 0.13 \quad \text{ps} , \quad \tau\,(B_d^0) = 1.43 \pm 0.12 \quad \text{ps} , \\ \tau\,(B_s^0) &= 1.41 \pm 0.22 \quad \text{ps} , \quad \tau\,(\Lambda_b) = 1.07 \pm 0.15 \quad \text{ps} . \end{aligned} \tag{6.42}$$

Two main sources of background contribute to the total background event number: the most important comes from B-hadron 2-body decays, while the other is mainly due to B-hadron multi-body decays. We estimated the background in a mass window of $\pm 1\sigma_B$ around the B_d^0 mass, considering $N_B = N_{B2d} + N_{Bcomb}$ and applying the same selection criteria as for the signal event sample [6.42].

The combinatorial background was estimated making use of a sample of some 70 million $b\bar{b}$ events produced earlier with a selection on the b-quark transverse momentum, i.e. requiring that $p_t^b > 10$ GeV/c [6.42].

The Peterson fragmentation function was used, with the PYTHIA default value $\epsilon_b = 0.006$ [6.46]. The effects from additional event pile-up were not considered.

CMS does not provide particle identification, i.e. the capability of distinguishing between pions, kaons and protons. This leads to a largely irreducible 2-body decay background, as one has to assign the pion mass to protons and kaons as well.

The expected number of signal events N_S is given by

$$\begin{aligned} N_S \;=\; & 2\, L_{\mathrm{int}}\, \sigma_{b\bar{b}} \times \mathrm{BR}\,(\bar{b} \to B_d^0) \times \mathrm{BR}\,(B_d^0 \to \pi^+\pi^-) \times \\ & \times \mathrm{BR}\,(b \to \mu\, X) \times A^\mu\, A^\pi\, \epsilon^c , \end{aligned} \tag{6.43}$$

where $L_{\rm int}$ is the LHC integrated luminosity after one year, A^{μ} and A^{π} are the muon and pion acceptances after the kinematical cuts, and ϵ^{c} is the acceptance of the cuts chosen with the signal selection criteria.

The aim of this analysis is the optimisation of the kinematical cuts and selection criteria, to maximise the number of signal events and, at the same time, the signal to background ratio.

The event selection procedure applied, both to the signal and to the background event samples, has been the following [6.42]:

- kinematical selection of events with one muon with $p_t > 9$ GeV/c and with two hard charged tracks with $p_t > 5$ GeV/c; particle pseudorapidities within $|\eta| \leq 2.4$ (CMS pseudorapidity coverage). The muon and pion acceptances for the signal sample become respectively $A^{\mu} \simeq 0.01$ and $A^{\pi} \simeq 0.26$;

- assignment of the pion mass to the two hard charged tracks;

- selection on the 'distance' $\Delta R^{\pi^+\pi^-}$ between the pion candidates. ΔR is defined as

$$\Delta R = \sqrt{\Delta\eta^2 + \Delta\varphi^2}\,, \tag{6.44}$$

  and it is required that

$$\Delta R^{\pi^+\pi^-} < 1\,. \tag{6.45}$$

- selection on the 'scaled' transverse impact parameter for each of the pion candidates:

$$\sigma_{IP} = \frac{T}{\sigma_T} > 3\,; \tag{6.46}$$

  T is the 'measured' transverse impact parameter. This selection allows to start the time-integration from a favourable value (t_{cut});

- reconstruction of the common vertex of the pion candidates and measurement of the B_d^0 candidate transverse momentum;

- selection on the angle $\Delta\alpha$ between the transverse momentum of the B_d^0 candidate and the vector formed by the primary vertex and the B_d^0 decay vertex; it is required that

$$\Delta\alpha < 100 \text{ mrad}\,; \tag{6.47}$$

- application of the *isolation* criterion: the isolation parameter of the B_d^0 candidate is defined as

$$I = \sum_{\Delta R<1} \frac{p_t(h)}{p_t(B)}\,, \tag{6.48}$$

cuts	signal		background
	g-fusion	g-splitting	
$\Delta R < 1$	1	1	1
$\sigma_{IP} > 3$	0.48	0.44	0.03
$\Delta\alpha < 100$	0.48	0.44	0.01
$I < 0.3$	0.43	0.36	0.003
ϵ_f^c, ϵ_s^c	0.43	0.36	

Table 6.2. Acceptances of the cuts applied, for signal and background events ($B_d^0 \to \pi^+\pi^-$ channel, with 4.8 GeV/c^2 < M($\pi^+\pi^-$) < 5.8 GeV/c^2) [6.42].

where h stands for *hadrons;* it is required that

$$I < 0.3 \quad \text{for} \quad p_t(h) > 2 \text{ GeV/c} . \tag{6.49}$$

The acceptance factors are summarised in table 6.2, and the distributions of the parameters ΔR, σ_{IP}, $\Delta\alpha$ and I are shown in fig. 6.20 for $B_d^0 \to \pi^+\pi^-$ signal events, and in fig. 6.21 for background events other than 2-body decays. The dashed curves in fig. 6.20 correspond to the same distributions, obtained with a previous analysis [6.41].

If one assumes that the gluon splitting mechanism contributes two times more to the total production cross section than the gluon fusion mechanism [6.2], the average signal acceptance using the selection criteria becomes [6.42]

$$\epsilon^c = \frac{\epsilon_f^c + 2\,\epsilon_s^c}{3} \simeq 0.38 . \tag{6.50}$$

Substituting now the appropriate values in (6.43), one obtains the total number of expected signal events:

$$\begin{aligned} N_S &= 2 \times 10^4 \text{ pb}^{-1} \cdot 0.5 \text{ mb} \times (0.40 \cdot 2 \cdot 10^{-5} \cdot 0.1) \times 0.01 \times 0.26 \times 0.38 \\ &\simeq 7900 . \end{aligned} \tag{6.51}$$

Within a $\pm\sigma_B$ invariant mass window around the B_d^0 mass, and considering the appropriate track reconstruction efficiency, we have

$$\begin{aligned} N_S(\pm\sigma_B) &= 7900 \times 0.90 \cdot (0.95)^2 \times 68\ \% \\ &\simeq 4300 , \end{aligned} \tag{6.52}$$

where 0.90 and 0.95 are the average track reconstruction efficiencies for muons and pions respectively.

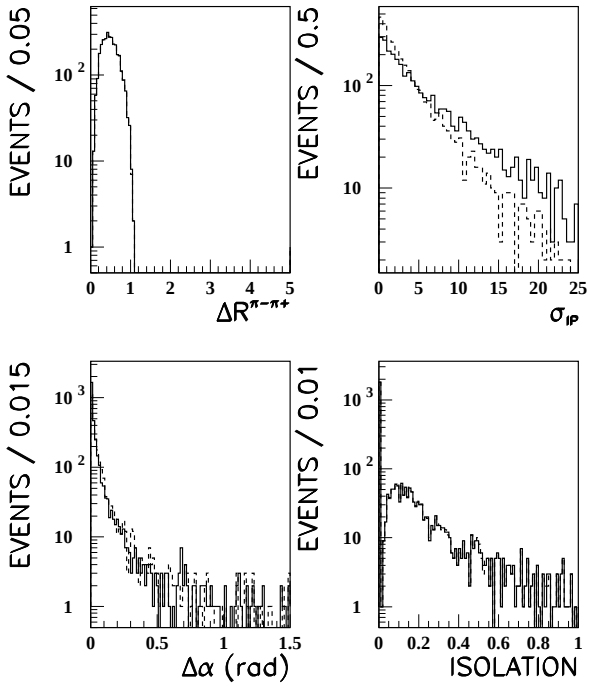

Fig. 6.20. Distributions of relevant variables for $B_d^0 \to \pi^+\pi^-$ signal events [6.42].

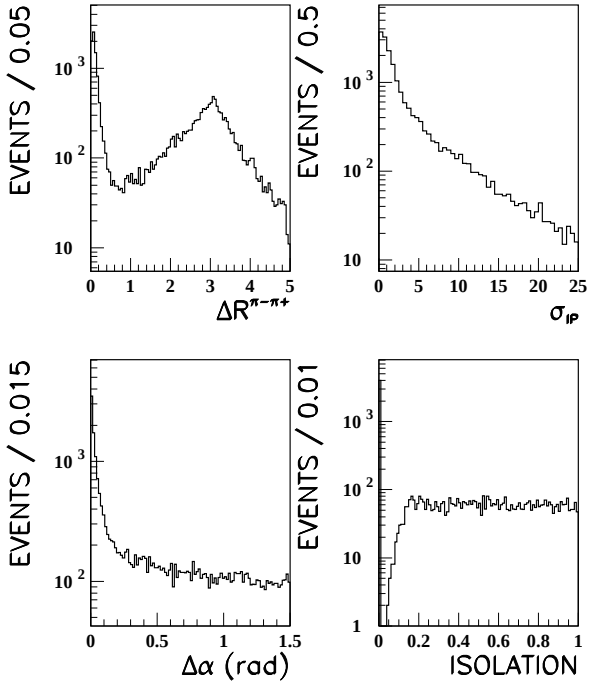

Fig. 6.21. Distributions of relevant variables for $B_d^0 \to \pi^+\pi^-$ combinatorial background events [6.42].

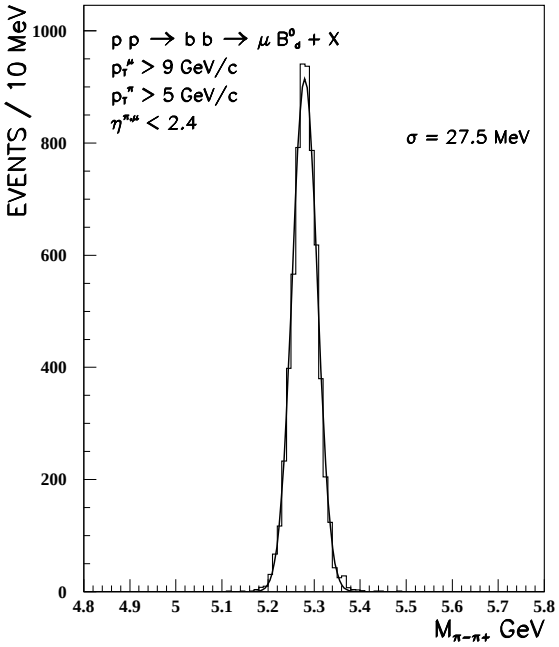

Fig. 6.22. $B_d^0 \to \pi^+\pi^-$ mass resolution [6.42].

The expected $B_d^0 \to \pi^+\pi^-$ mass resolution with the chosen kinematical event selection is given by the fitted value of σ_B, 27.5 MeV/c^2 (fig. 6.22). The mass resolution is the main criterion to reduce the B-hadron 2-body decay background. About half of this background comes from $B_d^0 \to K\pi$ decays, which peak at 5.24 GeV/c^2, i.e. just below the B_d^0 mass (5.28 GeV/c^2). The rest is mainly due to $B_s^0 \to K\pi$, $B_s^0 \to KK$ and $\Lambda_b \to p\,\pi$ decays. The smaller B_s^0 production probability makes the first two background contributions less important, and $\Lambda_b \to p\,\pi$ has an asymmetric contribution. Fig. 6.23 [6.42] shows the overall contamination of the $B_d^0 \to \pi^+\pi^-$ events around the B_d^0 mass, given by these decays.

'Quasi-2-body' decays, such as $B_d^0 \to \rho\pi$, $B_s^0 \to K^*\pi$, $B_s^0 \to K\rho$ and $\Lambda_d \to K\rho$, have been neglected as they are thought to contribute less than 1 % to the background [6.42].

We suppose that the acceptances for the 2-body decay background events are the same as for signal events. Taking a symmetric window $[-\sigma_B; +\sigma_B]$ around the B_d^0 mass, we obtain $N_{B2d} \simeq 3400$ events, and a 2-body contamination

$$\frac{N_{B2d}}{N_S + N_{B2d}} \simeq 45\ \% \ . \tag{6.53}$$

To evaluate the number of combinatorial background events, the same selection criteria were applied to the 70 million $b\bar{b}$ event sample, and ~50 combinatorial background events passed the selection. Rescaling to the number of $b\bar{b}$ events expected

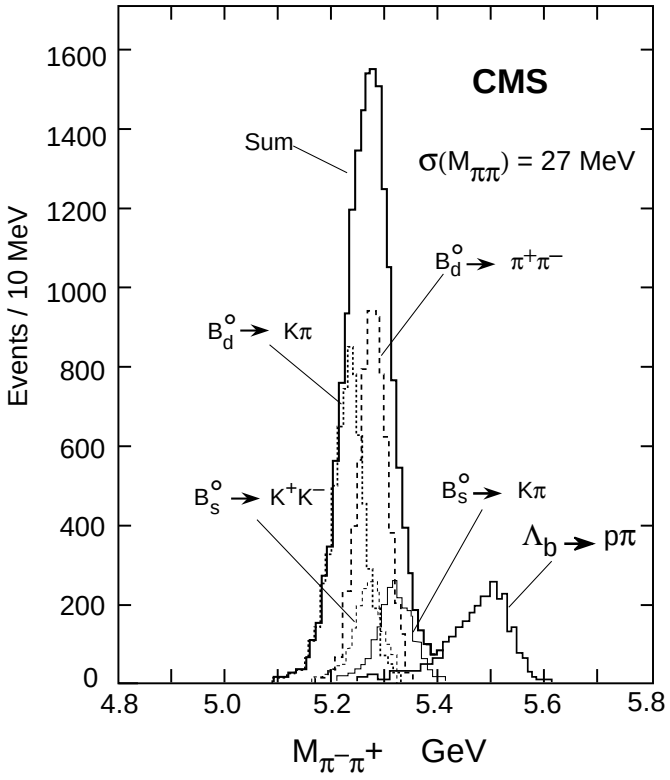

Fig. 6.23. Contamination of $B_d^0 \to \pi^+\pi^-$ signal events around the B_d^0 mass [6.42].

yearly, and in a $\pm\sigma_B$ invariant mass window centered on the B_d^0 mass, we estimated $N_{Bcomb} \simeq 400$ events. Fig. 6.24 shows the superimposition of all the signal and background events expected [6.42].

Table 6.3 shows a summary for the measurement of $\sin 2\alpha$. The integration over time will start at $t_{\rm cut}/\tau \simeq 0.5$, i.e. where the local minimum is reached (fig. 6.19). This value corresponds to $ct_{\rm cut} \simeq 200$ μm, i.e. to the expected secondary vertex resolution; the dilution factor due to the integration over time, obtained from (6.28), is then $D_{\rm int} = 0.67$, having considered $x_d \simeq 0.69$, and the PYTHIA default value $\tau = 1.31$ ps.

Using the appropriate dilution factors discussed above, the expected sensitivity to $\sin 2\alpha$, with a total number of signal and background events of ~4300 and ~3800 respectively, within a $\pm\sigma_B$ B_d^0 mass window, and with an overall dilution factor $D_{\rm tot} \simeq 0.30$, results to be

$$\delta(\sin 2\alpha) \simeq 0.057 \quad \text{(symmetric mass window)} . \tag{6.54}$$

The use of an asymmetric mass window $[-1.5\sigma_B; +2\sigma_B]$ around the B_d^0 mass would increase the number of signal and background events to ~5700 and ~6100 respec-

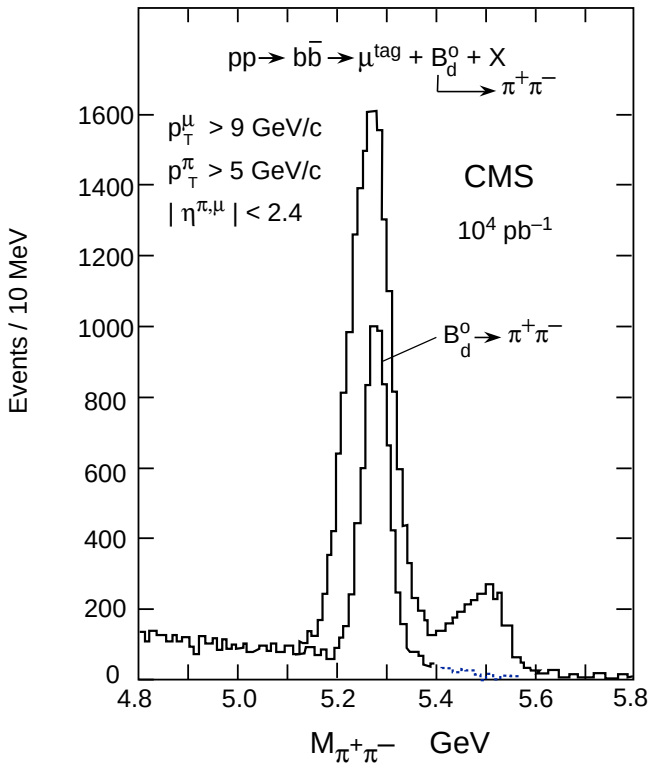

Fig. 6.24. Invariant mass spectrum for $B_d^0 \to \pi^+\pi^-$. $\sigma(B_d^0) = 27.5$ MeV [6.42].

tively, with an overall dilution factor of ~0.28. The sensitivity to $\sin 2\alpha$ would then be

$$\delta(\sin 2\alpha) \simeq 0.050 \quad \text{(asymmetric mass window)} . \tag{6.55}$$

The following uncertainties were used to estimate a systematic error:

- $b\bar{b}$ production cross section for $p_t^b > 10$ GeV/c: ± 30 %,
- relative B_d^0 / B_s^0 production probability: ± 30 %,
- BR$(B_d^0 \to \pi^+\pi^-)$/BR$(B_d^0 \to K\pi)$ ratio: ± 30 %,
- overall dilution factor $D_{\rm tot}$: ± 10 %,

leading to an expected sensitivity to $\sin 2\alpha$ of

$$\delta(\sin 2\alpha) \simeq 0.050\ ^{+0.018}_{-0.014} \quad \text{(asymmetric mass window)} \tag{6.56}$$

for an asymmetric mass window. It should be noted that all of the above listed parameters will be known more precisely by the time of LHC operation.

$\sin 2\alpha$ **measurement**	$p_t\,(\mu_{\rm tag}) > 9$ GeV/c
N(signal) $(B_d^0 \to \pi^+\pi^-)$	4300
N$(B_d^0 \to K\pi)$	1500
N$(B_s^0 \to KK)$	1250
N$(B_s^0 \to K\pi)$	500
N$(\Lambda_b \to p\,\pi)$	150
N(2-body background)	3400
N(combin. background)	400
N(background)	3800
N(total)	8100
D(mix)	0.75
D(tag)	0.76
$\sqrt{\text{D(background)}}$	0.73
D(int)	0.67
$\delta(\sin 2\alpha)$ (time-int.)	0.057
D(tot)	0.30
$\delta(\sin 2\alpha)$ (time-dep.) $_{[\sin 2\alpha \sim 0.4]}$	0.070

Table 6.3. Measurement of $\sin 2\alpha$: summary ($\pm\sigma_B$ symmetric B_d^0 mass window).

The results presented could be improved if the number of signal events were to increase, as $\delta(\sin 2\alpha) \propto 1/\sqrt{N_S}$, accordingly to (6.40). To achieve this goal, it would be possible to consider:

- the implementation of the secondary vertex reconstruction technique instead of the scaled transverse impact parameter, allowing softer cuts which would increase the signal sample while the combinatorial background would be kept under control;

- the reduction of the B-hadron 2-body decay contamination by introducing a means of particle identification for hadrons [6.47];

- an increase in the single muon trigger rate, which would enable softer kinematical cuts to be applied to the tagging muon, and would increase significantly the available statistics.

Finally, the possibilities of electron tagging and triggering for the semileptonic decay of the associated b-quark produced should be investigated.

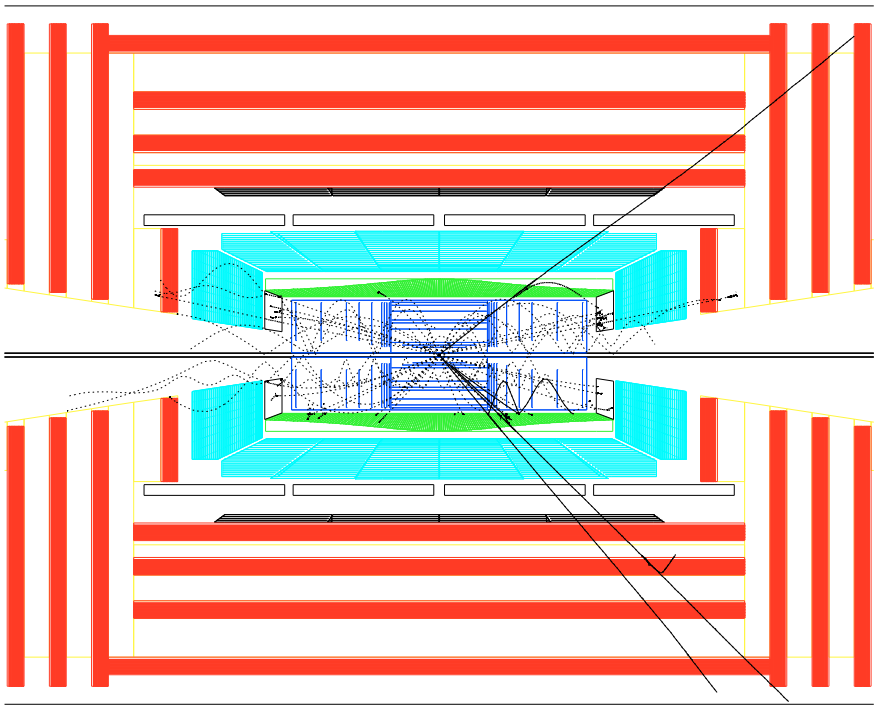

Fig. 6.25. A $b\bar{b} \to B_d^0\ (\bar{B}_d^0)\ + \mu_{\rm tag} \to J/\psi\, K_s^0\ + \mu_{\rm tag} \to \mu^+\mu^-\ \pi^+\pi^-\ + \mu_{\rm tag}$ event [6.2].

6.5.2 The $B_d^0\ (\bar{B}_d^0) \to J/\psi\, K_s^0$ channel

The decay $B_d^0\ (\bar{B}_d^0) \to J/\psi\, K_s^0$ is a very clean channel, with a clear signature and a limited background; it allows the measurement of the CP-violating parameter $\sin 2\beta$, the only one which is theoretically predicted to have a non-zero lower bound. Relatively high branching ratio and good triggering possibilities are further advantages; recent results e.g. from CDF at Fermilab are already rather encouraging.

Simulations for the $B_d^0\ (\bar{B}_d^0) \to J/\psi\, K_s^0$ channel were performed similarly to the case of the $B_d^0 \to \pi^+\pi^-$ channel. For the event tagging, it was required that the associated B-hadron produced should have a semileptonic decay with a production of a *muon,* i.e. giving the overall decay

$$b\bar{b} \ \to\ B_d^0\ (\bar{B}_d^0)\ +\ \mu_{\rm tag}\ \to\ J/\psi\, K_s^0\ +\ \mu_{\rm tag}\ \to\ \mu^+\mu^-\ \pi^+\pi^-\ +\ \mu_{\rm tag}\ ; \qquad (6.57)$$

an event of this kind is shown in fig. 6.25, at the particle level within the CMS detector [6.2]. Two muons are required to reconstruct the J/ψ mass, and the additional reconstructed muon with the highest transverse momentum was considered to be the tagging muon.

The possibilities of a semileptonic decay with the production of an electron, as well as the $J/\psi \to e^+e^-$ decay, are presently under investigation.

Similarly to (6.43), the expected number of signal events N_S is given by

$$\begin{aligned} N_S \;=\; & 2\, L_{\rm int}\, \sigma_{b\bar{b}} \;\times \\ & \times \mathrm{BR}\,(\bar{b} \rightarrow B_d^0) \times \mathrm{BR}\,(B_d^0 \rightarrow J/\psi\, K_s^0) \times \mathrm{BR}\,(J/\psi \rightarrow \mu^+\mu^-) \times \\ & \times \mathrm{BR}\,(K_s^0 \rightarrow \pi^+\pi^-) \times \mathrm{BR}\,(b \rightarrow \mu\, X) \times A^{\rm trig}\, \epsilon^c\,, \end{aligned} \tag{6.58}$$

where $A^{\rm trig}$ is the overall trigger acceptance and ϵ^c is the efficiency of the event selection criteria. The following decay branching ratios were assumed [6.34]:

(a) $\mathrm{BR}\,(B_d^0 \rightarrow J/\psi\, K_s^0) \;=\; 3.3 \cdot 10^{-4}$;

(b) $\mathrm{BR}\,(J/\psi \rightarrow \mu^+\mu^-) \;=\; 0.0597$;

(c) $\mathrm{BR}\,(K_s^0 \rightarrow \pi^+\pi^-) \;=\; 0.6861$;

(d) $\mathrm{BR}\,(\mathrm{b} \rightarrow \mu\, X) \;=\; 0.105$.

Before the trigger acceptance and the selection cuts, the number of expected signal events results then to be $\sim 5.7 \cdot 10^6$ per year. The trigger for these events will be provided by a combined two-muon trigger, which requires that at least two muons have a transverse momentum p_t^μ higher than a threshold depending on pseudorapidity [6.34]:

$$\begin{aligned} & p_t^\mu > 4.5\ \mathrm{GeV/c} \quad \text{if} \quad 0.0 \le |\eta| \le 1.5\ ; \\ & p_t^\mu > 3.6\ \mathrm{GeV/c} \quad \text{if} \quad 1.5 < |\eta| \le 2.0\ ; \\ & p_t^\mu > 2.6\ \mathrm{GeV/c} \quad \text{if} \quad 2.0 < |\eta| \le 2.4\ . \end{aligned} \tag{6.59}$$

The three muons will all be required to be within the rapidity acceptance region, i.e. $|\eta| < 2.4$, and the third muon is required to reach at least the first muon station, i.e. to be recognised.

The following selection criteria are then applied to the decay muons and pions, and to the reconstructed K_s^0 [6.34]:

- selection on the rapidity and on the transverse momentum of the two pion candidates from the K_s^0 decay: $|\eta^\pi| \le 2.4$ and $p_t^\pi \ge 0.7$ GeV/c;
- selection on the K_s^0 transverse flight path $d_t(K_s^0)$: 2 cm $\le d_t(K_s^0) \le$ 40 cm;
- invariant mass constraints applied to the reconstructed J/ψ and K_s^0 masses, which are required to be within a $\pm 2\sigma$ window around their nominal values.

The kinematical parameters of all charged particles were smeared with Gaussian distributions, according to the parameterisations summarised above, to simulate the detector response. No primary vertex constraint was applied.

	$p_t\,(\mu_{\rm tag})$ (GeV/c)				
	> 3.0	> 3.5	> 4.0	> 4.5	> 5.0
$N_{\rm sig}$	10300	9200	8000	6800	5500
$N_{\rm back}$	900	900	800	700	500
$N_{\rm tot}$	11200	10100	8800	7500	6000
wrong tags	18.0 %	16.0 %	14.5 %	14.0 %	13.0 %
D(tag)	0.64	0.68	0.71	0.72	0.74
$\delta(\sin 2\beta)$	0.047	0.046	0.048	0.051	0.055

Table 6.4. Number of events, wrong tag fraction, overall dilution factor and expected sensitivity to $\sin 2\beta$ for different cuts imposed on the tagging muon transverse momentum [6.34].

The resolutions of the $J/\psi(\mu^+\mu^-)$, $K_s^0\,(\pi^+\pi^-)$ and $B_d^0\,(J/\psi\,K_s^0)$ reconstructed masses were found to be respectively 16 MeV/c^2, 8.6 MeV/c^2 and 12 (22) MeV/c^2, the latter with (without) having applied J/ψ and K_s^0 mass constraints [6.34]. Also the B_d^0 reconstructed mass was then required to be within a $\pm 2\sigma$ window around its nominal mass.

A reconstruction efficiency of 95 % for the two most energetic muons was assumed, along with an efficiency of 90 % for the third muon [6.34].

A final requirement is imposed on the transverse momentum of the tagging muon, to limit the fraction of wrong tags. The expected number of events, for different p_t cuts of the tagging muon, is shown in table 6.4 along with the wrong tag fraction and the corresponding overall dilution factor [6.34]. The dilution factors were estimated with a technique similar to the case of the $B_d^0 \to \pi^+\pi^-$ channel. The estimated sensitivities to $\sin 2\beta$, obtained from (6.40), are also listed for the different cases.

The main sources of background to this channel, which would fake the $\mu^+\mu^-\pi^+\pi^-$ signature, are [6.34]:

- inclusive J/ψ or ψ' production following B-hadron decays, which represents the largest contribution;
- direct J/ψ or ψ' production;
- combinatorial background, giving the smallest contribution to the total number of background events.

For all of the above, two charged hadrons would pass the K_s^0 selection criteria, and the event would pass the J/ψ and B_d^0 mass cuts. An additional muon, e.g. from

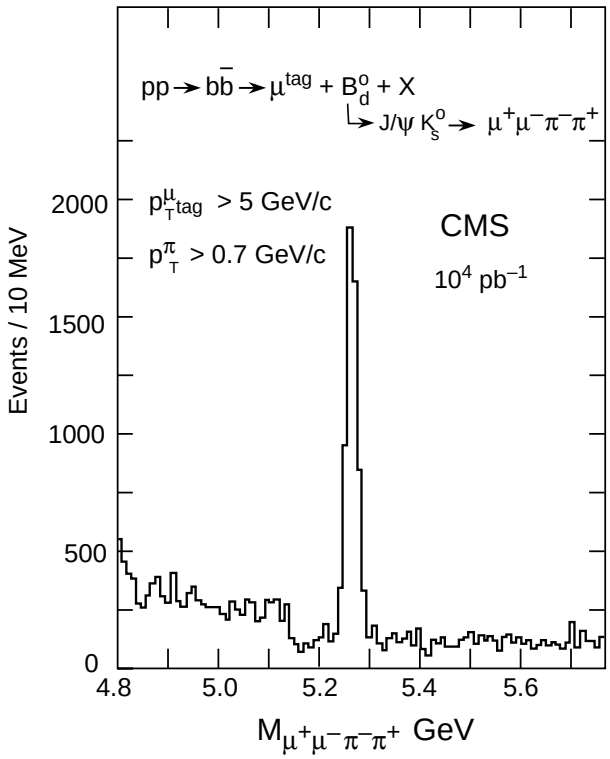

Fig. 6.26. The invariant mass spectrum for $B_d^0 \to J/\psi\, K_s^0$. $\sigma(B_d^0) = 12$ MeV with mass constraints, $\sigma(B_d^0) = 22$ MeV without mass contraints. $\sigma(J/\psi \to \mu^+\mu^-) = 16$ MeV [6.34].

b, c, K or π decays, would be interpreted as a tagging muon. The same selection criteria were applied as for the signal events. Fake K_s^0 were greatly rejected by having required their transverse decay length to be $d_t\,(K_s^0) \geq 2$ cm [6.34].

Fig. 6.26 shows the invariant mass spectrum for $B_d^0 \to J/\psi\, K_s^0\,(\mu^+\mu^-\pi^+\pi^-)$, after all selection cuts, in the case of $p_t\,(\mu_{\rm tag}) > 5$ GeV/c, which gives ~5500 signal events in a $\pm 2\sigma$ mass window around the B_d^0 mass, and an overall signal to background ratio about 10:1.

Finally, table 6.5 shows a summary of the $\sin 2\beta$ measurement with CMS for two of the $p_t\,(\mu_{\rm tag})$ cuts used for this analysis [6.34].

Concluding, the expected sensitivity to the CP-violation parameter $\sin 2\beta$, achievable in a time-integrated measurement, can be quoted to be [6.34]

$$\delta(\sin 2\beta) \;\simeq\; 0.048 \quad (\text{for } p_t\,(\mu_{\rm tag}) > 4 \text{ GeV/c}) \tag{6.60}$$

and

$$\delta(\sin 2\beta) \;\simeq\; 0.055 \quad (\text{for } p_t\,(\mu_{\rm tag}) > 5 \text{ GeV/c})\,, \tag{6.61}$$

using the CMS design version and the physics simulation assumptions as presented

$\sin 2\beta$ **measurement**	$p_t\,(\mu_{\rm tag})$	
	> 4 GeV/c	> 5 GeV/c
N(signal) $(\mu_{\rm tag} + J/\psi \to \mu^+\mu^- + K^0_s)$	8000	5500
N(background) $(\mu_{\rm tag} + \mu^+\mu^- + \pi^+\pi^-)$	800	500
N(total)	8800	6000
D(mix)	0.75	0.75
D(tag)	0.71	0.74
$\sqrt{\rm D(background)}$	0.95	0.96
D(int)	0.47	0.47
$\delta(\sin 2\beta)$ (time-int.)	0.048	0.055
D(tot)	0.48	0.51
$\delta(\sin 2\beta)$ (time-dep.) $_{[\sin 2\beta \sim 0.6]}$	0.038	0.044

Table 6.5. Measurement of $\sin 2\beta$: summary.

in [6.37][7].

Two examples of the issues connected with this analysis, which I have also addressed, are presented below.

The first concerns the CMS geometrical acceptance for muons in the very forward detector regions, i.e. for $|y| \sim 2.2$–2.6; the importance of those regions for the number of geometrically acceptable events, and thus for the achievable sensitivity to $\sin 2\beta$, is shown in fig. 6.27, where the normalised number of $B^0_d \to J/\psi\, K^0_s$ events N and the differential dN/dy are plotted as functions of the rapidity y.

A two-muon trigger was imposed to select events, simulated at the particle level, using variable transverse momentum thresholds improved with respect to (6.59):

$$\begin{aligned} p^\mu_t &> 4.5 \text{ GeV/c} \quad \text{if} \quad 0.0 \le |\eta| \le 1.5\,; \\ p^\mu_t &> 3.5 \text{ GeV/c} \quad \text{if} \quad 1.5 < |\eta| \le 2.0\,; \\ p^\mu_t &> 2.5 \text{ GeV/c} \quad \text{if} \quad 2.0 < |\eta| \le 2.4\,. \end{aligned} \tag{6.62}$$

The third muon was required to be at least identified and reconstructed, i.e. its transverse momentum was required to be greater than a threshold, again variable

[7]The issues of pattern recognition and false secondary vertices, identified because of mismeasured tracks, has only been partially considered for the physics channels relevant to CP-violation. As it has been described, for the $B^0_d \to J/\psi\, K^0_s$ channel reconstruction efficiencies of 95 % for each of the two most energetic muons and 90 % for the third muon have been assumed, and for $K^0_s \to \pi^+\pi^-$ a dedicated study including pattern recognition and reconstruction efficiency was performed [6.35, 6.37, 6.40]; for $B^0_d \to \pi^+\pi^-$ efficiencies of 95 and 90 % were assumed for each pion and for the tagging muon respectively. The implications on the sensitivities should remain within the quoted systematic errors, but more detailed studies are still needed.

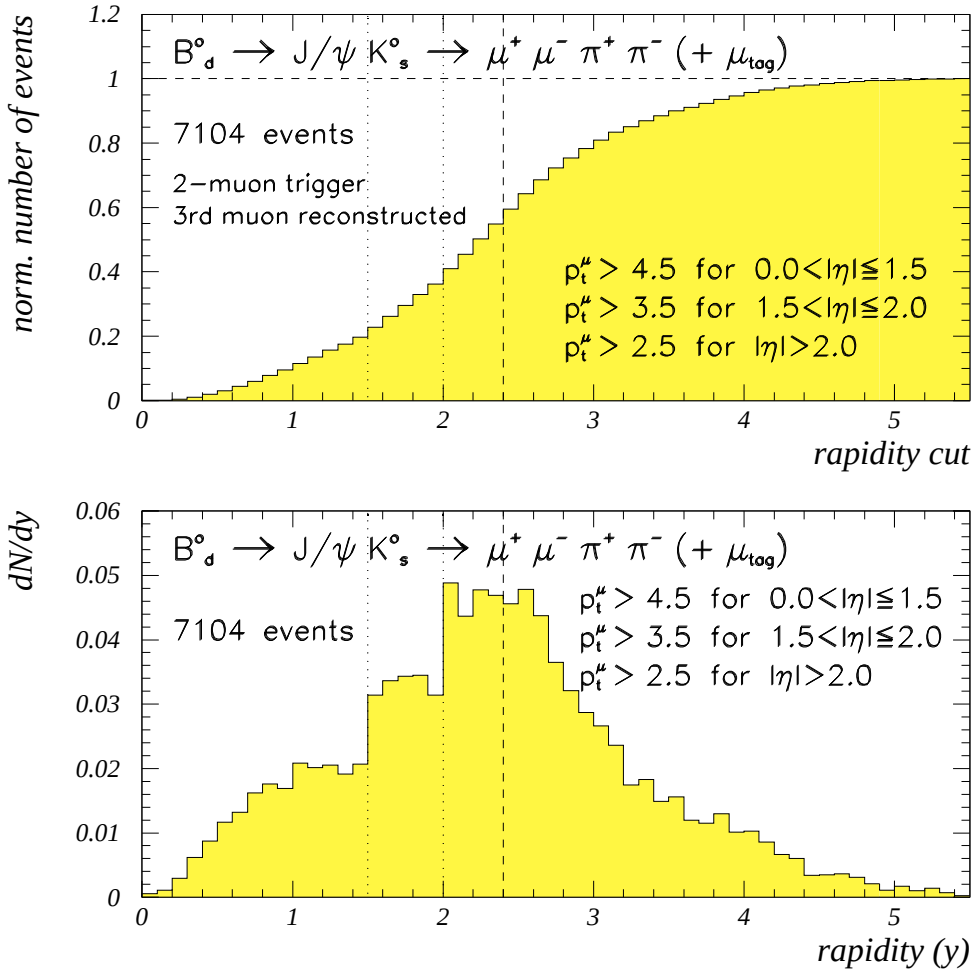

Fig. 6.27. CMS forward muon acceptance: normalised number of events N and differential dN/dy as a function of rapidity y for $B_d^0 \rightarrow J/\psi\, K_s^0 \rightarrow \mu^+\mu^-\pi^+\pi^- + \mu_{\rm tag}$.

with $|\eta|$, but lower than (6.62):

$$\begin{aligned} p_t^\mu &> 4.0\ \text{GeV/c} \quad \text{if} \quad 0.0 \leq |\eta| \leq 1.5\ ; \\ p_t^\mu &> 3.0\ \text{GeV/c} \quad \text{if} \quad 1.5 < |\eta| \leq 2.0\ ; \\ p_t^\mu &> 2.0\ \text{GeV/c} \quad \text{if} \quad 2.0 < |\eta| \leq 2.4\ . \end{aligned} \tag{6.63}$$

The rapidity region 2.0–3.0 is extremely relevant to the total number of events for this channel, and the region considered in these studies extends presently up to $|\eta| = 2.4$.

As an example, if the rapidity coverage could be extended in the forward regions up to $|\eta| \leq 2.6$, we could geometrically accept ~15 % more events compared to the present geometry; on the other hand, if CMS were to reduce the forward muon acceptance to $|\eta| = 2.2$, ~20 % of the events would be lost.

The rapidity region $\sim 2.0 \leq |\eta| \leq \sim 2.7$ corresponds to a rather flat top in the spectrum of the differential number of events, causing relatively important changes in the number of accepted events with small modifications of the muon acceptance in the forward regions.

The second example refers to the optimisation of the multiple muon trigger for low luminosity data taking, aimed at increasing the trigger rate, and therefore the number of recorded events, but remaining within acceptable limits for overall event rates and data storage. This opportunity was investigated in the barrel region, taking into account the most recent developments of the muon trigger algorithm and rate studies [6.48].

Fig. 6.28 shows the normalised number of events N and the differential $dN/dp_t^{\rm cut}$, as functions of $p_t^{\rm cut}$ in the central region, i.e. for $|\eta| \leq 1.5$, again for the $B_d^0 \rightarrow J/\psi\, K_s^0$ channel. The negative sign of the differential $dN/dp_t^{\rm cut}$ is due to the decrease of the number of signal events with increasing $p_t^{\rm cut}$.

A two-muon trigger was applied to the tagging muon and to one of the two muons from the J/ψ decay, using a variable threshold in the barrel region:

$$\begin{aligned} 2.5 \text{ GeV/c} < p_t^{\rm cut}(\mu) < 6.5 \text{ GeV/c} \quad &\text{if} \quad 0.0 \leq |\eta| \leq 1.5 \,; \\ p_t^{\mu} > 3.5 \text{ GeV/c} \quad &\text{if} \quad 1.5 < |\eta| \leq 2.0 \,; \\ p_t^{\mu} > 2.5 \text{ GeV/c} \quad &\text{if} \quad 2.0 < |\eta| \leq 2.4 \,, \end{aligned} \tag{6.64}$$

while the second muon from the J/ψ decay was required to be at least identified ($p_t > 2$ GeV/c).

The plot of the number of events, normalised with respect to the value corresponding to $p_t^{\rm cut}(\mu) = 4.5$ GeV/c, shows the importance of lowering the transverse momentum threshold as much as possible, to increase the number of recorded events relevant to this analysis. If, e.g., the threshold in the central region could be lowered from $p_t^{\rm cut}(\mu) = 4.5$ GeV/c to $p_t^{\rm cut}(\mu) = 4.0$ GeV/c or $p_t^{\rm cut}(\mu) = 3.5$ GeV/c [6.48], the number of accepted events, within the full geometrical coverage, would increase by $\sim$20 % and $\sim$40 % respectively, with an increase as high as $\sim$70 % if the threshold could be lowered e.g. to $p_t^{\rm cut}(\mu) = 3.0$ GeV/c.

The realistic possibilities of implementation of an extended very forward muon coverage and of a lower muon transverse momentum threshold in the barrel region have not yet been fully investigated. These studies were performed to understand in a preliminary way their relevance to the overall physics performance of the experiment as a whole, and both were shown to be very important to the CMS potential for B-physics in general, and for the $B_d^0 \rightarrow J/\psi\, K_s^0$ channel in particular.

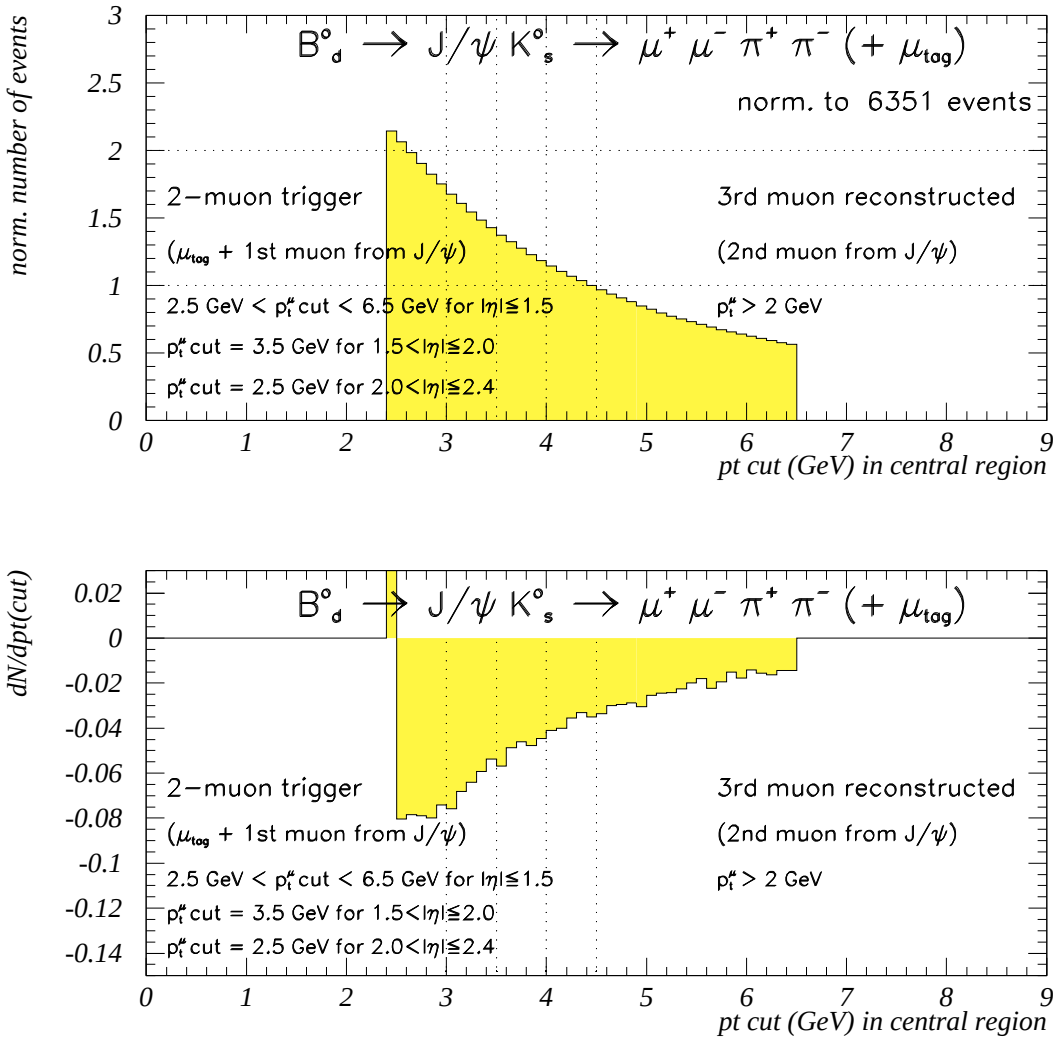

Fig. 6.28. Muon transverse momentum threshold in the CMS central region: normalised number of events N and differential $dN/dp_t^{\rm cut}$ as a function of $p_t^{\rm cut}$ for $B_d^0 \to J/\psi\, K_s^0 \to \mu^+\mu^-\pi^+\pi^- + \mu_{\rm tag}$. The negative sign of the differential $dN/dp_t^{\rm cut}$ is due to the decrease of the number of signal events with increasing $p_t^{\rm cut}$.

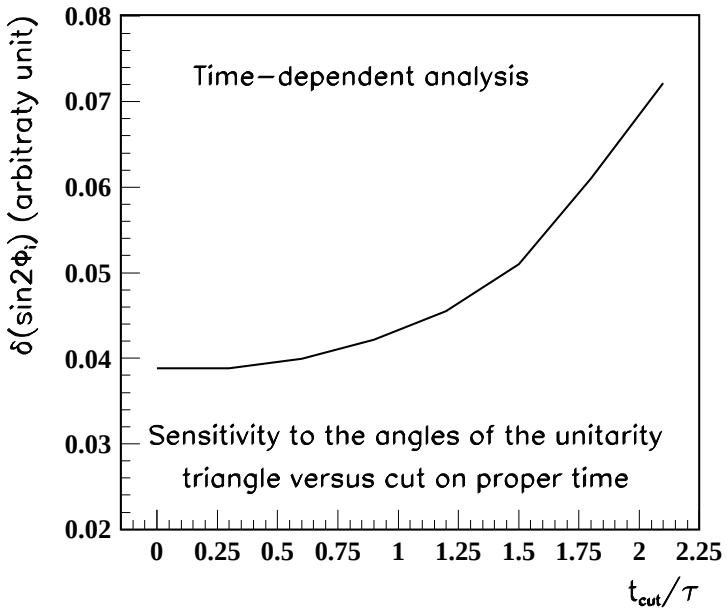

Fig. 6.29. Sensitivity to the angles of the unitary triangle as a function of the cut on the proper time (time-dependent analysis) [6.25].

6.6 Time-dependent asymmetries

The evaluation of the sensitivities to the time-dependent asymmetries was performed making use of the same numbers of signal and background events and dilution factors estimated with the time-integrated analyses.

An original method was developed for this purpose [6.49]. It consists in fitting to the expected line shape, having taken into account all dilution factors, some 'experimental' points. These points have been obtained by distributing, accordingly to an exponential decay distribution convoluted with the expected time-dependent behaviour – for a given input value of $\sin 2\phi_i$, – the number of relevant signal events as a function of the corresponding B_d^0 proper decay time.

The error of the fit, i.e. the estimated sensitivity to $\sin 2\phi_i$, is obviously dominated by the limited statistics which will be available in one year of low luminosity operation at LHC [6.25].

Fig. 6.29 shows the sensitivity to the angles of the unitary triangle as a function of the cut on the proper time: in this case, there is no local minimum, but the curve is rather flat between $t_{\rm cut}/\tau = 0$ (i.e. applying no cut to the B^0 proper time) and $t_{\rm cut}/\tau \simeq 0.5$, and no strong dependence is found up to $t_{\rm cut}/\tau \simeq 1$.

$\sigma(d_t)$	$\sigma(t/\tau)$ $\langle p_t(B_d^0)\rangle \simeq 14$ GeV/c	$\sigma(t/\tau)$ $\langle p_t(B_d^0)\rangle \simeq 7.5$ GeV/c
100 μm	0.09	0.16
200 μm	0.18	0.33
300 μm	0.26	0.49
400 μm	0.35	0.65
500 μm	0.44	0.81

Table 6.6. Transverse secondary vertex resolution $\sigma(d_t)$ and B_d^0 proper time resolution $\sigma(t/\tau)$ for $B_d^0 \to \pi^+\pi^-$ ($\langle p_t(B_d^0)\rangle \simeq 14$ GeV/c) and $B_d^0 \to J/\psi\, K_s^0$ ($\langle p_t(B_d^0)\rangle \simeq 7.5$ GeV/c).

Table 6.6 shows the relation between the transverse secondary vertex resolution $\sigma(d_t)$ and the B_d^0 proper time resolution $\sigma(t/\tau)$, for the two channels considered. It depends on the average B_d^0 transverse momentum $\langle p_t(B_d^0)\rangle$, which is $\sim$14 GeV/c in the case of the $B_d^0 \to \pi^+\pi^-$ channel, and $\sim$7.5 GeV/c in the case of $B_d^0 \to J/\psi\, K_s^0$. This difference is due to the different event selection criteria used in conjunction with the initial muon trigger algorithms.

From simple kinematical considerations,

$$\sigma(d_t) \;=\; \gamma\ \langle\beta_t\rangle\, c\ \sigma(t) \;=\; \frac{\langle p_t\rangle}{m}\,\sigma(t)\;, \tag{6.65}$$

where $\langle\beta_t\rangle$ is the average B_d^0 velocity in the transverse plane, in units of the speed of light c ($\langle\beta_t\rangle = \langle v_t\rangle/c$), γ is the corresponding Lorentz factor, m is the B_d^0 mass and $\sigma(t)$ is the B_d^0 proper time resolution, in natural units. The B_d^0 proper time resolution $\sigma(t/\tau)$, in units of the lifetime τ, is then

$$\sigma\left(\frac{t}{\tau}\right) \;=\; \frac{1}{\tau}\,\frac{m}{\langle p_t\rangle}\,\sigma(d_t)\;, \tag{6.66}$$

where $\langle p_t\rangle$ is the average B_d^0 transverse momentum. Numerically, having substituted in (6.66) the appropriate values, one obtains

$$\sigma\left(\frac{t}{\tau}\right) \;\simeq\; \frac{1}{81.3}\,\frac{\sigma(d_t)\,(\mu\mathrm{m})}{\langle p_t\rangle\,(\mathrm{GeV/c})}\;. \tag{6.67}$$

Using as an example the channel $B_d^0 \to J/\psi\, K_s^0$, a number of parameters were made to vary, with respect to their 'reference' value shown in table 6.7, to investigate the consequences on the estimated sensitivity to $\sin 2\beta$ with the time-dependent analysis. The results can be summarised as follows:

1. input value of $\sin 2\beta$: 0.3, 0.4, 0.6 (fig. 6.30). The absolute sensitivity is

reference parameter	value
input value of $\sin 2\beta$	0.6
sec. vertex resolution in transverse plane	200 μm
points used in fit	all $(t/\tau > 0)$
total dilution factor D(tot)	0.51
tagging muon transverse momentum cut	$p_t\,(\mu_{\rm tag}) > 5$ GeV/c
number of signal events	5500

Table 6.7. Reference values of the parameters used for the evaluation of the sensitivity to $\sin 2\beta$ with a time-dependent analysis.

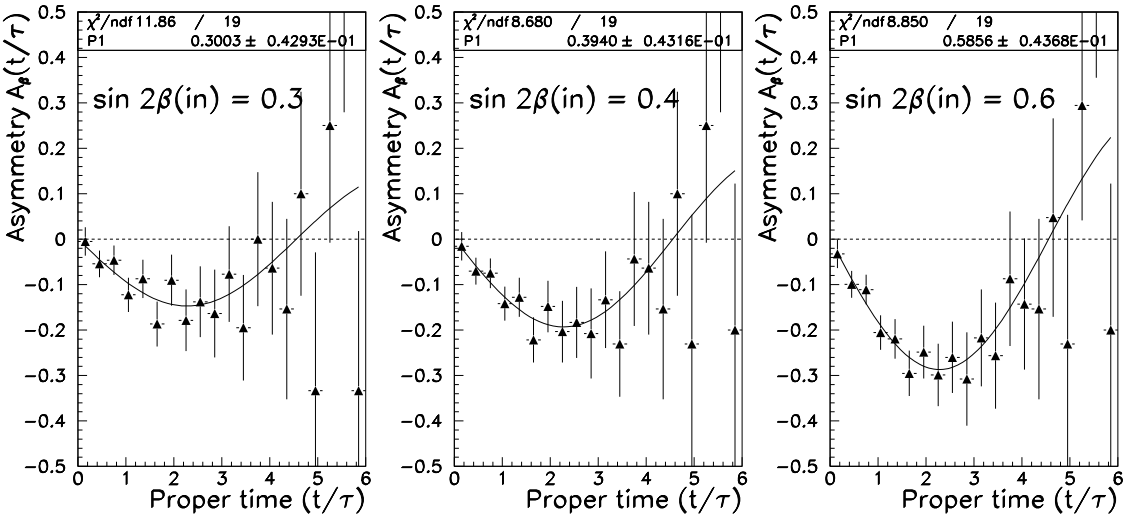

Fig. 6.30. Time-dependent sensitivity to $\sin 2\beta$: input value of $\sin 2\beta$ (0.3, 0.4, 0.6).

essentially unchanged (0.300 ± 0.043, 0.394 ± 0.043, 0.586 ± 0.044), but obviously the relative sensitivity varies from $\sim$14 % in the case of an input value of $\sin 2\beta$ of 0.3, down to $\sim$11% and $\sim$7% for the values of 0.4 and 0.6; on the other hand, the result of the fit is more accurate in the first case (0.300) than e.g. in the third (0.586);

2. total dilution factor $D_{\rm tot}$: 0.3, 0.5, 0.6 (fig. 6.31). Keeping the same number of events, the estimated sensitivity degrades from 0.036 (for $D_{\rm tot} = 0.6$) to 0.070 (for $D_{\rm tot} = 0.3$). This shows the importance of obtaining a total dilution factor as high as possible. This case does not refer to a realistic physical situation, but it does show the dependence of the sensitivity on the total dilution factor;

3. number of points included in the fit (fig. 6.32). The predicted sensitiv-

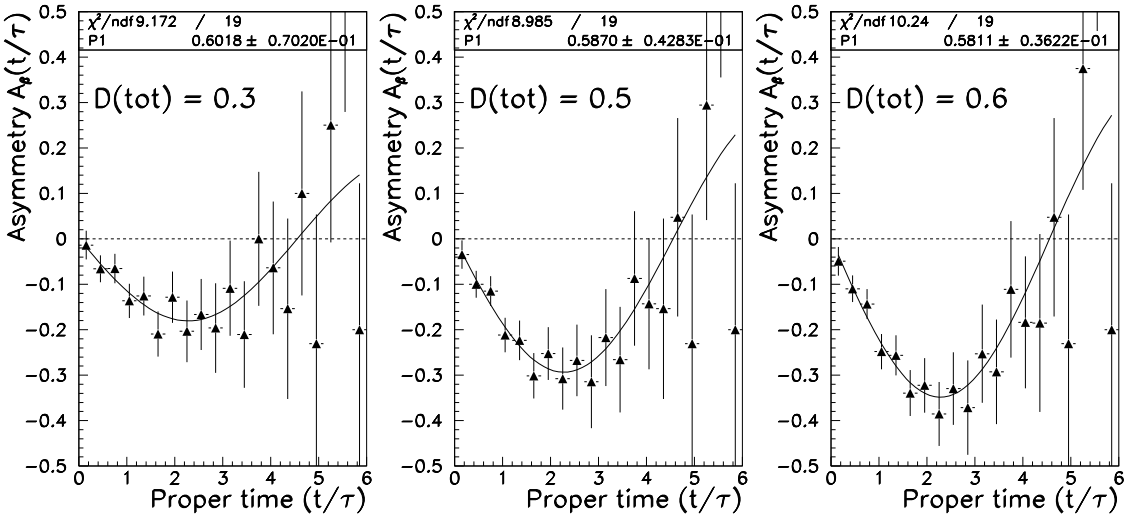

Fig. 6.31. Time-dependent sensitivity to $\sin 2\beta$: total dilution factor (0.3, 0.5, 0.6).

ity, always for the same values of the reference parameters, does not change significantly if varying the limits of the fit, i.e. including all points (fit 1), excluding the first two points ($t_{\rm cut}/\tau \simeq 0.6$, fit 2) or considering $0.6 < t/\tau < 4.5$ (fit 3). The histogram was binned in intervals of $t/\tau = 0.3$;

4. total number of events (fig. 6.33). These plots show that the expected sensitivity varies with the number of events – signal + background – obtained from the time-integrated analysis performed. Depending on the cut on the tagging muon transverse momentum, we obtain
   - with $p_t(\mu_{\rm tag}) > 4$ GeV/c, 8800 events: $\sin 2\beta = (0.579 \pm 0.038)$,
   - with $p_t(\mu_{\rm tag}) > 4.5$ GeV/c, 7500 events: $\sin 2\beta = (0.577 \pm 0.040)$,
   - with $p_t(\mu_{\rm tag}) > 5$ GeV/c, 6000 events: $\sin 2\beta = (0.588 \pm 0.044)$,

   always for the reference input value $\sin 2\beta = 0.6$. They show a decrease in sensitivity, due to the increase in the corresponding total dilution factors.

A similar analysis of the parameters was made in the case of the $\sin 2\alpha$ evaluation. The reference values of the parameters used are shown in table 6.8. As an example, because of the similarities with the previous case, only two series of plots are presented here:

1. fig. 6.34 shows the time-dependent sensitivities when the input value of $\sin 2\alpha$ is 0.4, 0.6 or 0.8. The fit output is respectively (0.438 ± 0.069),

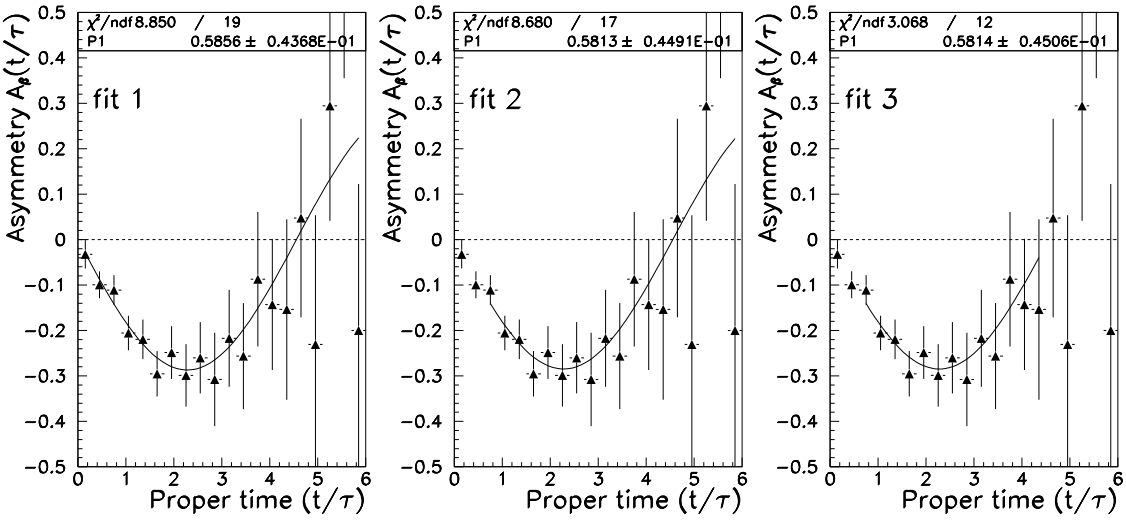

Fig. 6.32. Time-dependent sensitivity to $\sin 2\beta$: number of points included in the fit.

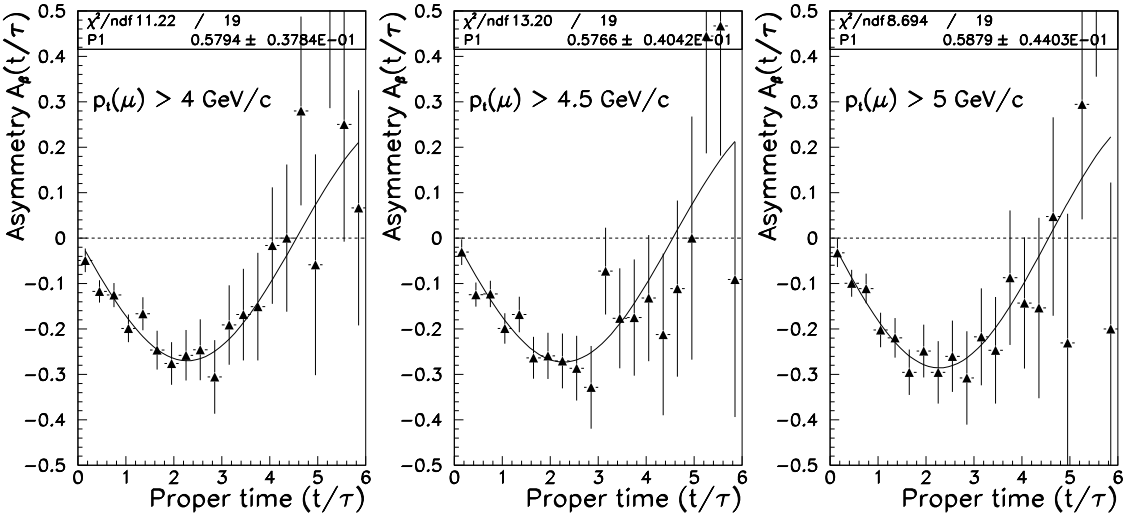

Fig. 6.33. Time-dependent sensitivity to $\sin 2\beta$: number of events (signal + background), depending on the cut on the tagging muon transverse momentum ($p_t(\mu_{\rm tag}) > 4$ GeV/c, 8800 events; $p_t(\mu_{\rm tag}) > 4.5$ GeV/c, 7500 events; $p_t(\mu_{\rm tag}) > 5$ GeV/c, 6000 events).

reference parameter	value
input value of $\sin 2\alpha$	0.4
sec. vertex resolution in transverse plane	200 μm
points used in fit	$t/\tau > 0.6$
total dilution factor D(tot)	0.30
tagging muon transverse momentum cut	$p_t\,(\mu_{\rm tag}) > 9$ GeV/c
number of signal events	4300

Table 6.8. Reference values of the parameters used for the evaluation of the sensitivity to $\sin 2\alpha$ with a time-dependent analysis.

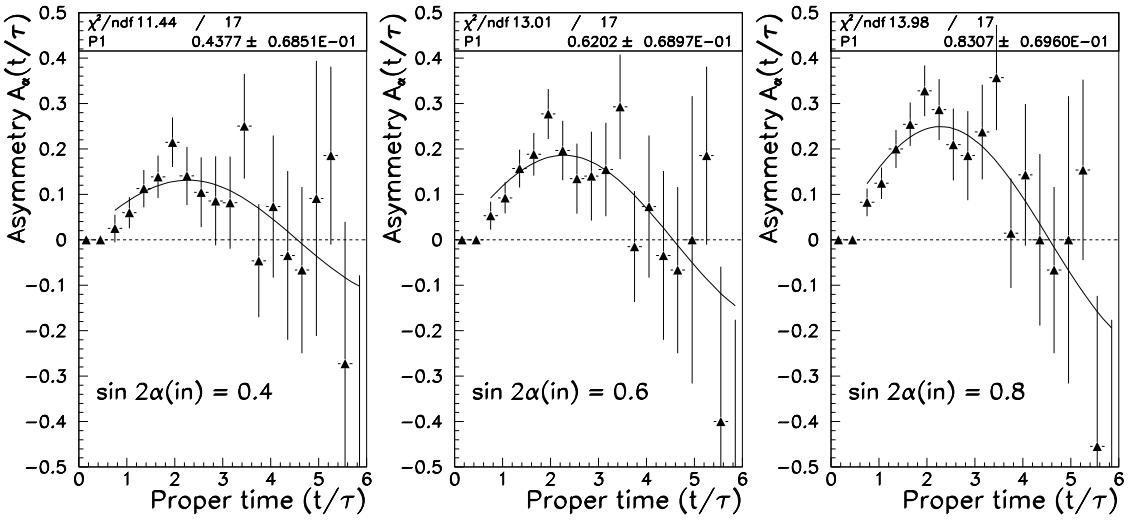

Fig. 6.34. Time-dependent sensitivity to $\sin 2\alpha$: input value of $\sin 2\alpha$ (0.4, 0.6, 0.8).

(0.620 ± 0.069) and (0.831 ± 0.070), showing an unchanged absolute sensitivity, but with corresponding relative sensitivities improving from $\sim$16 % to $\sim$11 % and $\sim$8 %;

2. fig. 6.35 shows the sensitivities if the number of signal events could be increased from 4000 e.g. to 5000 and 6000, keeping all the other reference parameters unchanged. The sensitivity would improve from 0.071 to 0.063 and 0.058 respectively. This case, again, does not correspond to a realistic situation, but it shows the importance of enriching the signal sample as much as possible.

The results of the time-dependent analyses presented in the Technical Proposal are summarised in fig. 6.36, which shows the expected time-dependent asymmetries

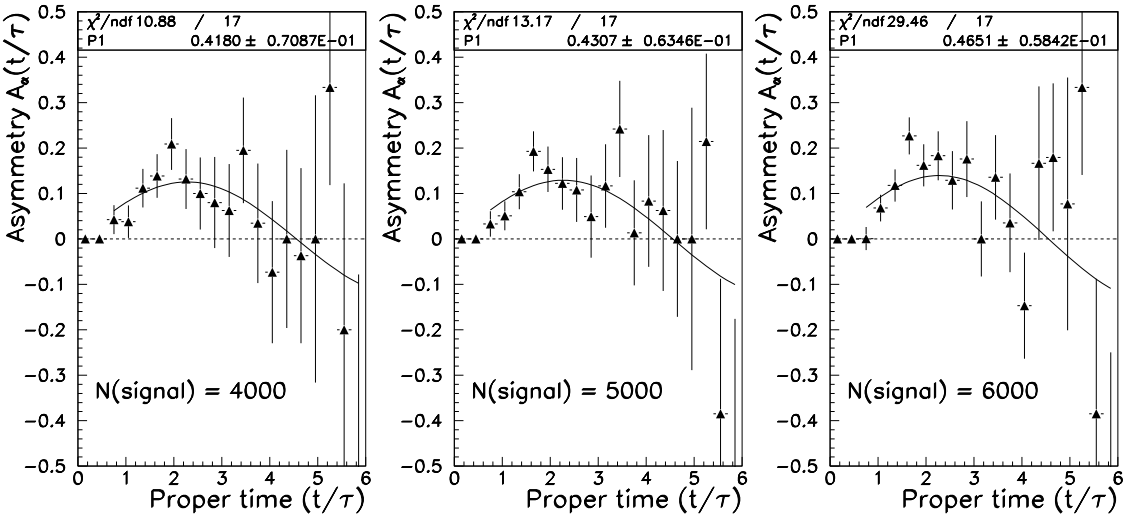

Fig. 6.35. Time-dependent sensitivity to $\sin 2\alpha$: number of signal events (4000, 5000, 6000).

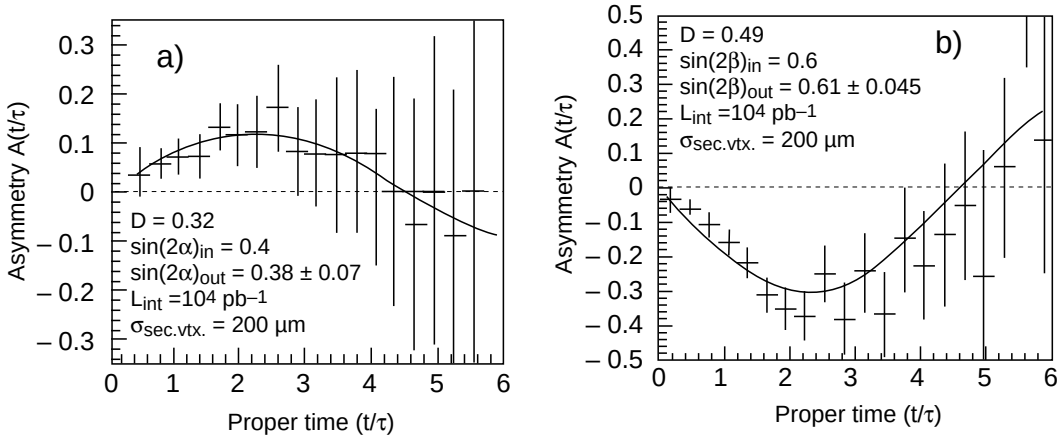

Fig. 6.36. Expected time-dependent asymmetries for $B_d^0 \to \pi^+\pi^-$ – symmetric mass window – (left) and $B_d^0 \to J/\psi\, K_s^0$ (right).

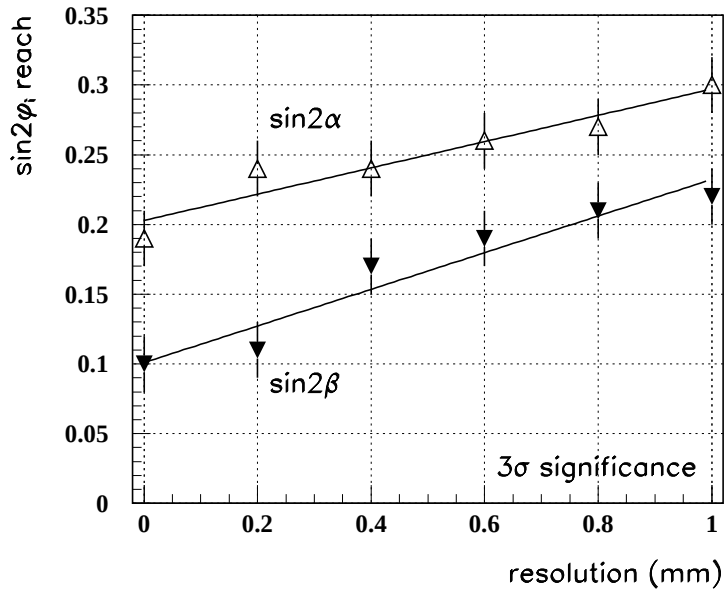

Fig. 6.37. Lowest measurable values of $\sin 2\alpha$ and $\sin 2\beta$ as functions of the secondary vertex resolution (time-dependent analysis).

for $B_d^0 \to \pi^+\pi^-$ (symmetric mass window) and $B_d^0 \to J/\psi\, K_s^0$. $\delta(\sin 2\alpha)$ is $\sim$0.072 and $\delta(\sin 2\beta)$ is $\sim$0.046, for input values of $\sin 2\alpha = 0.4$ and $\sin 2\beta = 0.6$ respectively.

For the time-dependent analysis of the B^0 decays, an appropriate secondary vertex reconstruction is needed. We considered the capability of measuring the CP violating parameters as a function of the secondary vertex resolution in the transverse plane. The lowest value of $\sin 2\phi_i$, measurable with a 3σ significance, was estimated as a function of the experimental resolution, and the behaviour is summarised in fig. 6.37 for the two channels used, with linear fits also shown. In both cases there is a quasi-linear dependence, with a more pronounced slope obtained for $B_d^0 \to J/\psi\, K_s^0$ because of the smaller average p_t of the B_d^0 selected ($\sim$7.5 GeV/c) with respect to the case of the $B_d^0 \to \pi^+\pi^-$ channel, where the average p_t of the B_d^0 is $\sim$14 GeV/c. Therefore, the measurement of $\sin 2\beta$ is more sensitive to the secondary vertex resolution.

From the same figure it can be inferred that CMS would be sensitive to (time-dependent) CP violation down to $\sin 2\alpha \simeq 0.2$ and $\sin 2\beta \simeq 0.1$, having taken into account the dilution factors discussed above.

A simplified estimate of the systematic error was also made, assuming e.g. the

following uncertainties on the

- $b\bar{b}$ production cross section: ± 30 %,
- muon tagging dilution factor D_t : ± 10 %,
- value of x_d : ± 0.07,
- secondary vertex reconstruction accuracy in the transverse plane: ± 50 %,

and using also different initialisations of the random number generator.

The following estimated sensitivities achievable with time-dependent measurements were finally obtained (tables 6.3 and 6.5):

$$\delta(\sin 2\alpha) \simeq 0.070\,^{+0.014}_{-0.011} \quad (\text{for } \sin 2\alpha \sim 0.4)\,, \tag{6.68}$$

$$\begin{aligned} \delta(\sin 2\beta) &\simeq 0.044\,^{+0.014}_{-0.012} \quad (\text{for } \sin 2\beta \sim 0.6\,,\ p_t\,(\mu_{\text{tag}}) > 5 \text{ GeV/c})\,, \\ \delta(\sin 2\beta) &\simeq 0.038\,^{+0.012}_{-0.010} \quad (\text{for } \sin 2\beta \sim 0.6\,,\ p_t\,(\mu_{\text{tag}}) > 4 \text{ GeV/c})\,. \end{aligned} \tag{6.69}$$

6.7 Other B-physics studies

Even though I have been mainly involved in the investigation of the possibilities of CP-violation studies with the CMS apparatus, other possible B-physics issues which can be addressed at the LHC deserve a brief discussion.

The observation of $B_s^0/\bar{B}_s^0$ oscillations is an important goal in particle physics, and it becomes more difficult to achieve the higher the value of x_s . B_s^0 flavour both at production and at decay must be measured; therefore, in CMS we will use the self-tagging decay mode

$$B_s^0/\bar{B}_s^0 \rightarrow D_s^{\mp}\pi^{\pm} \rightarrow \phi\,\pi^{\mp}\pi^{\pm} \rightarrow K^+K^-\,\pi^{\mp}\pi^{\pm}\,, \tag{6.70}$$

where the potential of event reconstruction and the branching ratios are more favourable.

The B_s^0 flavour at production is tagged with the semileptonic (muon) decay of the associated b-hadron, the flavour at decay is known by the charge of the reconstructed D_s. To obtain the value of x_s , the distribution in proper time of the unlike-sign pairs $(D_s^{\pm}\mu^{\mp})$ is subtracted from the distribution of the like-sign pairs $(D_s^{\pm}\mu^{\pm})$, and the maximum amplitude of the Fourier transform $F(x_s)$ of the difference plot will correspond to the most probable harmonic of the oscillation.

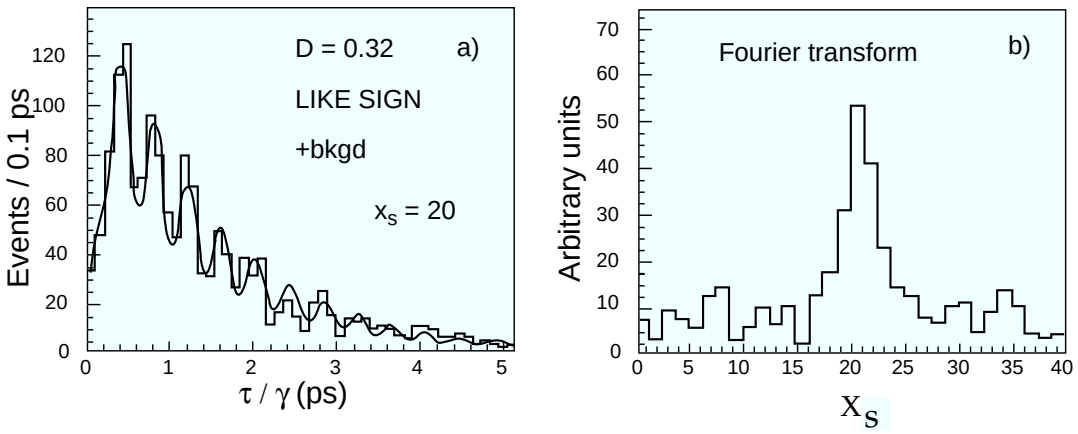

Fig. 6.38. Observability of $B_s^0/\bar{B}_s^0$ oscillations in CMS [6.37].

In this analysis, the resolution in proper time – or in decay length – for the reconstructed secondary vertices plays a crucial role. As a result, the performance of the innermost tracking layers is critical. After having applied trigger and selection cuts, the expected numbers of signal events after one year of operation at low luminosity (10^4 pb^{-1}) is ~2400, with some ~800 corresponding background events; the estimated upper limit to the observable value of x_s is around $x_s \sim 30$.

The observability of $B_s^0/\bar{B}_s^0$ oscillations in CMS is presented in fig. 6.38 [6.37], showing the proper time distribution of like sign pairs, and the Fourier transform $F(x_s)$ of the subtracted distribution, having supposed $x_s = 20$.

The 1995 updated measurements give $11.7 \leq x_s \leq 29.7$ as most probable range, having taken e.g. $f_{B_d}\sqrt{\hat{B}_{B_s}} = 230$ MeV, i.e. the central value of lattice-QCD estimates, but no reliable C.L. can be assigned to it [6.24]. The Standard Model would predict large values for x_s, above the ALEPH 95 % C.L. lower limit of $x_s > 8.8$ [6.50].

The observability of oscillations being strongly dependent on the number of signal events, other B_s^0 decay modes could be examined to increase the signal sample [6.2, 6.37].

The $B_s^0 \to \mu^+\mu^-$ decay is a Flavour Changing Neutral Current (FCNC) suppressed decay, very sensitive to new physics beyond the Standard Model which could enhance the SM predicted branching ratio (2–4 $\times$ 10^{-9} [Ali et al.–Buras]) by an order of magnitude.

Table 6.9 shows the expected number of signal and background events with 10^4 pb^{-1} of data taken at low luminosity (CMS) [6.51]: the selection criteria and the cuts and mass constraints imposed allow an extremely powerful background

cuts	**signal**	**background**
$p_t^\mu > 4.3$ GeV/c, $\|\eta\| < 2.4$	82.0	3.58×10^8
$0.4 < R_{\mu\mu} < 1.2$, $p_t^{\mu\mu} > 12$ GeV/c	45.7	3.53×10^7
isolation ($p_t^{\rm ch} > 1$ GeV/c)	20.7	2.50×10^5
vertex acceptance, $\|\eta\| < 2.1$	16.5	2.03×10^5
vertex cuts: $R > 3 \times \sigma_{\|\|}$, $\chi^2 < 2.5$, $\alpha < 0.04$	12.1	1818
mass constraint: $M_{\mu\mu} = M_B \pm 1.7\sigma_{\mu\mu}$	11.0	16 (< 63 at 90 % c.l.)

Table 6.9. Signal and background events for $B_s^0 \to \mu^+\mu^-$ (10^4 pb^{-1}) [6.51].

rejection, with an expected upper limit to the branching ratio, at the 90 % confidence level, supposing no signal was found in the collected data, as low as 2.4×10^{-9} after one year and 1.4×10^{-9} after three years at low luminosity. The 1995 upper limit from CDF at Fermilab is 8.4×10^{-6} at the 90 % confidence level.

The main selection criteria and cuts consist of requiring that the two muons originate from a common secondary vertex, and after invariant mass reconstruction the events have B^0 masses within appropriate windows. The Bs should also be well isolated, no B-jet being created in such purely leptonic decays [6.2, 6.37, 6.51].

Other possible B-physics studies have been considered and evaluated: large samples of B events will be collected using inclusive low-p_t single- and dimuon triggers, statistics being limited only by an acceptable rate of data storage on permanent media.

Precise measurements of the differential cross-section $\mathrm{d}\sigma/\mathrm{d}p_t$ for b-quark production will provide a test of QCD and add data to existing results.

A large number of beauty baryons will be produced, allowing studies of B-baryon spectroscopy, measurements of polarisation and of weak decay parameters, and possibly the search for CP violating effects in the baryonic sector.

Some $\sim 2 \times 10^5$ events are expected for the channel

$$\Lambda_b \to J/\psi\,\Lambda \to \mathrm{p}\pi\mu\mu\ , \tag{6.71}$$

$\sim 7 \times 10^2$ events for

$$\Xi_b^0 \to J/\psi\,\Lambda \to \mathrm{p}\pi\mu\mu\ , \tag{6.72}$$

and $\sim 8 \times 10^3$ events for

$$\Xi_b^- \to J/\psi\,\Xi^- \to \mathrm{p}\pi\pi\mu\mu\ , \tag{6.73}$$

Experiment (Machine)	**Type (Geometry)**	$\sqrt{s}$ [GeV] ($\mathcal{L}\left[\frac{10^{32}}{\mathrm{cm}^2\ \mathrm{s}}\right]$)	$\sigma_{b\bar{b}}$ [μb] ($\sigma_{b\bar{b}}/\sigma_{\mathrm{tot}}$)	$b\bar{b}$ pairs per year
CDF II (Tevatron)	$p\bar{p}$ collider (central)	2000 (0.2–0.5)	50 (0.1 %)	$\sim 10 \cdot 10^9$
HERA-B (HERA)	p-wire (fixed target)	40 (10–30)	0.01 (10^{-4} %)	$\sim 0.1 \cdot 10^9$
BABAR (PEP-II)	e^+e^- asym (3.1 $\times$ 9 GeV)	10.6 (30-100)	0.001 (20 %)	$\sim 0.03 \cdot 10^9$
BELLE (Tristan-II)	e^+e^- asym (3.5 $\times$ 8 GeV)	10.6 (20-100)	0.001 (20 %)	$\sim 0.02 \cdot 10^9$
CDF/DØ III (Tevatron)	$p\bar{p}$ collider (central)	2000 (0.5–2.0)	50 (0.1 %)	$\sim 25 \cdot 10^9$
ATLAS/CMS (LHC)	pp collider (central)	14000 (10-200)	500 (0.8 %)	$\sim 5000 \cdot 10^9$
LHC-B (LHC)	pp collider (forward)	14000 (0.5-8)	500 (0.8 %)	$\sim 250 \cdot 10^9$

Table 6.10. Parameters of the proposed CP-violation experiments with B-mesons [6.27, 6.53].

with signal to background ratios of ~20, ~0.07 and ~2 respectively.

Finally, heavy B-hadrons such as the B_c meson will be copiously produced for the first time at the LHC.

Bound-state models and QCD effects in heavy quark decays will be studied; masses and lifetimes of these states could be measured [6.34, 6.37, 6.52].

6.8 Conclusions

Measurements of CP-violation in the B-sector are in preparation, with different experimental programmes worldwide. Table 6.10 attempts to summarise a few parameters of the proposed CP-violation experiments with B-mesons, as of 1994, with the expected number of $b\bar{b}$ pairs produced per year – considered of 10^7 s – at the lowest of the quoted luminosities [6.27, 6.53].

CDF and DØ at FNAL (US), BABAR at SLAC (US), HERA-B at DESY (Germany), BELLE at KEK (Japan), and finally ATLAS, CMS and LHC-B at CERN (Switzerland) will perform these studies extensively; asymmetric B-factories and $p\bar{p}/pp$ colliders will allow both discoveries and collection of significant statistical samples, as well as comparisons of results.

The first measurements of CP-violating asymmetries will be probably performed by the end of this decade, and B-physics at the LHC will be an important complement to this research programme, allowing to improve results but also enabling measurements impossible anywhere else.

B-hadron decays, and in particolar neutral B-meson decays, will provide in the near future a powerful test of the Standard Model description of CP-violation, as they will give experimental information on the phases of the CKM matrix elements.

It will be soon possible to search for any manifestation of physics in the B-sector beyond the Standard Model, or else to confirm the model in one of the few yet not fully tested domains, thanks to precision measurements [6.27, 6.32, 6.53, 6.55].

[...] I have on different occasions referred to the essential question that preoccupies the musician, just as it demands the attention of every person moved by a spiritual impulse. The question [...] always and inevitably reverts back to the pursuit of the One out of the Many.

So, in concluding, I once more find myself before the eternal problem implied by every inquiry of an ontological order, a problem to which every man who feels out his way through the realm of dissimilarity—whether he be an artisan, a physicist, a philosopher, or a theologian—is inevitably led by reason of the very structure of his understanding.

[...]

In truth, there is no confusion possible between the monotony born of a lack of variety and the unity which is a harmony of varietes, an ordering of the Many.

"Music," says the Chinese sage Seu-ma-tsen in his memoirs, "is what unifies." This bond of unity is never achieved without searching and hardship. But the need to create must clear away all obstacles. I think at this point of the gospel parable of the woman in travail who "hath sorrow, because her hour is come: but as soon as she is delivered of the child, she remembereth no more the anguish, for joy that a man is born onto the world." How are we to keep from succumbing to the irresistible need of sharing with our fellow men this joy that we feel when we see come to light something that has taken form through our own action?

For the unity of the work has a resonance all its own. Its echo, caught by our soul, sounds nearer and nearer. Thus the consummated work spreads abroad to be communicated and finally flows back towards its source. The cycle, then, is closed. And that is how music comes to reveal itself as a form of communion with our fellow man—and with the Supreme Being.

Igor Stravinski, *Poetics of Music,* lectures at Harvard College (1939-1940), transl. by A. Knodel and I. Dahl, Harvard Univ. Press (1942, 1947, 1970), epilogue, 140-142.

Bibliography

[i.1] M. T. De Vito, *Dennis Sciama: la spiegazione dell'universo (Dennis Sciama: the explanation of universe),* Videosapere, RAI 1, TV-broadcast on 28 August 1995.

[i.2] M. Hack, *Anche gli scienziati hanno bisogno degli alieni (Also scientists need aliens),* Corriere della Sera, 1st October 1995.

[i.3] D. H. Perkins, *Introduction to High Energy Physics,* Addison-Wesley Publ. Co., Inc. (1987).

[i.4] Contemporary Physics Education Project, *Standard model of fundamental particles and interactions* chart, LBL, Berkeley (1990).

[i.5] F. Abe et al., *Observation of top quark production in $\bar{p}p$ collisions with the CDF detector at Fermilab,* Fermilab-pub-95/022-E (1995).

[i.6] J. Ellis et al., *The top quark and Higgs boson masses in the Standard Model and the MSSM,* preprint CERN TH/7261-94 (1994).

[i.7] A. Blondel, *Precision electroweak physics at LEP,* preprint CERN-PPE/94-133 (1994).

[i.8] G. 't Hooft, *Renormalization of massless Yang-Mills fields,* Nucl. Phys. B33 (1971) 173-199; G. 't Hooft, *Renormalizable lagrangians for massive Yang-Mills fields,* Nucl. Phys. B35 (1971) 167-188.

[i.9] Y. L. Dokshitzer, V. A. Khoze, A. H. Mueller, S. I. Trojan, *Basics of Perturbative QCD,* Editions Frontières, Gif-sur-Yvette (1991).

[i.10] S. Weinberg, *Conceptual foundations of the unified theory of weak and electromagnatic interactions,* Rev. Mod. Phys. 52, 515-523 (1980);
A. Salam, *Gauge unification of fundamental forces,* ibid. 52, 525-532 (1980);

S. L. Glashow, *Towards a unified theory: threads in a tapestry,* ibid. 52, 539-543 (1980);
Nobel lectures in physics, 1979.

[i.11] For a general review of the Standard Model many gauge theory textbooks exist, among which:
L. B. Okun, *Leptons and quarks,* North Holland, Amsterdam (1982);
E. Leader, E. Predazzi, *An introduction to gauge theories and the 'new physics',* Cambridge University Press (1982);
I. J. R. Aitchinson and A. J. G. Hey, *Gauge theories in particle physics: a practical introduction,* Adam Hilger Ltd., Bristol (1982);
K. Huang, *Quarks, leptons and gauge fields*, 2nd ed., World Scientific, Singapore (1992).

[i.12] M. Kobayashi and T. Maskawa, *CP-violation in the renormalizable theory of weak interaction,* Prog. Theor. Phys. 49, no. 2, 652-657 (1973).

[i.13] H. E. Haber and G. L. Kane, *The search for supersymmetry: probing physics beyond the standard model,* Phys. Rep. 117, Nos. 2-4, 75-263 (1985).

[i.14] P. Langacker, *Grand unified theories and proton decay,* Phys. Rep. 72, no. 4, 185-385 (1981).

[i.15] A. Filippi, private communications (1995).

Chapter 1

[1.1] M. Pimiä et al., *Compact Muon Solenoid,* Proc. Large Hadron Collider Workshop, Aachen, 4-9 October 1990, eds. G. Jarlskog and D. Rein, CERN 90-10, vol III (1990) 547.

[1.2] *CMS Expression of Interest,* Proceedings of the General Meeting on LHC Physics and Detectors, Evian, 5-8 March 1992, p. 165.

[1.3] *CMS Letter of Intent,* CERN/LHCC 92-3, LHCC/I1, 1 October 1992.

[1.4] The CMS Collaboration, *The Compact Muon Solenoid Technical Proposal,* CERN/LHCC 94-38, LHCC/P1, 15 December 1994.

[1.5] Ch. W. Fabjan, *LHC: Physics, Machine, Experiments,* CERN-PPE/95-25, 17 February 1995, presented at the Meeting of the Canadian, American and

Mexican Physical Societies, CAM '94, September 26-30, 1995, Cancun;
LHC: the Large Hadron Collider – conceptual design, CERN/AC/95-05 (LHC), 20 October 1995.

[1.6] L. Montanet et al., Phys. Rev. D50, 1173 (1994) (Review of particle properties).

[1.7] as in ref. [i.3].

[1.8] *CMS - Compact Muon Solenoid: a general purpose detector for the LHC,* CMS TN/94-133, 5 January 1994.

[1.9] D. Denegri, *The CMS detector and physics at the LHC,* CMS TN/95-167 (1995).

[1.10] G. Wrochna, *The muon system of the CMS detector at LHC,* Nucl. Instr. and Meth. A 344 (1994) 98-104.

[1.11] S. Dasu et al., *CMS Level 1 calorimeter trigger performance studies,* CMS TN/94-285, 28 December 1994.

[1.12] N. Ellis, T. Virdee, *Experimental challenges in high-luminosity collider Physics,* Annu. Rev. Nucl. Part. Sci. 1994, 44:609-53.

Chapter 2

[2.1] as in ref. [1.4].

[2.2] M. Huhtinen and C. Seez, *Uncertainties in fluences and doses at the CMS inner tracker,* CMS TN/95-133 (1995).

[2.3] F. Kuntz and A. Strasser, A.E.R.I.A.L. Strasbourg, private communications (1992-1993).

[2.4] S. Watts and M. Robbins, Brunel University, private communications (1992-1993).

[2.5] P. Clay, Imperial College, London, private communications (1992-1994).

[2.6] as in ref. [1.6].

[2.7] D. Vitè, *Exposure of MOS capacitors to ionising radiation,* CERN-RD20 TN/93-19, July 1993.

[2.8] A.E.R.I.A.L., Strasbourg, internal note.

[2.9] S. Sotthibandhu, *Radiation damage studies of silicon detectors,* PhD thesis, Imperial College, London.

Chapter 3

[3.1] S. M. Sze, *Semiconductor Devices — Physics and Technology,* J. Wiley & Sons, New York (1985).

[3.2] J. E. Gover, J. R. Srour, *Basic radiation effects in nuclear power electronics technology,* American Nuclear Society, June 1985, short course on Radiation Effects in Microelectronics, Boston, Sandia Labs Report SAND85–0776 (1985).

[3.3] G. Parker, *Introductory Semiconductor Device Physics,* Prentice Hall (1994).

[3.4] E. H. Nicollian, J. R. Brews, *MOS (Metal Oxide Semiconductor) Physics and Technology,* John Wiley & Sons (1982).

[3.5] A. Giraldo, *Resistenza alla radiazione del Foxfet in rivelatori a microstrip in silicio (Foxfet radiation resistance on silicon microstrip detectors),* Master's thesis, University of Padova, Italy (1993).

[3.6] P. Richman, *MOS field-effect transistors and integrated circuits,* John Wiley & Sons, New York (1973).

[3.7] K. H. Zaininger, *Electron bombardment of MOS capacitors,* Appl. Phys. Lett., vol. 8 no. 6 (1966) 140-142.

[3.8] A. S. Grove and E. H. Snow, *A model for radiation damage in metal-oxide-semiconductor structures,* Proc. IEEE, no. 54 (1966) 894-895.

[3.9] R. C. Hughes et al., *Dual dielectric silicon metal-oxide-semiconductor field-effect transistors as radiation sensors,* J. Appl. Phys. 65 (5), 1972-1976 (1989).

[3.10] as in ref. [2.7].

[3.11] RD20 Status Report 1993, CERN/DRDC 93-30, 17 August 1993.

Chapter 4

[4.1] G. Hall, *Semiconductor particle tracking detectors,* Reports on Progr. in Physics (1993).

[4.2] A. Peisert, *Silicon microstrip detectors,* in *Instrumentation in high energy physics,* F. Sauli ed., World Scientific, Singapore (1992).

[4.3] as in ref. [3.2].

[4.4] A. Holmes-Siedle and L. Adams, *Handbook of radiation effects,* Oxford University Press (1993).

[4.5] E. Borchi and M. Bruzzi, *Radiation damage in silicon detectors,* La Rivista del Nuovo Cimento, vol. 17 no. 11 (1994).

[4.6] RD20 proposal, CERN/DRDC 91-10 (1991).

[4.7] R. Wheadon, *RD20 p-side test structures (IC/SI),* RD20/TN/3.

[4.8] R. Wheadon, *RD20 n-side test structures (IC/SI),* RD20/TN/2.

[4.9] RD20 status report 1992, CERN/DRDC 92-28, 13 May 1992.

[4.10] as in ref. [3.11].

[4.11] A. Holmes-Siedle et al., *Radiation tolerance of single-sided silicon microstrips,* the RD20 collaboration, Nucl. Inst. and Meth. A 339 (1994) 511-523.

[4.12] The RD20 collaboration, R. Wheadon, *Radiation tolerance studies of silicon microstrip detectors for the LHC,* Nucl. Inst. and Meth. A 342 (1994) 126-130.

[4.13] J. Matheson et al., *Radiation damage studies of field plate and p-stop n-side silicon microstrip detectors,* the RD20 collaboration, preprint CERN-PPE/94-223, submitted to Nucl. Inst. and Meth. A.

[4.14] E. Fretwurst et al., *Radiation hardness of silicon detectors for future colliders,* Nucl. Inst. and Meth. A 326 (1993) 357-364.

[4.15] G. Hall et al., *Calculation of the geometrical capacitance of silicon microstrip structures using a variational approach,* Nucl. Inst. and Meth. A 326 (1993) 228-233.

[4.16] D. Vitè, *Sviluppo di rivelatori a microstrip per i futuri collisionatori adronici (Development of microstrip detectors for future hadron colliders),* Master's thesis, University of Torino (Italy), November 1991.

[4.17] as in ref. [3.5].

[4.18] R. Wheadon, private communication (1996).

[4.19] M. Edwards, private communication (1996).

Chapter 5

[5.1] W. R. Leo, *Techniques for nuclear and particle physics experiments,* Springer-Verlag, 1987.

[5.2] as in ref. [1.6].

[5.3] as in ref. [i.3].

[5.4] Y.-S. Tsai, *Pair production and bremsstrahlung of charged leptons,* Rev. Mod. Phys., vol. 46 no. 4 (1974) 815-851.

[5.5] as in ref. [1.4].

[5.6] *CMS Status report and milestones,* CERN/LHCC 93-48, 15 October 1993.

[5.7] D. Vitè, *Radiation length budget of the CMS central detector,* CMS TN/93-110 (1993).

[5.8] R. Ribeiro, *Material budget calculation of the CMS inner tracker (Technical Proposal),* CMS TN/94-306 (1994).

[5.9] R. Ribeiro, *Material budget calculation of the CMS inner tracker,* CMS TN/94-145 (1994).

[5.10] as in ref. [1.3].

[5.11] D. Vitè, *Radiation length studies for the CMS silicon tracker,* CMS TN/93-94 (1993).

[5.12] GEANT – *Detector description and simulation tool,* CERN Program Library W5013, AS group, CN division, CERN, Geneva.

[5.13] *PAW – Physics Analysis Workstation,* CERN Program Library Q121, AS group, CN division, CERN, Geneva.

[5.14] G. Hall, T. Meyer, R. Ribeiro, G. Smadja, G. Tonelli, private communication (1993).

[5.15] Ch. Seez, private communication (1995).

Chapter 6

[6.1] P. Nason, D. Dawson and K. Ellis, Nucl. Phys. B303 (1988) 607;
A. de Rújula and R. Rückl, ECFA 84-85 and CERN 84-10 (1984), vol. II, 571;
A. B. Kaidalov and O. Piskunova, Zeit. für Phys. C30 (1986) 145.

[6.2] The CMS collaboration, *B-physics and CP violation studies in CMS,* CERN/LHCC 93-49 (1993).

[6.3] H.-U. Bengtsson and T. Sjöstrand, Comp. Phys. Commun. 46 (1967) 43.

[6.4] T. Sjöstrand, PYTHIA 5.7 *and* JETSET 7.4: *physics and manual,* Comp. Phys. Commun. 82 (1994) 74.

[6.5] J. H. Christenson, J. W. Cronin, V. L. Fitch and R. Turlay, *Evidence for the 2π decay of the K_2^0 meson,* Phys. Rev. Lett. 13 (1964) 138.

[6.6] A. Del Rosso, *Realizzazione di un sistema di trigger per un esperimento di violazione di CP nel decadimento dei mesoni K neutri (Realisation of a trigger system for an experiment of CP violation with neutral kaon decays),* Master's thesis, University of Perugia, Italy (1994).

[6.7] G. Grawert, G. Lüders and H. Rollnik, *The TCP theorem and its applications,* Fortschr. der Phys. 7 (1959), 291-328.

[6.8] N. Cabibbo, *Unitary symmetry and leptonic decays,* Phys. Rev. Lett. 10, 531 (1963).

[6.9] S. L. Glashow, J. Iliopoulos and L. Maiani, *Weak interactions with lepton-hadron symmetry,* Phys. Rev. D, vol. 2 no. 7, 1285-1292 (1970).

[6.10] J.-E. Augustin et al., *Discovery of a narrow resonance in e^+e^- annihilation,* Phys. Rev. Lett. 33, 1406-1408 (1974).

[6.11] J. J. Aubert et al., *Experimental observation of a heavy particle J,* Phys. Rev. Lett. 35, 1404-1406 (1974).

[6.12] S. W. Herb et al., *Observation of a dimuon resonance at 9.5 GeV in 400-GeV proton-nucleus collisions,* Phys. Rev. Lett. 39, 252-255 (1977);
W. R. Innes et al., *Observation of structure in the* Υ *region,* Phys. Rev. Lett. 39, 1240-1242 (1977).

[6.13] M. Kobayashi and T. Maskawa, *CP-violation in the renormalizable theory of weak interaction,* Prog. Theor. Phys. 49, no. 2 (1973), 652-657.

[6.14] M. L. Perl et al., *Evidence for anomalous lepton production in* e^+–e^- *annihilation,* Phys. Rev. Lett. 35, 1489-1492 (1975);
M. L. Perl et al., *Properties of anomalous* $e\mu$ *events produced in* e^+–e^- *annihilation,* Phys. Lett. 63 B, 466-470 (1976).

[6.15] D. J. Gross and R. Jackwin, *Effect of anomalies on quasi-renormalizable theories,* Phys. Rev. D, vol. 6 no. 2 (1972) 477-493.

[6.16] C. Itzykson and J.-B. Zuber, *Quantum field theory,* McGraw-Hill (1990).

[6.17] as in ref. [i.3].

[6.18] L. Wolfenstein, *Parametrization of the Kobayashi-Maskawa matrix,* Phys. Rev. Lett. 51, no. 21 (1983), 1945-1947.

[6.19] as in ref. [1.6].

[6.20] A. Ali and D. London, *Implications of the top quark mass measurement for the CKM parameters,* x_s *and CP asymmetries (revised and updated),* preprint CERN TH/7398-94 and UdeM-GPP-TH/94-06 (1994), submitted to Zeit. für Phys. C.

[6.21] ECFA Workshop on a European B-meson factory, Desy, Hamburg, Germany and CERN, Geneva, Switzerland (1991-1992), *B-physics working group report,* R. Aleksan and A. Ali eds., ECFA 93-151 and DESY 93-053 (1993).

[6.22] G. Nardulli, *Theory review of CP violations in B decays at hadron colliders,* Nucl. Inst. and Meth. A 333 (1993) 3-11.

[6.23] A. Ali, *CKM update,* B^0–$\bar{B}^0$ *mixings and rare B decays – a review,* Nucl. Inst. and Meth. A 351 (1994) 1-7.

[6.24] A. Ali and D. London, *CP violation and flavour mixing in the Standard Model,* presented at the 6th Int. Workshop on Heavy Flavour Physics, Pisa, Italy, 6-10 June 1995, preprint DESY 95-148 and UdeM-GPP-TH/95-32 (1995).

[6.25] A. Kharchilava and D. Vitè, *CP violation: measurement of the time-dependent asymmetry in the channels* $B_d^0 \to \pi^+\pi^-$ *and* $B_d^0 \to J/\psi\, K_s^0$ *,* CMS TN/94-193 (1994).

[6.26] H. Albrecht et al., *A study of* $\bar{B}^0 \to D^{*+} l^- \bar{\nu}$ *and* $B^0\bar{B}^0$ *mixing using partial* D^{*+} *reconstruction,* the ARGUS collaboration, Phys. Lett. B 324 (1994), 249-254.

[6.27] R. Forty, *CP violation and* $B^0/\bar{B}^0$ *mixing,* XXVII Int. Conf. on High Energy Physics, Glasgow, Scotland, 20–27 July 1994, CERN-PPE/94-154 (1994).

[6.28] Abe et al., *Measurement of the* B^+ *and* B^0 *meson lifetimes,* Phys. Rev. Lett. 72, 3456 (1994).

[6.29] M. Gronau, *CP violation in neutral-B decays to CP eigenstates,* Phys. Rev. Lett. 63, 1451-1454 (1989).

[6.30] M. Gronau, *Large penguin effects in the CP asymmetry of* $B_d^0 \to \pi^+\pi^-$ *,* SLAC-PUB-5911 (1992), and Phys. Lett. B 300 (1993), 163-168.

[6.31] M. Gronau and D. London, *Isospin analysis of CP asymmetries in B decays,* Phys. Rev. Lett. 65, 3381-3384 (1990).

[6.32] D. London, *CP violation in the B system: what's old, what's new ?,* prep. UdeM-LPN-TH-94-199 and Proceedings of the *5th conference on the intersections of particle and nuclear physics,* St. Petersburg, Florida, USA (1994).

[6.33] M. Chaichian and A. Fridman, *On a possibility for measuring effects of CP violation at pp colliders,* Phys. Lett. B 298 (1993), 218-223.

[6.34] D. Denegri et al., *B physics and CP violation studies with the CMS detector,* Nucl. Inst. and Meth. A 351 (1994) 95-110.

[6.35] D. Denegri et al., *B physics and CP violation studies with the CMS detector at LHC,* Int. Journ. Mod. Phys. A, vol. 9 no. 24, 4211-4255 (1994).

[6.36] V. Karimäki, *Fast tracker response simulation,* CMS TN/94-275 (1994).

[6.37] as in ref. [1.4].

[6.38] D. Denegri et al., *Justifications for a microvertex detector in CMS,* CMS TN/94-258 (1994).

[6.39] as in ref. [5.12].

[6.40] J. F. Hassard and S. Margetides, *Tracking for B physics in CMS,* Proceedings of the *Snowmass meeting on B physics in Hadron Colliders,* July 1993.

[6.41] A. Kharchilava, *Study of the $B_d^0 \to \pi^+\pi^-$ decay,* CMS TN/93-114 (1993).

[6.42] A. Kharchilava, P. Pralavorio and D. Vitè, *CP violation: study of the $B_d^0 \to \pi^+\pi^-$ decay for the Technical Proposal,* CMS TN/94-328 (1994).

[6.43] Buskulic et al., Phys. Lett. B 311 (1993) 425, and *First measurement of the B_s^0 meson mass,* the ALEPH coll., preprint CERN-PPE/93-97 (1993).

[6.44] Albajar et al., Phys. Lett. B 273 (1991) 540, and the UA1 coll., preprint CERN-PPE/91-202 (1991).

[6.45] R. Forty, *The lifetime and mixing of B hadrons,* preprint CERN-PPE/93-165 (1993), presented at the XIII International Conference on Physics in Collision, Heidelberg, Germany, 16-18 June 1993.

[6.46] C. Peterson et al., *Scaling violation in inclusive e^+e^- annihilation spectra,* Phys. Rev. D 27 (1983) 105.

[6.47] Y. Lemoigne, Physics simulation group, September 1994.

[6.48] G. Wrochna, private communication (1994-1995).

[6.49] A. Kharchilava, private communication (1994-1996).

[6.50] the ALEPH collaboration, *Limit on B_s^0 oscillation using a jet charge method,* preprint CERN-PPE/95-084 (1995), Phys. Lett. B 356 (1995) 409.

[6.51] A. Nikitenko and A. Starodumov, *On the possibility to observe the $B_s^0 \to \mu^+\mu^-$ decay with CMS,* CMS TN/94-186 (1994).

[6.52] D. Vitè, *B-physics prospects with ATLAS and CMS at the LHC,* presented at the 6th Int. Workshop on Heavy Flavour Physics, Pisa, Italy, 6-10 June 1995, CMS TN/95-010 (1995).

[6.53] CDF-DOC-Advisory-Public/2436;
DESY-PRC/94-02 (1994);
SLAC/443;
KEK-Report/94-2 (1994);
CERN-LHCC/92-3 (1992); CERN-LHCC/92-4 (1992); CERN-LHCC/93-50 (1993).

[6.54] P. Pralavorio, private communication (1994-1996).

[6.55] B. Kayser, *How B decays can test the Standard Model of CP violation,* prep. NSF-PT-94-3 and Proceedings of the *XVI Kazimierz meeting on elementary particle physics,* Kazimierz, Poland (1993).